

**Biochemical characterisation of
the translocation of material
through the protective antigen
(PA) Pore.**

**Susan Amanda Shorter [B.Sc. (Hons),
M.Sc.]**

A thesis submitted in partial fulfilment of
the requirements of the University of
Greenwich for the Degree of Doctor of
Philosophy.

April 2017

Declaration

I certify that the work contained in this thesis, or any part of it, has not been accepted in substance for any previous degree awarded to me, and is not concurrently being submitted for any degree other than that of Doctor of Philosophy being studied at the University of Greenwich. I also declare that this work is the result of my own investigations, except where otherwise identified by references and that the contents are not the outcome of any form of research misconduct.

Susan Shorter (Candidate)

.....

PhD Thesis Supervisors

Dr Simon Richardson (1st Supervisor)

Dr Paul Dyer (2nd Supervisor)

Acknowledgements

I would like to thank firstly my supervisors, Dr. Simon Richardson, and Dr. Paul Dyer for their constant support, advice and guidance throughout the years, and the opportunities that have been made to me.

I would also like to thank Dr. Beatrice Cottazo and Professor Peter Griffiths for assistance with SANS analysis, Dr Rob Barker, for assistance in fitting Neutron Reflectometry data, and help and guidance with these experiments. I would also like to thank Dr. Marie Pettit and Dr. Paul Dyer for use of HDSC and CD data discussed within the thesis and thanks to Dr Ian Slipper and Andrew Hurt for assistance with SEM and TEM image capture.

A special thanks to my laboratory colleagues Emma Coakley, Monique Aurora Morgana Patrick and Becki Jones for constant support, laughter and coffee.

Finally, I would also like to thank my partner Ronnie, for putting up with me working late nights, and weekends and giving me support throughout this study, and to my daughter Layla for always putting a smile on my face.

Abstract

Biochemical Characterisation of the translocation of material through the protective antigen (PA) Pore

Bacillus anthracis secretes a tripartite protein complex, forming the toxin known as anthrax toxin. It is composed of the catalytically active proteins, lethal factor (LF) and oedema factor (EF), and protective antigen of 83 kDa (PA83). This toxin complex mediates cytosolic entry through the formation of an oligomeric PA pore, facilitating translocation of LF and EF, an event critical for EF and LF to exert their cytotoxic effects. The requirements for translocation are still poorly understood, and essential for understanding the limitations and possible utility to this pore. Once the dynamics of translocation are more clearly understood, therapeutics for inhibiting LF and EF toxicity could be developed for anthrax treatment, as well as the potential to develop this pore into a drug delivery platform. The project outlined herein was to evaluate the requirements for molten globular (MG) transition during translocation of LF and EF through the PA pore. This study documented the translocation of a variety of biochemically and thermodynamically distinct constructs (protein and protein:DNA), and their ability to pass through the PA pore. Pore translocation was detected by monitoring gene modulation, toxicity, fluorescent microscopy and neutron reflectometry. The ability of LFn-GAL4, antisense oligonucleotide (ASO) complex to translocate and mediate gene modulation was assayed *in vitro*. The components of this complex were found to be non-toxic individually and together (PA83, LFn-GAL4:ASO). This complex was found to be able to deliver ASOs and mediate cytosolic access as demonstrated by the decreased level of endogenous syntaxin 5 post-treatment (77 % \pm 11.6). Then the ability of LFn-Ricin toxin A chain (RTAC) to translocate through the pore was evaluated by cytotoxicity. This demonstrated limited

cytotoxicity *in vitro*, indicating that this cationic protein either couldn't translocate or once translocated was no longer a functional enzyme. Further to this, LFn-GFPs ability to translocate, assayed in the presence and absence of the PA pore. LFn-GFP demonstrated translocation in the presence and absence of PA in HeLa cells over 4, 6 and 16 hours. In the presence of PA cytosolic signal increased over this time frame (from 0% of the input to 4%) whereas in the absence of PA cytosolic signal decreased from 4% to 0%). Binding and translocation of deuterated LFn-GFP with the both a lipid-nanodisc and a lipid-nanocomplex (NC – a nanodisc containing the protective antigen pore) was followed in real time at pH7.4 and 37°C mimicking physiological conditions and at pH 5.5 mimicking the acidity of late endosomes. Measurements were performed in a variety of solvents, namely H₂O, D₂O, SiMW and 4MW. Neutron reflectometry (NR) measurements showed approximately 90% coverage of ND and approximately 10% coverage of NC at the silica/solvent interface. A significant change in spectra was observed following addition of dLFn-GFP, alteration of pH from pH7.4 to pH5.5 resulted in translocation of LFn-GFP into the PA layer on the NC as determined by a decrease in hydration of the ND and an increase in hydration of the PA layer.

Table of Contents

Abstract	IV
Table of Contents	VI
Abbreviations	IX
List of Tables	XII
List of Figures	XII
Chapter 1 - Introduction	1
1.1 Anthrax	1
1.11 Aetiology of anthrax	2
1.12 Zoonotic transmission of anthrax	4
1.13 Anthrax treatment in humans	6
1.2 Global consequences of anthrax	7
1.21 Bioterrorism	7
1.22 Agricultural and veterinary risk	8
1.3 ATx assembly and cellular internalisation	9
1.4 PA, EF and LF molecular dynamics and function	15
1.41 Lethal Factor (LF)	15
1.42 Oedema Factor (EF)	16
1.43 Protective Antigen of 83 KDa (PA83)	18
1.44 Protective Antigen Pore	19
1.5 Protein translocation across the PA pore	23
1.51 PA pore physiology in relation to translocase function	25
1.6 Aims of this thesis	31
Chapter 2 - Material and Methods	32
2.1 Materials	32
2.11 Chemicals List	32
2.12 Equipment List	33
2.13 Stock Solutions	34
2.14 Gels for Electrophoretic separations	36
2.15 Organisms and cells	37
2.16 Antibodies	37
2.17 Plasmid Templates	38
2.2 Methods	40
2.21 Sub-cloning into bacterial expression vectors.	40
2.22 Plasmid Purification	43
2.23 Protein expression and characterisation	45
2.24 Characterisation of recombinant proteins	48
2.25 Mammalian cell culture	50
Chapter 3 A study into the capacity of the PA pore to deliver a supramolecular assembly to the cytosol.	56
3.1 Novelty statement	56
3.2 Introduction	56
3.21 Antisense Oligonucleotides	58
3.22 Antisense mode of activity	58
3.23 Problems with antisense as a therapeutic	59

3.2 Chapter Specific Methods	62
3.21 Scanning electron microscopy	62
3.22 ASO Annealing	63
3.23 ASO transfection experiments	63
3.3 Results	63
3.31 PA83 production and characterisation	63
3.32 Characterisation of LFn-Gal4 protein production	68
3.33 PA and LFn-GAL4 <i>in vitro</i> toxicity profiles	70
3.34 Antisense Oligonucleotide Design and Characterisation	81
3.35 Transfection Experiments	83
3.4 Discussion	87
3.5 Conclusion	92
Chapter 4 To determine whether a thermodynamically plastic cationic substrate (LFn-RTAC) can translocate through the PA pore.	94
4.1 Novelty Statement	94
4.2 Introduction	94
4.21 Exogenous protein translocation through the PA pore	94
4.22 Protein Translocation through the PA pore	95
4.23 Ricin Toxin	97
4.3 Chapter Specific Methods	99
4.31 <i>In vitro</i> RTBC binding assay	99
4.32 HeLa <i>In vitro</i> coupled translation assay	99
4.4 Results	101
4.41 Characterising RTAC and RTBC	101
4.42 Developing and Characterising Protein Constructs	103
4.43 LFn-RTAC ability to facilitate translational arrest	105
4.44 The PA dependent cytosolic translocation of LFn-RTAC	107
4.5 Discussion	109
4.6 Conclusion	111
Chapter 5 Investigating the ability of the PA pore to translocate structurally stable fluorescent molecules.	113
5.1 Novelty Statement	113
5.2 Introduction	113
5.21 Translocation models	115
5.22 Translocating Proteins	116
5.3 Chapter Specific Methods	119
5.31 Fluorescent Spectroscopy	119
5.32 LFn-GFP Translocation Studies	119
5.33 Preparation of post-nuclear supernatant	119
5.4 Results	121
5.41 Protein Production and characterisation	121
5.411 LFn-GFP protein production and characterisation	121
5.412 LFn-YFP protein production and characterisation	127
5.413 LFn-mCherry protein production and characterisation	131
5.42 Characterisation of markers for subcellular fractionation (using Western blot) and indirect immunofluorescence microscopy	134
5.43 Fluorescent protein cytosolic translocation in Vero cells	141
5.44 Fluorescent protein translocation using HeLa cells	144
5.45 Subcellular fractionation	149
5.5 Discussion	154
5.6 Conclusions	163

Chapter 6 – Investigating the structural dynamics associated with cargo binding and translocation in real time.	164
6.1 Novelty Statement	164
6.2 - Introduction	164
6.21 Nanodisc Technology	166
6.22 Protective Antigen characterisation	167
6.23 Neutrons to investigate functional proteins	168
6.3 Chapter Specific Methods	171
6.31 Materials	171
6.32 Methods	171
6.321 Preparation of Nanodisc (no protein inserted)	171
6.322 Preparation of Nanocomplex (containing PA and LFn-Cys).	171
6.3221 LFn-Cys on beads	171
6.3222 Preparation of Nanodisc mixture	172
6.3223 Preparation of the pre-pore	172
6.3224 Nanocomplex formation	172
6.33 Transmission electron microscopy	172
6.34 Analysis of nanodiscs and nanocomplexes by Flow Cytometry	173
6.35 Determination of translocation events using Neutron Reflectometry	173
6.3 Results	175
6.31 Developing and characterising protein constructs	175
6.311 Production and characterisation of LFn-Cys protein	175
6.312 Membrane scaffold protein production and characterisation	179
6.32 Development and characterisation of PA inserted into lipid nanodisc	182
6.321 Characterisation of lipid-nanodiscs and nanocomplexes by TEM	185
6.322 ND characterisation by Flow Cytometry	187
6.33 Production of deuterated proteins and NC formation using deuterated proteins	194
6.34 Determination of LFn-GFP translocation using Neutron Reflectometry	200
6.4 Discussion	212
6.5 Conclusion	215
Chapter 7 General Discussion and Future works	216
7.1 General Discussion	216
7.2 Future Works	221
7.21 Can the PA pore deliver a supramolecular assembly to the cytosol (Chapter 3)?	221
7.22 Can a thermodynamically plastic cationic substrate (LFn-RTAC) translocate through the PA pore (Chapter 4)?	221
7.23 Can structurally stable fluorescent molecules translocate through the PA pore (Chapter 5)?	222
7.24 Can the structural dynamics associated with cargo binding and translocation be evaluated by neutron reflectometry in real time (Chapter 6)?	222
7.25 What is the effect of Octomerisation on Protein Translocation?	223
7.26 Is the PA pore a dynamic system?	223
Chapter 8 References	224
Chapter 9 Appendices	239
9.1 Plasmid sequencing	239
9.2 PropKa Output	243
9.3 Thermostability of LFn-GFP	244
9.4 Radiolabelling of Oligonucleotides	248
9.5 Effects of EGCG on the A-B toxin <i>C.difficile</i>	249
9.6 Scattering Length Density Calculator Outputs	250

Abbreviations

Abbreviation	Meaning
2xYT	2x yeast extract and tryptone digest media
Alix	ALG-2 (apoptosis linked gene 2) interacting protein
AP-1	Adaptor protein 1
AP-2	Adaptor protein 2
APS	Ammonium persulphate
ASO	Antisense oligonucleotide
ATP	Adenosine triphosphate
ATx	Anthrax toxin
b.p.	Base pairs
BiP	Binding immunoglobulin protein
BME	2-mercaptoethanol
BSA	Bovine serum albumin
cAMP	cyclic adenosine monophosphate
CDC	Centre for Control Disease
cDNA	coding DNA
CI	Clathrin independent
CLIC	Clathrin / Caveolae independent carriers
CM	Calmodulin
CME	Clathrin mediated endocytosis
CMG2	Capillary morphogenesis protein 2
CML	Chronic myelogenous leukaemia
CPP	Cell Penetrating Peptides
DARPin	Designed Ankyrin Repeat Protein
DMEM	Dulbecco's-minimal essential Medium
DMSO	Dimethyl sulfoxide
DNA	Deoxyribonucleic acid
dsDNA	Double stranded DNA
dsRNA	Double stranded RNA
DTAC	Diphtheria toxin A chain
DTBC	Diphtheria toxin B chain
DTx	Diphtheria toxin
ECL	Enhanced chemiluminescence
EDTA	Ethylenediaminetetra acetate
EE	Early endosome
EEA1	Early endosomal antigen 1
EF	Ooedema factor
EGFP	Enhanced green fluorescent protein
EGFR	Epidermal growth factor receptor
ER	Endoplasmic reticulum
ERK	Extracellular signal-regulated kinases
ESCRT	Endosomal sorting complex required for transport

FBS	Foetal bovine serum
FDA	Food and drug administration
GM130	Golgi marker 130 kDa
HRP	Horse radish peroxidase
ILV	Intraluminal vesicles
IMAC	Immobilised metal ion affinity chromatography
IPTG	Isopropyl -D-1-thiogalactopyranoside
JHF	Juvenile hyaline fibromatosis
Kbp	Kilo base pairs
kDa	Kilo Daltons
LAMP	Lysosomal associated membrane protein
LBPA	Lysobisphosphatidic acid
LBPA	Lipid lysobisphosphatidic acid
LDH	Lactate dehydrogenase
LDL	Low-density lipoprotein
LE	Late endosome
LF	Lethal factor
LFn	NT domain 1 Lethal Factor
LFn-Cys	Lethal Factor domain 1, Cys
M6PR	Mannose 6-phosphate receptor
MAPK	Mitogen activated protein kinase
MAPKK	Mitogen activated protein kinase kinase
MD	Muscular dystrophy
MG	Molten globular
MTT	3-(4,5-dimethylthiazol-2-yl)-2,5-diphenyltetrazolium bromide
MVB	Multi-vesicular bodies
MW	Molecular weight
nt	nucleotide
PA	Protective antigen
PA20	Protective antigen 20 KDa
PA63	Protective antigen 63 KDa
PA83	Protective antigen 83 KDa
PAGE	Polyacrylamide gel electrophoresis
PBS	Phosphate buffered saline
PCR	Polymerase chain reaction
PDB	Protein databank
pDNA	Plasmid DNA
PEG	Poly(ethylene-glycol)
PEI	Poly(ethyleneimine)
PI3K	Phosphoinositide 3-kinase
piRNA	piwi interacting RNA
PLL	Poly(L-lysine)
PM	Plasma membrane
psi	Pounds per square inch
Rab	Ras associated in brain
Raf	Rapidly accelerated fibrosarcoma
Ras	Rat associated sarcoma
RE	Recycling endosome
RISC	RNA induced silencing complex

RNA	Ribonucleic acid
RNAi	RNA interference
RP	Richardson-Piper media
rpm	Rotations per minute
RTAC	Ricin Toxin A Chain
RTBC	Ricin Toxin B Chain
RTx	Ricin toxin
SCID	Severe combined immunodeficiency disease
SDS	Sodium dodecyl sulphate
shRNA	short hairpin RNA
siRNA	Short interfering RNA
SLO	Streptolysin O
SNAP25	synaptosome-associated protein of 25 KDa
SNAREs	Soluble <i>N</i> -ethylmaleimide-sensitive factors
SOC	Super optimal broth
STx	Shiga toxin
SV40	Simian virus 40
Syn5	Syntaxin 5
TAE	Tris-acetate EDTA
tasiRNA	trans-acting siRNA
TCA	Trichloroacetic acid
TEM8	Tumour endothelial marker 8
TEMED	<i>N, N, N' N'</i> -tetramethylenediamine
TfR	Transferrin receptor
TGN	<i>Trans</i> -Golgi network
TGN46	<i>Trans</i> -Golgi marker 46
Tsg101	Tumour susceptibility gene 101
TxR	Texas Red [®]
Ub	Ubiquitin
UEV	Ubiquitin binding domain
UIM	Ubiquitin interacting motifs
UIM	Ubiquitin interacting motifs
v/v	volume for volume
VEGF	Vascular endothelial growth factor
VEGFR	Vascular endothelial growth factor receptor
Vps	Vacuolar protein sorting
w/v	Weight for volume
WGA	Wheatgerm agglutinin
ΔpH	Change in pH

List of Tables

Table 1.111 The immunological and haemodynamic affects of anthrax toxin virulence factors.	3
Table 1.121 Summary of <i>B.anthraxis</i> routes of infection and examples of outbreaks.	5
Table 1.221 Number of human anthrax cases reported in the EU for 2008-2012.	9
Table 2.11 Chemical List and suppliers	32
Table 2.12 Equipment and supplier list.	33
Table 2.161 Primary antibodies	37
2.162 Secondary Antibodies	38
Table 2.171 PCR products, PCR products size and template plasmids used for sub-cloning into pET151 Directional TOPO.	39
Table 2.172 Recombinant gene and primers used for PCR and sequencing.	39
Table 3.31 Summary of Protein toxicity IC ₅₀	78
Table 5.1 Examples of translocase substrates which have been investigated for their ability to translocate through the PA pore.	114
Table 5.41 Summary of Protein toxicity IC ₅₀	133
Table 6.21 - Examples of integral membrane protein successfully self-assembled into nanodiscs (SEC - bacterial secretory protein, TAR - Aspartate Receptor).	167
Table 6.241 Examples of membrane proteins studies using neutrons.	170
Table 6.31 Summary of protein yields when cultured in D ₂ O.	197

List of Figures

Figure 1.31 Anthrax Toxin Assembly and Trafficking.	14
Figure 1.41 Structures of protective antigen (PA), lethal factor (LF) and oedema factor (EF) subunits.	17
Figure 1.431 Showing the Structural comparison of the protomers of the PA pore and prepore.	20
Figure 1.432 Structure of the PA pore.	22
Figure 3.21 Antisense oligonucleotides complexed with LFn-Gal4.	57
Figure 3.311 PA83 Fusion Construct.	65
Figure 3.312 PPA83 protein eluted from TALON® resin of pooled fractions by SDS-PAGE and Coomassie staining.	66
Figure 3.313 Protein production optimisation, evaluated by protein elution from TALON® resin by SDS-PAGE and Coomassie staining.	66
Figure 3.314 Protein production optimisation, evaluated by SDS-PAGE and Coomassie staining.	67
Figure 3.321 LFn-GAL4 fusion construct.	69
Figure 3.322 Protein elution from TALON® resin of eluted fractions by SDS-PAGE and Coomassie staining.	70
Figure 3.331 Growth curves of HeLa cells.	71
Figure 3.332 Growth curves of Vero cells.	71
Figure 3.333 SEM images of HeLa cells treated under four different conditions.	73
Figure 3.335 Toxicity profile of Dextran in HeLa cells at 24, 48 and 72 hours.	75
Figure 3.336 Toxicity profile of PA in HeLa cells at 24, 48 and 72 hours.	76
Figure 3.337 Toxicity profile of LFn-GAL4 in HeLa cells at 24, 48 and 72 hours.	76
Figure 3.338 Toxicity profile of LFn-GAL4 + ASO in HeLa cells at 24, 48 and 72 hours.	77
Figure 3.339 Toxicity profile of PA, ASO, and LFn-GAL4 at varying concentrations in HeLa cells at 24, 48 and 72 hours.	77
Figure 3.353 Analysis of membrane destabilisation caused by PA.	79

Figure 3.354 The localization of PA with LBPA is shown at 4 h(A) and 8 h(B) in Vero cells.	80
Figure 3.341 Antisense oligonucleotides complexed with LFn-Gal4.	82
Figure 3.342 Characterisation of ASO.	82
Figure 3.351 Western blot analysis of HeLa whole cell lysate 48 hours post treatment with either PBS, ASO or siRNA.	84
Figure 3.352 Analysis of PA: LFn-GAL4: Syn5-ASO treated HeLa cells at 24 hours by Western blot.	86
Figure 3.12 LFn-GAL4 delivery of plasmid DNA in Vero cells.	90
Figure 3.41 Possible Anthrax Translocation Models.	92
Figure 4.22 Challenges encountered during translocation.	96
Figure 4.411 The effect of eGCG upon RTBC activity.	102
Figure 4.412 The effects of eGCG upon RTAC activity.	102
Figure 4.421 LFn-RTAC <i>in silico</i> design and characterisation.	104
Figure 4.431 LFn-RTAC activity compared to cRTAC in a cell free expression system.	106
Figure 4.441 PA dependent delivery of LFn-RTAC.	108
Figure 4.442 PA dependent delivery of LFn-RTAC.	108
Figure 5.4111 LFn-GFP fusion construct.	122
Figure 5.4112 Protein characterisation of eluted fractions from TALON® resin by SDS-PAGE and Coomassie staining.	123
Figure 5.4114 Toxicity profile of LFn-GFP in HeLa cells at 24, 48 and 72 hours.	125
Figure 5.4115 Toxicity profile of PA + LFn-GFP in HeLa cells at 24, 48 and 72 hours.	125
Figure 5.4116 Comparative toxicity profile of PA + LFn-GFP or LFn-GFP.	126
Figure 5.4121 LFn-YFP fusion construct.	128
Figure 5.4122 Characterisation of protein elution from TALON® of pooled fractions by SDS-PAGE and Coomassie staining.	129
Figure 5.4123 Toxicity profile of PA + LFn-YFP in HeLa cells at 24, 48 and 72 hours.	129
Figure 5.4124 Toxicity profile of LFn-YFP in HeLa cells at 24, 48 and 72 hours.	130
Figure 5.4131 LFn-mCherry fusion construct.	132
Figure 5.4132 Characterisation of protein elution from TALON® resin, of pooled fractions by SDS-PAGE and Coomassie staining.	133
Figure 5.421 Western blot of Vero whole cell lysate for different cellular markers.	135
Figure 5.422 Western blot of HeLa whole cell lysate for different cellular markers.	135
Figure 5.423 Late endosome/lysosome positive structures, labelled in Vero cells using different florescent probes; to measure for cross talk of fluorescent emission through of fluorescence into other channels.	138
Figure 5.424 Co-localisation studies of LAMP 1 positive structure with WGA-TXS RED labelled structures, 4 hours post exposure.	139
Figure 5.425 Expression of common markers in Vero cells.	140
Figure 5.431 Translocation of LFn-GFP in Vero cells at 5, 15 and 30 minute incubation in the presence and absence of PA.	142
Figure 5.432 Control experiments for unspecific binding of secondary anti rabbit conjugated to A488 in Vero cells.	143
Figure 5.441 Translocation of LFn-GFP in HeLa cells at 5 minutes incubation in the presence and absence of PA.	147
Figure 5.442 Control experiments for unspecific binding of secondary anti rabbit conjugated to A488 in HeLa cells.	148
Figure 5.451 Western blot analysis of HeLa subcellular fractionation 4, 6 and 16 hours post treatment LFn-GFP.	150
Figure 5.452 Western blot analysis of HeLa subcellular fractionation 4, 6 and 16 hours post treatment LFn-GFP and PA.	152
Figure 5.453 Western blot analysis of HeLa whole cell lysate.	153
Figure 5.51 Structural analysis of LFn-GFP by HS-DSC and CD spectroscopy.	159
Figure 5.52 Comparison of fluorescent probe structure.	161
Figure 6.323 TEM analysis of ND.	186
Figure 6.324 TEM analysis of NC.	186
Figure 3.325 Flow cytometry analysis of Buffer solutions.	190
Figure 3.326 Flow cytometry analysis of ND and NC.	191
Fig 3.328 Flow cytometry analysis of ND and NC to evaluate the affect of cell mask.	193
Figure 3.327 Flow cytometry analysis of ND and NC.	192

Figure 6.3131 Deuterated MSP1D1 Protein elution from TALON® resin and determination of concentration and purity of pooled fractions by SDS-PAGE and Coomassie staining.	196
Figure 6.3132 Deuterated PA Protein elution from TALON® resin and determination of concentration and purity of pooled fractions by SDS-PAGE and Coomassie staining.	196
Figure 6.3133 Deuterated LFn-GFP Protein elution from TALON® resin of pooled fractions by SDS-PAGE and Coomassie staining.	197
Figure 6.3134 Deuterated LFn-Cys Protein elution from TALON® resin of pooled fractions by SDS-PAGE and Coomassie staining.	197
Figure 6.3135 Western blot analysis of NC and ND.	199
Figure 6.3136 showing Western blot results for NC formation.	199
6.341 Neutron Reflectometry Fit for hND at 10°C and 37°C.	202
6.342 Neutron Reflectometry Fits for ND + LFn-GFP.	204
6.343 Neutron Reflectometry Fits for NC with PA in different orientations.	208
6.344 Neutron Reflectometry Fit for NC with PA in the correct orientation at 10°C and 37°C.	209
6.345 Neutron Reflectometry Fits for NC + LFn-GFP.	211
Figure 7.12 Postulated models of protein translocation through the PA pore.	219
Figure 9.21 PropKa output for LFn-RTAC.	243
Figure 9.31 Excitation spectra of LFn-GFP.	245
Figure 9.32 Emission spectra of LFn-GFP treated at 70°C.	245
Figure 9.32 Emission spectra of LFn-GFP treated at 80°C.	246
Figure 9.33 Emission spectra of LFn-GFP treated at 85°C.	246
Figure 9.34 Emission spectra of LFn-GFP treated at 90°C.	247
Figure 9.41 Characterisation of ASO.	248
Figure 9.51 Effect of eGCG on <i>C.difficile</i> Toxin B.	249

CONFERENCE PRESENTATIONS AND PUBLICATIONS

Conference Presentations

Title: **Characterisation of a novel oral vaccine delivery system.**

Date: 27th April 2016

Type: Poster presentation

Co-authors: Marie W Pettit, Susan Shorter, Paul Dyer, Simon C. W. Richardson.

Details: UK Neutron and Muon Users Meeting 2013, University of Warwick

Title: **Anthrax pore biology: Characterisation by neutron scattering and application to cytosolic antisense and siRNA delivery.**

Date: 27th April 2016

Type: Poster presentation

Co-authors an A. Shorter, Peter C. Griffiths, Simon C. W. Richardson, Les Baillie and Paul D. R. Dyer

Details: Medical Biodefense Conference, Munich, Germany.

Title: **Efficient delivery of antisense agents using endocytic back fusion.**

Date: 12th October 2015

Type: Poster presentation

Co-authors Paul D. R. Dyer, Susan A. Shorter, Alex S. Gollings, Monique M. A. Patrick, Mark Eccleston, Simon C. W. Richardson

Details: 11th Annual Meeting of the Oligonucleotide Therapeutics Society, Leiden, Netherlands.

Publications

Title: **Disarmed anthrax toxin delivers antisense oligonucleotides and siRNA with high efficiency and low toxicity.**

Date: Dec 2015

Type: Journal publication

Co-authors Paul D.R. Dyer, Thomas R. Shepherd, Alexander S. Gollings, Susan A. Shorter, Monique A.M. Gorringer-Patrick, Chun-Kit Tang, Beatrice N. Cattoz, Les Baillie, Peter C. Griffiths.

Details: Journal of controlled release, 220(A), 316–328.

Title: **An *in vitro* evaluation of epigallocatechin gallate (eGCG) as a biocompatible inhibitor of ricin toxin.**

Date: March 2016

Type: Journal publication

Co-authors Paul D.R. Dyer, Thomas R. Shepherd, Alexander S. Gollings, Susan A. Shorter, Monique A.M. Gorringer-Patrick, Chun-Kit Tang, Beatrice N. Cattoz, Les Baillie, Peter C. Griffiths.

Details: *Biochimica et Biophysica Acta*, 1860 (7), 1541–1550

Title: **The potential of toxin-based drug delivery systems for enhanced nucleic acid therapeutic delivery.**

Date: May 2016

Type: Journal publication review

Co-authors :Susan A. Shorter, Alexander S. Gollings, Monique A. M. Gorrington-Patrick, J. Emma Coakley, Paul D. R. Dyer & Simon C. W. Richardson

Details: Expert opinion in drug delivery, 7:1-12.

Chapter 1 - Introduction

1.1 Anthrax

Bacillus anthracis is the causative agent of the potentially fatal bacterial infection, Anthrax (Chen *et al.*, 2015). For the infection to become established, endospores enter the body and germinate, to produce the vegetative bacteria, which secrete anthrax toxin (ATx) (Liu *et al.*, 2004). *B. anthracis* infection is zoonotic, with grazing herbivores reported to be particularly susceptible to infection, *i.e* very few species are unaffected by *B. anthracis* (Collier and Young 2003). Human zoonosis typically results from contact with infected animals or contaminated animal products derived from infected animals (Doganay and Welsby 2006). Although zoonotic infection is relatively rare within the western world, there exists a growing need for anthrax countermeasures to be developed, spurred on by instances of bioterrorism such as in the 2001 “Amerithax” attack in the United States (Jernigan. *et al.*, 2002). During the Amerithax attack, the US postal system was used to disseminate spores and deliver them to targeted individuals (Section 1.21). The Centre for Disease Control (CDC) has classified anthrax to be a class A agent, in part due to its reported persistence in the environment. The economic impact and human mortality rate following exposure to *B. anthracis* even after antibiotic treatment (Donagay *et al.*, 1986, Henderson *et al.*, 2002) highlights the need for further investigations into the tripartite toxin system essential for anthrax toxicity.

1.11 Aetiology of anthrax

B. anthracis, the aetiological agent of anthrax, is a spore forming, gram-positive, rod-shaped bacterium containing two virulence factor encoding plasmids; pXO1 and pXO2 (Chitlaru *et al.*, 2011). The pXO-1 plasmid contains the *pag*, *lef* and *cya* genes encoding the three proteins that collectively form ATx. These proteins are: Protective antigen of 83 KDa (PA83), Oedema factor (EF) and Lethal Factor (LF). The PA83 protein forms the cell binding B-subunit, whereas LF and EF form the A-subunits, mediating toxicity upon their translocation to the cytosol of the cell. The pXO2 plasmid encodes a poly- γ -glutamic acid capsule, essential for *B. anthracis* virulence and is thought to inhibit the phagocytic destruction of *B. anthracis* (Figure 1.111).

There are three characteristic forms of the anthrax disease, which are determined by the route of infection. These are through abrasions in the skin (cutaneous anthrax), by inhalation (pulmonary anthrax) and after ingestion (gastrointestinal anthrax) (Cryan *et al.*, 2011) (Table 1.121). *B. anthracis* spores, are captured by local tissue macrophages, which migrate to the lymph nodes where the spores germinate to give rise to the vegetative, replicative, toxin producing bacillus (Sanz *et al.*, 2008).

The tripartite ATx toxin has been reported to contribute to several pathological states during anthrax infection, including: haemorrhage, oedema, necrosis, systemic organ failure, and finally death in mammals, including humans by triggering immunomodulating and cytolytic processes in the infected cells (Moayeri and Leppla., 2004) (Table 1.111). These processes of immunomodulation by the exotoxins EF and LF, as well as key virulence factors (exocapsule) facilitating escape from immune clearance, and contributes to its capacity to overwhelm innate host defences (Spencer, 2003).

	Macrophages, dendritic cells (DC) and lymphocytes	Neutrophils	Cardiac tissue	Vascular effects	Pro-inflammatory cytokines
Poly-γ-D-glutamic acid capsule	Promotes PA binding to the cells, and potentiates LT	Impairs phagocytosis hindering immune surveillance of cell surface antigens	Increases LT activity by inducing myocardial dysfunction	Acts synergistically with LT to induce hypotension	Potentiate cytokine generation by LT
Lethal Toxin	Impairs DT maturation, lymphocytes activation and antigen presentation and recognition	Impairs tissue phagocytosis	High dose directly impairs myocardial function	Lower cardiac output and diastolic dysfunction	Promotes low levels of cytokine release in the late stages of anthrax infection
Edema Toxin	Immune evasion via inhibition of T cell activation. Promotes migration of infected monocytes	An increase in cAMP impairs phagocytosis and oxidative burst	Indirect effects caused by cAMP	Hypotension and vasodilation	Immune suppression, and cytokine suppression

Table 1.111 The immunological and haemodynamic effects of anthrax toxin virulence factors.

Showing the effects of each virulence factor on immunological cells, cardiac tissue, vascular effects and cytokines. (Adapted from Arstenstein *et al.*, 2011).

1.12 Zoonotic transmission of anthrax

Animals acquire anthrax via the ingestion of *B. anthracis* spores, which are more resistant to adverse environmental conditions than the vegetative cells (Liu *et al.*, 2004). When bacilli are released by dying or dead animals into the environment, sporulation occurs upon the exposure of the bacillus to atmospheric air (Spencer 2003). Transmission of the spores to human is rare under normal circumstances, though can be mediated by exposure to infected animals, animal products or spores within the soil. Examples include people (*i.e.* tanners) working with skins from infected animals (Nguyen *et al.*, 2010). There are four main groups of anthrax disease dependent on route of transmission (Table 1.121). Anthrax infection is rarely seen outside well-defined geographical areas. In Europe (northern Europe and the middle of Europe) anthrax disease in animals is mostly absent, and only occurs in sporadic cases. However, anthrax within Turkey, Greece, the Balkan countries, Italy and Russia, still remains relatively common (Dixon *et al.*, 1999) (Table 1.221).

<i>B. anthracis</i> route of infection	Cause	Summary examples of <i>B. anthracis</i> infection	Reference
Intestinal	Typically caused by the ingestion of contaminated meat.	This form is typically associated with larger outbreaks, rather than sporadic. With treatment, it has approximately a 37% survival rate. Although these cases were mostly seen in the developing world which may affect survival.	Sirisanthana <i>et al.</i> , 2002
Cutaneous	Caused from the processing of animal products.	This accounts for approximately 95% of human cases. In 2011 three people were diagnosed with cutaneous anthrax, after dealing with infected animals that had died from anthrax infection. There is a 5% mortality rate associated with cutaneous route of infection (Đurić <i>et al.</i> , 2012).	Đurić <i>et al.</i> , 2012
Pulmonary inhalation anthrax	Caused by spore inhalation,	Such anthrax outbreaks have occurred from the processing of animal hides for drums (Anaraki <i>et al.</i> , 2008) and by intentional spore release as those in 2001 within the postal system, with a mortality rate (when treated) of 50%.	Jernigan <i>et al.</i> , 2001; Anaraki <i>et al.</i> , 2008
Intravenous	Caused by anthrax spores introduced into a person, intravenously	An outbreak of injection anthrax in 2012 was thought to be due to the contamination of a batch of heroin. Presenting cases in Germany, Denmark, France, and the United Kingdom. This demonstrated a 30% mortality rate.	Grunow <i>et al.</i> , 2012
Table 1.121 Summary of <i>B. anthracis</i> routes of infection and examples of outbreaks.			

1.13 Anthrax treatment in humans

Although the transmission of anthrax between humans has been documented to be rare (Inglesby *et al.*, 1999), after the 2001 Amerithrax attack (attributable to bioterrorism), there has been renewed interest in finding more effective prophylaxis and treatment (Anaraki *et al.*, 2008). The ATx component PA83 is strongly immunogenic, and neutralisation of this protein by the body's immune system has been sufficient to prevent the onset of disease (Mamedov *et al.*, 2016). This statement is highlighted by the fact that most of the approved anthrax vaccines entail some form of PA83 containing preparation (Chitlaru *et al.*, 2011). Currently, in Europe and the US there are two licensed anthrax vaccines for human use, which are composed of partially purified PA and adjuvants. These are:

Anthrax Vaccine Adsorbed (AVA, biothrax; USA), composed of aluminium hydroxide adsorbed sterile filtrate of cultures of the non-proteolytic V770-NP1-R strain (Bartlett *et al.*, 2002). This has been FDA approved since the 1970, for; pre-exposure prophylaxis, for persons at risk of acquiring this occupationally. This however has not been FDA approved for post-exposure prophylaxis, though is recommended by the CDC to be used post-exposure in conjunction with other treatments (Cybulski *et al.*, 2009).

Anthrax Vaccine Precipitated (AVP; UK) is composed of aluminium-phosphate precipitated culture supernatant, containing antigen produced by the virulent Sterne strain of the bacterium (Baillie *et al.*, 2004).

Post-exposure treatment has focused upon alleviating the symptoms associated with the pathology, including surgery, as well as antibiotic support to reduce the bacterial load.

This need is driven by the fact that antibiotics (which have been shown to be effective against *B. anthracis*), do not stop toxin-induced pathology (Jernigan *et al.*, 2001; Bravata *et al.*,

2007). Evidence has shown that when high toxin concentrations have been reached, LT and ET can cause host death directly (Liu *et al.*, 2014).

Efforts to combat the effect of the toxin have included the use of humanised monoclonal antibodies, targeting toxin-components. These have shown the post-challenge protection of macrophages by competing with host cell receptors for PA binding (Maynard *et al.*, 2002). This approach demonstrated high serum half-life, and protection in rat models. More recently, mice treated with human monoclonal antibodies against LF and PA pre-challenge, conferred 100% protection (Albrecht *et al.*, 2007). The FDA have approved recombinant human immunoglobulin G1 λ monoclonal antibody that blocks the binding of PA to its cell receptor, thereby inhibiting pore formation and internalisation of oedema and lethal toxins.

This treatment (Raxibacumab) was FDA approved in December 2012 for the treatment of inhalational anthrax (Kummerfeldt *et al.*, 2014; Dubel *et al.*, 2014). Additionally, adefovir diphosphate, a drug approved for the treatment of chronic hepatitis B virus infection is thought to inhibit the adenylyl cyclase activity of EF (Shen *et al.*, 2004). In order to augment the above with more effective treatments it is critical to understand the biology of ATx.

1.2 Global consequences of anthrax

Due to the diseases' lethality, there remains the possibility of serious threats to the human population. These risks may be thought of as being either derived through either bioterrorist or agricultural activities.

1.21 Bioterrorism

The US CDC has deemed Anthrax to be one of the most likely agents to be used in a biological attack, and is defined as a class A agent (Atlas 2002) as it is; effective, cheap, easy to produce, and is naturally occurring (Henderson 1999).

These facts in conjunction with ease of infection (respiratory), severity, and the environmental persistence of the spores (Brookmeyer *et al.*, 2005), make finding new and more effective ways of treating this disease a priority. On account of the above, and common to all bioterror threats, there also exists the perception of this agent in the minds of the public, with the capacity to cause panic and terror in the minds of the populous.

The use of *B. anthracis* has been demonstrated to have the potential as an agent of bioterrorism, examples including attacks in both Japan and the US. In Tokyo, the cult “Aum Shinrikyo” in 1993 (Inglesby *et al.*, 2002, Bossi *et al.*, 2004) intentionally released *B. anthracis* spores (Keim, *et al.*, 2001, Harris., 2006). Fortunately, this episode used a non-encapsulated (non-lethal) strain of *B. anthracis* though was one of the first documented instances of intentional release of an aerosol containing *B. anthracis* (Takahashi *et al.*, 2004). The 2001 “Amerithax” attack in the United States (Jernigan. *et al.*, 2002) where the US postal system was used to disseminate spores and deliver them to targeted individuals. This attack resulted in 11 cases and 5 deaths (Jernigan *et al.*, 2002).

1.22 Agricultural and veterinary risk

Anthrax is a threat to agriculture with outbreaks reported in Africa, Australia, Bangladesh, Brazil, Canada, China, Sweden, and the United States (Bann, 2012), (Table 1.221), causing economic harm. Improved sanitation and the implementation of prophylactic veterinary quarantine measures have reduced the incidence of the disease, however there is still a problem as under harsh environmental conditions the bacterium forms a dormant spore which can persist in the soil for an indefinite amount of time (Bann 2012). This can cause the re-emergence of anthrax despite, lying dormant for decades, and this has recently been seen with the re-emergence of anthrax in Australia after flooding unearthed anthrax spores. This resulted in the infection and death of 53 cattle and 1 horse (Durrheim *et al.*, 2009).

Country	2012	2011	2010	2009	2008
Germany	4	0	1	1	0
Bulgaria	1	1	3	2	1
Greece	0	2	0	1	0
UK	6	0	28	10	1
Romania	0	2	0	0	0

Table 1.221 Number of human anthrax cases reported in the EU for 2008-2012.
European centre for control disease, surveillance report 2012.

The economic consequences of livestock disease are vast; approximately 17.5 billion dollars are lost each year due to diseased livestock and poultry (Jones *et al.*, 2002, Singh and Prasad 2008), in spite of implementing surveillance and eradication campaigns. This wastage accounts for 17% of animal products in the developing world (Jones *et al.*, 2002). This further emphasises the aforementioned need for more effective prophylactic and treatments regimes to combat this disease. Understanding the nature of the pathology is critical to generating more effective treatment. As mentioned previously (Section 1.13), treating the bacterial load is not efficient, requiring a need to focusing upon ATx exotoxins.

1.3 ATx assembly and cellular internalisation

B. anthracis virulence factors and ATx component's PA, LF and EF have been shown to be, individually non- toxic. In order for ATx to function, it has been shown to require assembly into an active holotoxin complex comprising of: LF or EF bound to a PA oligomer (the PA pre-pore) (Collier 2009). PA83 interacts with cell surface receptors: predominantly tumour

endothelial marker 8 (TEM8) and capillary morphogenesis gene (CMG2). These receptors have been reported to be ubiquitously expressed (Liu *et al.*, 2009) and each has been documented to contain a single extracellular von Willebrand factor A domain, as well as a single transmembrane region (Bradley *et al.*, 2001). The physiological functions of TEM8 and CMG2 remain poorly defined, however diseases resulting from mutations in the genes imply that these proteins have important physiological functions (Cryan *et al.*, 2011). For example, TEM8 has been demonstrated to be unregulated in some cancers (colorectal) (St Croix *et al.*, 2000), and similarly, CMG2 has also been identified in some rare autosomal recessive conditions (juvenile hyaline fibromatosis (JHF) and infantile systemic hyalinosis) (Hanks *et al.*, 2003; Dowling *et al.*, 2003).

A third receptor was found to interact and expedite PA internalisation (β 1-integrin (α 4 β 1- and α 5 β 1) in mouse macrophages (Martchenko *et al.*, 2010). However, this would seem to be a low affinity receptor (Liu *et al.*, 2013). This conclusion were supported by a 2009 study (Liu *et al.*, 2009), which showed that the *in vivo* toxicity of ATx in mice was primarily mediated by CMG2 (TEM8^{-/-}), and in some part TEM8 (CMG2^{-/-}) (Liu *et al.*, 2009). This was corroborated further using a fusion protein derived from LF and the catalytic domain of *Pseudomonas aeruginosa* exotoxin A (FP59). Here CMG2 expressing mice (TEM8^{-/-}) and wild type control mice succumbed to a 5 μ g PA + 5 μ g FP59 challenge, and TEM8 expressing (CMG2^{-/-}) mice were completely resistant to this dose (Liu *et al.*, 2013).

PA83 has been reported to require proteolytic cleavage (by a furin-like protease) in order to be activated and this occurs at an RKKR motif incorporated into PA domain I. There have been several studies identifying this as a key step, essential for PA lethality as mutations to this motif render mutant ATx non-toxic. For example, it was found that replacing the RKKR motif with an RXXR motif was 13-fold less toxic than WT toxin (Klimpel *et al.*, 1992). This

cleavage event has been shown to be independent of cell binding, with furin-like proteases present in the blood (Moayeri *et al.*, 2007; Feld *et al.*, 2010). This cleavage event results in the dislocation of a 20-kDa N-terminal fragment (Figure 1.31) from PA63, exposing flat hydrophobic surface which serves as the binding site for LF and EF within domain I, allowing further assembly (Feld *et al.*, 2010). Two assembly pathways have been described: a cell-surface pathway (predominantly heptameric pores (Abrami *et al.*, 2004) and a plasma-based/extracellular pathway (predominantly octomeric (Kintzer *et al.*, 2010).

PA assembles into both heptameric and octomeric complexes in solution and on cell surfaces (Kintzer *et al.*, 2009; Kintzer *et al.* 2010) and both pores can translocate EF and LF with similar efficiencies and rates (Kintzer *et al.*, 2009). It had previously been noted (Kintzer *et al.*, 2009) that the octomeric pre-pore was more stable (Kintzer *et al.*, 2009; Kintzer *et al.*, 2010). This was observed in bovine plasma using LF mediated assembly (Kintzer *et al.*, 2010a). However, further investigation of this using receptor mediated assembly was reported to stabilise both PA₇ and PA₈, suggesting that anthrax toxin assembly may be a way to regulate toxin activity; with PA₇ localising near site of infection, and PA₈ circulating systemically (Kintzer *et al.*, 2010).

After pore formation, and LF and EF binding, the receptor bound PA₇: (LF/EF)₃ or PA₈:(F/EF)₄ complex (Thoren *et al.*, 2011) partitions into lipid rafts (Abrami *et al.*, 2003). After lipid raft association, a conserved lysine residue of the cytoplasmic tail of the receptor (Lys³⁵² in TEM8 and Lys³⁵⁰ in CMG2) is ubiquitinated, an event mediated by a cellular E3 ligase. Ubiquitination subsequently promotes endocytosis of the receptor:toxin complex in a clathrin dependent manner (Collier 2009;Abrami *et al.*, 2010). Following internalisation, key to the cytosolic translocation of EF and LF is the trafficking of the receptor:ATx complex onto intraluminal vesicles (ILVs), derived from the invagination of the early endosome (EE)

membrane, into the lumen of the EE. The importance of ILVs was exemplified using mutant idIF (ifIF) cells (which lack vesicular structures within the early endosome), where, due to degradation of ϵ -COP, inhibiting ECV/MVBs formation (Abrami *et al.*, 2004), the effects of EF and LF were not observed after treatment with ATx. Naturally, EE and late endosomes (LE) are multivesicular organelles (Huotari and Helenis., 2011) with LEs often designated multivesicular bodies (MVB).

ILVs form through the sequential action of the various ESCRT complexes, which regulate and facilitate the luminal invagination of the EE limiting membrane.

A model for ATx trafficking suggests that PA mediates the translocation of LF into the lumen of ILVs (Abrami *et al.*, 2004), these vesicles and their contents are delivered to the late endosome/lysosome (Puhar and Montecucco 2007) and that EF and LF are translocated across the PA pore into the lumen ILV. Within the ILV lumen EF and LF may re-fold in a sheltered environment (Abrami *et al.*, 2005). This ILV then fuses to the limiting membrane of the endomembrane compartment, and releases LF into the cytosol (see Figure 1.31). This hypothesis was supported by data demonstrating that cells treated with ALIX (specific for endocytosis) siRNA, and ATx showed a dramatic drop in LF activity *i.e.*, MAPKK hydrolysis relative to wild type cells (Abrami *et al.*, 2004).

It has been suggested that LF can be transmitted from cell to cell via exosomes, allowing for the long-distance ATx action and accounting for the long ATx half-life detected in mice (Abrami *et al.*, 2013). There is strong evidence that back-fusion and EF (or LF) release into the cytosol occurs primarily in the late endosomes, with sorting and ILV formation in EEs. Experiments investigating the importance of microtubule-dependent transport using nocodazole resulted in delayed LF-dependent MEK1 cleavage, due to access to late endosomes and lysosomes being impaired (Abrami *et al.*, 2004). Over expression of Ras–

related protein 7 (Rab7, a small GTPase responsible for regulating late endosomal homotypic and heterotypic fusion) also delayed cleavage of MEK1 (Abrami *et al.*, 2004). In addition, cells fed with a monoclonal antibody against the lipid lysobisphosphatidic acid (LBPA; Gruenberg, 2001), a lipid unique to endosomes and necessary for ILV function, also delayed the cleavage of MEK1 by LF. This indicates that the requirement for transport of LF to late endosomes is a general feature of ATx intoxication (Abrami *et al.*, 2004). In order to understand the translocation even over the PA pore and into the lumen of the ILV, EF, LF and PA will be considered individually and functioning together.

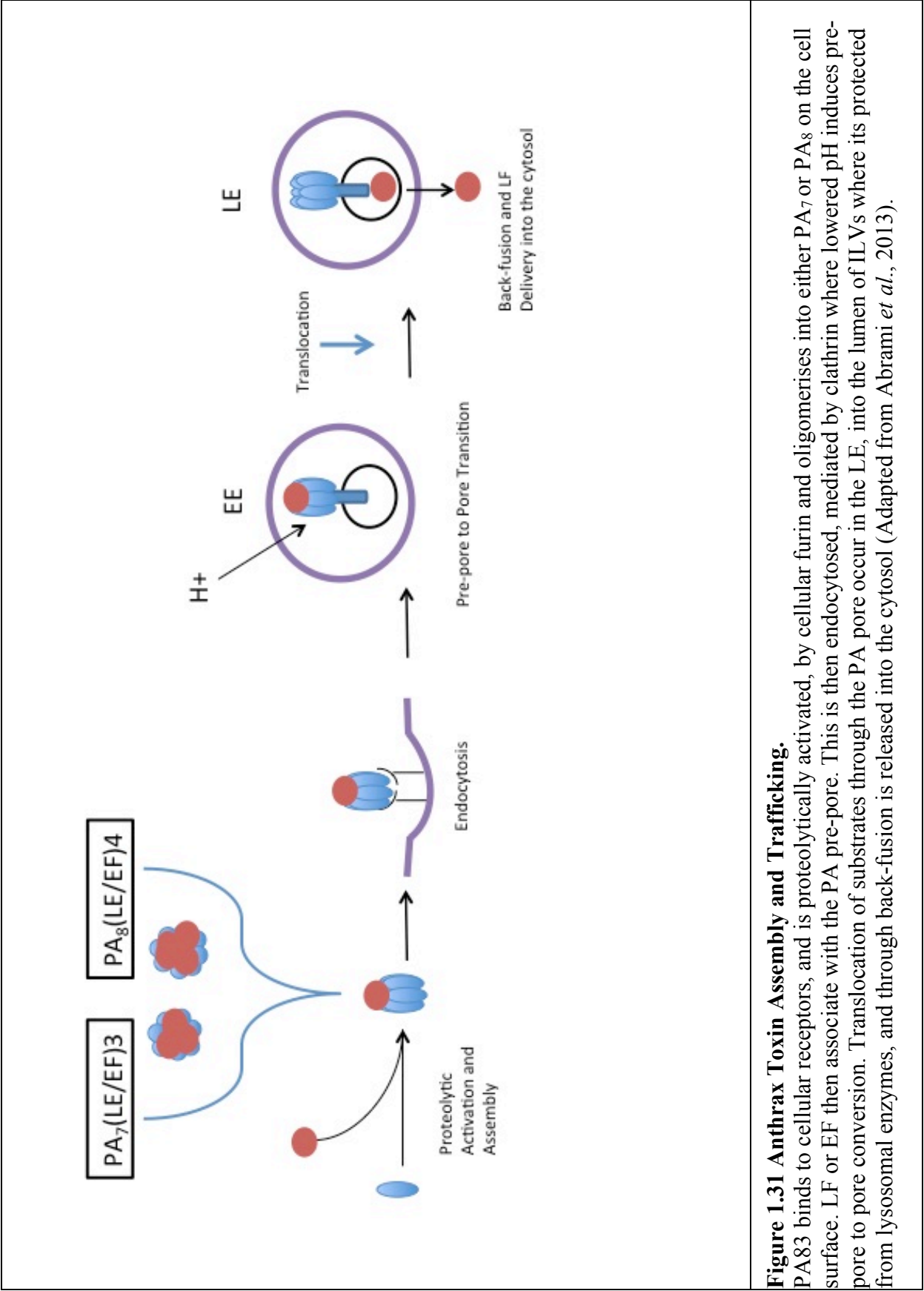


Figure 1.31 Anthrax Toxin Assembly and Trafficking. PA₈₃ binds to cellular receptors, and is proteolytically activated, by cellular furin and oligomerises into either PA₇ or PA₈ on the cell surface. LF or EF then associate with the PA pre-pore. This is then endocytosed, mediated by clathrin where lowered pH induces pre-pore to pore conversion. Translocation of substrates through the PA pore occur in the LE, into the lumen of ILVs where its protected from lysosomal enzymes, and through back-fusion is released into the cytosol (Adapted from Abrami *et al.*, 2013).

1.4 PA, EF and LF molecular dynamics and function

1.41 Lethal Factor (LF)

LF is a zinc metalloprotease that cleaves at least 5 members of the (cytosolic) mitogen-activated protein kinases (MAPK) kinase (MAPKK) protein family. Specifically, LF cleaves the N-termini of MAPKK within the host cell, resulting in MAPKK inactivation (Abrami *et al.*, 2013). The MAPKK family of response regulators has been reported to be involved in immune activation, and numerous cellular functions, including cell regulation, immune modulation and inflammatory suppression. MAPKKs are involved in most signal transduction pathways including extracellular signal–regulated kinases (ERK 1/2), Stress-activated protein kinases (SAPK)/Jun amino-terminal kinases (JNK) and p38 signalling pathways (Chavarría-Smith *et al.*, 2013). Consequently, the deactivation of MAPKK provides substantial advantages for the propagation of *B. anthracis*.

LF contains four domains, shown diagrammatically (Figure 1.41 B). Domain I bind to the activated form of PA83 (PA63) (Figure 1.41 A), via an interaction with the PA63 multimer (Section 1.3). LF domains II, III and IV create a clamp to hold the N-terminal tail of MAPKK-2 before cleavage (Pannifer *et al.*, 2001). It has previously been shown that the truncated form of lethal factor domain I (AA 1-255) was sufficient to access the cytosol without causing toxicity *in vitro*, this has been termed LFn (Arora and Leppla 1993; Gupta *et al.*, 2008).

1.42 Oedema Factor (EF)

EF is a potent calmodulin-dependent adenylate cyclase (Leppla *et al.*, 1982) that catalyses the synthesis of cyclic AMP (cAMP) in the cytosol of the host cells (Molin *et al.*, 2006), resulting in increased levels of intracellular cAMP. Increased levels of cAMP alter cell signalling, inhibit phagocytosis and tissue ion fluxes causing oedema (Tang *et al.*, 2009). EF has two domains (Figure 1.41 C) and domain I (red) interacts with PA63. Domain II (blue), is responsible for the adenylate cyclase activity of EF, leading to an uncontrolled increase in intracellular cAMP within host cells (Molin *et al.*, 2006; Froude *et al.*, 2011). Increased intracellular cAMP levels can cause cardiovascular dysfunction, tissue damage, and mortality (Tang *et al.*, 2009). Similar to LFn, the N-terminal domain of EF (EFn 1-254aa) has been reported to be able to facilitate translocation through the PA pore (Leuber *et al.*, 2008, Lacy *et al.*, 2002). However, it has been found that EFn translocates slower than LFn (Wynia-Smith *et al.*, 2012).

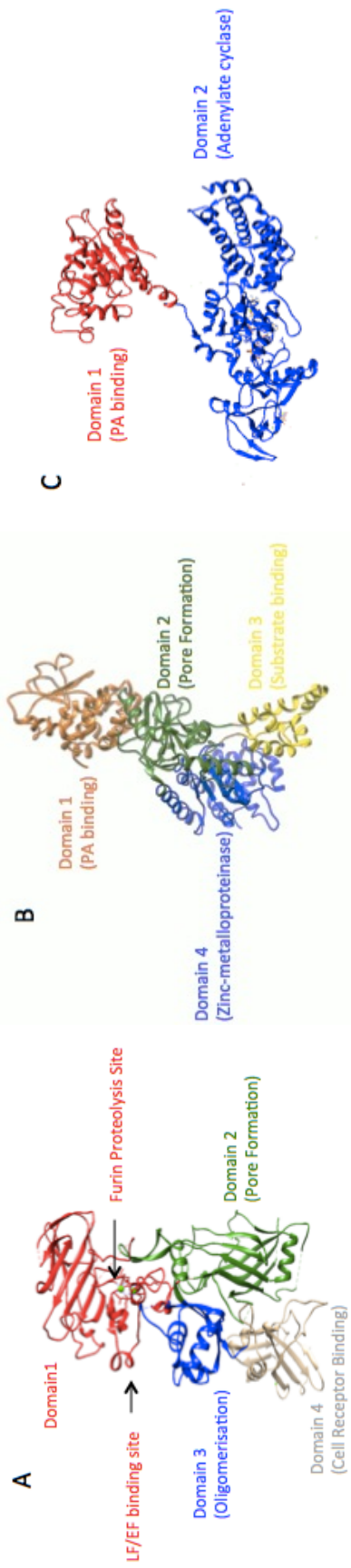


Figure 1.41 Structures of protective antigen (PA), lethal factor (LF) and oedema factor (EF) subunits. PA structure has been obtained using file 1ACC from the Protein Data Bank (A). LF and EF structures are derived from the files 1JKY and 1XFV, respectively (B and C).

1.43 Protective Antigen of 83 KDa (PA83)

Protective antigen (PA) of 83 KDa is a central component of the ATx complex as it forms a translocase channel capable of binding LF and EF, and translocating them to the lumen of an intraluminal vesicle (ILV), within a late endosome (LE) or multivesicular body (MVB). ILV back fusion eventually results in the release of the luminal content of the ILV into the cytosol (Bhatnagar 2001). Proteolytic activation at the (PA83) RKKR motif (Klimpel *et al.*, 1992), by a furin-like protease, generates a nicked form of PA (PA63), releasing a 20 kDa N-terminal (PA20) fragment. This leaves PA63 free to oligomerise and bind EF or LF forming a precursor, pre-pore (Young and Collier 2007). PA83 has four different domains, which are all critical to various stages of toxin assembly, trafficking and translocation (Figure 1.41 A). PA63 contains residues 168-258 of domain I (red) and the remaining 3 domains (Bann 2012). Domain I of PA is N-terminal and has been reported to contain the RKKR protease recognition site (Collier 2009) and after cleavage, the remaining segment of domain I (that forms the N-terminus of PA63) has been reported to require two calcium ions thought to stabilize the binding sites for LF and EF (Gao-Sheridan *et al.*, 2003). Domain II has been reported to contain a large disordered loop, which, under reduced pH, undergoes a conformational re-arrangement allowing the seven 2 β 2–2 β 3 loop of domain II to combine to form a 14-strand trans-membrane β -barrel channel (Miller *et al.*, 1999) as well as lining the lumen of the pore (Lacy *et al.*, 2004). Domain III mediates the self-association of PA63, a key step in cytotoxicity of ATx, with mutations within domain III inhibiting the oligomerisation of PA63 (Modridge *et al.*, 2001). Domain IV is primarily involved in binding to cellular receptors and maintaining structure. This domain has relatively little contact with the rest of the protein (Figure 1.41) (Williams *et al.*, 2009; Young and Collier 2007).

1.44 Protective Antigen Pore

Crystallisation studies of the PA pore have been reported to be difficult, due to the tendency of the PA pore to aggregate in aqueous buffers, making the analysis of its structure by electron microscopy difficult (Collier 2009). This issue has been overcome, stabilising PA pore by using the chaperonin, GroEL, which increased the number of PA pores formed on model membranes (Katayama *et al.*, 2008).

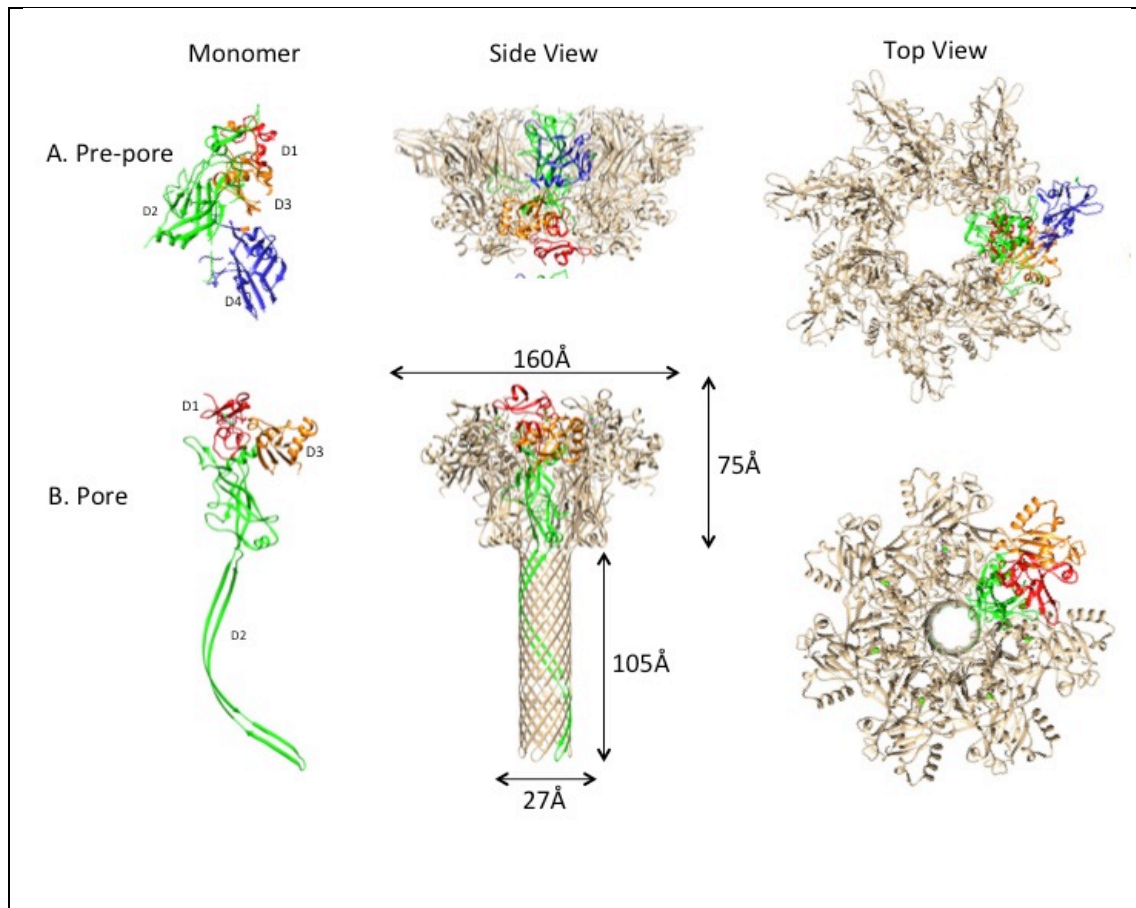


Figure 1.431 Showing the Structural comparison of the protomers of the PA pore and prepore.

A, Monomer, Top and side views of the atomic model of the PA pre-pore shown as ribbons. Domains are colour coded D1 – red, D2 – green, D3 – Orange, D4 Blue (PDB ID: 1TZO). B, Monomer, Top and side views of the atomic model of the PA pre-pore shown as ribbons. Domains are colour coded D1 – red, D2 – green, D3 – Orange (PDB 3J9C) (Jiang *et al.*, 2015).

A subsequent methodology was able to avoid PA63 aggregation in solution, by binding PA63 (and eventually the entire prepore) to an inert matrix (Ni support resin) (Katayama *et al.*, 2010) and inserting them into lipid nanodiscs.

Using the above models, the PA pore was determined to display a mushroom-shaped morphology; with a relatively thin tubular “stem”, proximal to the point of membrane insertion and a distally thicker “cap” composed of seven globular domains extending outward (Figure 1.431). This correlated with data from the previous studies using GroEL, despite

some stem size discrepancies, due to the “stem” being deformed by GroEL (Katayama *et al.*, 2010). After reconstruction, the PA pore was predicted to have a height of $\sim 180\text{\AA}$ (from the top of the cap to the bottom of the nanodisc) and the “cap”, distal to the nanodisc, to have a width of $\sim 130\text{\AA}$. The “stem” proximal to the nanodisc was reported to have an external diameter of 38\AA . These predictions correspond to previously modelled crystal structures (Nguyen 2004; Bann 2012; Collier 2009). Additional modelling data using similar techniques, generated models of the PA pore (in lipid nanodiscs) bound to LFn, which resulted in 10\AA increase in “cap” diameter, reflecting LFn-bound to the distal “cap” (Akkaladevi *et al.*, 2013) (Figure 1.432). The PA pore lumen averages $\sim 35\text{\AA}$ in diameter, narrowing to $\sim 15\text{\AA}$ at the Φ -clamp (Krantz *et al.*, 2005). This key feature of the lumen of the pore is made of conserved phenylalanine (Phe⁴²⁷) residues that plays a major role in protein translocation through the pore and forms the ϕ -clamp (Krantz *et al.*, 2005).

The pore lumen is lined with polar residues and carries a predominantly negative charge (Nguyen 2004). The PA translocase channel can be divided into three sections: (I) the substrate docking surface in the cap (called the α -clamp site), (II) A critical hydrophobic constriction point about one-third of the distance into the translocase (called the ϕ -clamp site) and (III) the highly charged solvophilic β -barrel stem portion, which comprises the bottom two-thirds of the translocase (Thoren and Krantz 2011). It has been suggested that these clamps represent dynamic binding sites for polypeptides allowing the translocation of substrates, favouring unfolding, whilst still preventing tight specific binding interactions, which would hinder translocation (Feld 2012). The events associated with substrate translocation have been documented and are critically evaluated in the next section (Section 1.5).

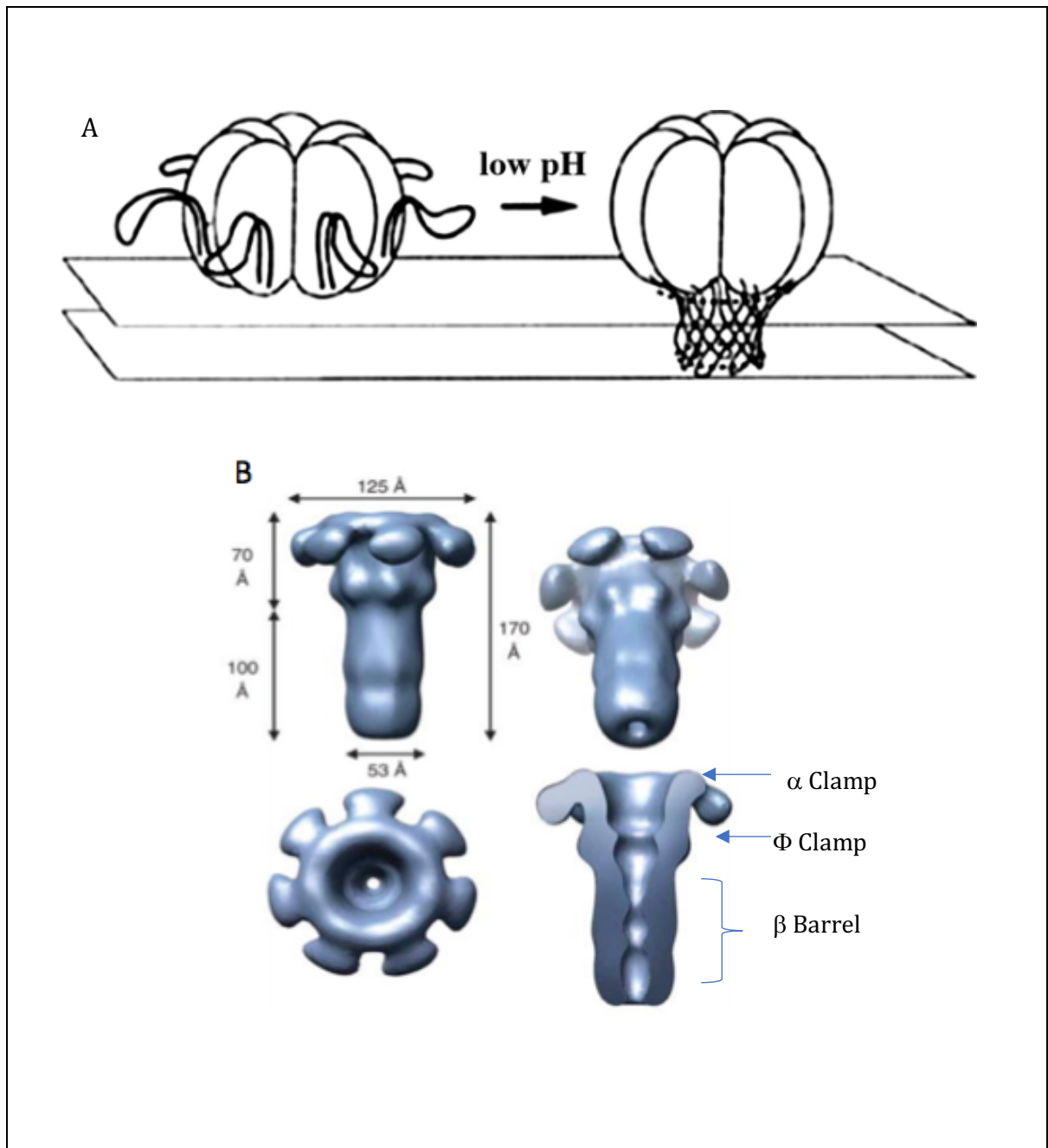


Figure 1.432 Structure of the PA pore.

Prepore-to-pore conversion (*A*) Upon acidification, the $2\beta 2$ – $2\beta 3$ loops in domain 2 move to the base of the heptamer to form a 14-strand transmembrane β -barrel (Sun *et al.*, 2008). PA pore structure (*B*) showing three-dimensional reconstructions of GroEL-bound PA pore with sizes labelled (Katayama *et al.*, 2008).

1.5 Protein translocation across the PA pore

Data from modelling and electrophysiology studies of the PA pore suggest that the extended β -barrel stem is unable to accommodate structures larger than ~ 10 to 15 \AA in diameter (Thoren *et al.*, 2011; Krantz *et al.*, 2004), requiring LF and EF to unfold during translocation. It has been shown that LF translocation is initiated by entry of the N-terminus into the pore and that translocation proceeds in an N- to C-terminal direction. Further, deleting more than 20 residues from the N-terminus of LFn ablated translocation in CHO-K1 cells (Zhang *et al.*, 2004 A). In order for proteins to destabilise and unfold, a chemo-mechanical force would be required to facilitate translocation of the LF and EF. This can be explained by thermodynamic analysis of conformational stabilities of LF and EF in relation to the acidic pH of endocytic vesicles. These acidic conditions (pH 6.5 – 5.5) are sufficient to destabilise the native structures of LFn and EFn, and facilitates the unfolding in a four-state process termed: N-I-J-U. The N-I transitions (from native to the intermediate), occurs within the pH range of the endosome (pH5-6), and retains large amounts of secondary structure, resulting in the formation of “molten globule” (MG) state. The second intermediate (J), was shown to contain less secondary structure than I, however at physiological endosomal pH is populated maximally ($\sim 5\%$) and is expected that this translocation intermediate is a threaded polypeptide in a more extended conformation. U is an unfolded state which is typically not reached under physiological conditions. (Krantz *et al.*, 2004).

Substrate charge has also been speculated to be important for translocation (Janowiak *et al.*, 2010). The N-terminal regions of LF and EF are not identical in sequence, however both have a net positive charge causing the N-terminus to be drawn by electrostatic attraction into the negatively charged pore (Collier and Young 2009).

This has been supported by findings that the fusion of a 6xHis tag to N-terminally truncated forms of LF (which do not translocate) restored the ability of LF to translocate (Zhang *et al.*, 2004). Further to this, the fusion of polycationic motifs (e.g., six – Lys residues) to the N-terminus of diphtheria toxin a chain (DTA) enabled DTA to translocate into the cytosol (although this was with a lower efficiency the LFn-DTA (Blanke *et al.*, 1996). Lysine-conjugation has also been used to facilitate the cytosolic entry of PNAs however caution when evaluating these data should be exercised especially in relation to the proclivity of small positively charged cell-penetrating peptides (CPPs) (such as Octa-Arginine or TAT derived CPPs) to deliver macromolecules.

The literature surrounding the driving forces of translocation both *in vitro* and *in vivo* studies have shown that translocation has more requirements than simply acid-induced MG transition for the translocating substrate (Krantz *et al.*, 2005; Young and Collier 2007, Rainey *et al.*, 2005). In order to explain the translocation of LF and EF through the PA pore the chemo-mechanical coupling of an energy source to the physical unwinding of the substrate polypeptide may be required. Two models of protein translocation have been described (i) an active pushing/ pulling mechanism and (ii) a passive Brownian-ratchet mechanism (Thoren and Krantz 2011).

The active push/pull hypothesis requires protein motifs within the translocase to contain critical binding sites, which engage the substrate polypeptide. These domains move, pulling and pushing the substrate polypeptide upon cycles of ATP hydrolysis (Thoren and Krantz 2011). However, LFn has been shown to enter and translocate through PA pores in lipid bilayer (with the aid of positive voltages) (Basilio *et al.*, 2011; Krantz *et al.*, 2006; Zhang *et al.*, 2004; Neumeyer 2006). Indicating that all of the necessary translocation machinery is contained within the PA pore, not requiring ATP (Young and Collier 2007).

The Brownian-ratchet hypothesis requires the thermal diffusive motion of the polypeptide chain in a directional manner.

This hypothesis has been speculated to be driven by an external energy gradient, forcing the translocation of LF and EF to the cytosol (*i.e.*, pH). It was also thought that substrate refolding would be facilitated by chaperones (Thoren *et al.*, 2011). However, the Brownian-ratchet hypothesis has a problem in the form of substrate unfolding, as this mechanism isn't thought to generate enough force to denature a folded protein. Consequently, PA would only be able to translocate pre-unfolded substrates. In support of this hypothesis, it has been shown that under endosomal acidic conditions, LFn does form a MG intermediate, with a loss of tertiary structure (Krantz *et al.*, 2005). The chemical gradient (ΔpH) in this model for translocation is a proton motive force generated by the acidic environment of the endosome. It has also been demonstrated that full length LF translocation requires an acidic endosomal (Wynia-Smith *et al.*, 2012). Both of the aforementioned hypotheses require the coordinated interaction of the substrate with the various clamps (Section 1.44) within the PA pre-pore and pore (Section 1.44). Further common to both hypothesis is the first event associated with substrate:translocase interaction *i.e.*, substrate docking.

1.51 PA pore physiology in relation to translocase function

As previously outlined there are several notable features within the PA pore. These are the α -clamp, the Φ -clamp and the β -barrel forming the "stem" (Section 1.4). These clamps also allow the channel to interact with the substrate non-specifically, going from high affinity to low affinity binding in a dynamic system, preventing tight binding interaction which would inhibit translocation as opposed to facilitate it (Wynia-Smith *et al.*, 2012; Feld *et al.*, 2012). Consequently, the various clamps associated with PA oligomers are further detailed herein.

1.511 The α -clamp

PA's α -clamp has been reported to bind to an array of amino acid sequences (Feld *et al.*, 2010), favouring a generally helical shape. The first α -helix and β -strand of each unfolding LFn was shown to bind to the α -clamp and this was demonstrated using a disulphide cross-linked LFn mutant (Feld *et al.*, 2010). This observation led to the inference that the PA channel had the ability to help unfold domain I of LF, concluding that there could be a process that was repeated on each folded region of the substrate during translocation. However, the exact degree of substrate destabilisation on the surface of the PA oligomer remains unknown (Feld *et al.*, 2012; Thoren *et al.*, 2011).

1.512 The Φ -clamp

The ϕ -clamp consists of seven Phe⁴²⁷ residues contributed by separate PA63 chains, and within the lumen of the PA pore. These have been shown to align, forming a narrow constriction. It has been reported that this site can facilitate the unfolding of the MG substrate by interacting directly with the substrate in the $1\alpha 1 - 1\beta 1$ region of domain I of LF/EF and acting as a chaperone (Krantz *et al.*, 2005). Activity has been proposed to be in two ways *i.e.*, as a chaperonin and as a seal for the proton gradient against the passage of ions (Janowiak *et al.*, 2010). This site also has many identified analogues among protein translocases, demonstrating the general importance of the site to the mechanism of translocation (Feld *et al.*, 2012). This site has a ratchet like quality, with mutation of this site causing substrate diffusion, backsliding, and retro-translocation (Krantz *et al.*, 2005). Mutations to this site to almost any residue (except Trp, Tyr, or Leu) result in a loss of ATx toxicity (Sun *et al.*, 2008).

The mutation of this Phe⁴²⁷ to an Ala almost abolished toxicity in Chinese hamster ovary-K1 (CHO-K1) cells (Sellman *et al.*, 2001). Changing this site has shown differential inhibition on conformational transition and/or translocation of the ATx complex. Changing Phe⁴²⁷ to a lysine, arginine, aspartic acid, or glycine strongly inhibited conformational transition of the heptameric PA prepore to the pore, blocking pore formation in membranes. Additionally, if this amino acid is changed to a histidine, serine, or threonine it had no effect on conformational transition of the pore, but inhibited translocation instead (Sun *et al.*, 2008).

Precisely how the Φ -clamp interacts with substrate polypeptides to promote translocation remains uncertain, however evidence has shown that the Φ -clamp interacts preferentially with hydrophobic aromatic compounds. Moreover, it was also documented that the Φ -clamp site actively unfolds LFn during translocation (Krantz *et al.*, 2005; Thoren *et al.*, 2011; Thoren *et al.*, 2009). To caveat the above, the Φ -clamp still requires the ability of the rest of the channel to couple the driving force (Δ pH) to translocation, as the Φ -clamp isn't sufficient on its own (Krantz *et al.*, 2005).

Substrate unfolding and translocation through the pore is still poorly understood, yet recent efforts have highlighted some key features, with synergistic actions of MG formation induced by endosomal pH, the α -clamp substrate destabilisation and binding, the Φ -clamp, and Δ pH-driven charge-state ratchet. This has mostly been demonstrated using LFn and EFn, with inference of similar mechanism for the full-length models. This would suggest that the full-length substrate (as opposed to LFn or EFn) also has to unfold; due to the size of the pore the substrate would likely need to be an extended chain (Basilio *et al.*, 2011).

Limits to the above hypothesis include the refolding of the substrate after translocation. Following translocation, the substrate would need to detach from the channel, and subsequently refold into fully functional enzymes in the cytosol, none of which has been

demonstrated. LF and EF are three times larger than LFn, and as of their nature have essential catalytic domains that must remain functional after transport.

Additionally, translocation has been studied using non-cell systems (Basilio *et al.*, 2011, Krantz *et al.*, 2006) and at non-physiological pH's (pH c|t 7.2|5.5 and 5.5|5.5 as opposed to pHc|t 5.5|7.2). These *in vitro* studies using PA assembled into a lipid membrane monitored LFn (or LFn-fusion protein) translocation. Translocation was inferred by monitoring LFn-induced current blockade. As these systems were effectively non-physiological, it was difficult to extrapolate physiological conclusions from them. Some of the conclusions that are pertinent are that during translocation LFn adopts an extended-chain configuration as it translocates (Basilio *et al.*, 2011); unfolding its tertiary and secondary structure, forming an extended chain of amino acids. For a substrate to undergo complete unfolding a large force would be required, as well as complex re-folding essential for LF and EF activity.

Some of the evidence indicating that there may be other potential mechanism at play during substrate translocation are based on the translocation of LFn fusion proteins which display an even wider array of chemical complexity and complexity of configuration than LF or EF. Examples include Diphtheria toxin A chain (DTA) with a N-terminal LFn domain or short tracts of cationic residues (6xHis) (Blanke *et al.*, 1996). To further add to this, it was demonstrated that an LFn-GFP fusion protein was able to translocate through the PA pore. As is well documented GFP is a highly stable, complex fluorescent structure (Basilio *et al.*, 2011; Zornetta *et al.*, 2010).

Interestingly however an LFn-mCherry fusion was not able to translocate through the pore, which led the authors to conclude that mCherry was more resistant to unfolding. Given that mCherry and GFP have similar structures but do differ in overall surface -charge, this conclusion may require further substantiation. Additionally, there was a lack of evidence that

after MG transition, further unfolded (into an amino acid chain), was essential for translocation. This was due to LF requiring 45 Å, as opposed to the 15 Å available at the Φ -clamp of the PA pore (Nguyen 2004).

1.513 Translocation Powered by a Δ pH

There is evidence to support a proton gradient- driven Brownian ratchet mechanism driving PA substrate translocation (Wynia-Smith *et al.*, 2012). Substrate unidirectional movement was explained by Brownian motion, and the ratchet is the electrostatic trap created via cycles of acidic residue protonation and de-protonation on either side of the channel's charge-selectivity filter (Thoren *et al.*, 2011) *i.e.*, the Φ -clamp. Here, substrate acidic residues protonate within the endosomal lumen, where the pH is \sim 5.5. Once translocated through the PA pore, the substrate reaches a higher pH in the lumen of ILVs (neutral cytosolic pH) the protein de-protonates thereby allowing an electrostatic repulsion to develop between the negatively charged channel and the exiting polypeptide chain. This would trap the protein on the opposite side of the membrane, enhancing Brownian motion and enforcing directionality. Recently studies have demonstrated the importance of pH driven translocation (Pentelute *et al.*, 2010). Negative charges from sulfonic acid groups attached artificially to LF_n which, drastically inhibited translocation, supporting the notion that the PA pore is cation-selective as these residues cannot be protonated, which is responsible for the inhibition (Basilio *et al.*, 2009).

1.514 Translocation-Coupled Unfolding

Driving forces are critical to protein translocation; it has been demonstrated by Thoren *et al.*, 2009 that three distinct barriers to LF's translocation exist: substrate docking, an unfolding barrier and a translocation barrier. In part, the MG transition of proteins within endosome facilitate destabilisation of the translocating substrate. It is still thought that the PA channel

can only accommodate an α -helix, (Basilio *et al.*, 2011), where it was stated that “LF undergoes complete polypeptide linearisation” as it travels through the pore. This has led to a discrepancy with how a partially unfolded substrate can be fully unfolded during translocation. Linearisation would require a great deal of energy given its entropic instability. Given all of the above, there is still much to understand regarding the nature of PA pore translocation. In an attempt to learn more about this event we proposed the following study (Section 1.6).

1.6 Aims of this thesis

The aims of this thesis were to investigate whether MG transition and further unfolding events were an essential step for movement across the PA pore. To accomplish this the dynamic nature of the PA pore was investigated in relation to the translocation of cargo with varying physicochemical properties by asking the following questions:

Does PA pore have the capacity to deliver a supramolecular assembly to the cytosol?

This question was posed to examine whether an anionic payload could be a translocation target if it were bound to LFn using a conjugation protocol that did not utilise poly(Lysine) or other polycations. This was interesting as previous studies had failed to disentangle the membrane lytic effects of poly(Lysine) from the PA pore translocation event.

If thermodynamically plastic cationic substrates can translocate through the PA pore?

Here ricin A chain was fused to LFn and its ability to translocate through the PA was examined. Given that ricin is thought to unfold to access the cytosol from the ER and that it has a net positive charge it is a useful tool to examine some of the hypotheses that have surrounded PA pore translocation.

Investigating the ability of the PA pore to translocate structurally stable fluorescent molecules. Given the variability in the electrophysiological data this question was posed in cell culture systems and was designed to address the dynamic nature of the PA pore through the use of several thermodynamically stable protein fluorophores.

Can ATx assembly and translocation be measured in real time? Here neutron reflectometry was used to define the binding and entry into the PA pore of LFn-GFP to PA. LFn-GFP was used as the bulky and thermodynamically stable nature of the GFP domain was interesting regarding the literature base around these substrates which has been demonstrated to translocate.

Chapter 2 - Material and Methods

Common materials and reagents are listed. Where these are specific to a particular chapter, they have been detailed therein rather than in the text that follows (Chapter 2).

2.1 Materials

2.11 Chemicals List

Table 2.11 Chemical List and suppliers	
Chemical	Supplier
Thiazolyl blue tetrazolium bromide (MTT reagent)	Sigma-Aldrich (Dorset) UK
Isopropyl β-D-1-thiogalactopyranoside (IPTG)	Sigma-Aldrich (Dorset) UK
Sodium azide	Sigma-Aldrich (Dorset) UK
Nitrocellulose membrane (0.2μm pore size)	Sigma-Aldrich (Dorset) UK
Bovine serum albumin (BSA)	Sigma-Aldrich (Dorset) UK
Coomassie brilliant blue R-250	BioRad (Hemel Hempstead, UK).
Acrylamide / bis-acrylamide	BioRad (Hemel Hempstead, UK).
Ammonium persulphate (APS)	BioRad (Hemel Hempstead, UK).
2-mercaptoethanol (BME),	BioRad (Hemel Hempstead, UK).
Sodium dodecyl sulphate (SDS)	BioRad (Hemel Hempstead, UK).
Tris-base	Thermo Fisher Scientific (Paisley, UK).
Ampicillin	Thermo Fisher Scientific (Paisley, UK).
Glycerol	Thermo Fisher Scientific (Paisley, UK).
Imidazole	Thermo Fisher Scientific (Paisley, UK).
Sodium chloride	Thermo Fisher Scientific (Paisley, UK).
Glycine	Thermo Fisher Scientific (Paisley, UK).
Agarose	Thermo Fisher Scientific (Paisley, UK).
TALON (6xHisTag purification resin)	Clontech (Saint-Germain-en-Laye France)
Dimethyl sulphoxide	Sigma-Aldrich (Dorset) UK
N-propyl-gallate	Sigma-Aldrich (Dorset) UK
Poly(ethyleneimine) (PEI) (Mw~&60,000)	Sigma-Aldrich (Dorset) UK
Dextran (Avg mol wt 35,000 - 45,000)	Sigma-Aldrich (Dorset) UK
Dulbecco's minimal essential medium (DMEM)	Thermo Fisher Scientific (Paisley, UK).
Foetal bovine serum (FBS)	Thermo Fisher Scientific (Paisley, UK).
Trypsin*EDTA	Thermo Fisher Scientific (Paisley, UK).
Penicillin*streptomycin*glutamine	Thermo Fisher Scientific (Paisley, UK).

GreenTaq	Thermo Fisher Scientific (Paisley, UK).
Gel Red,	Biotium (Cambridge UK)
HeLa IVT assay	Promega (Southampton UK)
Transfection kit R	Lonza (Cambridge UK)

2.12 Equipment List

Table 2.12 Equipment and supplier list.	
Equipment	Supplier
Agarose Gel Electrophoresis Systems	BioRad (Hemel Hempstead UK).
Mini-PROTEAN® Tetra Cell	BioRad (Hemel Hempstead UK).
Mini Trans-Blot® Electrophoretic Transfer Cell	BioRad (Hemel Hempstead UK).
PowerPac™ HC Power Supply	BioRad (Hemel Hempstead UK).
Forma orbital shaker	Thermo Fisher Scientific (Paisley, UK).
Multiscan EX Microplate photometer	Thermo Fisher Scientific (Paisley, UK).
French press apparatus	Thermo Fisher Scientific (Paisley, UK).
Dry Heat block	Thermo Fisher Scientific (Paisley, UK).
NanoDROP 2000	Thermo Fisher Scientific (Paisley, UK).
Heraeus fresco 21	Thermo Fisher Scientific (Paisley, UK).
Sorvall® RC 6 Plus	Thermo Fisher Scientific (Paisley, UK).
Sorvall® Discovery M120	Thermo Fisher Scientific (Paisley, UK).
Class II Laminar Flow Cabinet	Thermo Fisher Scientific (Paisley, UK).
Electroporator Lonza	Lonza (Cambridge UK)
Nikon Eclipse 90i Nikon	Nikon (Surrey UK)
NIS Elements 3.2	Nikon (Surrey UK)
Lasergene 12	DNASTAR (Wisconsin USA)
FEG SEM (Hitachi SU8030).	Hitachi-hightech (Berkshire UK)
Ecomax x-ray film automatic processor	Photon Imaging Systems (Swindon UK)

2.13 Stock Solutions

Yeast extract and tryptone digest (2x) media (2xYT) was prepared by mixing the following components into distilled water to a final volume of 1000 mL: bacto-tryptone (16 g), bacto-yeast extract (10 g) and NaCl (5 g). This was then sterilised in an autoclave using a liquids cycle (121°C for 40 mins for 500 mL), and the appropriate antibiotics were added once the media had cooled below 55°C. This solution was then stored at 4°C.

Agar plates (2xYT): was prepared by mixing: bacto-tryptone (16 g), bacto-yeast extract (10 g) and, NaCl (5 g), agar (15 g). This was then made up to 1000 mL with deionised water. This solution was then autoclaved (121°C for 40 mins for 500 mL). Once cooled below 55°C, the appropriate antibiotics were added. This solution was then aliquoted into plates, left to solidify, and stored at room temperature.

The 0.5 M tris-HCl (pH 6.8) was prepared by dissolving 60 g of tris base in 800 mL of deionised water. The pH of the solution was adjusted to 6.8 with 6N HCl and the final volume was made up to 1000 mL with deionised water.

SDS running buffer (10x) was prepared by mixing tris base (30.2 g), glycine (188 g), SDS (10 g) and adjusting the volume to 1000 mL with deionised water.

Laemmli sample buffer was prepared by mixing 0.5 M tris-HCl (pH 6.8) (1 mL), glycerol (0.8 mL), SDS (10% w/v) (1.6 mL), 2-Mercaptoethanol (BME) (0.4 mL), bromophenol blue (1% w/v) (0.4 mL), and deionised water (3.8 mL).

SDS (10% (w/v)): was prepared by adding SDS (10 g) to deionised water to a final volume of 100 mL.

Towbin electro-blotting buffer was prepared by adding tris-base (3 g) and glycine-HCl (14.08 g) to deionised water (800 mL) and methanol (200 mL). To this solution SDS (5 mL 10% (w/v)) was added and the pH adjusted to 8.3. The volume was then brought to 1000 mL with deionised water.

Blocking solution (Western blot) was prepared by adding non-fat dried milk (5 g) to 1x PBS (100 mL final volume) containing Tween 20 (0.01% (v/v)).

Tris Acetate Ethylenediaminetetraacetic acid (EDTA) (TAE) (50x) buffer was prepared by mixing tris-base (242 g) with glacial acetic acid (57.1 mL) and 0.5M EDTA (pH 8.0) (100 mL). The volume was then adjusted to 1000 mL with deionised distilled water.

Blocking buffer was prepared by adding goat serum (1 mL) to 49 mL of 1x PBS.

Formalin (2% (w/v)) in PBS: 5 mL of 10x PBS was placed in a glass beaker. Double distilled de-ionized (dddi) H₂O (30 mL) was added and the preparation heated using a microwave oven until it was ~80°C. Paraformaldehyde (PAF) (Fisher) (1 g) was added. To help dissolve the PAF 1 mL of 5 N NaOH was added and the preparation agitated by gentle aspiration. The pH was then neutralised by add 900 µl of 5 N HCl and then HCl drop wise to pH 7.4. The final volume was then made up to 50 mL. This solution was made fresh daily.

Triton Extraction buffer was prepared by adding 5 mL of 10x PBS, glycine (190 mg *i.e.*, 50 mM in 50 mL) was added. Triton-X-100 was added to a final concentration of 0.2% (v/v). H₂O was added to make the final volume up to 50 mL. This solution was made fresh daily.

Mounting Media: *N*-propyl gallate (10 mg) (Sigma) was placed in a 1.5 mL sterile Eppendorf tube. To this 100 µl of PBS (10x), 400 µl glycerol and 500 µl H₂O were added.

Tris-buffered saline (TBS) was prepared by combining tris HCl (24 g), tris base (5.6 g) and NaCl (88 g), were dissolved in 900 mL H₂O. The pH was adjusted to 7.6 using 1N HCl or NaOH as appropriate and the volume adjusted to 1000 mL with H₂O.

Phosphate buffered saline (PBS) (10x): NaCl (80 g), KCl (2 g), Na₂HPO₄ (14.4 g) and KH₂PO₄ (2.4 g) were dissolved in 800 mL distilled water. The pH was then adjusted to 7.4 before adjusting the volume to 1000 mL with distilled water.

Where necessary, this solution was sterilised by autoclaving as previously detailed (121°C for 40 mins for 500 mL)

Coomassie brilliant blue R-250 staining solution was prepared by mixing Coomassie brilliant blue R-250 (0.25g) with methanol (40 mL), deionised water (50 mL) and glacial acetic acid (10 mL).

Coomassie de-staining solution was prepared by combining methanol (40 mL) was added to deionised water (50 mL) and to this, glacial acetic acid (10 mL) was added.

Western blot blocking solution was prepared by adding non-fat dried milk (5g) to 1x PBS (100 mL final volume) containing Tween 20 (0.01% (v/v)).

2.14 Gels for Electrophoretic separations

Agarose gels was prepared by mixing to 100 mL TAE (1x), 1g of agarose was added. This solution was heated to boiling using a microwave oven. During heating the possibility of superheating this solution was avoided and after the agarose had dissolved, it was left to cool to 55°C prior to adding 10 µl of gel red (and casting the gel).

Acrylamide resolving gels (12 % (w/v)) were prepared by combining To 4.1 mL of deionised water, 3.3 mL acrylamide/bis-acrylamide (16:1) (30 % (w/v)) was added. Next, 2.5 mL of 1.5M tris buffer (pH 8.8), 0.1 mL 10 % (w/v) SDS, 0.05 mL 10 % Ammonium persulphate (APS) and 5 µl *N,N,N',N'*-tetramethylethylenediamine (TEMED) were also added and the preparation mixed by aspiration prior to casting the gel and removing any unwanted bubbles.

Acrylamide stacking gel (4 % ((w/v)) was prepared by mixing H₂O (3.4 mL), acrylamide/bis-acrylamide (16:1) (30 % (w/v)) (0.66 mL), 1.5M tris buffer (pH 6.8) (0.83 mL), SDS (10 % (w/v)) (50 µl), APS (50 µl), and TEMED (10 µl). The preparation was mixed by aspiration prior to casting the gel and removing any unwanted bubbles.

2.15 Organisms and cells

Bacterial cells: *E.coli* one shot[®] TOP10 chemically competent bacteria were used as a storage strain for cloning and plasmid propagation (Invitrogen; Paisley, UK). *E.coli* BL21*(DE3) cells chemically competent bacteria, were used for gene expression and recombinant protein production (Invitrogen; Paisley, UK). *E.coli* BL21 (DE3) chemically competent bacteria were used for reduced basal expression of genes pre-induction (Invitrogen; Paisley UK).

Mammalian cells: Vero E6 cells (African Green Monkey kidney epithelial; ATCC: CRL 1568) were adherent and required D-MEM, supplemented with FBS (10% v/v) and L-glutamine, penicillin streptomycin (1% v/v). Adherent HeLa cells (Human cervical carcinoma cells; ATCC: CCL2) required D-MEM, supplemented with FBS (10% v/v) and L-glutamine, penicillin, streptomycin (1% v/v). Both cell lines were maintained in a humidified atmosphere of 5% (v/v) CO₂ and at 37°C. There were both split twice a week at a ratio of approximately 20:1 using 1x trypsin: EDTA (Gibco, Paisley UK) (detailed in Section 2.251).

2.16 Antibodies

2.161 Primary antibodies

Table 2.161 Primary antibodies			
Antigen	Host	Cat No.	Supplier
Anti-Syn5	Rabbit PAb	HPA01358	Sigma Aldrich,
Anti- Derlin 1	Mouse MAb	SAB4200148	Sigma Aldrich,
Anti- Derlin 2	Rabbit PAb	D1194	Sigma Aldrich,
Anti- TfR	Mouse MAb	612124	BD Transduction labs
Anti- GM130	Mouse MAb	610822	BD Transduction labs
Anti- LAMP 1	Mouse MAb	H4A3,	DSHB
Anti- LAMP 2	Mouse MAb	H4B4,	DSHB
Anti- EEA	Mouse MAb	E41120	BD Transduction labs
Anti- TEM8	Rabbit PAb	ab21270	AbCam,
Anti- CMG 2	Mouse MAb	ab70499	AbCam
Anti-V5	Mouse MAb	R960	Invitrogen
Anti- V5	Rabbit PAb	ab9116	AbCam

Anti-6xHis	Mouse MAb	631212,	Clontech
Anti- GFP	Rabbit PAb	A11122	Invitrogen
Anti- PA	Rabbit PAb	ab13808	AbCam

2.162 Secondary Antibodies					
Antigen	Host	Cat No.	Supplier	Conjugate	Use
Rabbit IgG	Goat (PAb)	T-2767	Invitrogen	Texas Red	IF
Mouse IgG	Goat (PAb)	T-862	Invitrogen	AlexaFluor- 488	IF
Rabbit IgG	Goat (PAb)	A-11008	Invitrogen	Texas Red	IF
Mouse IgG	Goat (PAb)	A-11001	Invitrogen	AlexaFluor- 488	IF
Rabbit IgG	Donkey (PAb)	NA934	GE Healthcare	HRP	IB
Mouse IgG	Sheep (PAb)	NA931	GE Healthcare	HRP	IB

2.17 Plasmid Templates

Plasmids encoding the N-terminal domain of *B. anthracis* Lethal Factor (LF) and Protective Antigen (PA) were kindly donated by Professor Les Baillie (Welsh School of Pharmacy, University of Cardiff). For sub-cloning into a more convenient *E.coli* expression vector, template genes encoding for both LFn and PA were located in the bacterial expression cassette, pQE30 (Qiagen, Crawley, UK). Plasmids encoding LFn-Cys and LFn-YFP (cloned into pET151/D TOPO) were developed using recombinant PCR (Section 2.212) and subsequently sub-cloned into pET151/D TOPO plasmid vector (Invitrogen, Paisley, UK). LFn-mCherry and LFn-RTAC were designed using LaserGene and synthesised by BBI (BioBasic Inc (Ontario, Canada)) using a proprietary codon optimisation algorithm specific to *E.coli* and subsequently sub-cloned into pET151/D TOPO plasmid vector (Invitrogen, Paisley, UK). The plasmid encoding LFn-GAL4 (in pET151/D TOPO) was taken from Dyer *et al.*, 2015. The plasmid encoding LFn-GFP (in pET151/D TOPO) was made from Rab-5 eGFP and the LFn sequence from Dyer *et al.*, 2015. The cloning for this construct was performed by Dr Marie Petit, and final characterisation (complete sequencing) was completed by me herein. LFn sequence was taken from Dyer *et al.*, 2015 for all plasmids

encoding LFn. Table 2.171 has a list of plasmids developed, and accession numbers for reference for the sequences listed below.

Table 2.171 PCR products, PCR products size and template plasmids used for sub-cloning into pET151 Directional TOPO.			
PCR product	PCR predicted size b.p.	Template plasmids	Origin - accession number/reference
LFn-RTAC	1611	LFn-RTAC in PUC57 synthesised by BBI (BioBasic Inc)	GQ479437 - RTAC
LFn-mCherry	1569	LFn-mCherry in PUC57 synthesised by BBI (BioBasic Inc)	JX155245.1 mCherry
LFn-YFP	1506	YFP in LFn-GAL4 in pET151/D TOPO.	AIZ66126 - YFP
LFn-GFP	1527	LFn-GFP pET151/D TOPO.	JN232535.1- GFP
LFn-Cys	801	LFn-Cys in pET151/D TOPO.	Dyer <i>et al.</i> , 2015
LFn-GAL4	1197	LFn-GAL4 in pET151/D TOPO.	Dyer <i>et al.</i> , 2015
PA83	2214	PA83 in pQE30	Dyer <i>et al.</i> , 2015

Table 2.172 Recombinant gene and primers used for PCR and sequencing.	
Product	Primers
LFn-cys	5' CACCTAAAGGAGGAAAGGATCCATG 3'
	5' TTAGCAGCATCTAGACAGGTTGATTTCTTGTTTC 3'
LFn-RTAC	5' CACCTTAAAACTGAGAAGAAG 3'
	5' TTAATGGAACGTAACAAGACG 3'
LFn (YFP fragment)	5' CACCTAAAGGAGGAAAGGATCCATG 3'
	5' CTCCTCGCCCTTGCTCACAGACAGGTTGATTTCTTGTT 3'
(LFn fragment) YFP	5' AAGAAATCAACCTGTCTGTGAGCAAGGGCGAGGAGCT 3'
	5' TTAATTGTACAGCTCGTCCAT 3'
LFn-YFP	5' CACCTAAAGGAGGAAAGGATCCATG 3'
	5' TTAATTGTACAGCTCGTCCAT 3'
LFn-mCherry	5' CACCTTAAAACTGAGAAGAAG 3'
	5' TTATTTGTACAGTTCATCCATGCC 3'
T7	5' TAATACGACTCACTATAGGG-3'

2.2 Methods

2.21 Sub-cloning into bacterial expression vectors.

2.211 *In silico* cloning

Plasmid maps were constructed using the SeqBuilder, application within the LaserGene suit of DNA analysis tools (DNASar, Madison, WI, USA). The sequence for the vector (pET151/D TOPO) was contained within the SeqBuilder application.

The PCR ligation sites were located and the gene sequence was inserted. PCR fragment size estimations were then made. From this, primers were designed, including four nucleotides (CACC) to facilitate directional ligation of the PCR product (Table 2.172).

2.212 DNA amplification using the Polymerase Chain Reaction (PCR)

The high fidelity and ability to amplify blunt end PCR product made Accuzyme[®] (BioLine, London, UK) an appropriate choice of polymerase to amplify PCR construct for sub-cloning. The PCR reaction mixture (using Accuzyme[®]) was set up according to the manufacturer's instructions. On ice, the following components were added to the reaction: 0.5 µl of template plasmid (5 ng) (see table 2.171 for plasmids used as a template for each PCR construct), 0.3 µl of each oligonucleotide primer, 5' and 3' and 12.5 µl of Accuzyme polymerase master mix (containing dNTPs, MgCl₂ and buffer). Nuclease free water was added to a final volume of 25 µl.

The PCR reaction was completed using an annealing temp of 52°C for all constructs with an elongation step of 1-3 min cycle suitable for amplifying a 1Kb/min PCR product (appendices 1.2). Recombinant PCR was used to develop the template for LFn-YFP. Initially PCR products were made for LFn using LFn-GAL4 as the template plasmid. The primer designed had a 3' 20 bp extension with a sequence specific for YFP. During the PCR cycles in the

thermocycler, this would incorporate a 20bp YFP sequence specific segment on the 3' of the LFn PCR product.

Similarly the PCR product for YFP was made by designing the 5' forward primer with a 20 bp sequence specific for the 3' end of LFn. This would incorporate a 5' 20 bp LFn sequence onto the YFP. These PCR products (LFn and YFP) were then mixed, and amplified. This was then checked (by gel electrophoresis) for correct product size (-1506bp), and used for ligation into pET151 Directional TOPO.

2.213 Agarose Gel Electrophoresis

This was achieved by preparing a 1 % (w/v) agarose gel in TAE buffer (Section 2.13).

Loading dye was added to the PCR sample (1 µl of 6x loading dye was added to 5 µl of PCR product), the entire volume (6 µl) was then loaded into a well. A DNA ladder was added to a separate well to calibrate the gel and allow an approximation of PCR product size. This gel was then run at 80 volts for 45 mins to allow separation of the PCR product based on DNA fragment size. This was visualised and recorded using a UV (405nm) trans-illuminator.

2.214 PCR ligation reaction into pET151 Directional TOPO[®] expression vector

Cloning reactions were carried out using the Champion pET151 Directional TOPO[®] *E.coli* expression kit (Invitrogen, Paisley, UK) as per the manufacturer's instructions. Prior to the reaction PCR products were diluted to obtain a 1:1 molar ratio of DNA: Vector. Briefly, 0.5 µl of PCR amplified DNA, diluted to an appropriate stoichiometry, was added to 1 µl of salt solution (1.2 M NaCl, 0.06 M MgCl₂), and 0.5 µl of TOPO[®] vector. Sterile water was added to total reaction volume of 6 µl. The reaction mix was incubated at room temperature for 20 mins. A vial of *E.coli* TOP10 chemically competent one shot[®] bacteria were thawed on ice for 10 mins. The TOPO[®] reaction mix (3 µl) was added to one vial (50 µl) of chemically competent

One Shot[®] *E.coli* TOP10 and incubated on ice for 30 mins. The cells were heat shocked for 30 seconds at 42°C and immediately returned to ice.

Super optimal culture (SOC) media (Invitrogen, Paisley, UK) was added (250 µl) and bacterial cells incubated in an orbital shaker for 1 hour at 37°C(200 rpm).

The *E.coli* culture was spread on pre-warmed 2xYT plus ampicillin (final concentration 200 µg/mL) agar plates and incubated overnight at 37°C.

Transformants, as denoted by colony growth were evaluated for gene insertion into the vector by PCR using a gene specific primer and a vector specific primer (T7) (Table 2.172).

Transformants positive for the gene in question were cultured overnight in 2xYT liquid media (Section 2.12), and plasmids extracted (Section 2.221). These were then subjected to mini induction (Section 2.231), DNA sequencing (Section 2.216) and bacterial stocks frozen (Section 2.215).

2.215 Freezing bacterial cultures

The long-term storage of bacteria was achieved by freezing them at -80°C. This was achieved by culturing the desired bacteria in 10 mL 2xYT containing the appropriate amount of the relevant antibiotic overnight at 37°C whilst shaking at 180 rpm. Following this, an equal volume of sterile 14% (v/v) DMSO in 2xYT was added to the culture. A 1000 µl aliquot was then placed in a polystyrene box, which was then placed into the -80°C freezer to facilitate a drop in temperature of about 1°C/min. A description of the frozen culture was then added to the laboratory plasmid database (iData3; (<http://www.idatapartners.com>)).

2.216 DNA Sequencing

DNA was diluted to a concentration of 20 ng/µl for each reaction. Primers were prepared at a concentration of 3.2 µM. These primers were designed to provide sequencing data describing

both the open reading frame (ORF) and the surrounding expression vector. Sequencing reactions were sent to DNAseq, (University of Dundee, UK).

Once the sequences were received, they were aligned using the SeqMan application integral to the LaserGene DNA analysis suit (DNASar Madison, WI, USA). The ORF was then identified and any alterations that may have occurred during the cloning process were determined (plasmid sequences available in appendices 9.1).

2.22 Plasmid Purification

2.221 Plasmid purification – Miniature-scale preparation (mini-prep)

A 10 mL culture of the chosen transformant was prepared by culturing over night at 37°C in an orbital shaker set to 200 rpm. Of this culture, 1.5 mL was placed into a sterile 1.5 mL Eppendorf tube. This was then centrifuged at 13,000 rpm for 1 minute. The supernatant was then discarded, leaving a pellet. This was then repeated using the same Eppendorf. The pelleted bacterial cells were then re-suspended by adding 250 µl of P1 buffer, subject to disaggregation by gentle aspiration. Then, 250 µl of Buffer P2 was added and the reaction sealed prior to being inverted 6 times to mix the solution thoroughly. Buffer N3 (350 µl) was added to the reaction and mixed by inverting the sealed tube. This reaction was then subject to sedimentation under high g (21000 x g) for 10 mins at room temperature in a tabletop micro-centrifuge. This formed a white pellet. The supernatant from this was transferred into a QIAprep spin column, which was then cleared at 21 000 x g for 60 seconds also at room temperature prior to the flow-through being discarded. Buffer PE (750 µL) was added to the QIAprep spin column and cleared as before. The flow-through from this was then discarded. The DNA was eluted by placing the QIAprep column in a 1.5 mL micro-centrifuge tube, to this Buffer EB, (50 µl) was added. This was left to stand for 1 min, and eluted at 21000-x g for 60 seconds also at room temperature (QIAprep miniprep handbook).

2.222 Plasmid Purification – Mega-scale Preparation (Mega-prep)

The copy number of the plasmid was determined, and the required volume of cells cultured overnight (high copy – 500 mL or low copy 2500 mL). The bacterial culture was then sedimented by centrifugation at 6000-x g for 15 mins at 4°C. The supernatant was then removed and discarded. This was then suspended in 50 mL of buffer P1. To this 50 mL of buffer P2 was added. This was then vigorously inverted 5 times, and 50 mL of buffer P3 was added to the same solution. After incubation on ice for 30 mins, it was then subjected to further centrifugation for 30 mins at 15 000 x g, to clear the bacterial lysate. To prepare the QIAGEN-tip, 35 mL of buffer QBT was added and allowed to flow through by gravity flow. The supernatant was then added to the tip, and preparation was passed over the column by gravity flow. Following this 200 mL of buffer QC was allowed to run through the resin by gravity flow. The DNA was then eluted using 35 mL of buffer QF, and collected in a clean sterile micro-centrifuge tube. The collected DNA was then subjected to isopropanol precipitation (Section 2.223).

2.223 Isopropanol Precipitation of DNA

Room temperature isopropanol (0.7 volumes) was added to the DNA solution, and subject to 10 000 x g for 10 min at 4°C. The supernatant was carefully removed, so as not to disturb the pellet. The pellet was washed with 70 mL of ethanol. This was then subjected to 10 000 x g for 10 min at 4°C. The remaining pellet was dried and re-suspended in sterile water.

2.224 DNA concentration quantification

DNA concentrations were determined using the NanoDrop 2000, 2 µl of sample was loaded onto the pedestal, the lid replaced, and the reading taken.

2.23 Protein expression and characterisation

For protein expression, the bacterial expression vector with the gene of interest was transformed into *E.coli* BL21*(DE3) for LFn-Cys, LFn-GAL4, pLFn-GFP expression, or *E.coli* BL21(DE3(pLysS)) for PA83 expression.

2.231 Transformation of *E.coli*

A vial of chemically competent One Shot[®] *E.coli* BL21*(DE3) /BL21(DE3(pLysS)) BL21(DE3) /BL21(DE3(pLysS)) was thawed on ice for 15 mins. Plasmid DNA (5 ng) was added to the bacteria and incubated on ice for 30 mins. Bacteria were then heat shocked for 30 seconds at 42°C and immediately placed on ice. SOC media (250 µl) was added to the bacteria and incubated in an orbital shaker for 1 hour (37°C; 200 rpm). This was then added to 10 mL of 2xYT plus (200 mg/mL ampicillin) liquid media and incubated overnight in an orbital shaker (37°C; 200 rpm).

2.231 Mini-induction' protein expression protocol

E.coli BL21*(DE3) / BL21(DE3(pLysS)) cells were transformed with plasmid DNA and incubated overnight. This culture was then used to inoculate fresh 2xYT media, 1.5 mL of overnight transformed culture was added to 13.5 mL of 2xYT media, with a selective antibiotic (200 mg/mL ampicillin), and incubated in an orbital shaker for 75mins (37°C; 200 rpm). IPTG was added to a final concentration of 1 mM and incubated for a further 2 hours (37°C; 200 rpm). The culture was centrifuged at 6000 rcf (g) for 20min and the supernatant discarded. The pellet was dissolved in 200 µl of Laemmli sample buffer with 10% (v/v) BME. The sample was then evaluated for expressed protein by SDS-PAGE and western-blot immune-detection.

2.232 Large-scale production and purification of protein

Overnight cultures of transformed *E.coli* BL21(DE3) or BL21(DE3(pLysS)) were used to inoculate 1000 mL of 2xYT (200 mg/mL ampicillin) liquid culture media. This was placed in an orbital shaker (37°C; 200 rpm) for 3 hours. Isopropyl β -D-1-thiogalactopyranoside (IPTG) (250 μ l, 1M) was added to the inoculated culture to induce protein expression and the culture incubated for a further 3 hours. This was then subjected to centrifugation at the cells sedimented at 6 000 x g for 10 mins at 4°C. The supernatant was discarded and the pellet stored at -80°C until required.

2.233 Large-scale production and purification of PA

Transformed *E.coli* BL21(DE3(pLysS)) were spread on pre-warmed 2xYT plus ampicillin (200 μ g/mL) agar plates and incubated overnight at 37°C. Individual colonies were used to inoculate 10 mL of 2xYT, plus ampicillin (200 μ g/mL) and incubated overnight in an orbital shaker (37°C; 200 rpm). These overnight cultures of transformed *E.coli* were transferred to 1000 mL of 2xYT, plus ampicillin (200 μ g/mL) liquid culture media, and incubated in the orbital shaker (37°C; 200 rpm) for 3 hours. Isopropyl β -D-1-thiogalactopyranoside (IPTG) (250 μ l, 1M) was added to the inoculated culture media to induce protein expression and incubated for a further 3 hours. The resulting cells were sedimented at 6 000 x g for 10mins, the supernatant discarded and the pellet stored at -80°C until required.

2.234 Bacterial cell lysis by French press

Bacterial lysates were prepared from frozen bacteria, thawed on ice and re-suspended in 30mLs of PBS. Complete[®] EDTA- free protease inhibitor cocktail (Roche, Netherlands), prepared as a 50-times stock solution, was added to give a 5 x final concentration. The cell suspension was decanted into the French Press pressure cell and mounted onto the French press apparatus. Bacteria were lysed at a pressure of 1500 pound per square inch (psi) and the

lysate was collected in a sterile 50 mL centrifuge tube. The procedure was repeated 3 times. Sodium azide was added to the resultant suspension to a final concentration of 0.02% (w/v) and the particulates separated by sedimentation at 18 000 x g for 20 mins at 4°C.

2.235 Protein purification by immobilised metal ion affinity chromatography (IMAC)

Proteins containing a 6xHis affinity purification motif were purified by immobilised metal ion chromatography (IMAC) using the manufacturers protocol (Clontech, CA, US). Briefly, an affinity column was prepared by aliquoting 1.5 mL TALON His-site purification resin (Clontech, CA, US), to a column. Which was washed with 5x bed volumes of PBS (total volume ~5 mL), and 5x bed volumes of 10 mM imidazole in PBS (total volume ~5 mL). The protein lysate was applied to the resin bed at 4°C and allowed to run through by gravity flow. The column was then washed with 5x bed volumes of 10mM imidazole. Eluted protein was collected as 1 mL fractions by the addition 150 mM imidazole in PBS. Each fraction was evaluated for protein concentration and purity using SDS PAGE, Coomassie staining (Section 2.241) and ImageJ analysis (Section 2.242). The TALON[®] purification resin was regenerated using EDTA to strip the resin, and then 10 x bed volume of cobalt chloride was added to the resin to regenerate (according to manufacturer's instructions).

2.236 Dialysis of purified proteins

Pooled purified proteins (typically 5 mL) were transferred into dialysis tubing and sealed. The tubing containing the purified sample was placed in 4 l of PBS and incubated for 2 hours at 4°C using a stir bar and magnetic stirrer. The PBS (4 l) was exchanged for fresh PBS and incubated for a further 2 hours. This was repeated a further 2 times. The sample was removed from the tubing, sterilised using a 10 mL sterile syringe and 0.2 µm filter (Fisher Scientific, UK), and aliquoted into sterile Eppendorf tubes and stored at -80°C until required. An aliquot of purified protein was used to estimate protein concentration.

2.24 Characterisation of recombinant proteins

2.241 Sodium dodecyl sulphate polyacrylamide gel electrophoresis (SDS-PAGE)

A 10% (w/v) resolving was made by combining: deionised water (4.1 mL), acrylamide/bis-acrylamide (30 % w/v, 29:1) (3.3 mL), 1.5M tris buffer (pH 8.8) (2.5 mL), SDS 0.1 mL 10% (w/v), APS (50 µl) 10% (w/v)) and 5 µL TEMED. This was then cast, allowing room to load a stacking gel and comb and left to set for 15-20mins. A 4 % (w/v) SDS-PAGE stacking gel was then prepared by combining: deionised water (3.4 mL), acrylamide/bis (0.66 mL), 1.5 M tris buffer (pH 6.8) (0.83 mL), SDS (10 % (w/v)) (50 µl), APS 50 µl) 10 % (w/v)) and 10 µl TEMED. This was the added to the top of the resolving gel, and a comb placed in it. This was then allowed to set for a further 10-15 mins. The comb was then removed and the gel was set up into the Mini-Protean[®] Tetra cell system. This tank was filled with 1xSDS running buffer (Section 2.13). The prepared samples were then loaded into the wells, with 10 µl of Spectra[™] Multicolour broad range protein ladder (Thermo Fisher; 26623). This setup was then run at 200V for 50 mins, to separate the protein bands allowing an estimation of apparent molecular weight.

2.242 Coomassie stain and gel drying

After electrophoretic separation, gels were removed and immersed in Coomassie brilliant blue R-250 staining solution (Section 2.13) for 1 hour on an orbital shaker (room temperature, 200 rpm). The gel was de-stained by using Coomassie de-stain (Section 2.13) for 3 hours. This was then removed and placed in PBS containing 5% (v/v) glycerol for 30 mins and dried using a gel drying kit (Promega, Southampton, UK). A gel-drying sheet was hydrated, and placed on a flat surface. The SDS PAGE gel was placed on the gel-drying sheet, and a second moistened gel-drying sheet was placed on top. This was then assembled into the gel drying frame and each side clamped. Any air bubbles were excluded and left to dry overnight.

2.243 Image J analysis to evaluate protein concentration

Protein concentration was estimated using both SDS-PAGE and Coomassie staining or Western blot analysis in conjunction with the ImageJ software package (NIH, USA). Briefly, known quantities of BSA (5 μ g, 2.5 μ g, 1 μ g) were subject to SDS-PAGE alongside purified proteins in Laemmli sample buffer.

The gel was stained with Coomassie brilliant blue R-250, de-stained, dried using a Promega gel drying system (Promega, Southampton, UK, Section 2.243), and scanned using CanoScan Lide 120. The resultant image was analysed, density of protein bands of unknown concentration was referenced to the density of known concentration of BSA. Care was taken not to overload the gel with too much protein, in instances where protein concentration was high, appropriate dilutions were performed to maintain the linear detection range of Coomassie stained gel (1 to 20 μ g of protein).

2.244 Western Blot

After protein separation by SDS-PAGE, the gel along with 0.2 μ m pore size, nitrocellulose, membrane (cut to fit the gel) (Sigma-Aldrich, Dorset, UK), Whatman filter paper (Fisher Scientific, Loughborough, UK) and fibre pads (Bio-Rad, Herts, UK) were assembled in the transfer cassette. Once this has been assembled, the cassette was loaded into a tank, which contained a magnetic flea, an ice pack and was filled with towbin buffer. The electrophoresis power pack associated with the transfer apparatus (BioRad, Herts, UK) was then set at 400mA for 1 hr. Once the transfer was complete, the membrane was removed and washed with water. This membrane was then submerged in 2% (w/v) of Ponceau-S in (0.1 % (w/v) in 5% acetic acid). The membrane was then washed with distilled water and the success of the protein transfer evaluated. The membrane was then placed into 3 mL of blocking solution, and subject to gentle agitation using an orbital shaker (37°C and 180 RPM) for 1 hr. The membrane was then removed and placed into 3 mL of fresh blocking solution, with the

appropriate dilution of primary antibody (Rabbit anti-GFP 1:3000 dilution, all other primary antibodies 1:1000). This was then incubated for a further hour in the orbital shaker set at 37°C and 180 RPM. The membrane was then washed three times for five mins in PBS containing Tween-20 (0.001% v/v). The membrane was then incubated with the secondary antibody conjugated to horseradish peroxidase (HRP), again in 3 mL of blocking solution in the orbital as before (either anti rabbit-HRP, anti-goat HRP or anti-mouse HRP). The membrane was then removed and washed a further three times in PBS Tween-20, for five mins as before. The presence of the secondary antibody denoting the presence and relative abundance of the target protein was then assayed using chemiluminescence. To this end, 1 mL of each ECL reagent (1 and 2) was added to the membrane at room temperature simultaneously.

This was then placed in transparency film and exposed using a lightproof autoradiography cassette and X-Ray film for varying times depending on signal (range from 2 secs to 24 hours). The X-Ray film was then developed using a photon x-ray film automatic processor (Photon), briefly the film was placed in the machine, and went through developer and fixative solutions, the film came out dry and was evaluated for chemiluminescence signal.

2.25 Mammalian cell culture

2.251 Cell Passaging

Vero cells were propagated in Dulbecco's Modified Eagle's medium (DMEM) media supplemented with 5% (v/v) FBS (v/v), 5% (w/v) L-glutamine, penicillin streptomycin. HeLa cells were propagated in Modified Eagle's Medium (MEM) media supplemented with 5% FBS (v/v), 5% L-glutamine, penicillin streptomycin. These cells were cultured in a 75cm² flask, at 37°C in a humidified atmosphere of 5% CO₂ and split twice a week.

To split the cells, the flasks were taken from the incubator and their external surface swabbed with 70% (v/v) methanol spray. The flask was then placed into a class II laminar flow hood.

The cell monolayer was washed x3 with 10 mL of sterile PBS taking care to use good aseptic practice. Following the aforementioned wash steps, 1 mL of trypsin: EDTA was added. The cells were then left to incubate at 37°C with 5% (v/v) CO₂ for five mins or until cells had detached. The trypsin was inhibited with the addition of 9 mL of complete media containing 10% (v/v) FBS. Gentle aspiration was used to disaggregate the cells. Following this 9 mL of this culture was disposed of to facilitate a 1:10 split ration. A further 9 mL of media was added. This culture was then placed back into the incubator, and cells were allowed to grow.

2.252 Mammalian whole cell lysate preparation

Each well in a 6 well plate was washed three times in PBS, the PBS dissuaded and Laemmli Sample Buffer (+ 10% (v/v) BME) (40 µl) added and the culture. The lysate was collected and vortexed for 2 mins with a small amount of glass beads to sheer some of the genomic DNA and reduce the viscosity of the sample. The sample was then subject to sedimentation for 5 mins at 6000 x g. Finally, 10-50 µl of this sample was then loaded on a polyacrylamide and subject to electrophoresis (Section 2.241).

2.253 Preparation of Subcellular fractionation

Mammalian cells (Vero and HeLa) were seeded into two 150 mm² plates at a density of 5×10^6 cells in 15 mL of culture media and culture was incubated using standard culture conditions for 24 hours. After the incubation period, cells were washed three times with PBS (10 mL for each wash). To the cells sterile PA (50 µg/mL) and, sterile LFn-GFP (20 µg/mL) (in complete media) were added and incubated for an appropriate time under standard culture conditions. Following this, the media was discarded and the cells were washed three times with chilled PBS (10 mL), with the last PBS wash was removed as completely as reasonably possible, by blotting the side of the plates with tissue. Complete[®] EDTA-free Protease inhibitor cocktail (PI) tablet (ROCHE, Burgess Hill, UK) was dissolved into 1 mL PBS,

giving a stock solution of 50x. To the first plate, 250 μ l of Complete EDTA-free Protease inhibitor cocktail (PI) (50x) (dissolved in HES) was added to the cells. The cells were then harvested using a sterile disposable cell scraper (rubber policeman) (Fisher Scientific, Loughborough, UK). The cell suspension was then transferred into the second plate. Cells were scraped and transferred into a sterile Eppendorf tube. This process was then repeated using 200 μ l of PBS containing PI and the cell suspension pooled.

The homogenate was lysed by vigorous passage (10 x) through a 21-gauge needle. Nuclei and non-lysed cells were sedimented at 2 000 x g for 2 mins at 4°C and the supernatant was transferred to a new sterile Eppendorf tube (Fisher Scientific, Loughborough, UK). The pellet was then re-suspended in 200 μ l of PI and subject to a second round of lysis, again using a 21-gauge needle as before. The supernatant was transferred to a 1 mL centrifuge and cytosolic and membrane fraction separated by ultracentrifugation 100,000 x g. The membrane fraction was dissolved in LSB (plus 20% (v/v) BME) at a final protein concentration of 10 μ g/ μ L and stored at -20°C prior to western blot analysis.

The cytosolic fraction was subject to trichloroacetic acid (TCA) precipitation. Briefly, cold stock solution of TCA (100 % (v/v)) was added to make a 20 % final concentration and incubated for 30 mins at 4°C. The sample was subject to sedimentation at 14 000 rcf (g) for 10 mins and resultant supernatant decanted. Cold acetone (1 mL) was added to the pellet and subject to sedimentation at 14 000 rcf (g) for 5 mins and resultant supernatant decanted. The pellet was subject to two further washes in cold acetone and air-dried at 40°C for 1 hour. The pellet (cytosolic fraction) was dissolved LSB (plus 20 % (v/v) BME) to a final protein concentration of 10 μ g/ μ L and stored at 20°C prior to western blot analysis. An estimation of protein concentration was carried out using BCA protein analysis before sample was dissolved in LSB.

2.254 Fixing, staining and mounting cells for epifluorescent microscopy

Cells were prepared for fluorescence microscopy by adding PA, and an LFn-construct protein (Table 2.171), cells were seeded at 5×10^5 , left under normal culture conditions for 24hrs. To these cells PA83 and LFn-construct were added at 50 $\mu\text{g}/\text{mL}$ and 20 $\mu\text{g}/\text{mL}$ respectively. The cells were subjected to fixation and mounting as described below. Vero and HeLa cells were fixed using 2% (w/v) formalin. Prior to fixation cells were washed three times with PBS.

2.2541 Fixation using formalin

A 2% (w/v) formalin solution was prepared by adding 5 mL of 10x PBS to a beaker, 30 mL of deionised water was added and heated in a microwave until boiling. To this 1g of paraformaldehyde (PAF) was added. To dissolve the PAF, 1 mL of 5N NaOH was added. The pH of this solution was then re-adjusted with the addition of 5N HCl to pH 6.8, and water added to 50 mL. This solution was then placed onto cells for fixation for 20mins. If the cells were not further subjected to immune-staining, then blocking solution was added for 30mins, and cells were mounted. Cover slides were fixed by placing 40 μl of the solution to a glass slide, and the corresponding cover slip placed facedown onto the mounting media. The excess mounting media was then removed, and the cover slips sealed. Fixed cells were then visualised using the Nikon Eclipse 90i epifluorescence microscope.

2.2542 Methanol fixation

Pre-chilled methanol (-20°C for 10 mins) was added to Vero cells to be stained with anti-LAMP-1/-2 antibodies and incubated for 5 mins at -20°C . PBS was added to the methanol and washed a further three times with PBS. Cells were incubated for 1 hour with FBS blocking buffer. Subsequently cells were washed three times with PBS and hybridised with the appropriate primary antibody.

2.2543 Primary antibody hybridisation for immunofluorescence experiments

Appropriate dilutions of primary antibody were made using FBS blocking buffer and 40 μ l was 'spotted' onto Parafilm (Fisher Scientific, UK). The corresponding cover slip was placed face down onto the aliquoted antibody. Cells were incubated in a sealed container with a paper towel saturated with PBS, to prevent evaporation and desiccation of the antibody, for 1 hour at room temperature. Cells were washed three times with PBS to remove excess un-hybridised antibodies.

2.2544 Secondary antibody hybridisation for immunofluorescence experiments

Secondary antibodies conjugated to a fluorophore (Table 2.152), were diluted in FBS blocking buffer (1:400). Hybridisation followed the same protocol as for the primary antibody hybridisation step, washed three times in PBS, and mounted to glass microscope slides.

2.2545 Mounting

Mounting media containing 4',6-Diamidino-2-Phenylindole, Dihydrochloride (DAPI) nuclear stain, were added to a clean glass slide and the corresponding coverslip was placed face down, avoiding bubbles. Excess mounting media was removed by blotting with absorbent paper. Coverslips were then sealed using nail polish. Slides were then imaged using an Eclipse 90i overhead fluorescent microscope (Nikon, Japan), using Nikon Digital Camera (DS-Qi1Nc) and attached to a computer running Elements Advanced Research software (Nikon, Japan).

2.255 Protein Toxicity MTT Assay

Suspended (trypsin treated) cells were seeded into sterile flat-bottomed 96-well plates at a density of 1×10^4 HeLa cells/well and 1×10^3 HeLa cells/well and incubated for 24 hours under

standard conditions. Stock solutions of sterile PEI (positive control) and dextran (negative control) and protein for toxicity assays were prepared in cell culture media.

Cell culture media was removed from the adherent cells and replaced with media containing the appropriate dilutions of PEI, Dextran or protein varying in concentration. A row of adherent cells, with 100 μ l of complete media only was used as a negative (100% viable) control. Treated cells were incubated, under standard conditions for the allotted time. Cell viability was assessed by the addition of 10 μ l of sterile 3-(4,5-dimethylthiazol-2-yl)-5-(3,4-diphenyltetrazolium bromide) (MTT) (5 mg/mL) and incubated for 4 hours under standard conditions. Following incubation cell culture media was replaced with 100 μ l of dimethyl sulfoxide (DMSO) and incubated at room temperature for 30 mins. The 96-well plates were read at 540 nm using a microtitre plate reader. Results were expressed as viability (%) relative to the untreated control cells. Statistical analysis of toxicity profiles was performed at IC₅₀. Statistical analysis, using an unpaired T test, was performed using Prism 6 software (GraphPad, CA, US) and p-values obtained. For growth curves cells were cultured for over a 10 day period, and every 24hrs one row (of 6 duplicates wells) were subjected to MTT assay. The data was collected and plotted using Prism[®]. Doubling times of the cell lines were calculated using the formulae; $DT = T \ln 2 / \ln(X_e / X_b)$ where : T is the incubation time in any units, X_b is the absorbance at the beginning of the incubation time, X_e is the absorbance at the end of the incubation time (ATCC animal cell culture guide, 2014). Where there is a linear relationship between MTT absorbance and cell proliferation (Freimoser *et al.*, 1999).

2.256 Quantitation of protein concentration using BCA assay

BCA reagent was mixed at a ratio of 50:1 (V/V) with CuSO₄.5H₂O and this was then incubated with sample for 30 minutes at 37°C prior to assaying their optical density at a wavelength of 562nm. Absolute protein quantities and protein concentration were calculated using a standard curve.

Chapter 3 A study into the capacity of the PA pore to deliver a supramolecular assembly to the cytosol.

3.1 Novelty statement

Here it was demonstrated, for the first time, that polyanionic antisense oligonucleotide containing the GAL4 binding sequence could exert a measurable pharmacological antisense effect (indicative of cytosolic translocation) within a living cell when incubated with LFn-GAL4 and PA protein. These data were published in 2016 (Dyer *et al.*, 2015). **Significance:** These data challenge the existing literature by demonstrating, for the first time, that either a supramolecular assembly can act as a substrate for the PA translocase or that the substrate for the PA translocase could be anionic.

3.2 Introduction

The PA translocase has been described as a pore that can selectively translocate cationic cargo and that this cargo needs to unfold in order to pass through the translocase (Section 1.5). It has been previously reported that both GFP and plasmid DNA (condensed with poly-L-lysine) could enter the cell via the PA pore. However, neither of these studies generated direct and definitive data relative to the workings of the PA translocase as: GFP may unfold (Bann 2012) and PLL and PLL polyplexes are intrinsically membrane lytic (Cardarelli *et al.*, 2016). Here, LFn fused in frame to the DNA binding region of a *S.cerevisiae* transcription factor (GAL4), was used to form a non-covalent complex with a pair of antisense oligonucleotides containing a double stranded GAL4 binding sequence. This served as an experimental substrate used to answer the question: Is protein unfolding necessary for translocation through the PA pore?

If the proteins unfold then the anionic DNA will become dislocated from the complex and unable to cross the PA pore due to its charge (Wynia-Smith *et al.*, 2012). If the supramolecular assembly remains intact, then it may be able to facilitate the entry and

passage of the antisense oligonucleotide over the PA pore. The assay for the translocation of the proposed substrate (*i.e.* a supramolecular assembly) was a measurement of pharmacological antisense activity mediated by the antisense sequence described (Figure 3.21).

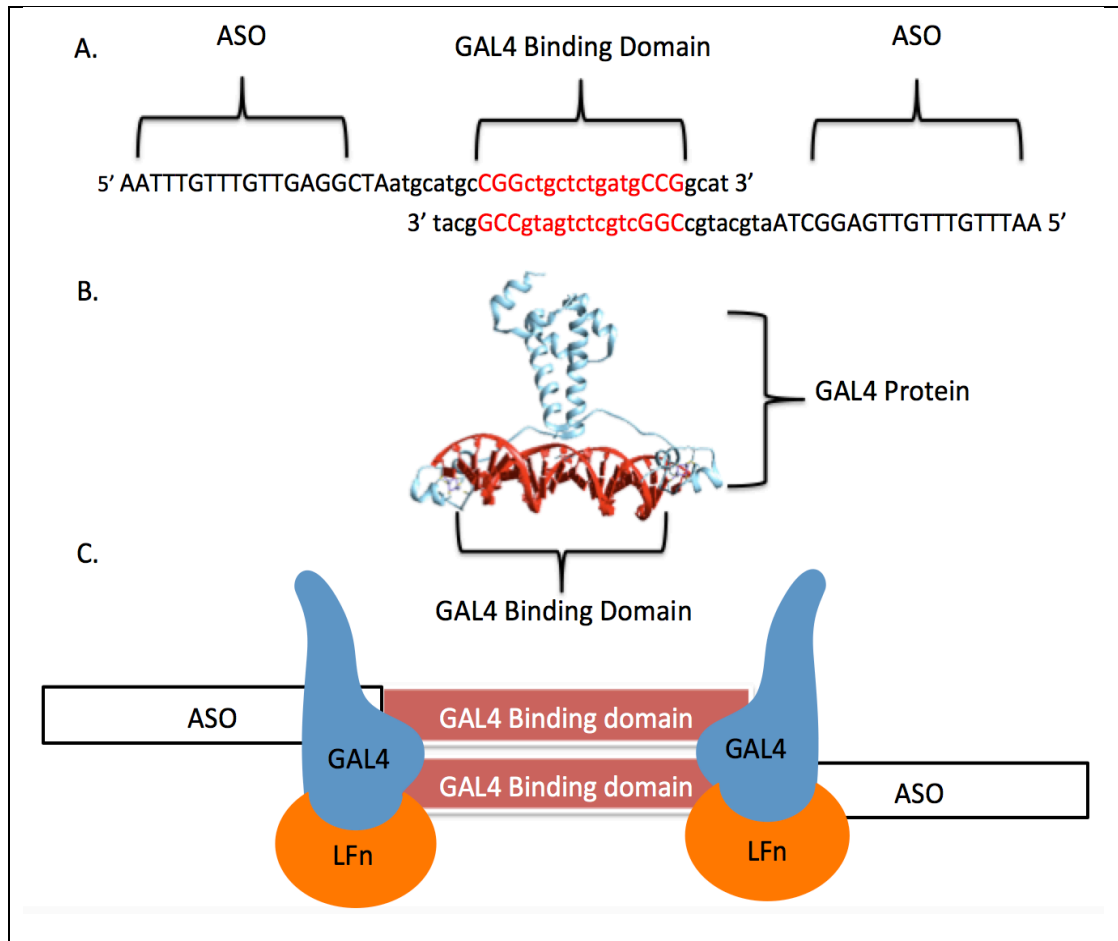


Figure 3.21 Antisense oligonucleotides complexed with LFn-Gal4. Schematic representation of the designed ASO containing a sequence, specific for syntaxin, and a LFn-Gal4 binding domain. With the antisense sequences targeted towards Syntaxin 5 over hanging of this complimentary (GAL4 binding) region. A. shows the oligonucleotide sequences, with the complimentary GAL4 binding domain. C. was generated in Chimera, by using this shows GAL4 (blue ribbon) protein dimerisation around the ASO sequence (red). C. shows a schematic representation of this system, with the designed ASO and LFnGAL4

3.21 Antisense Oligonucleotides

Recently there has been renewed interest in the therapeutic application of antisense oligonucleotides by the pharmaceutical industry (Sharma *et al.*, 2014). To date, this has resulted in the FDA approving five medicines for clinical use. Fomivirsen was the first FDA approved (Vitravene) therapy; this uses antisense technology, developed by ISIS Pharmaceuticals to treat CMV retinitis. It is injected directly into the eye, for patients who have failed previous treatments (de Smet *et al.*, 1999).

Mipomersen (Kynamro) was approved by the FDA as an orphan drug to inhibit apo B-100 synthesis and used to treat familial hypercholesterolemia (FH). It was administered by subcutaneous injection (Wong *et al.*, 2014). It failed to be granted market approval by the EMA. Alicaforsen, was granted orphan status by the FDA designed to inhibit the production of human intracellular adhesion molecule (ICAM)-1 for the treatment of inflammatory bowel disease and pouchitis (Hosten *et al.*, 2014). It is currently under phase III evaluation.

EXONDYS 51 (eteplirsen) was licensed by the FDA as an antisense oligonucleotide used for the treatment of Duchenne muscular dystrophy (DMD) in patients who have a confirmed mutation of the DMD gene that is amenable to exon 51 'skipping'. There has been controversy over this decision as a clinical benefit to the patient is yet to be established (Aartsma-Rus and Krieg 2016). Finally, Nusinersen (Spinraza) was developed for the treatment of spinal muscular atrophy (SMA) and has been reported to alter the splicing of survival motor neuron 2(SMN2) pre-mRNA in order to increase production of full-length SMN protein (Wood 2016).

3.22 Antisense mode of activity

Once within the nucleo-cytosolic compartments antisense oligonucleotides will specifically bind to the target mRNA in a sequence specific manner, forming an RNA hybrid duplex.

Halting protein synthesis occurs by RNase H activity enhancing translational arrest. This can work by steric blocking, halting translation apparatus once bound to the target mRNA (Lundin *et al.*, 2015). Chemical modification of the ASO sugar-phosphate backbone has led to improved stability, binding and specificity (Kole *et al.*, 2012) though the problem of bioavailability remains. These enhancements have made antisense oligonucleotides suitable for therapeutic application in treating a myriad of diseases with a genetic basis even if the targeting of these ASOs to the nucleocytosolic compartment remains sub-optimal (Juliano 2016).

3.23 Problems with antisense as a therapeutic

There are still issues with accessibility of these oligonucleotides to their targets (the cytosol), tissue targeting (dependent upon disease), stability (in biological systems) and PK-PD, which need to be improved for before the realisation of antisense oligonucleotides as a therapeutic tool can be reached (Fiset and Gounni *et al.*, 2001). Both *in vivo* and *in vitro*, access to the nucleocytosolic compartment represents a fundamental rate-limit associated with ASO functionality. This is due to the physicochemical nature of the ASOs and their inability to cross hydrophobic lipid bilayers, critical for a therapeutic effect (Diaz and Stein 2002).

Although there have been many advances associated with the chemical modifications of ASO (*i.e.*, the synthesis of phosphorothioate, phosphorodiamidate morpholino oligomer (PMO or protein nucleic acid (PNA) ASO homologues) which facilitate more success with *in vitro* delivery; with improved carriers (cationic lipids, cationic polymers), as well as ASO chemical modifications (phosphothioates, neutral backbones) the uptake of ASO to the cell is still insufficient.

In vivo delivery faces more complex problems; despite these systems demonstrating high gene silencing activity *in vitro* their success *in vivo* is limited. Carriers of ASO used *in vivo* have been hampered by toxicity, low efficacy, cost and specificity. Excepting target organs

such as the liver, kidney and the intestines where naked ASO has been demonstrated to be effective (Geary *et al.*, 2015). The issue here is twofold, requiring tissue specific delivery as well as intracellular compartment specific delivery (being the nucleus or the cytosol).

This presents an opportunity to use these “drugs” as tools to further understand the biology and mechanics driving PA pore translocation. The ability of *B. anthracis* toxin to mediate the translocation of material to the cytosol via the protective antigen (PA) pore has been well documented for peptides (Liao *et al.*, 2014), fluorescent proteins (Zornetta *et al.*, 2010) and nucleotides (Gaur *et al.*, 2002; Dyer, *et al* 2015). The documented ability of this A-B toxin to be able to deliver a variety of cargo to the cytosol has spurred on investigation into its potential to deliver therapeutics for example ASO, antibody mimics or cytotoxic T-lymphocyte (CTL) epitope (Dyer *et al.*, 2015 Liao *et al* 2014, Ballard *et al.*, 1998).

This method of cytosolic entry unlike other models, requiring formation of ILVs, where the cargo is transported is released into a compartment which is topologically the same as the cytosol, and so benefits from being protected from lysosomal enzymes, and protecting the cell from toxicity as is associated with other delivery methods such as cationic polymers (Lee 2007).

The translocation mechanism for ATx into ILVs is still vague (Brown *et al.*, 2015) with some limitations on the type of material that can be translocated (Liao *et al.*, 2014, Basilio *et al.*, 2011, Zornetta *et al.*, 2010). Given that fluorescent proteins such as GFP are very thermally stable, it is unlikely they would unfold completely during transit through the PA pore and this observation casts doubt upon the requirement of the translocase substrate to completely unfold during transit. Further, as the translocase substrate has been documented to require multiple cationic charges their exists, using the PA:LFn-GAL4:ASO system, the opportunity to question these assumptions experimentally.

Subsequently the investigation into this system as a delivery method for antisense oligonucleotides was undertaken. As there is a dependence of the cytosolic access for delivery being reliant on the presence of protective antigen pore, as well as truncations of lethal factor (LFn; residues 1-255) have been demonstrated to provide translocation through the PA pore without the associated toxicity with the rest of the protein (Milne *et al.*, 1995). Consequently, the overarching question this chapter aimed to answer was: can the PA translocase utilise a supramolecular assembly as a substrate, if part of that assembly is a polyanion (requiring the supramolecular assembly to remain intact during transit).

In order to address this, the more specific aims were:

- 1 To Produce and characterise recombinant PA and LF-GAL4 protein
- 2 To determine the *in vitro* toxicity profile of these constructs
- 3 To characterise an antisense oligonucleotide cargo that could interact with GAL4
- 4 To monitor the antisense activity of the ASO once bound to LFn-GAL4 and incubated with PA and HeLa cells *in vitro* indicative of membrane translocation.

3.2 Chapter Specific Methods

3.21 Scanning electron microscopy

Briefly, individual, sterile cover slips were placed in each well of a 24 well plate and cells (HeLa or Vero) were seeded at a density of 1×10^4 cells/well (in a final volume of 2mL of complete media) and kept in a humidified atmosphere of 5% (v/v) CO₂ at 37°C for 24 hours. The media was then removed from the wells and the cells were fixed by adding 1mL of 2.5% (w/v) glutaraldehyde in PBS and stored for 1h at room temperature in a fume cupboard. After 1h, the glutaraldehyde solution was removed and the cells were washed with 2mL PBS twice for 20min per wash. After removing PBS completely from the wells, 2mL of 1% (w/v) osmium tetroxide was applied into each well and incubated at room temperature for 1h. Cells were then washed with PBS as before. Cells were dried using increasing concentrations of graded ethanol in PBS over a concentration range of: 30%, 40%, 50%, 70%, 80%, 90%, 95% and 100%. Each concentration was applied and allowed to equilibrate for 20 minutes at room temperature and the process repeated twice. Finally, the cells were dried completely by applying 2mL of hexamethyldisilazane (HMDS) into each well and stored for 20min. After that HMDS was removed from the wells cells were left to dry overnight. Once dried, samples were coated with chromium before SEM analysis by placing slides in a chromium coater. The stub was mounted and placed inside the SEM (Hitachi SU8030). Once the microscope was adjusted for focus and stigmatism, images were collected (Hitachi SU8030), analysing backscattered and secondary backscattered electrons. The working distance was approximately 15mm with a voltage of 2.0kV.

3.22 ASO Annealing

Both forward and reverse antisense oligonucleotide designed to partially anneal as a mismatched pair were mixed and magnesium chloride added to a final concentration of 5mM. A heat block was set to 90°C and used to melt any spontaneously formed higher order structures (5 mins) formed by the oligonucleotides. The heat block was turned off, and the oligonucleotides allowed to cool to room temperature.

3.23 ASO transfection experiments

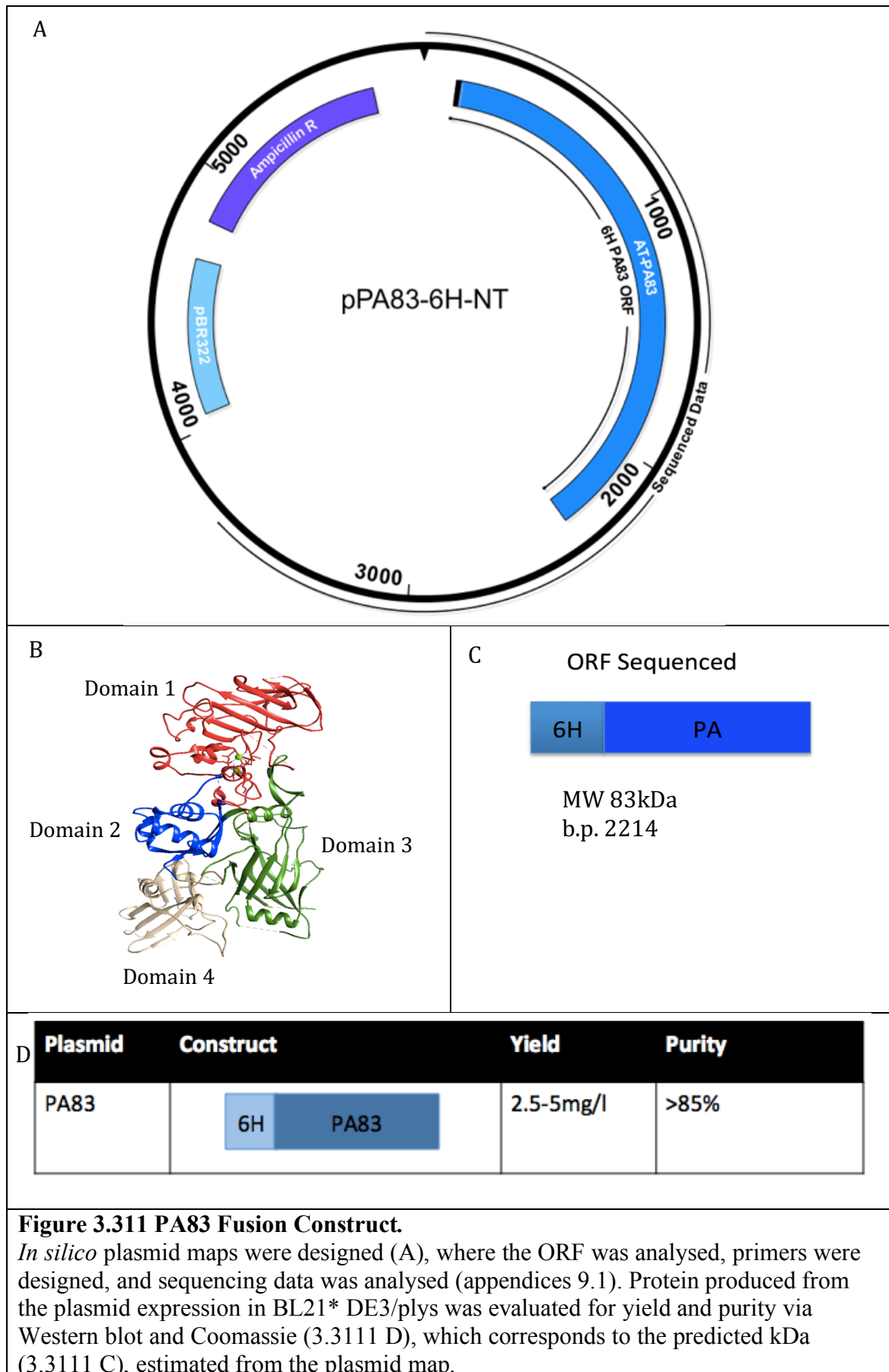
HeLa cells were seeded into a 6-well plate at a density of 1×10^6 . Cells were incubated for 4 hours in serum free media with PA (50 µg/mL), LFn-GAL4 (20 µg/mL) and annealed ASO-Syn5 (200pmol/mL), under standard cell culture conditions. Whole cell lysates were then prepared as previously described (Section 2.252). Syntaxin5 (Syn5) knockdown was evaluated at 24 hours by Western blot analysis as previously described (Chapter 2.242). The degree of knockdown was then quantified relative to that of a housekeeping gene (Early endosomal antigen 1 (EEA1)) using densitometry (Section 2.237).

3.3 Results

3.31 PA83 production and characterisation

Protective antigen (PA83) had previously been sub-cloned into the pQE30 vector and sequenced. The analysis of this showed correct sequence homology with PA83 published sequences (accession AAF86457), with the ligated DNA insert being maintained within the open reading frame with an N-terminal polyhistidine tag (6H). PA83 produced in One Shot[®] *E.coli* BL21*(DE3/plys) bacteria (Invitrogen, Paisley, UK) was detectable by both Coomassie stain and blot using an anti-PA polyclonal antibody at the predicted molecular weight of 83 kDa (Figure 3.311 C).

Protein purity had been analysed via SDS PAGE and Coomassie staining, this was determined to have >85% purity. PA83 protein yield was determined by densitometry with reference to BSA standards concentration (0.25mg/mL), and this produced 1.5 mg of PA per litre of bacterial culture (Figure 3.312). PA83 production was improved to produce higher yields of the protein. This was accomplished by changing the protocol, (Section 2.232 to 2.233). This generated between 2.5-5 mg of PA per litre of bacterial culture dependent on the time of culture post transformation. With a single transformation producing these quantities 5 days post transformation (Figure 3.113), as opposed to the previous method (Section 2.232) where a single transformation was entirely used for 1 litre of bacterial culture. However, as time continues post-transformation, the purity of PA83 decreases from >95% to <85%. This was especially evident at day 5 (Figure 3.313 B). This is most likely degraded PA, or other contaminant purified along with PA. PA production was also tested for temperature sensitivity and was found to produce a higher yield of PA83 when cultures at 37°C.



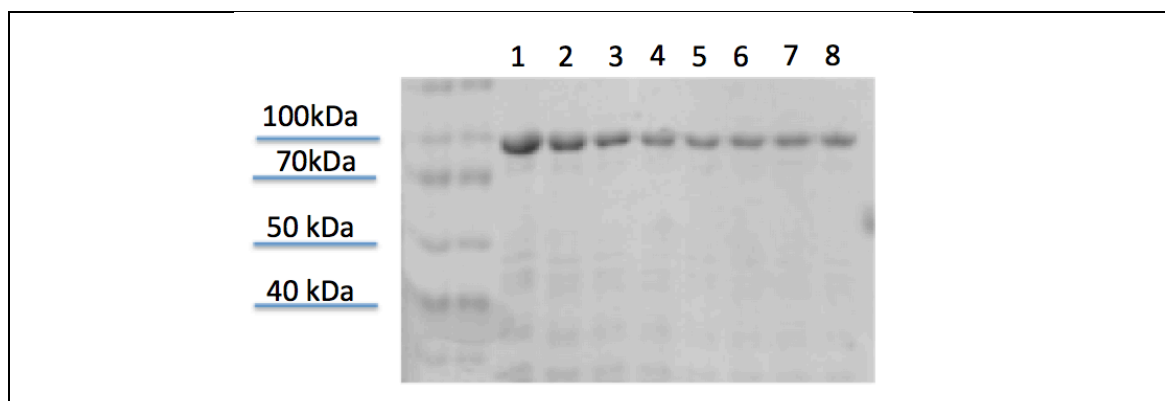


Figure 3.312 PPA83 protein eluted from TALON[®] resin of pooled fractions by SDS-PAGE and Coomassie staining.

PA83 yields and purity were determined via SDS PAGE, and Coomassie stain. Figure 3.112 shows fractions 1-8 (1mL eluted fractions) for PA, followed by BSA (0.25mg/mL). Concentrations were estimated by densitometry with reference to this BSA control. Eluted imidazole fractions were analysed for purity by the presence or absence of others proteins within the fractions protein bands at the estimated molecular weight were corroborated with Western blot analysis.

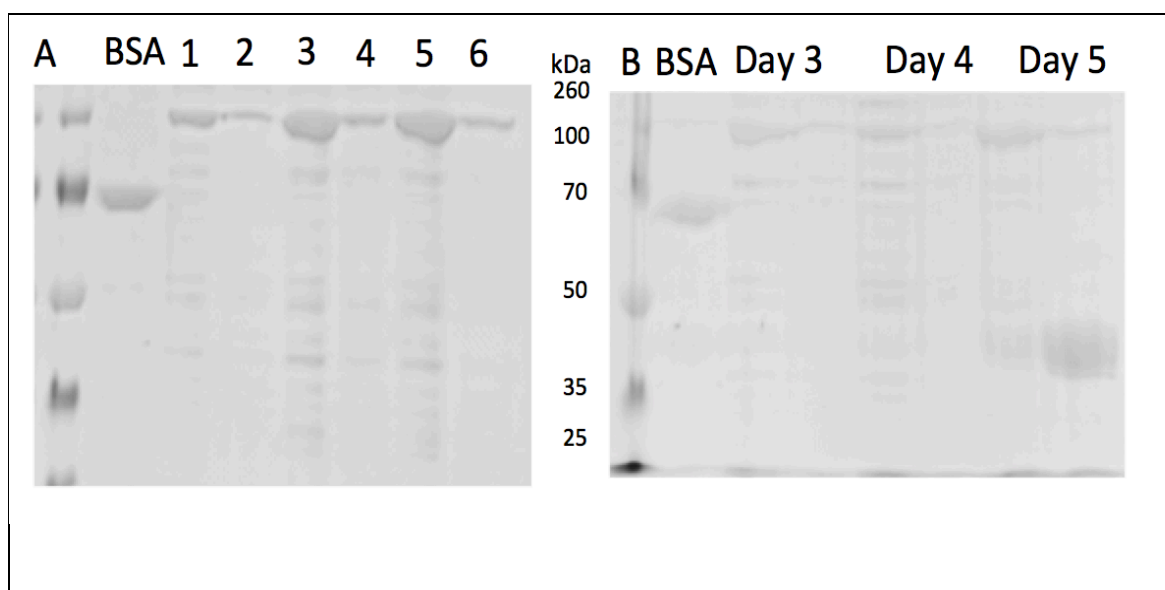


Figure 3.313 Protein production optimisation, evaluated by protein elution from TALON[®] resin by SDS-PAGE and Coomassie staining.

A shows eluted fraction of three different clonal population 1 and 2, are from the first and second imidazole eluted fractions of clonal population 1. Lane 3 and 4 are from the first and second eluted fractions of clonal population 2. Lane 5 and 6 are from the first and second imidazole eluted fraction from the third clonal population all cultured and induced post transformation. This single transformation was able to continually produce PA, 3 days, 4 days, and 5 days post transformation (B).

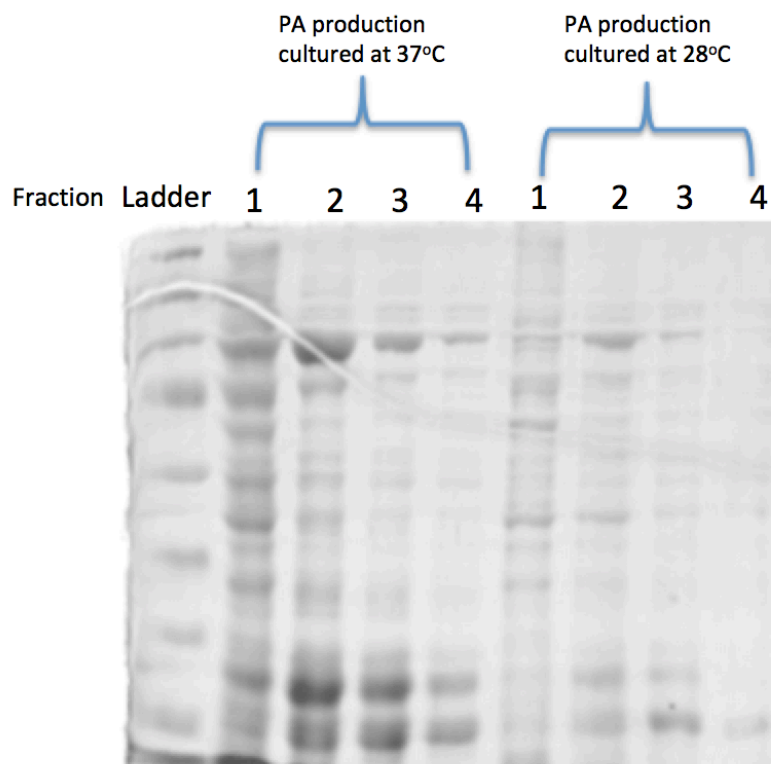


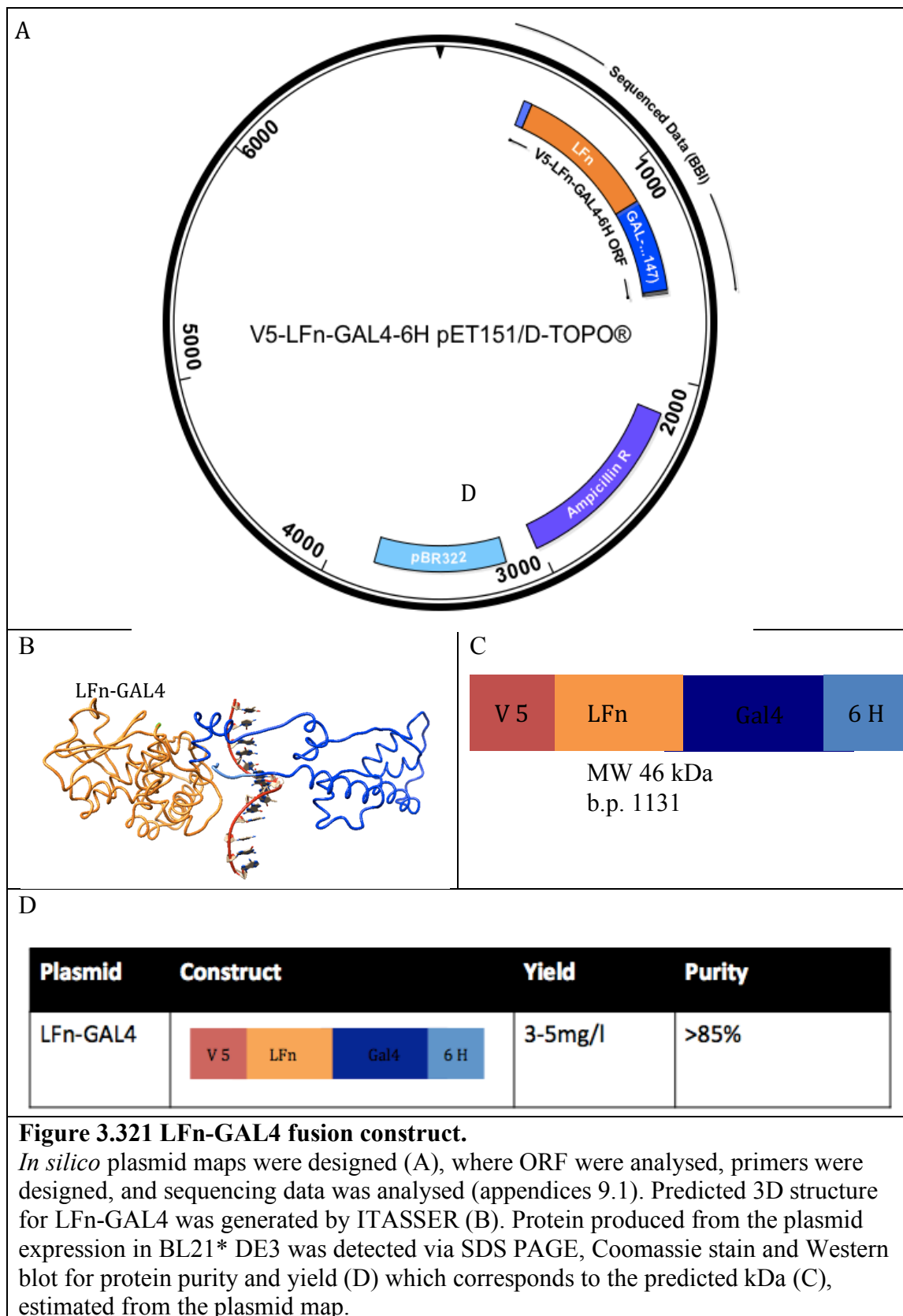
Figure 3.314 Protein production optimisation, evaluated by SDS-PAGE and Coomassie staining.

Analysis of protein fractions (1, 2, 3, and 4) by SDS-PAGE and Coomassie staining for PA production under two different temperatures (PA protein cultured at 37°C and B protein cultured at 28°C).

3.32 Characterisation of LFn-Gal4 protein production

Lethal factor fused in frame with GAL4 (1-147) had previously been sub-cloned into the pET151/D-TOPO expression vector, incorporating a C-terminal 6xHis and an N-terminal V5 epitope tag (Dyer *et al.*, 2015) (Figure 3.321 A). LFnGAL4 was produced in One Shot[®] *E.coli* BL21*DE3 bacteria (Invitrogen, Paisley, UK) was assayed by both Coomassie stain and immune blot using an anti-6xHis specific monoclonal antibody. Both of these detection methods identified a protein band at the predicted molecular weight (46 kDa; Figure 3.321 C) after analysis by SDS-PAGE.

LFn-GAL4 protein enrichment after metal ion affinity chromatography was assessed using SDS PAGE and Coomassie staining followed by densitometry using NIH Image J. LFn-GAL4 was determined to have > 85% purity. LFn-GAL4 protein yield was determined by densitometry with reference to BSA standard concentration, and this produced 4mg/l of protein (Figure 3.321 and 3.322).



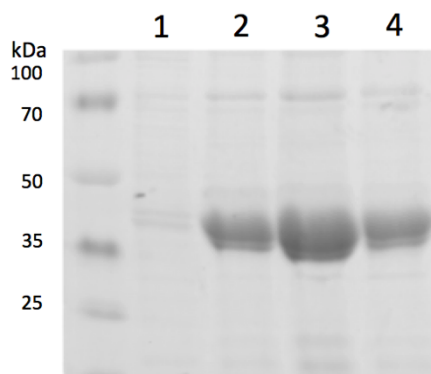


Figure 3.322 Protein elution from TALON[®] resin of eluted fractions by SDS-PAGE and Coomassie staining.

Evaluation of imidazole eluted fractions of LFn-GAL4 (fractions 1-4,) following SDS-PAGE and Coomassie staining. Concentrations were estimated by densitometry with reference to a BSA control (0.25mg/mL) and resulted in 3mg/l. Eluted imidazole fractions were analysed for purity by the presence or absence of others proteins.

3.33 PA and LFn-GAL4 *in vitro* toxicity profiles

The growth curves for HeLa and Vero Cell lines were evaluated using the MTT assay, using cells seeded at different densities (1×10^3 and 1×10^4) for both cell lines. From these data, the doubling times were calculated and were found to be 24 hours for HeLa cells, at both seeding densities (n=6). In HeLa cells seeded at 1×10^3 , the exponential growth phase where the doubling time was measured was from day 4-5, and at a seeding density of 1×10^4 the exponential growth phase where the doubling time was measured was from day 3-4 (Figure 3.331). This was similar in Vero where both seeding densities had 24 hours doubling time, however the doubling time, measured in the exponential growth phase was measured at day 1-2 for 1×10^4 and for Vero cells seeded at 1×10^3 the exponential growth phase where doubling time was measured was day 3-4 (Figure 3.332). The difference in the exponential growth phase in day is due to cell number. This finding was useful for evaluating growth patterns of both cell lines, as many of the studies involve using both cell lines over time course periods.

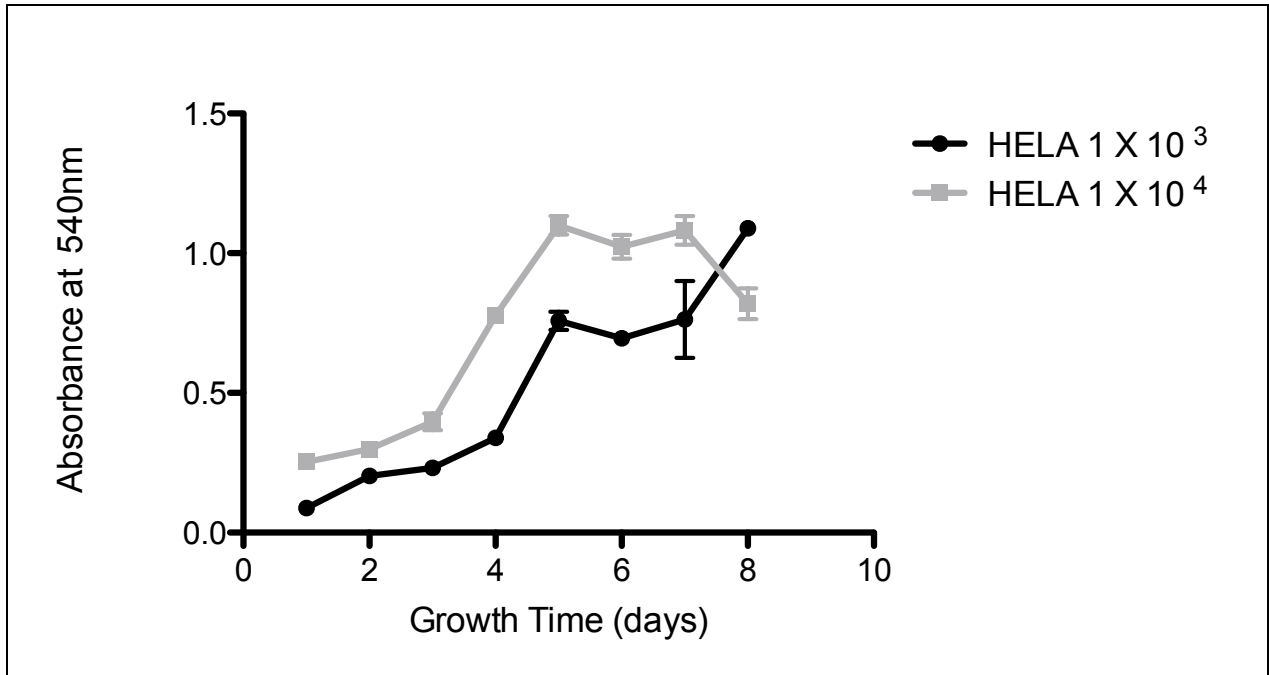


Figure 3.331 Growth curves of HeLa cells.

HeLa cells starting seeding density at 1×10^3 per well and 1×10^4 per well, $n=6$, evaluated by MTT.

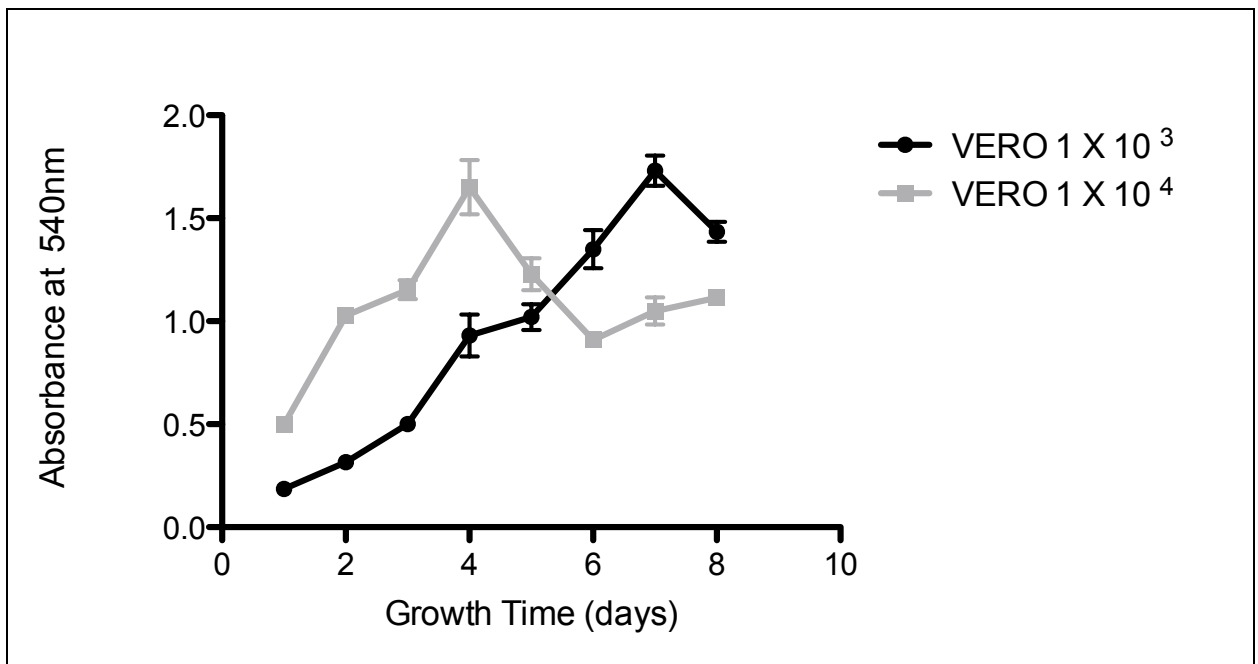


Figure 3.332 Growth curves of Vero cells.

HeLa cells starting seeding density at 1×10^3 per well and 1×10^4 per well, $n=6$, evaluated by MTT.

Scanning electron microscopy (SEM) images were taken of HeLa cells under four different treatments A, PBS treated, B, PA+LFn-GAL4+ASO, C, 10 μ g/mL PEI, D, 100 μ g/mL PEI (Figure 3.333). This was done to determine whether any gross morphological changes occurred after the prescribed treatments indicative of toxicity. As ATx undergoes capture by receptor-mediated endocytosis, and the payload (in this instance ASO) escapes lysosomal degradation by exiting the endomembrane system through back-fusion of an ILV, it was predicted that there would be dramatically less damage to the cell, relative to well-known transfection reagents such as poly (ethylene imine) (PEI). As a lack of toxicity was critical to the hypothesis under evaluation, these data are included herein.

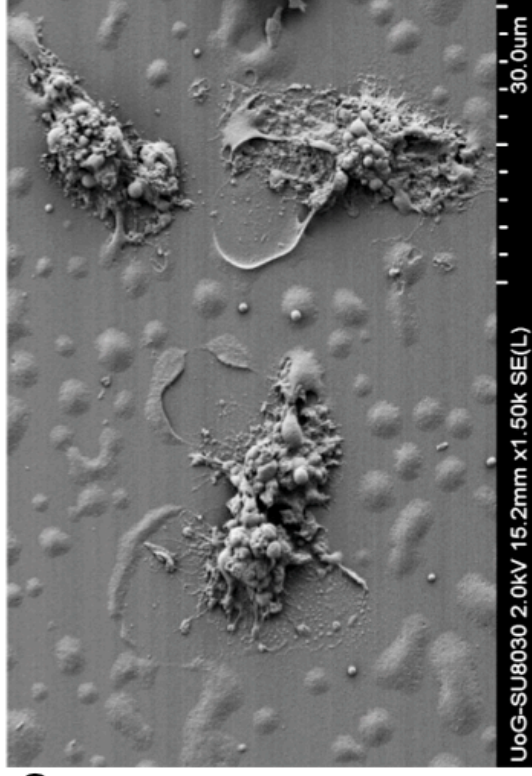
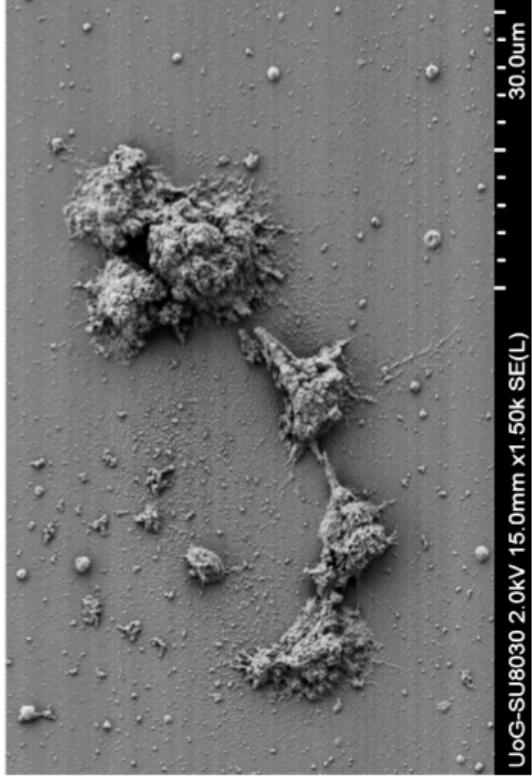
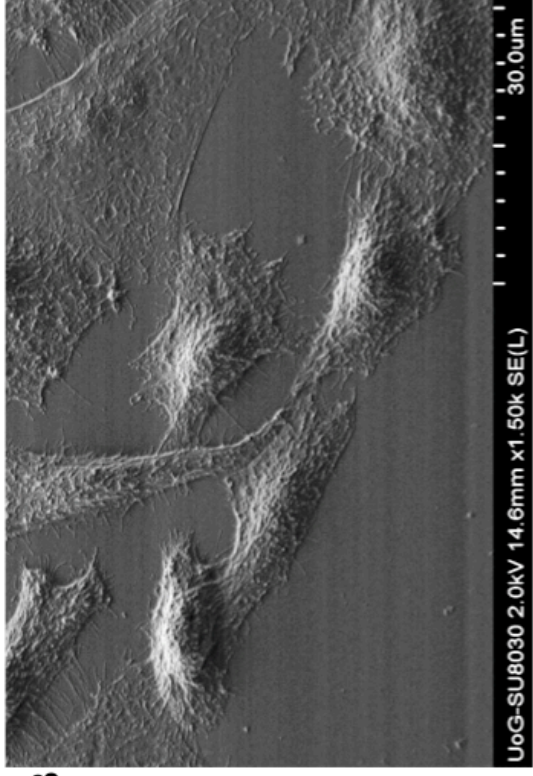
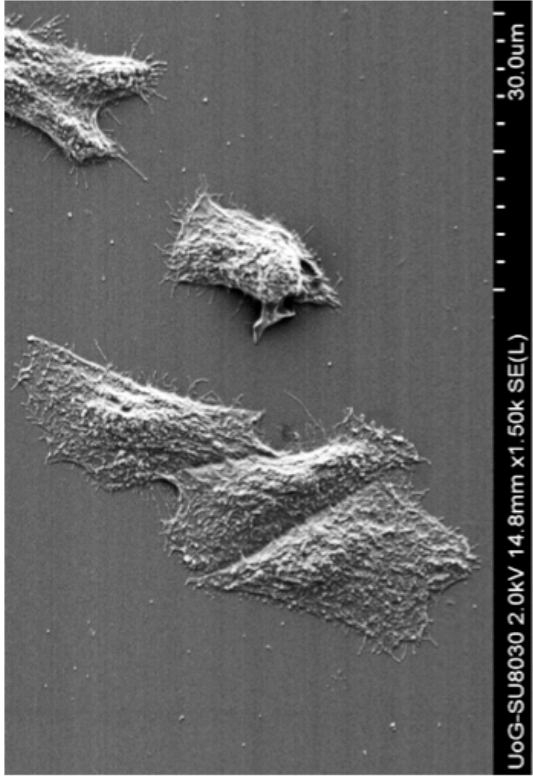


Figure 3.333 SEM images of HeLa cells treated under four different conditions. HeLa cells were treated with either PBS (A) PA:LFn-Gal4:ASO (B), Sublethal concentration of PEI (C, 10ug/mL) and a lethal concentration of PEI (100ug/mL). This demonstrated a marked difference in cell morphology based on cell treatment.

In order to try to control for membrane damage (and toxicity) being responsible for translocation, giving rise to false positive data later in this chapter, protein toxicity was evaluated for the recombinant proteins produced (LFn-GAL4, PA) and combination of these recombinant proteins (LFn-GAL4 +ASO and PA+LFn-GAL4+ASO) using the MTT assay (Hansen and Bross 2010). Positive and negative and controls of PEI (toxic) and dextran (non-toxic) (Figure 3.334 and 3.335 respectively) were also employed. Toxicity was tested in HeLa cells over a period of 24, 48 and 72 hours and expressed relative to an untreated population of the cell type used, accounting for differences in growth rate following the evaluation of toxicity by MTT assay. A summary of the IC₅₀ was generated (Table 3.31). The IC₅₀ of PA was >200µg/mL at 24 and 48hours, and 72 hours (Figure 3.336). LFn-GAL4 toxicity profile (Figure 3.337) showed an IC₅₀ >200µg/mL at 24, 48 and 72 hours. Lfn-GAL4 in the presence of ASO (Figure 3.338) and in the presence of both PA and ASO (Figure 3.339) both showed IC₅₀ >200µg/mL.

When compared to IC₅₀ of PEI (IC₅₀ 24 hours 51 ±13 µg/mL, 48 hours 51 ±3 µg/mL, and 72 hours 81 ±2.5 µg/mL), which was far more toxic than the PA:LFnGal4:ASO system.

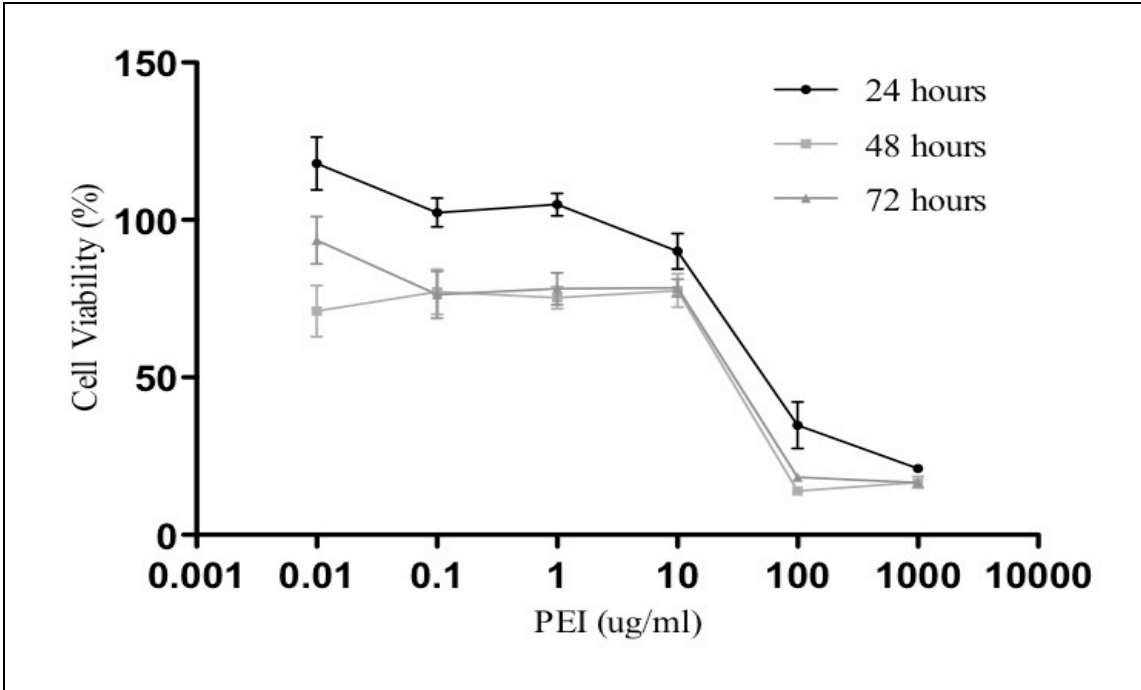


Figure 3.334 Toxicity profile of PEI in HeLa cells at 24, 48 and 72 hours. Toxicity profile of PEI in HeLa cells over 24,48 and 72 hours treated at increasing concentrations (0.1µg/mL – 1000µg/mL), with a seeding density of 1×10^4 HeLa cells (n=18).

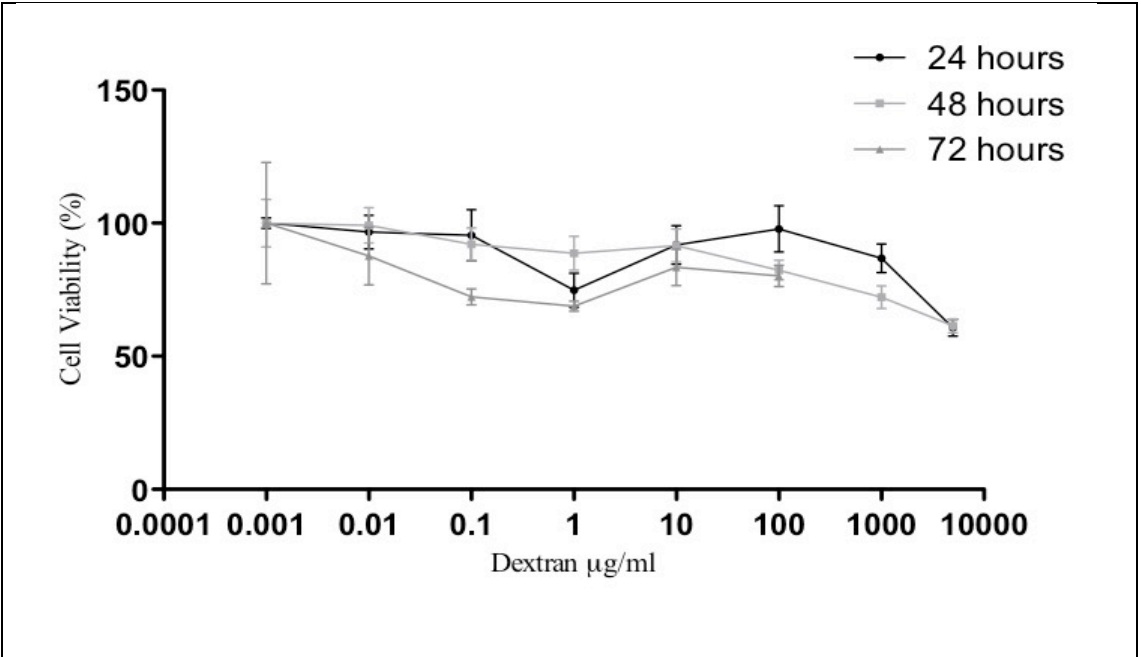


Figure 3.335 Toxicity profile of Dextran in HeLa cells at 24, 48 and 72 hours. Toxicity profile of Dextran in HeLa cells over 24,48 and 72 hours treated at increasing concentrations (0.1µg/mL – 1000µg/mL), with a seeding density of 1×10^4 HeLa cells (n=18).

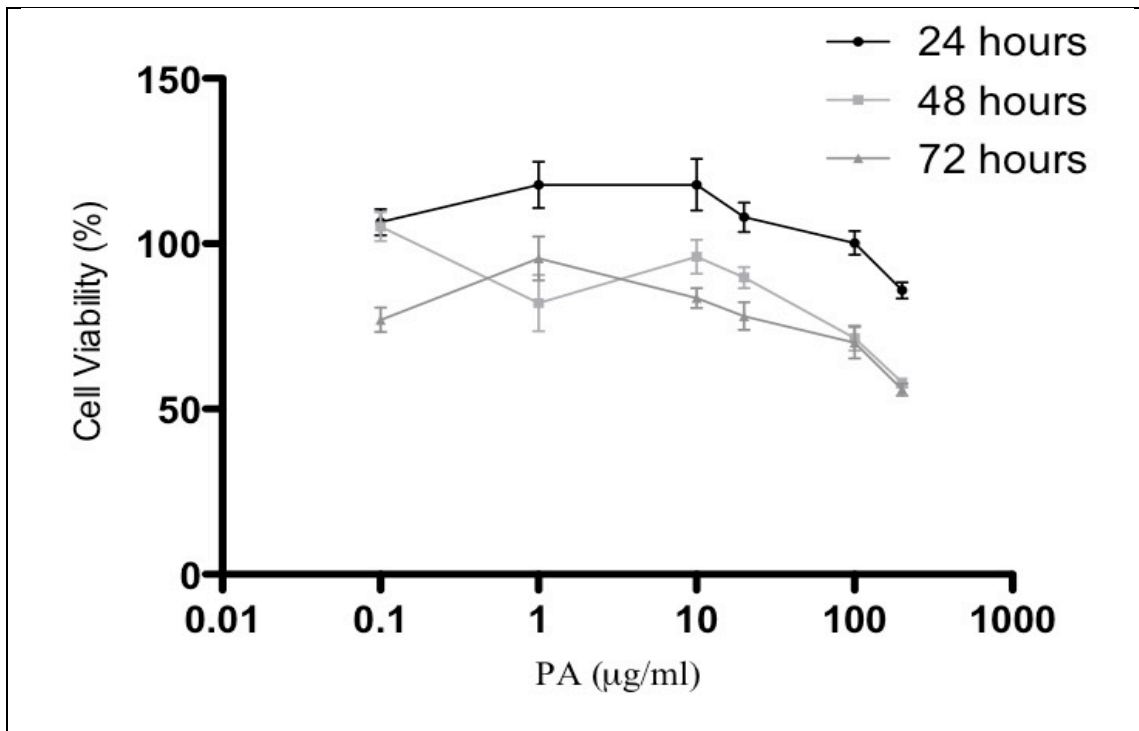


Figure 3.336 Toxicity profile of PA in HeLa cells at 24, 48 and 72 hours. Toxicity profile of PA in HeLa cells over 24,48 and 72 hours treated at increasing concentrations (0.1µg/mL – 200µg/mL), with a seeding density of 1x10⁴ HeLa cells (n=18).

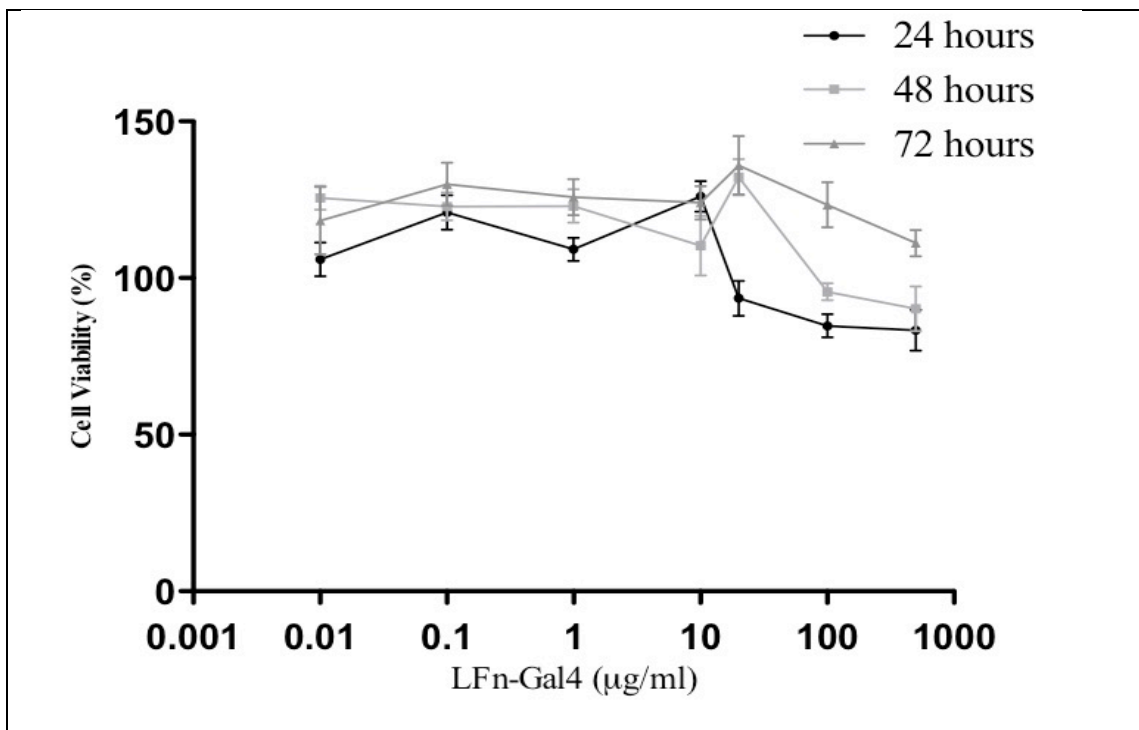


Figure 3.337 Toxicity profile of LFn-GAL4 in HeLa cells at 24, 48 and 72 hours. Toxicity profile of LFn-GAL4 in HeLa cells over 24,48 and 72 hours treated at increasing concentrations (0.1µg/mL – 200µg/mL), with a seeding density of 1x10⁴ HeLa cells (n=18).

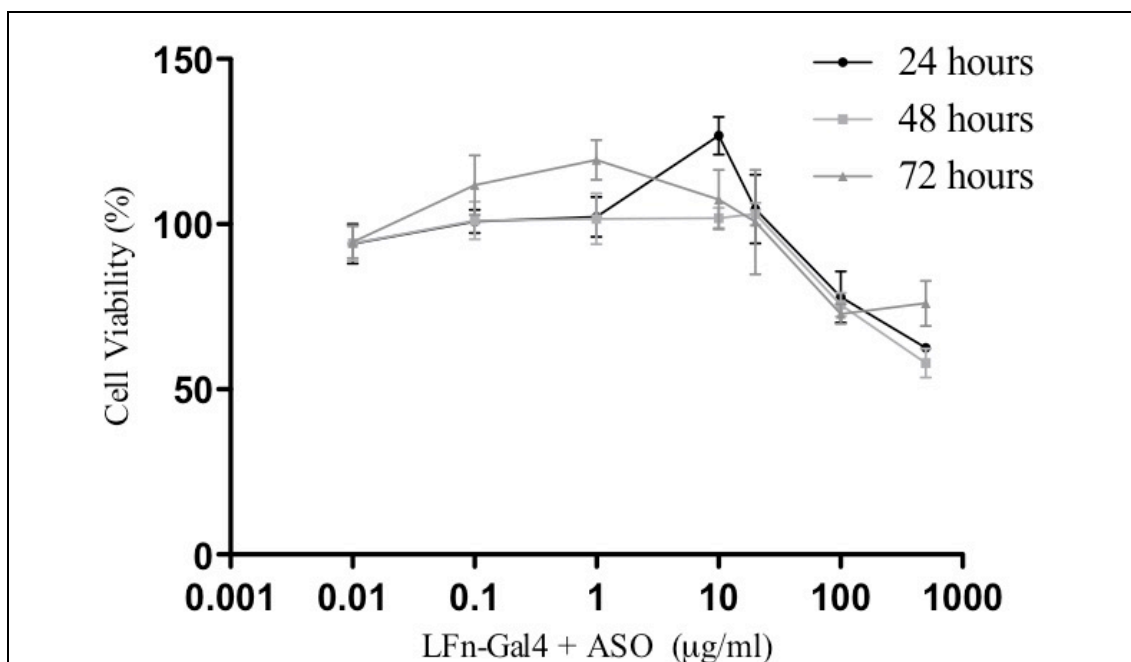


Figure 3.338 Toxicity profile of LFn-GAL4 + ASO in HeLa cells at 24, 48 and 72 hours.

Toxicity profile of LFnGAL4 + ASO in HeLa cells over 24,48 and 72 hours treated at increasing concentrations (0.1µg/mL – 200µg/mL), with a seeding density of 1×10^4 HeLa cells (n=18).

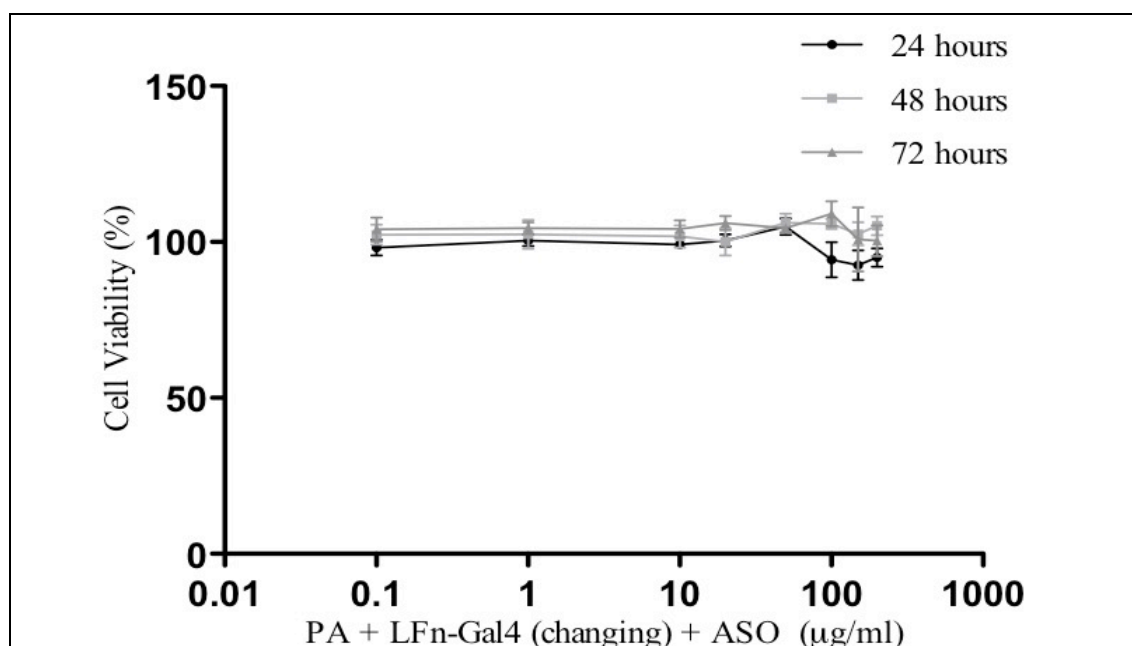


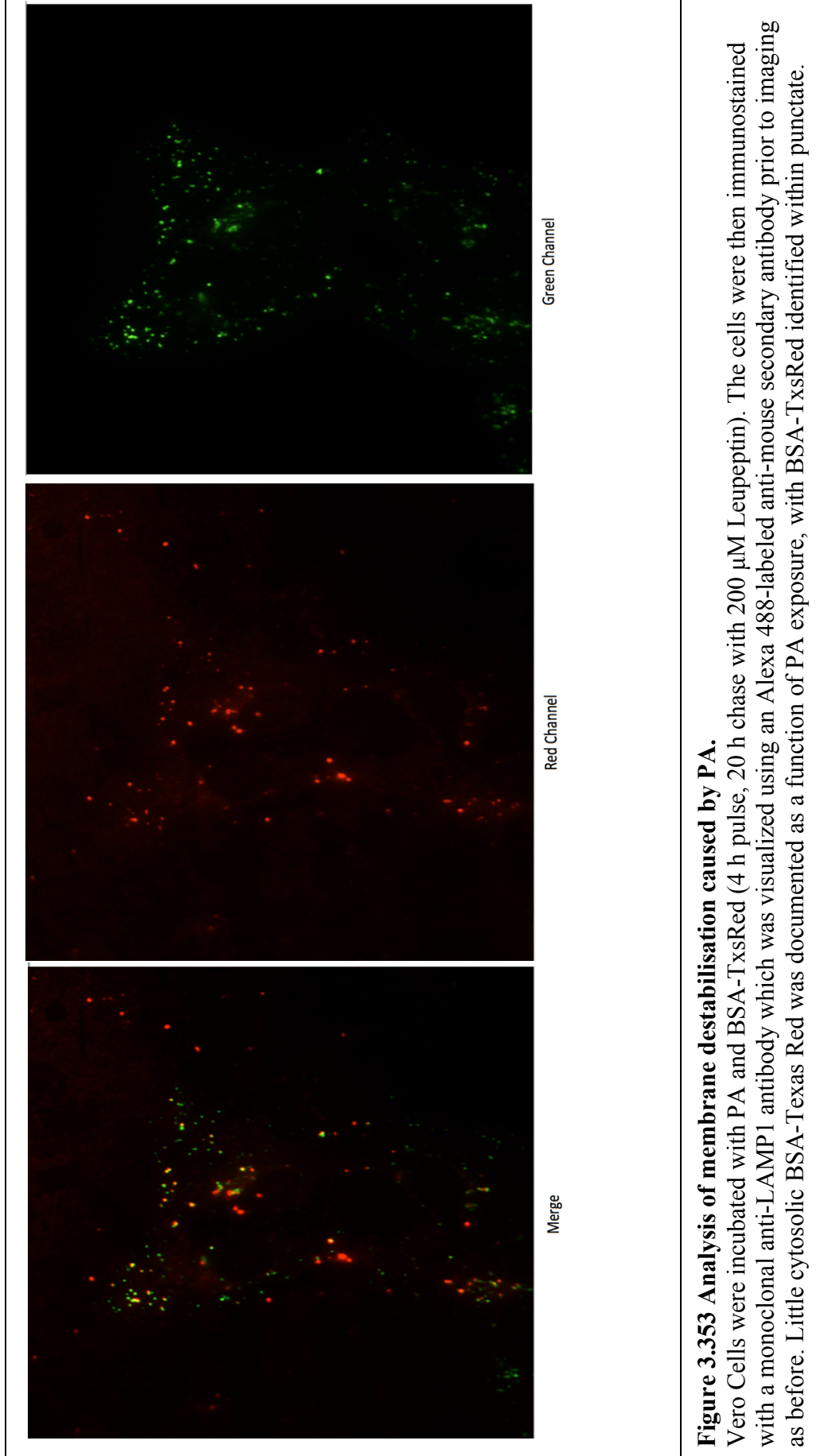
Figure 3.339 Toxicity profile of PA, ASO, and LFn-GAL4 at varying concentrations in HeLa cells at 24, 48 and 72 hours.

Toxicity profile of PA ASO, and LFn-GAL4 in HeLa cells over 24,48 and 72 hours, treated at increasing concentrations (0.1µg/mL – 200µg/mL), with a seeding density of 1×10^4 HeLa cells (n=18).

Table 3.31 Summary of Protein toxicity IC₅₀			
Treatment	24 Hours	48 Hours	72 Hours
PEI (µg/mL)	51 (±13)	51(±3)	81(±2.5)
Dextran (µg/mL)	>100	>100	>100
PA (µg/mL)	>200	>200	>200
LFnGal4 (µg/mL)	>200	>200	>200
PA+LFn- Gal4+ASO (µg/mL)	>200	>200	>200

To further address issue of other possible release mechanism such as membrane rupture of the endosomes, due to the PA pore, and release of the ASO, Vero cells were treated with PA, and BSA-TxsRed (Figure 3.353). The limited amount of cytosolic BSA, in conjunction with the presence punctate would support the backfusion model of translocation through the pore and release into the cytosol as opposed to membrane destabilisation.

Further to these, Vero Cells were treated with PA (Figure 3.345 4hrs (panel A) and 8hrs (panel B) these were then stained for LBPA. After an 8-hour incubation, there was a higher degree of co-localisation between PA and LBPA. This demonstrates the trafficking of PA to lysobisphosphatidic acid (LBPA) positive endocytic vesicles over time. Which supports the hypothesis of backfusion and translocation through the pore, as LBPA is critical to the formation of ILVs and backfusion.



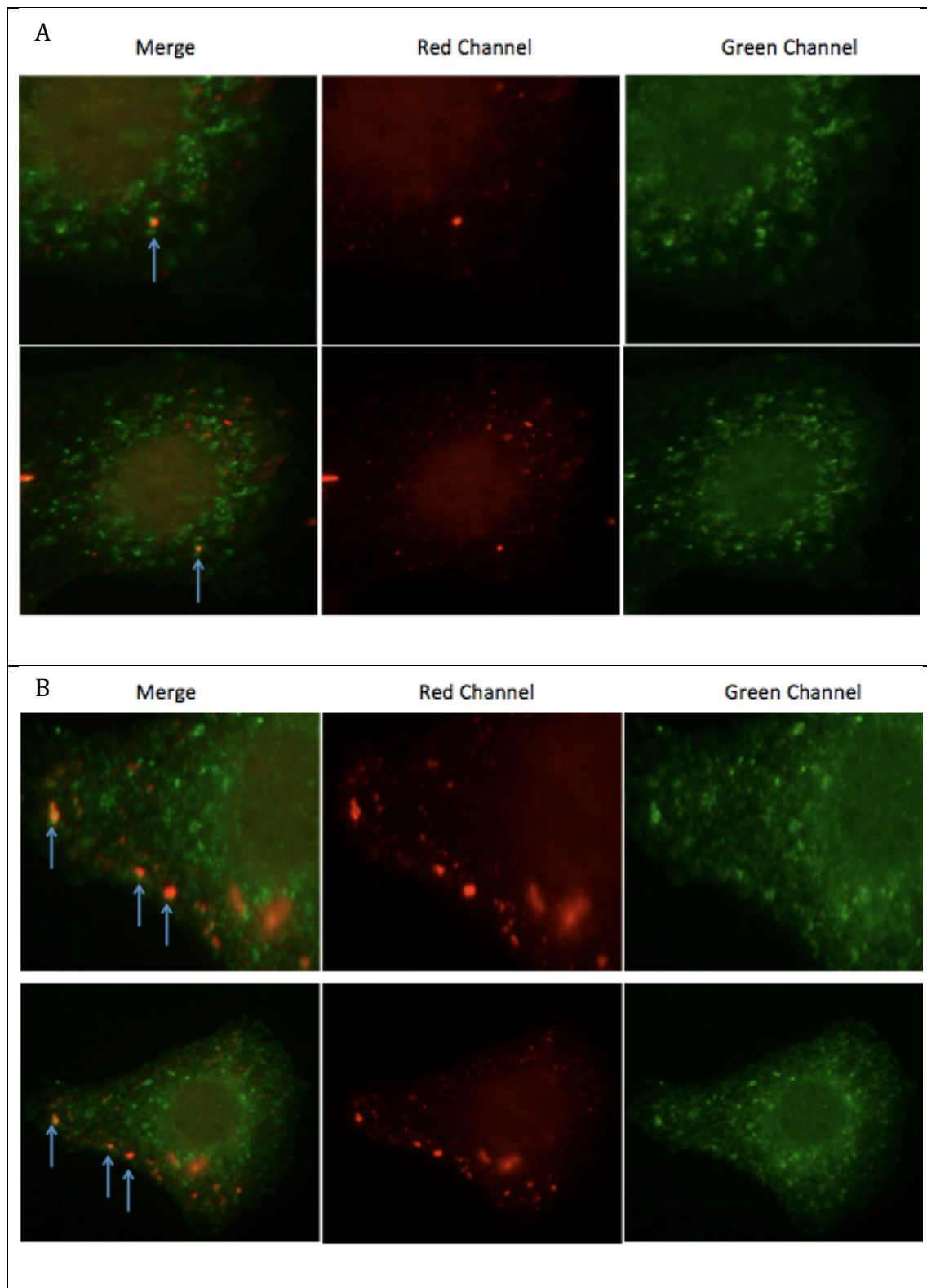


Figure 3.354 The localisation of PA with LBPA is shown at 4 h(A) and 8 h(B) in Vero cells.

Vero cells were Pulsed with PA for 4 h or 8 hours, and then assessed for co-localisation of PA(green) with LBPA (red). After 4 hours, there was limited co-localisation (blue arrows). After an additional 4 hours (B) there is a higher degree of co-localisation between PA and LBPA.

3.34 Antisense Oligonucleotide Design and Characterisation

ASOs were designed *in silico* to contain (atgcatgccggctgctctgatgccggcat) sequence that would allow the annealing of two strands to produce a GAL4 binding sequence (Figure 3.341). The 5' end of these sequences was extended to contain an antisense sequence (19nt) previously published to down-regulate the expression of syntaxin5 (aattgtttgttgaggcta) (Dyer *et al.*, 2015). Before the transfection experiments could proceed, the ASOs were characterised to ensure that a duplex could be formed after a period of annealing and this was analysed using a native PAGE gel (Figure 3.342). This shows single stranded oligonucleotides, that haven't undergone a re-annealing procedure, and (Figure 3.342 U) as well as the oligonucleotide that has undergone the annealing procedure (R). The difference in electrophoretic mobility would confirm that the complimentary ASO have annealed.

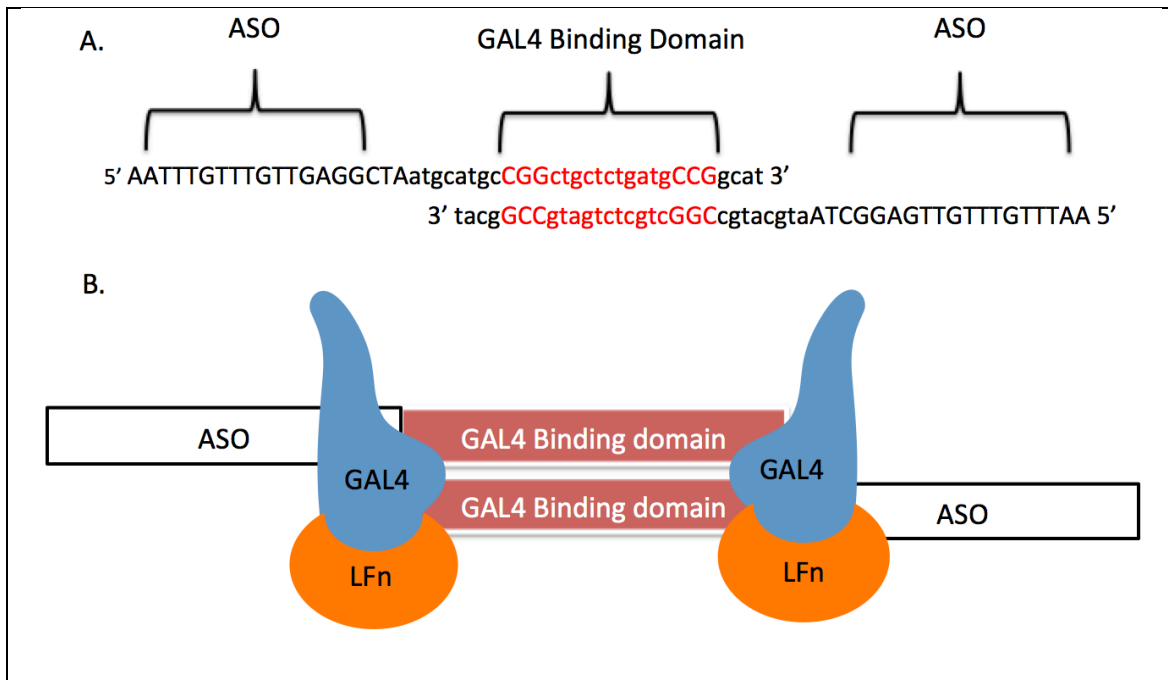


Figure 3.341 Antisense oligonucleotides complexed with LFn-Gal4.

Schematic representation of the designed and used ASO (A), with the LFn-Gal4 binding domain highlighted in red, within the complementary strands of the antisense oligonucleotide. With the antisense sequences targeted towards Syntaxin 5 over hanging of this complementary region. LFn-Gal4 dimerisation driven by the Gal4 DNA binding domain.

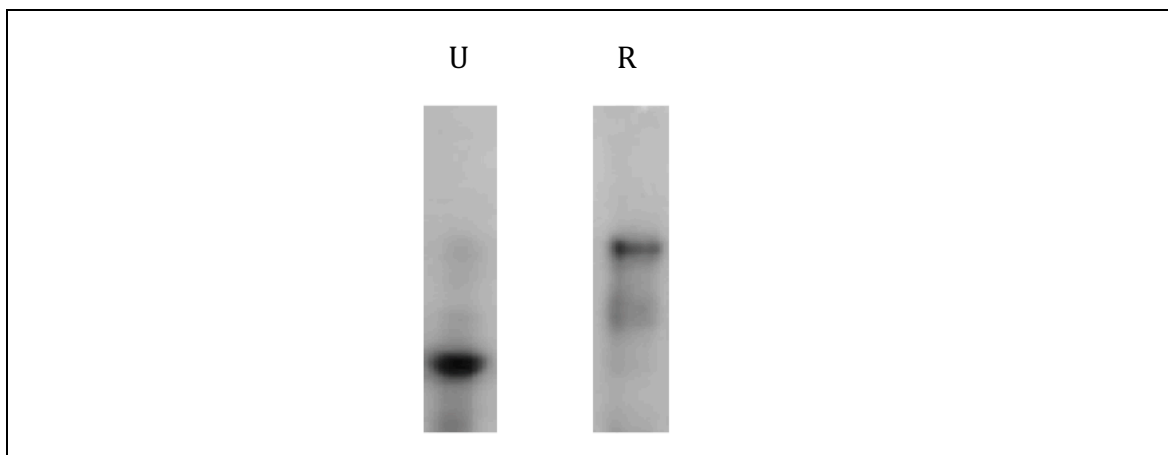
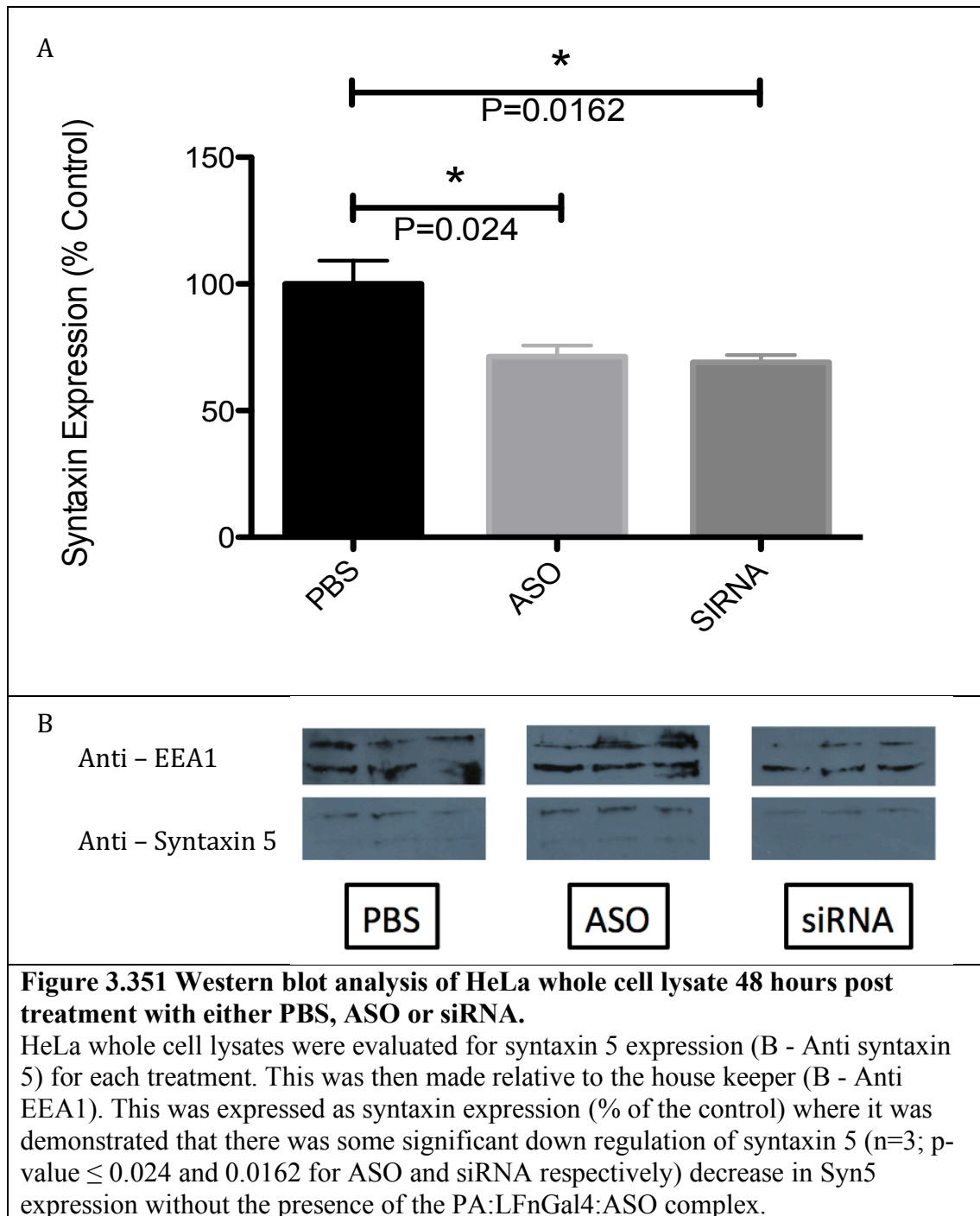


Figure 3.342 Characterisation of ASO.

Characterisation of ASO, initially (A) ASO was run on a 12% native PAGE, both untreated (U) and treated under a re-annealing procedure (R). The difference in electrophoretic mobility demonstrates annealing of the oligonucleotide.

3.35 Transfection Experiments

Initially HeLa cells were treated with PBS, siRNA or ASO (siRNA and ASO both targeted to syntaxin 5) to establish baseline levels of transfection (Figure 3.351). Transfection (Synt5 knockdown) is expressed normalised to that of a house keeper protein (EEA1) to control for any variation in cell number between experiments. The data demonstrates a significant down-regulation of the target gene ($P= 0.024$ and $P=0.0162$ for naked ASO and siRNAs respectively) it is considerably less than that reported using systems such as nucleofection and describes the noise floor relative to the membrane permeability of these experimental (translocase) cargos.



To assess the ability of a PA oligomer to translocate a protein:ASO complex, a supramolecular assembly consisting of the hybrid ASO and the LFn-GAL4 complex was generated (Section 3.22). Given that the ASO hybrid was anionic, and that PA translocase substrates has been reported to require a positive charge, translocation of the ASO was hypothesised to be dependant upon the maintenance of high order structure during translocation. The delivery of the ASO was measured by assaying the knockdown of the endogenous protein syntaxin 5. Figure 3.352 showed densitometry analysis of Western blots of HeLa whole cell lysate, 48 hours post treatment with either PA + LFn-GAL4:ASO or PA + LFn-GAL4 (N=3). These data showed a significant down-regulation in target gene expression (PA + LFn-GAL4:ASO) relative to untreated controls (P= 0.0016). This would indicate that the ASO is being delivered into the cytosol of the HeLa cells during this experiment.

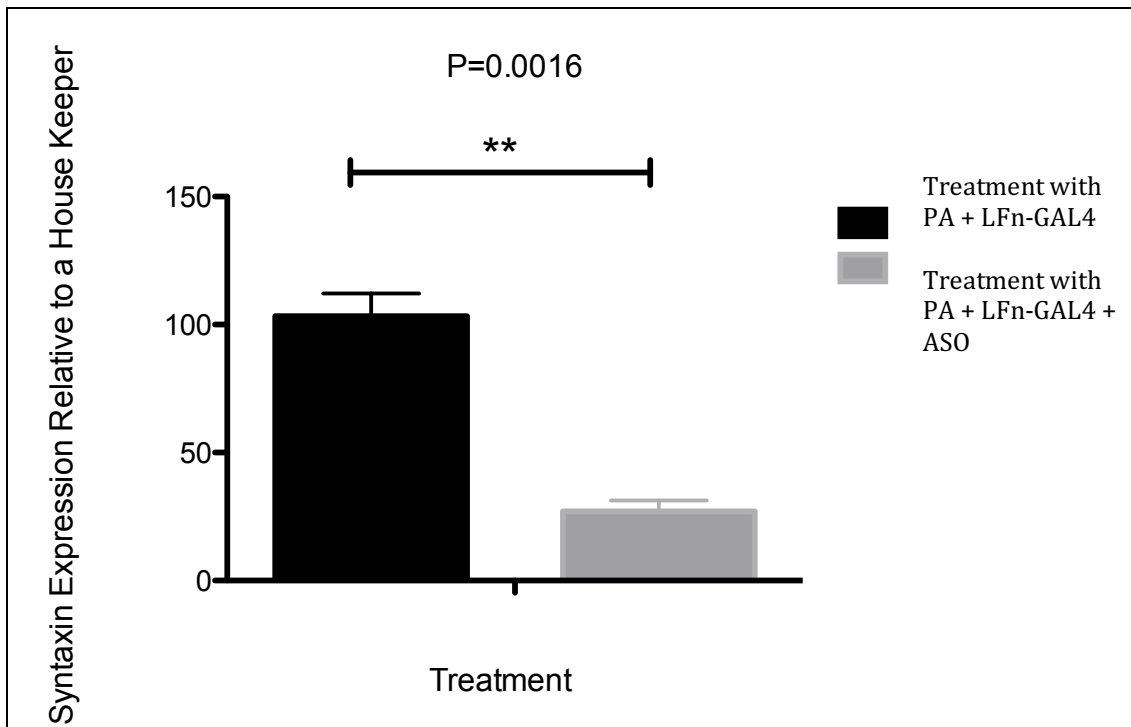


Figure 3.352 Analysis of PA: LFn-GAL4: Syn5-ASO treated HeLa cells at 24 hours by Western blot.

Graph showing syntaxin5 expression relative to a housekeeper 48 hours post-treatment with PA: LFn-GAL4: Syn5-ASO or PA: LFn-GAL4 by densitometry. This showed a significant (n=3; p-value ≤ 0.0016) decrease in Syn5 expression.

3.4 Discussion

The characterisation of the plasmids used to express the recombinant proteins (PA83 and LFn-GAL4) revealed that the sequences were as predicted. These results were aligned into a continuous sequence, where the ORF of the gene was evaluated (appendices 9.1).

The production and characterisation of recombinant proteins all appeared to be at the predicted molecular weight and repeated our published findings (Dyer *et al.*, 2015). The production of PA83 was optimised to be more efficient, and produced twice the yield of the original method.

Protein toxicity was compared to cationic polymer for used for DNA delivery (Luo 2000) and a biopolymer (dextran), known to be non-toxic (Richardson *et al.*, 1999). Although the data presented herein documents the IC₅₀ of PEI to be 51 µg/mL at 24 hours, which differs from published data (Aravindan *et al.*, 2013), this is explainable due to difference in the branching and difference in the average molar mass (M_w) for the polymer (Deng *et al.*, 2009).

The low *in vitro* toxicity associated with the PA:LFn-Gal4:ASO delivery system could possibly be attributed to the possibility that this system may use back-fusion after PA translocation to facilitate the cytosolic translocation of the anti-Syntaxin 5 ASO detailed above. This is opposed to destabilisation of endomembrane by polycations which is also responsible for mediating cell toxicity (Zhang *et al.*, 2014; Shorter *et al.*, 2017).

Given that polycation mediated membrane destabilisation is in no way localised to endomembrane, the SEM data contrasting cells exposed to PA:LFn-GAL4 to those exposed to PEI was not surprising. Cells exposed to PEI can be seen to be morphologically very different from the PBS or PA:LFN-GAL4:ASO treated cells, which look morphologically similar, *i.e.* no gross morphological deformation of the plasma membrane or cell shrinkage (Figure 3.333). Supporting these toxicity data, Figure 3.343 examines membrane disruption mediated by PA protein by assaying the release of vesicular BSA-TxsRed (or lack thereof)

from membrane bound structures within the cell. Defined punctate structures positive for BSA-TxsRed are visible, with minimal amounts cytosolic BSA-TxsRed evident, which would support the notion of back-fusion rather than membrane disruption, and associated toxicities. This could be further investigated, with investigating BSA-TxsRed distribution within cells that had been treated with PEI, to further support the toxicity profile of this method of DNA delivery for polycations.

Further experiment investigating the requirement for proteins such ALIX would also add weight to the argument that vesicle back-fusion was required for antisense activity (Abrami *et al.*, 2013).

As there was minimal toxicity associated with the PA:LFn-GAL4:ASO treatment, individually and in combination, and they demonstrated the ability to deliver active antisense agents to the cytosol without causing the non-specific leakage of vesicular BSA-TxR or otherwise causing toxicity at levels approximately 300% of background ASO activity, it was concluded that the PA pore must be somehow accommodating this supra molecular assembly or could translocate polyanions.

Initial investigation was carried out to study the effect of just ASO and siRNA (Figure 3.351), as ASO and siRNA have been documented to freely enter cell lines without the need of a transfection agent (Stein *et al.*, 2010, Zheng *et al.*, 2015). This showed some significant knockdown for both ASO and siRNA (29% and 31% respectively). With the addition of the delivery system (Figure 3.342) there was a 73% reduction in gene expression. This would indicate that the ability of PA to tolerate and translocate ASO, which are larger than the internal diameter of the pore is possible with no need for condensing agents such as is used by Gaur *et al.*, 2002.

It was reported by Gaur *et al.*, 2002 that LFn-Gal4 could be used to deliver plasmid DNA after the DNA was condensed using a (membrane destabilising) polycation (PLL). The formation of particulates or “toroids” from plasmids by polycations is well documented and these structures typically have a diameter of approximately 120nm (Golan *et al.*, 1999). This would be too big to fit through the PA pore making the pore translocation of PLL:DNA toroids unlikely.

Given that it has been known since the 1950s that PLL is membrane-lytic, a more probably explanation of these data is that the PLL portion of the complex is mediating membrane destabilisation facilitating the nucleocytosolic translocation of the plasmid. It is also possible that the membrane insertion of PA is contributing to this PLL mediated membrane stress. It has been previously demonstrated by Dyer *et al.* , (Paul Dyer, PhD Thesis 2013) that this system has the ability to translocate plasmid DNA without the need of a condensing agent (as previously shown by Gaur *et al.*, 2002). This would throw into question what the limitations of the protective antigen pore are. If proteins do unfold during translocation, plasmids cannot do this, and being bigger than the estimated smallest internal diameter (number) of the pore could it allow the delivery of other payloads. This would also allow for the investigation of the limitations of the PA pore it can accommodate.

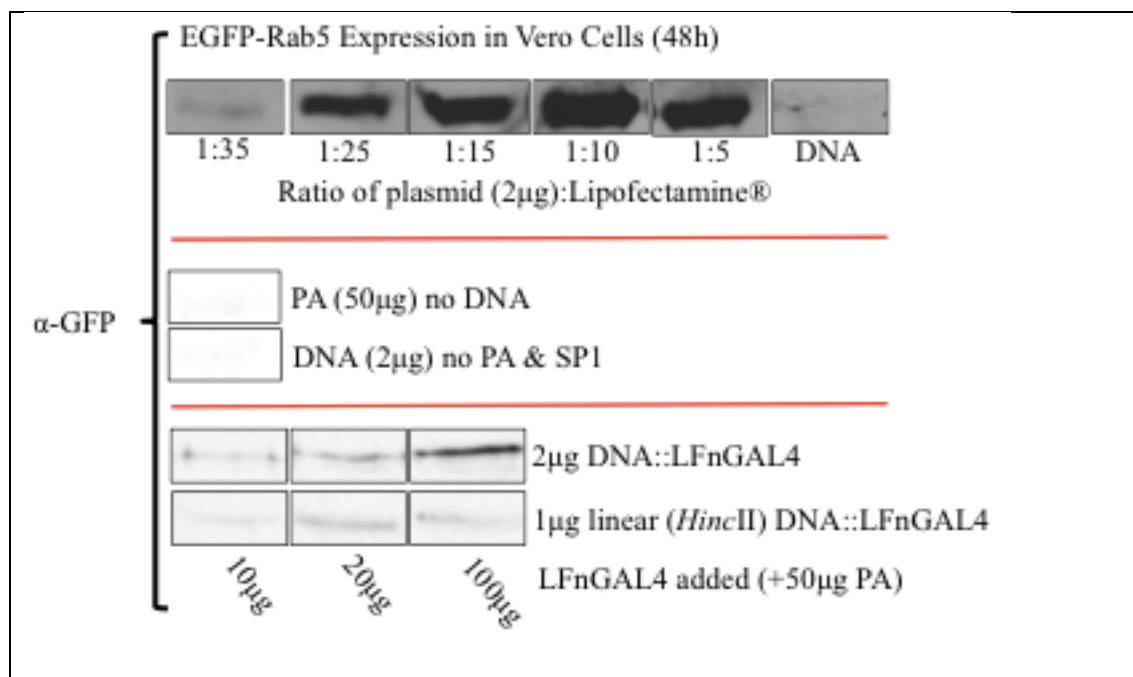


Figure 3.12 LFn-GAL4 delivery of plasmid DNA in Vero cells.

Proteins expression measured after 48hours compared to lipofectamine (Paul Dyer, PhD Thesis, data unpublished).

This study has provided indirect evidence that MG transition and polypeptide unfolding may not be essential for the whole protein in order to translocate. In the wild LF and EF are thought to lose their higher order structure in order for the PA pore to accommodate their size and ratchet through the internal lumen of the pore.

Furthermore, data presented here provides evidence for the ability of LFn-GAL4 to mediate cytosolic delivery of ASO, through maintained dsDNA binding domain. If molten globular transition was required for the protein to fit through the static PA pore with an internal lumen of 1.5nm the binding domain would be lost and so too the cargo (ASO) irrespective of driving forces and clamps within the pore and chaperonins. This would demonstrate that there are other factors involved in protein translocation, which may not require molten globular transition off the entire protein construct.

It could be a possibility that the energy harnessed through a charge-state Brownian ratchet mechanism is sufficient for the MG transition of LFn, which then acts through a ‘ball and chain’ mechanism (Figure 3.41 B) where LFn pulls the rest of the protein through the pore,

maintaining protein structure (except domain 1 of LF or LFn which still undergoes MG transition) but still facilitated by endosomal pH. Additionally, the differences in the translocation of substrates through either PA₈ or PA₇ have not been evaluated, and this may have an effect of the properties of translocation and the requirement of MG transition. Given the size of supramolecular assembly composed of a pair of ASOs and two LFn-GAL4 molecules that have been able to deliver a therapeutic payload to the cytosol, and the thought limitations of the PA pore evidence presented here begins to question the descriptions of material translocating across the PA pore where there may be other forces at work, such as a more flexible pore allowing dilation and the transit of larger material.

Alternatively, there could be a possibility of PA:LFn-Gal4:ASO facilitating translocation by proximal contact with the pore facilitating translocation and cytosolic release. However, given the diameter of the PA internal space (1.5 nm) and the diameter of the DNA duplex (2.0 nm) this would still leave questions as to the PA pores 'static' nature, and dependence of protein unfolding to facilitate translocation.

This highlights this protein-based delivery system as a potential therapeutic strategy, whilst also needing to investigate the limitations of deliverable payloads to the cytosol.

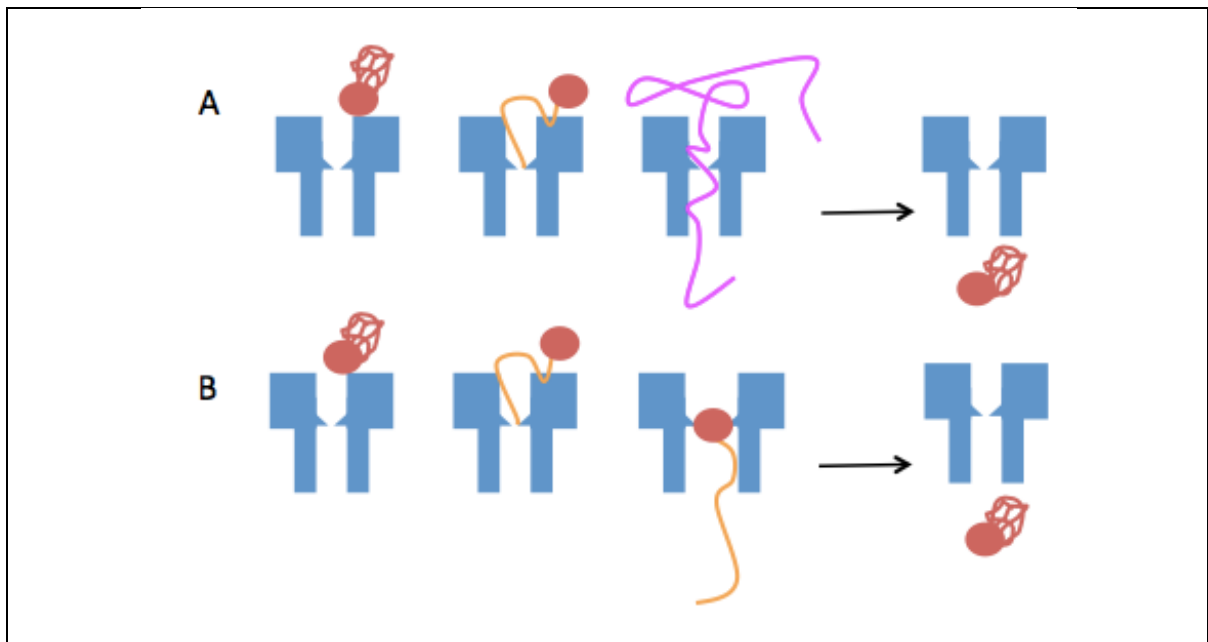


Figure 3.41 Possible Anthrax Translocation Models.

Brownian-ratchet model (A) protein (red) translocation through the PA pore (blue), substrate docking, domain 1 of LF, unfolding, and docking onto the pore, followed by unfolding and translocation through, with the protein re-folding. Another possible mechanism of protein translocation (B) protein docking, and partial unfolding, followed by translocation through the pore, in a 'ball and chain' mechanism, where part of the protein undergoes MG transition, initiates translocation, and pull the rest of the protein through in its native state.

3.5 Conclusion

The data presented here has demonstrated that the recombinant proteins (PA, LFnGal4) were produced at the concentrations required for ASO delivery. The designed ASOs could form a duplex. The PA:LFnGal4:ASO delivery system shows a much lower toxicity profile *in vitro*, more traditionally used delivery vehicles (PEI). This is most likely due to the lack of membrane disruption and the back-fusion delivery mediated delivery of the ASO into the cytosol. The PA:LFn-Gal4 are facilitating in the delivery of the ASO, decreasing gene expression as compared to cells treated with an equivalent amount of naked ASO. This brings into question the need for proteins to unfold during PA pore translocation.

Equivalently there are two other explanations of these data. The first is that higher order structure is being lost and the proteins are unfolding though this would require the

translocation of an anionic cargo which would be unlikely given the explanations describing the ratcheting of substrates through the PA translocase in the literature. The other is that the PA is causing the local destabilisation of endocytic vesicles however the persistence of BSA-TxR within vesicular intracellular structures herein casts doubt upon this explanation. This would question the limitations for translocation being based simply on unfolding of the translocating cargo.

Chapter 4 To determine whether a thermodynamically plastic cationic substrate (LFn-RTAC) can translocate through the PA pore.

4.1 Novelty Statement

To further explore the published work characterising translocase substrates *i.e.* that they should be both thermodynamically plastic and predominantly cationic, for the first time, a LFn-RTAC fusion protein was produced and characterised. The data presented herein has demonstrated, for the first time, that LFn-RTAC could inhibit *in vitro* translation in a cell free *in vitro* translation system at similar concentrations to commercial RTAC (cRTAC). HeLa cells treated with LFn-RTAC (100ng/mL and 200ng/mL) in the presence of PA, were found to not reach IC₅₀. Which was a far higher concentration than has been previously documented for RT holotoxin (Dyer *et al.*, 2016). **Significance:** Assaying the ability of exogenous material to translocate across the PA pore has provided an understanding of the substrate's physicochemical characteristics. This is critical to the understanding of ATx biology. Some of the data herein was published in Dyer *et al.*, 2016. Here it was shown that a cationic, thermodynamically plastic substrate that would be predicted to translocate over the PA pore efficiently did not, forcing a further re-evaluation of the literature defining PA pore biology.

4.2 Introduction

4.21 Exogenous protein translocation through the PA pore

The ability of the PA pore to deliver exogenous enzymes has been well documented; in 1992, for the first time, Arora *et al.*, (1992) described the delivery of genetic fusions of LF and fragments of *Pseudomonas* exotoxin A (PEA) a potent inhibitor of protein synthesis. Fusing LF to toxic enzyme provided an easy and fast reporter of translocation activity through measuring cell death.

This demonstrates both successful translocation, and also the re-folding of the enzymatic portion of the protein, responsible for toxicity. The N-terminal domain of LF has been used to initiate and facilitate translocation across the PA pore (Pannifer *et al.*, 2001, Zhang *et al.*, 2004). Further to this, the successful delivery of additional protein toxins has been shown for; diphtheria toxin A chain (DTA)(Arora and Leppla 1993), and shiga toxin (Arora and Leppla 1994) catalytic domain which have both been successfully delivered as LFn fusion proteins. These exogenous protein toxins all have thermodynamic plasticity in common as their enzymatically active A chains all require membrane translocation which has been reported to require varying degrees of a chain unfolding and re-folding.

The diversity in substrates published was highlighted by the translocation events documented in chapters 5 (Section 5.2), and highlighted the question regarding the limitations to protein translocation. Understanding this provides insight into the mechanisms driving PA translocation, and more widely upon PA biology. Does a substrate need to completely unfold to pass through the PA pore, or is the pore more dynamic than previously thought? Does a substrate need to be cationic for Brownian ratcheting, driving movement across the pore? At what point within this system is the limiting step, the α -clamp, or the ϕ -clamp?

4.22 Protein Translocation through the PA pore

The PA protein represents one way that has evolved to counter the problem of intracellular compartmentalisation, facilitating the translocation of an enzymatically active substrate across a biological barrier such as the endomembrane system.

Current theories explaining the mechanics of the PA translocase, suggest that the substrate must be initially unfolded and then transported across the pore. This is driven by a protomotive force (PMF) during possessive “Brownian ratcheting” (Krantz *et al.*, 2006), and that this is facilitated by the PA β -barrel's inner diameter, which is not thought to accommodate anything larger than an α -helix (Krantz *et al.*, 2004) (Section 1.5). In order for

unfolding to occur, an energy source for the physical unwinding of the polypeptide (a proton gradient) has been identified and this is necessary to overcome the wide array of issues such as; chemical complexity and the diversity of substrates, the chemical and conformational complexity associated with substrate recognition, mechanical resistance and counterproductive diffuse forces (Figure 4.22).

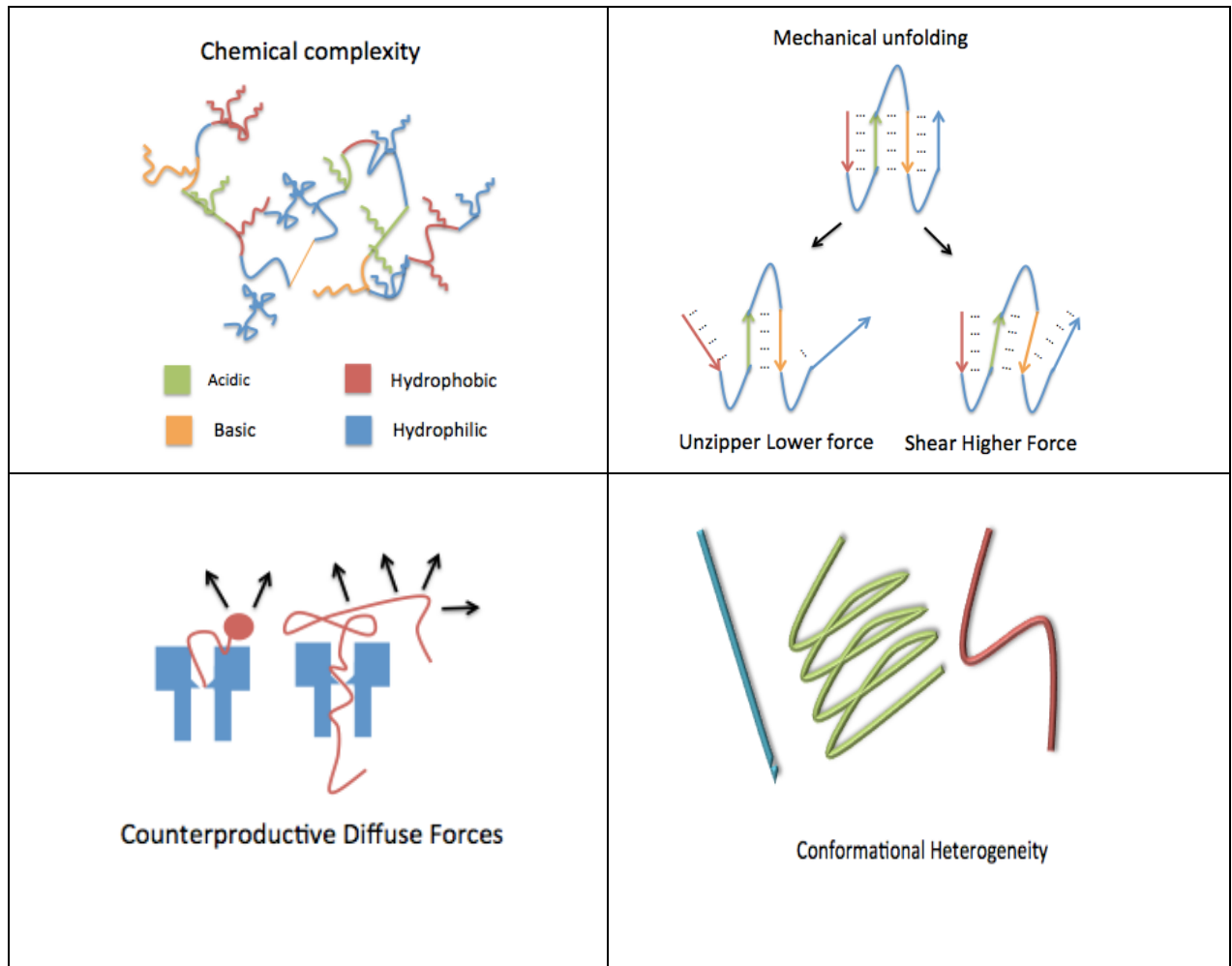


Figure 4.22 Challenges encountered during translocation.

Translocating substrates encounter many problems, initially the mechanical unfolding, and the driving forces behind this to overcome mechanical resistance. Unfolding polypeptide chains present a wide variety of combinational side chain chemistries to the channel, as well as conformational heterogeneity of translocating substrates. Additionally, these chemical and conformational complexities are problematic for substrate recognition (Adapted from Thoren *et al.*, 2011)

Although it has been demonstrated that there are some initial substrate destabilisation events caused by the acidic conditions within the endosome (Krantz *et al.*, 2004). It has been determined that the first α -helix and β -sheet of LFn are unfolded and docked into a cleft, called the α -clamp, a highly nonspecific binding site (Feld *et al.*, 2010). The ϕ -clamp has been shown to be required for translocation, and is composed of a ring of Phe⁴²⁷ residues (which bind non-specifically to aromatic, hydrophobic, and cationic functional groups). The ϕ -clamp provides a structural bottleneck for translocation as the opening has been modelled to be approximately 6Å in diameter. Distal to this and penetrating the membrane are a number of charged residues, creating patches of alternating electrostatic potential. However, the mechanism required in developing forces sufficient to unfold substrate proteins (which have been demonstrated to require extended unfolding, (Basilio *et al.*, 2011)) remain unclear under the proposed charge-state BR mechanism.

4.23 Ricin Toxin

Ricin Toxin (RT) is a cationic, type II ribosome-inactivating protein, produced by the castor bean. RT consists of ricin toxin B chain (RTBC) and ricin toxin A chain (RTAC). RTBC has been shown to be responsible for the binding to terminal galactose or *N*-acetyl-galactosamine residues on the cell membrane (Frankel 1996) and mediates the internalisation of the ricin toxin A chain (RTAC) *via* clathrin, caveolin and non-clathrin mediated endocytosis. Eventually trafficking the associated RTAC to the lumen of the endoplasmic reticulum (ER). RTAC once in the ER passes into the cytosol via a retrograde translocation even though the *Sec61p* translocon, which requires the unfolding of RTAC. Once in the cytosol intoxication occurs via the depurination and inactivation of ribosomes. Critically without RTBC to interact with membrane proteins and facilitate endocytosis the RTAC remains relatively non-toxic (Dyer *et al.*, 2015).

It has been demonstrated that an extract from green tea, epigallocatechin gallate (eGCG) has inhibitory activity against a number of protein toxins (Cherubin *et al.*, 2016). This extract specifically has an inhibitory effect on the ability of ricin toxin B chain to bind to cell surface receptors (Dyer *et al.*, 2016).

Given the literature around exogenous protein translocation (Chapter 2) the issue of material that can translocate has proven complicated, and seems to be dependent upon more than simply protein stability.

The overarching aim of this chapter was to investigate if a thermodynamically plastic cationic substrate (LFn-RTAC) could translocate through the PA pore in order to further investigate the physicochemical properties of a substrate. This was done with a view to gaining an insight into the mechanism of translocation (*i.e.* via Brownian ratcheting or otherwise) in support of our previous findings (chapter 3).

To achieve this, the more specific aims are to:

1. Investigate RTAC and RTBC on their ability to inhibit protein synthesis in a cell free system.
2. To develop and characterise LFn-RTAC production
3. To investigate the ability of LFn-RTAC to inhibit protein translation in a cell free system.
4. To test the PA dependent translocation of LFn-RTAC by cell viability.

4.3 Chapter Specific Methods

The LFn-RTAC plasmid development was described in (Chapter 2, Section 2.17 Plasmid Templates). The techniques used within this study for protein characterisation have also been discussed previously (Chapter 2 (Section 2.23)).

4.31 *In vitro* RTBC binding assay

Lactose-conjugated Sepharose (Sigma Chemical Company, Dorset UK) was washed 3 times in PBS and either recombinant RTBC (as a control), commercial RTBC (Vector Labs; Peterborough, UK) or commercial RTBC and eGCG was added. The column was washed with 10 column volumes of PBS. To the beads, 100 μ L of Laemmli SDS page buffer (containing 10% BME) was added and this was compared to an equivalent amount of input protein. Following the sedimentation of the beads at $12,000 \times G$ at room temperature for 2 min, the supernatant was analysed by SDS PAGE and Western blot. Detection was performed using an anti RTBC polyclonal antibody (AbCam; Cambridge, UK) and an anti-rabbit, HRP-conjugated secondary (Invitrogen, Paisley, UK) using Pierce™ ECL reagent (Thermo Scientific; Waltham, MA USA).

4.32 HeLa *In vitro* coupled translation assay

In vitro coupled translation assays were performed using a 1-Step Human Coupled IVT Kit (ThermoFisher (Loughborough, UK)) using the pCFE-GFP (turbo-GFP encoding) positive control, detected after SDS PAGE and Western blot using an anti-6xHis monoclonal antibody (Invitrogen, Paisley, UK) and an HRP conjugated anti-mouse secondary antibody (GE Healthcare (Little Chalfont, Bucks, UK)). Detection was performed using a picomolar stable ECL kit (ThermoFisher, Loughborough, UK). The reaction was allowed to run for 90 mins at 30°C.

Where stated, RTAC, RTBC or eGCG (dissolved in PBS) was used as a substitute for

nuclease-free water and PBS. Any osmotic effect exerted by the PBS was controlled for by using RTBC or eGCG in similar volumes of PBS to RTAC. Expression was determined by Image J analysis, relative to the proprietary endogenous housekeeper.

4.4 Results

4.41 Characterising RTAC and RTBC

Initially commercial RTBC (cRTBC) was assessed for its ability to bind to lactose conjugated Sepharose in the presence and absence of eGCG (100 μ M), compared to rRTBC (a negative control). These data (Figure 4.411) suggested the eGCG interacts with RTBC and inhibited its ability to bind to the sepharose beads. This could be due to an interaction between eGCG and the RTBC, which resulted in relaxed RTBC conformation (impacting upon RTBC lectinic activity, cell uptake and RTAC intracellular trafficking).

As the B chain has been proven to be responsible for cellular binding and uptake of RTAC. The ability of RTAC and RTBC in the presence or absence of eGCG was investigated on the ability to inhibit the expression of GFP in the *in vitro* translation assay to determine ricin subunit (A and B) ability to arrest ribosomal translation (Figure 4.412). As would be expected RTBC had no effect on the ability of the system to express GFP. Similarly, the addition of eGCG to the system had no effect on the expression of GFP. Conversely RTAC inhibited protein synthesis in both the presence and absence of eGCG, which would indicate the eGCG has no effect on the ability of RTAC to inhibit protein synthesis.

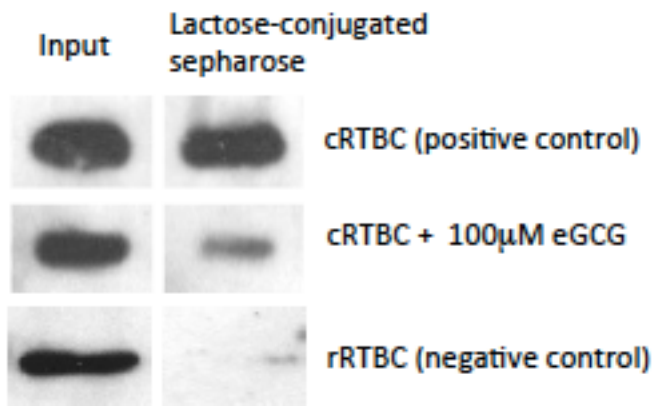


Figure 4.411 The effect of eGCG upon RTBC activity.

This Figure demonstrates the effect of eGCG (100 µM) upon RTBC's lectinic activity in relation to RTBC binding to lactose-conjugated Sepharose beads.

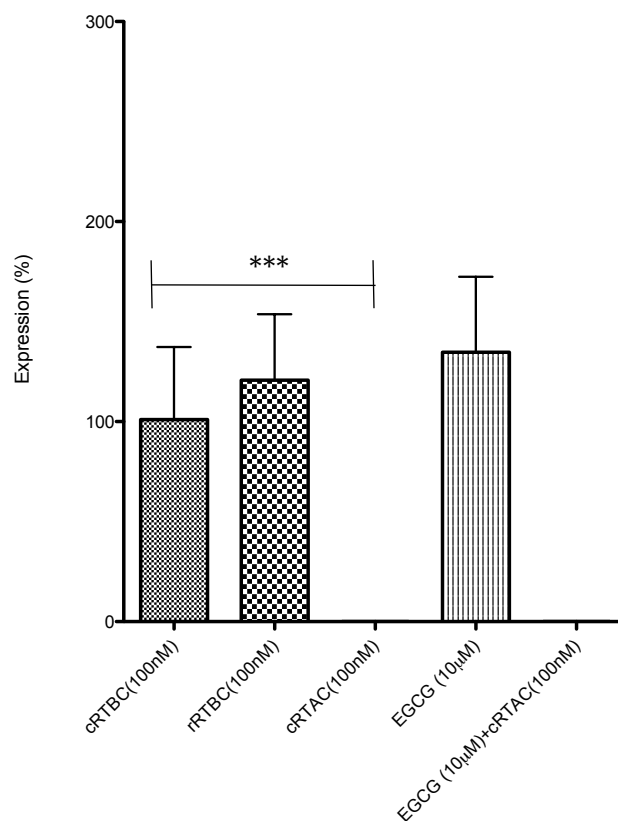


Figure 4.412 The effects of eGCG upon RTAC activity.

Documenting the effect of eGCG upon RTACs (100 nM) ability to inhibit *in vitro* translation as well as the effects of eGCG upon *in vitro* translation at concentrations of 10 µM N=3, P=0.0005.

4.42 Developing and Characterising Protein Constructs

As RTAC had the ability to inhibit protein synthesis in a cell free system LFn-RTAC was developed as a model system that could easily be used to assay PA specific delivery *i.e.* cell toxicity. To this end a pET151/D TOPO plasmid encoding LFn-RTAC was made and evaluated for protein production and purity. The *in-silico* cloning predicted the Mw of LFn-RTAC to be 56kDa as the LFn-RTAC construct also contained N-terminal 6xHis and V5 epitope tags (Figure 4.421 B). Sequencing of the plasmid indicated that LFn-RTAC had been successfully cloned into the pET151/D TOPO vector. Protein was characterised by Western blot using both 6xHis and RTAC specific primary antibodies (Figure 4.321 C). The LFn-RTAC was detectable by both antibodies at the predicted Mw however the 6xHis specific antibody did recognise multiple bands below and above the predicted apparent M_w . As there was only a singular band at the predicted Mw when the RTAC specific primary antibody was used, this could indicate some contaminants within the eluted protein, which contained 6xHis.

The eluted protein fractions were evaluated for purity and concentration (Figure 4.21 d). The most concentrated protein fractions (1, 2 and 3) were heavily contaminated and demonstrated <25% purity. However, fractions 4 and 5 showed >85% protein purity. However, protein concentration was extremely low at 0.2 mg/mL. Taking the fractions with the highest purity, this yielded 0.38 mg/L. Protective antigen had previously been characterised in chapter 3 (Section 3.3) for production, protein yield and purity.

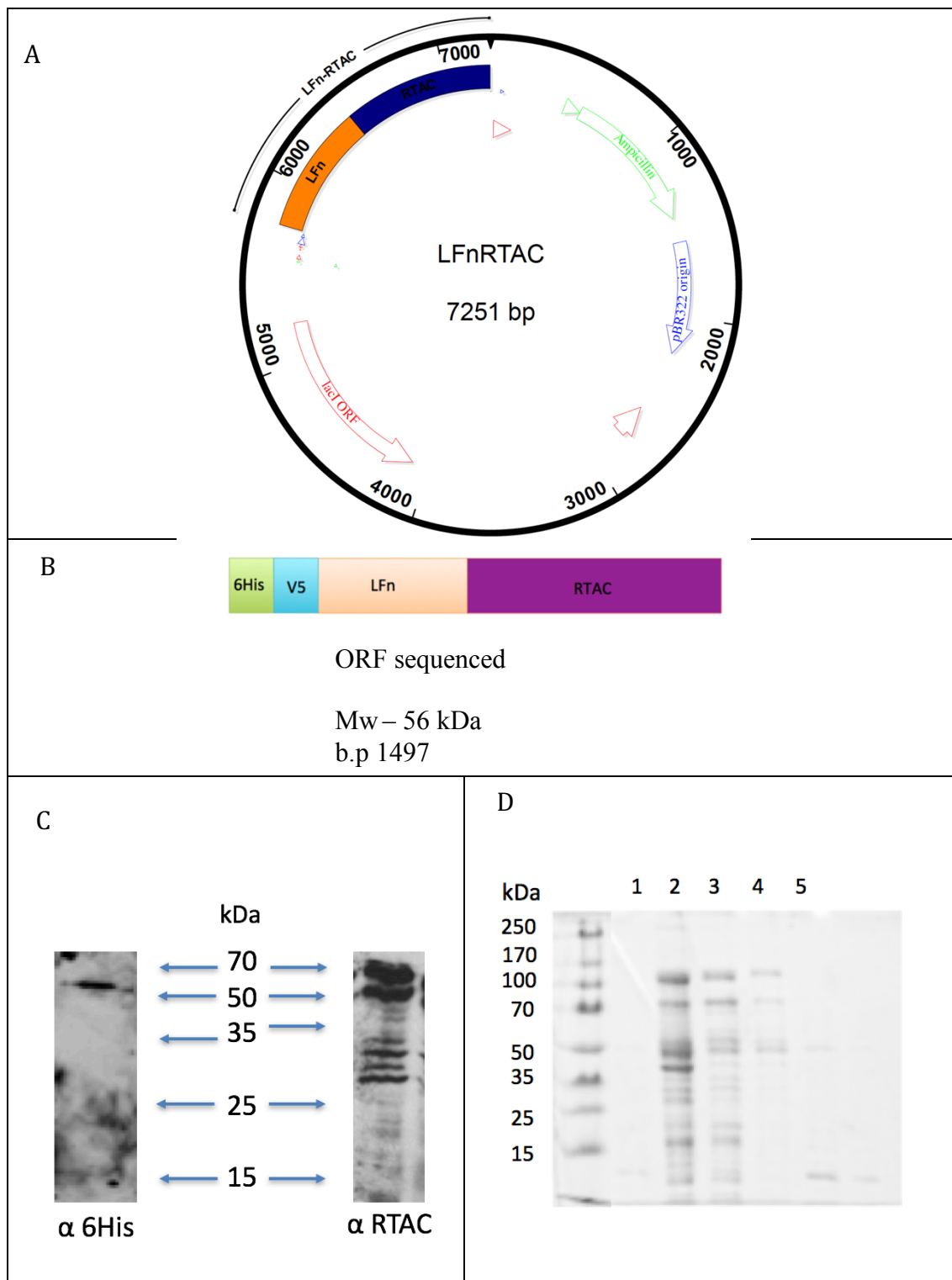


Figure 4.421 LFn-RTAC *in silico* design and characterisation.

In silico plasmid map were designed (A). Protein produced from the plasmid expression in BL21* DE3 was detected via Western blot for 6xHis and RTAC (C) which corresponds to the predicted kDa (B). Protein elution from TALON® resin and determination of concentration and purity of pooled fractions by SDS-PAGE and Coomassie staining fractions 1-5 (D).

4.43 LFn-RTAC ability to facilitate translational arrest

As RTAC has the ability to inhibit protein synthesis in a cell free system, LFn-RTAC was tested using the same assay to check that it was folded correctly and that the LFn portion of the molecule was not impeding activity. The was performed in order to assess the utility of LFn-RTAC as a model reagent that could be used to easily assay PA pore translocation by monitoring cell viability.

Consequently, cRTAC, cRTBC rRTBC and LFn-RTACs ability to inhibit protein translation in the cell-free *in vitro* translation (IVT) assay was established (Figure 4.431).

LFn-RTAC was able to mediate translational arrest at concentrations similar to that of cRTAC (relative to an untreated control designated “100% activity”). This indicated that LFn-RTAC was functional as an inhibitor of translation and that the RTAC portion of the molecule was correctly folded. RTBC (both commercial and recombinant) behaved predictably and didn’t affect protein translation.

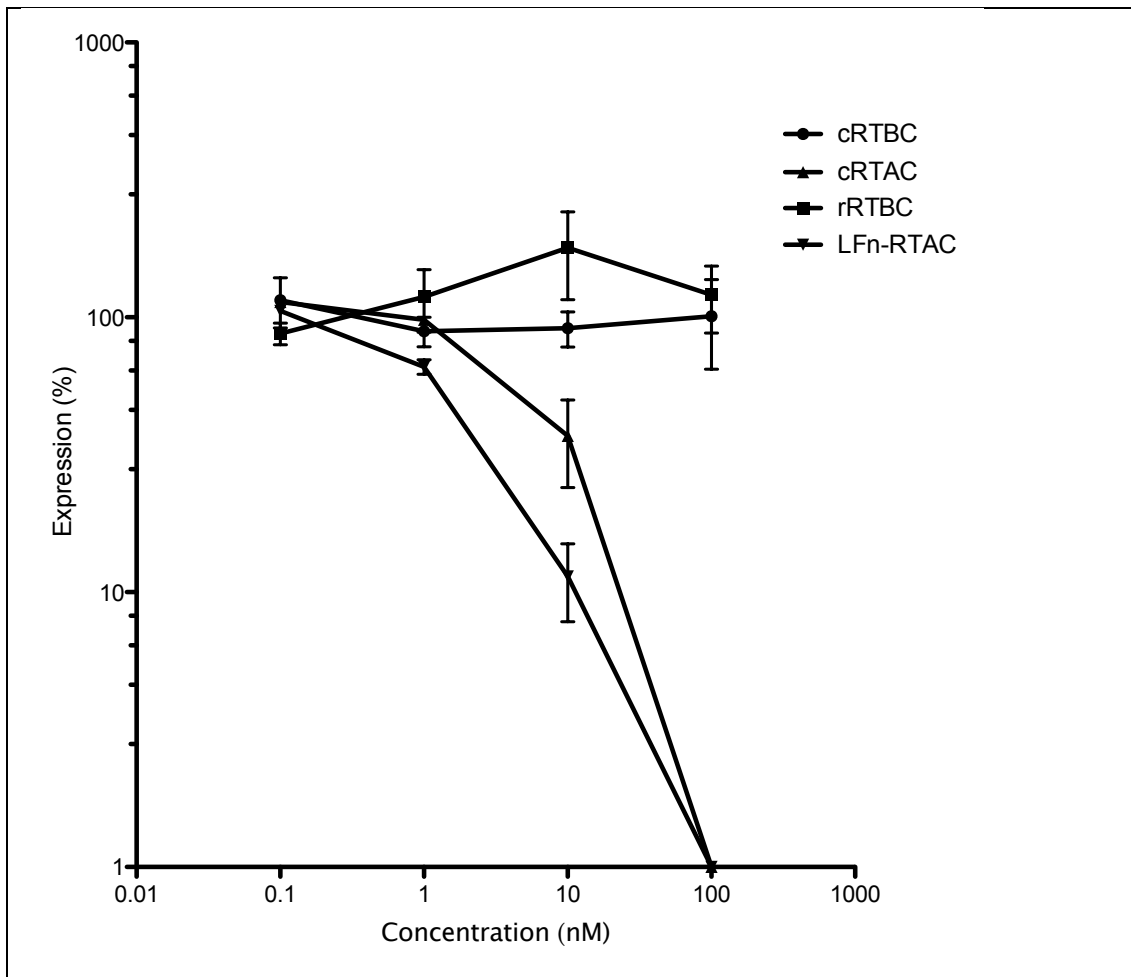


Figure 4.431 LFn-RTAC activity compared to cRTAC in a cell free expression system.

Demonstrates the effect of cRTBC, rRTBC, cRTAC and LFn-RTAC upon an *in vitro* translation assay over a range of concentrations. Data points represent $n=3 \pm \text{SEM}$ over a 90min assay period.

4.44 The PA dependent cytosolic translocation of LFn-RTAC

As LFn-RTAC inhibited protein synthesis with a similar efficiency to commercial RTAC, the ability of LFn-RTAC to act as a PA translocase substrate was investigated. LFn-RTAC (100 µg/mL and 200 µg/mL) was added to Vero cells in the presence or absence of PA, and after 48hrs cell viability was assayed using MTT. These results (Figure 4.441 and 4.442) demonstrated that LFn-RTAC with PA did exert some toxicity relative to the control containing LFn-RTAC and no PA, though was not as toxic as a similar concentration of RT holotoxin. When the IC₅₀ of RT holotoxin was considered (0.08 ng/mL (Dyer et al., 2016)) this reduction of toxicity was evident for each of the LFn-RTAC plus PA concentrations assayed. There was however a significant change in toxicity associated with the presence of PA for both concentrations, which increased as concentration of LFn-RTAC increased.

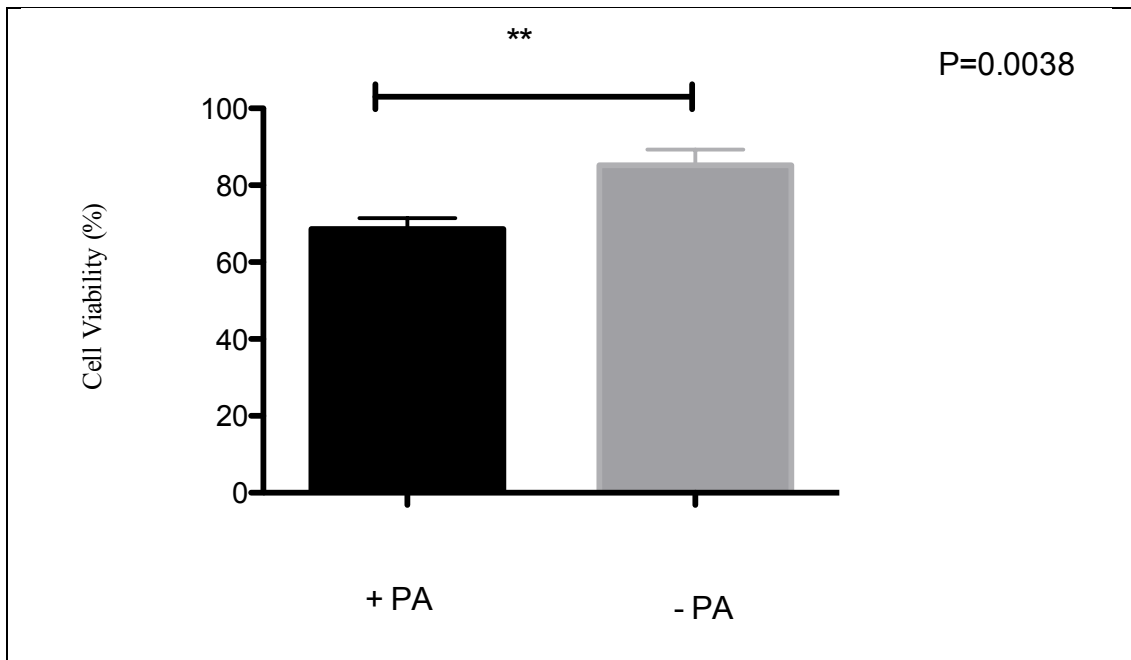


Figure 4.441 PA dependent delivery of LFn-RTAC.

Showing the cell viability (%) of HeLa cells treated with LFn-RTAC (100 µg/mL) in the presence and absence of PA (N=3) over 24 hours. IC₅₀ values not reached however, there was a statistical significance (P=0.0038)

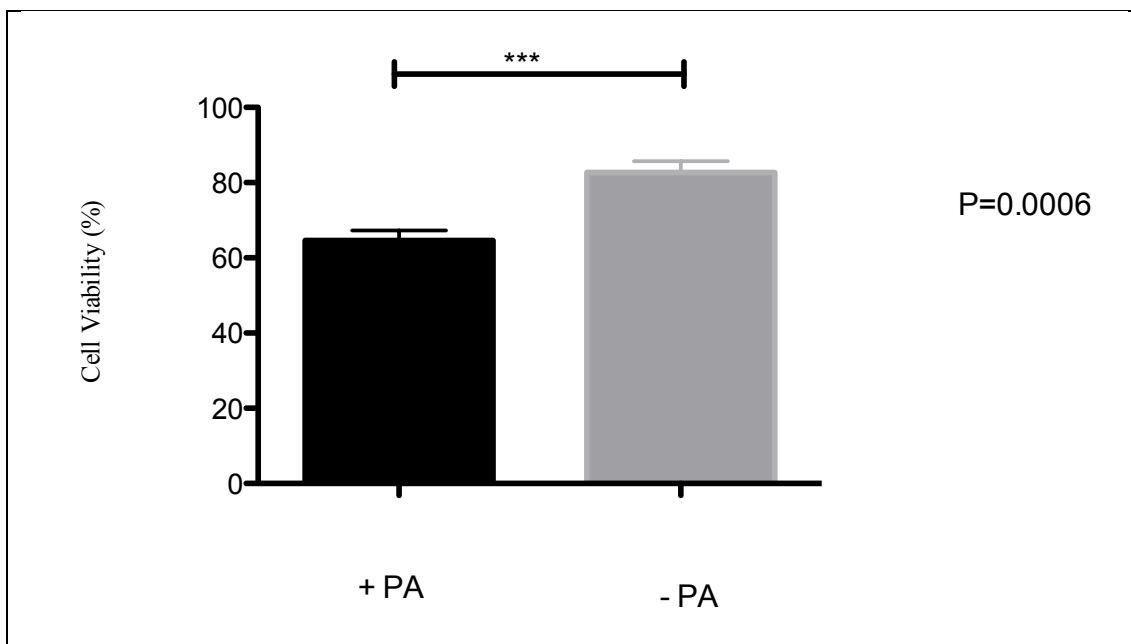


Figure 4.442 PA dependent delivery of LFn-RTAC.

Showing the cell viability (%) of HeLa cells treated with LFn-RTAC (200 µg/mL) in the presence and absence of PA (N=3) over 24 hours. IC₅₀ values not reached however; there was a statistical significance (P=0.0006).

4.5 Discussion

Here, cRTAC, cRTBC and LFn-RTAC were characterised within the context of cell receptor binding (RTBC), catalytic activity (RTAC and LFn-RTAC), toxicity (RTAC and RTBC) and PA dependent toxicity (LFn-RTAC), indicative of LFn-RTAC translocation through the PA pore PA.

It was demonstrated that cRTBC, responsible for receptor binding and facilitating trafficking to the ER (Lord and Spooner 2011) was inhibited by eGCG. This was thought to be due the conformational changes in RTBC affecting its ability to bind to galactose domains (Dyer *et al.*, 2016) and served as a negative control confirming the activity of the RTBC. EGCG has previously been shown to inhibit a panel for other protein toxins and on this basis, it was reasoned that it might inhibit RTBC. As is evident from the data this hypothesis was correct providing a control for use herein. The specificity of the inhibition of RTBC by eGCG has been further studied using *Clostridium difficile* toxin A and B (see appendices 9.5) and demonstrated a degree of eGCG specificity for the *C. difficile* B toxin (as opposed to the A toxin).

The plasmid sequencing and Western blot experiments indicated that RTAC had been successfully fused in frame with LFn and the protein produced was characterised for purity. After affinity chromatography enriching LFn-RTAC from bacterial lysate the protein contained additional bands that co-purified with the target protein in multiple fractions. However, several fractions, had >85%, which was deemed sufficient to further characterise experimentally. The protein yield however was low.

The sequence for LFn-RTAC had been codon optimised (using proprietary algorithm BioBasicInc) for production in *E.coli*. This could be due to the RTAC portion of the protein being toxic and affecting *E.coli* growth.

The ability of LFn-RTAC to inhibit protein translation in a cell free assay was established relative to commercial RTAC, again using eGCG as a negative control. This experimental investigation was critical if RTAC's ability to translocate over the PA pore was to be measured using cell viability. As the effect of LFn on the N-terminal domain as a fusion protein on the ability of RTAC to inhibit protein synthesis was unknown, a cell free *in vitro* translation assay was used to assess the ability of LFn-RTAC to depurinate ribosomes and inhibit translation. Recombinant LFn-RTAC inhibited the cell-free *in vitro* translation assay at a similar concentration (100 nM) to cRTAC. This indicated that LFn-RTAC had folded correctly and was capable of depurinating ribosomes, inhibiting protein synthesis as efficiently as RTAC made in the castor bean.

PA's ability to utilise enriched LFn-RTAC protein as a translocase substrate was assessed as it was anticipated that the LFn portion of this molecule (Melnyk *et al.*, 2005) would facilitate the entry of the RTAC portion into the α -clamp. Given that RTAC has been postulated to unfold as it translocates through the *Sec61p* translocon in the ER, the α -clamp driven unfolding of this molecule, its passage over the ϕ -clamp, ratcheting through the PA pore and subsequent re-folding should theoretically be possible.

Given the LFn-RTAC still functions as a type II ribosome inactivating protein (Figure 4.431), and toxic concentrations of ricin holotoxin were typically < the 10 ng/mL, the finding that IC₅₀ values were not reached when treated with 200 μ g/mL of LFn-RTAC was interesting (Wales, *et al.*, 1993, Mahal *et al.*, 1997, Dyer *et al.*, 2016) as this, if it was translocating through the PA would have been toxic.

There was however a statistically significant difference between LFn-RTAC at 100 μ g/mL and 200 μ g/mL in the presence of PA for (Figure 4.441 and 4.442 respectively). The increased concentration of LFn-RTAC also made the statistical significance (P value) greater,

which would indicate that with an increase in concentration there was a more specific toxicity associated with the addition of PA.

Whilst the mechanism and limitations of unfolding remain unclear, it has been suggested that this translocase works in a charge state Brownian ratchet mechanism, driven by ΔpH (from endosome pH 5.5 to cytosol pH 7.4), causing changes on the relative protonation states of the translocating material (Das and Krantz 2017).

It has been demonstrated that acidic residues on protenacious translocating material are essential to facilitate translocation through the cation selective PA pore (Blaustein *et al.*, 1989). However there remains also an anionic requirement where during translocation the protonation state of these change, being protonated during translocation (allowing it to pass through anion rejection sites within the translocase) and once in the cytosol becoming deprotonated and potentially being subjected to electrostatic repulsion, facilitating directional translocation overcoming diffuse forces. Which would suggest the chemical complexity of material translocating is critical to the successful translocation and re-folding.

4.6 Conclusion

This chapter has demonstrated that the ability of LFn-RTAC to inhibit protein translation similar to that of cRTAC. However, the ability of LFn-RTAC to translocate through the PA was limited.

This would suggest that PA was a poor translocase for LFn-RTAC, compared to the trafficking and associated toxicity associated with the holotoxin. It would seem that it the PA pore may still be facilitating some toxin translocation, given the affect the presence of PA has when compared to HeLa cells treated with LFn-RTAC alone. It could be potentially translocating far slower, or there could potentially be issues with re-folding once translocated, and so the RTAC doesn't maintain its enzymatic ability to depurinate

ribosomes. As the PA pore has been demonstrated to be cation selective (Blaustein, *et al.*, 2011), it would be assumed that this protein would be an ideal candidate for translocation through the PA pore, with the ability to evaluate the re-folding of the enzyme by its activity. The pI of LFn-RTAC was predicted using PropKa, a protein isoelectric point predictor (see PropKa output in appendices 9.2). This found that LFn-RTAC had an overall pI of pH 7.33. Which, at endosomal pH, means it will have a positive charge. This could suggest that the requirements for translocation are more complicated than overall charge, and may have more complex chemical requirements. Then the LFn-RTAC could be possibly held within the translocase as there are insufficient energetics generated to facilitate translocation due to positive charges within the complex.

Chapter 5 Investigating the ability of the PA pore to translocate structurally stable fluorescent molecules.

5.1 Novelty Statement

Data presented herein demonstrates the PA dependent and independent translocation of LFn-GFP into HeLa cells despite the high thermostability of the fluorescent construct.

Significance: Given the conflicting data regarding protein translocation, information into the ability of the PA translocase to translocate stable protein constructs with a wide array of side chain chemistries, which the α -clamp and ϕ - clamp have to unfold may help identify potential inhibitors of the translocase and so the exotoxins themselves.

5.2 Introduction

The intracellular delivery of peptide and protein therapeutics is limited by the plasma and endomembrane system within eukaryotic cells. This is due to the membrane acting as a barrier, compartmentalising the extracellular and intracellular environments and allowing mutually exclusive biochemistry to occur simultaneously within an organism or cell. An example of this would be the persistence of information and biochemistry associated with the nucleus which under normal homeostatic conditions is kept separate and discreet from the catabolism of the endolysosome. Given that the literature demonstrating the need for protein translocase substrates was challenged (Chapter 3), the aim of this chapter was to examine the translocation of a variety of cargo molecules over the PA translocase, specifically cargo displaying a variety of thermodynamic stability profiles.

By undertaking these experiments, it was hoped that more could be learnt about the ability of the PA pore to accommodate the translocation of molecules with a limited capacity to unfold. Further, the literature documents the translocation of a variety of substrates cross the PA

pore, often fused in frame to LFn. Select examples of these translocase substrates have been summarised (Table 5.1).

Substrate	PA translocate substrate?	Reference	Experimental Model
LFn-GAL4:DNA(PLL)	Yes	Gaur <i>et al.</i> , 2002	Cell System (Vero)
LFn-GAL4:DNA	Yes	PhD Thesis, unpublished data. Paul Dyer 2013.	Cell System (Vero)
LFn-GAL4:ASO	Yes	Dyer <i>et al.</i> , 2015	Cell System (Vero and HeLa)
LFn-mCherry	No	Zornetta <i>et al.</i> , 2010	Cell System (Baby hamster kidney cells (BHK))
LFn-GFP	Yes	Zornetta <i>et al.</i> , 2010,	Cell System (BHK) Cell System (HeLa)
LFn-YFP	No	Basillo et al 2011, Schiffmiller <i>et al.</i> , 2015	Cell Free system (planar lipid bilayers)
LFn-DTA	Yes	Boll <i>et al.</i> , 2004	Cell System (Chinese hamster ovary cells(CHO))
LFn-Mycobacterium tuberculosis	Yes	Mehra <i>et al.</i> , 2001	Cell System (Macrophages and CHO)
LFn-Antibody mimics	Yes	Verdurmen <i>et al.</i> , 2015, Liao <i>et al.</i> , 2014	Cell system (Human embryonic kidney cells)
LFn-Pseudomonas Exotoxin A	Yes	Bachran <i>et al.</i> , 2013	Cell System (CHO)

Table 5.1 Examples of translocase substrates which have been investigated for their ability to translocate through the PA pore.

Documenting whether PA could translocate the substrate and the experimental model that was used; cell model (this evaluates cytosolic delivery in a cell by cellular toxicity, microscopy, and immune detection), or a cell free system where by PA pore were isolated into planar lipid bilayers.

The translocation of these substrates (Table 5.1) over the PA translocase has been used as a method to investigate the structural requirements of protein translocation through the PA pore encompassing initiation, structural requirements required for translocation, and the specificity of the PA pore. Consequently, the existing models of PA translocase activity have been summarized (Section 5.21).

5.21 Translocation models

The synthetic translocase substrates documented (Table 5.1) consisted of LFn modified at the C-terminus (Khushner *et al.*, 2004), and their translocase activity has been dissected using three types of assay;

1) Western blot and microscopy to measure cellular uptake, this provides a semi-quantitative measure of translocated material (Backer *et al.*, 2007, Zornetta *et al.*, 2010, Rabideau *et al.*, 2015).

2) Electrophysiology of the PA pore isolated in planar lipid bilayers where changes in ion current are measured, before and after LFn constructs are added to artificial bilayers containing PA pore (Nablo *et al.*, 2013, Basilio *et al.*, 2011., Krantz *et al.*, 2006, Brown *et al.*, 2015).

3) Protein synthesis inhibition or cytotoxicity assays generally required the use of cells and have provided a sensitive means of measuring the translocation of a non-membrane permeable toxin. These tools and the cargos translocated have provided insights into the translocation process (Bachran *et al.*, 2013, Liao *et al.*, 2014, Blanke *et al.*, 1996).

5.22 Translocating Proteins

The N-terminal domain of LF was demonstrated to be a key initiator in the translocation of substrates by the PA translocase. A variety of proteins have been assayed typically by studying “in frame” fusions of LFn to the protein of interest: LFn- Diphtheria toxin a chain (DTA) (Milne *et al.*, 1995), LFn-Shiga toxin (ST) (Arora *et al.*, 1994) and LFn Pseudomonas exotoxin A (PEA) (Arora *et al.*, 1992). Further studies using an LFn-DTA mutant, documented the effect of an artificial intramolecular disulfide bond upon LFn-DTA translocation over the PA pore. The proteins inability to serve as a substrate for PA translocation was attributed to the disulphide bond hindering protein unfolding and consequently the translocation of this construct. This was in turn interpreted to demonstrate the requirements for MG transition and unfolding during the translocation process.

Measuring enzyme activity in the cytosol (after translocation) demonstrated the re-folding of protein (with enzymatic activity). However, the magnitude of this re-folding and the impact of re-folding upon substrate catalytic activity would also be dependent upon the degree of unfolding necessary for the protein to translocate over the PA pore. In an attempt to circumvent this uncertainty, a variety of fluorescent probes have also been used as translocase substrates.

These fluorescent probes include both small molecules *i.e.* Alexa Flour dyes (Backer *et al.*, 2007) and proteins such as green fluorescent protein (GFP) (Zornetta *et al.*, 2010, Basillo *et al.*, 2011). The use has been promoted by the apparent ease of use (and analysis) of these molecules, as well as interesting variability in biochemistry *i.e.* PI, charge, stability. Work characterising the thermostability of protein translocation has also been undertaken (Verdurmen *et al.*, 2014). One such study investigated the effects of Designed Ankyrin Repeat Protein (DARPin) with varying levels of thermodynamic stability and their ability to translocate across the PA pore; which relies on the pore generating the unfolding force,

limiting the ability of the pore to unfold cargo. Here it was demonstrated that pore translocation was not a size but a stability-issue, where PA could only translocate moderately stable cargoes as compared to pseudomonas exotoxin A (PEA), which could translocate proteins through the SEC machinery (Michealska and Wolf 2015). Here translocation through the SEC translocon was found to not be limited by the thermostability of the protein (Verdurmen *et al.*, 2014).

This was demonstrated where PEA was able to deliver DARPins of high thermostability (with this not being a limiting factor) and compare this to observation that PEA could also facilitate the delivery of GFP (Mohammed *et al.*, 2012) a thermodynamically protein.

Drawing conclusions that PEA was able to translocate both GFP and DARPins, whereas PA could not, this was due to stability of the translocating protein. However, PA has been demonstrated to deliver GFP fused to LFn (Zornetta *et al.*, 2010)., which would question the conclusion of the previous paper (Verdurmen *et al.*, 2014). This emphasizes the conflicting arguments defining the translocase properties of PA.

Another set of data documented LFn-YFP being able to initiate translocation but resulted in the YFP section of the protein arresting translocation (Basilio *et al.*, 2011). This would suggest that the MG transition and initiation of translocation of LFn, isn't a large enough force to drive translocation of mCherry and YFP and is yet however a sufficient driving force in the translocation of GFP.

To this end the aim of this chapter is to investigate the translocation of recombinant fusion proteins of LFn and stable fluorescent probes.

In order to address this, the aims of this chapter were:

1. To produce and characterise recombinant LFn-GFP, LFn-mCherry and LFn-YFP proteins.

2. To determine the *in vitro* toxicity profile of these constructs
3. To monitor the fluorescent probe translocation *in vitro* on HeLa and Vero cells by fluorescent microscopy and subcellular fractionation
4. To investigate fluorescent probe stability.

5.3 Chapter Specific Methods

5.31 Fluorescent Spectroscopy

LFn-GFP protein was kept at 4°C until it was to be used and then treated as defined (5 mins in a thermocycler (MJ mini, Biorad, Hertfordshire)) prior to spectrofluorometric analysis.

The excitation spectra were initially measured and the lambda max was taken and used as the wavelength of excitation. Which was measured at a single constant excitation wavelength, this was performed using 1mg/1mL of protein.

5.32 LFn-GFP Translocation Studies

HeLa cells were seeded at 1×10^4 into a 6-well plate with cover slips for 24 hours. Cells were incubated with PA (100 µg/mL), LFn-GFP (50 µg/mL) and both PA (100 µg/mL) and LFn-GFP (50 µg/mL) under standard cell culture conditions for a variety of incubation times.

Cells were fixed (Section 2.2541) and stained using primary (anti-GFP, Section 2.161) and secondary (anti-rabbit-Alexa flour 488, Section 2.161), LFn-GFP translocation was evaluated by epifluorescent microscopy.

5.33 Preparation of post-nuclear supernatant

Mammalian cells (Vero or HeLa) were seeded into two 150 mm² plates at a density of 5×10^6 cells in 15 mL of culture media and culture was incubated using standard culture conditions for 24 hours. After the incubation period, cells were washed three times with PBS (10 mL for each wash). The cells were dosed with the PA (50 µg/mL) or LFn-GFP (50 µg/mL) in complete media and incubated for an appropriate time under standard culture conditions.

Following this, culture media was discarded and the cells were washed three times with chilled (4°C PBS (10 mL), the last PBS wash was removed by blotting the inside rim of the two plates with tissue, whilst being careful not to disrupt the monolayer. Complete[®] EDTA-free Protease inhibitor cocktail (PI) tablet (ROCHE, Burgess Hill, UK) was dissolved into 1

mL PBS, giving a stock solution of 50x. To the first plate, 250 μ L 50x PI was added to the cell monolayer. The cells were then harvested using a sterile disposable cell scraper (rubber policeman) (Fisher Scientific, Loughborough, UK). The cell suspension was then transferred into the second plate. Cells were scraped and transferred into a sterile Eppendorf tube. This process was then repeated using 200 μ L of PI and the cell suspension pooled. The homogenate was lysed by being passed 10 times through a 21-gauge needle. Lysed cells were sedimented at 2 000 x g for 2 minutes at 4°C to remove intact cells and nuclei, resultant supernatant was transferred to a new sterile Eppendorf tube (Fisher Scientific, Loughborough, UK). The pellet was then re-suspended in 200 μ L of PI and subject to a second round of lysis, again using a 21-gauge needle as before. Protein concentration was then assessed (Section 2.256).

5.4 Results

5.41 Protein Production and characterisation

5.411 LFn-GFP protein production and characterisation

LFn had previously been synthesised in frame with green fluorescent protein (GFP), and sub-cloned into a pET151/D-TOPO expression vector. This was subsequently sequenced (see appendices 9.1). The analysis of the sequence results showed correct sequence alignment with the *in-silico* map (Figure 5.4111 A), the ligated DNA insert being maintained within the ORF, with N-terminal 6xHis V5 epitope tags. LFn-GFP protein produced in One Shot[®] *E.coli* BL21*DE3/plys bacteria (Invitrogen, Paisley, UK) was detectable by both Coomassie stain and immune blot using an anti-6xHis monoclonal antibody and an anti-GFP polyclonal antibody at the predicted molecular of 54 kDa (Figure 5.4111 C and D).

Protein purity was analysed using SDS PAGE and Coomassie staining, and was determined to be >85% purity (Figure 5.4112). LFn-GFP protein yield was determined by densitometry with reference to BSA standard concentration and was calculated to be 1.7mg/mL, yielding 8.5mg/L culture (Chapter 2.243).

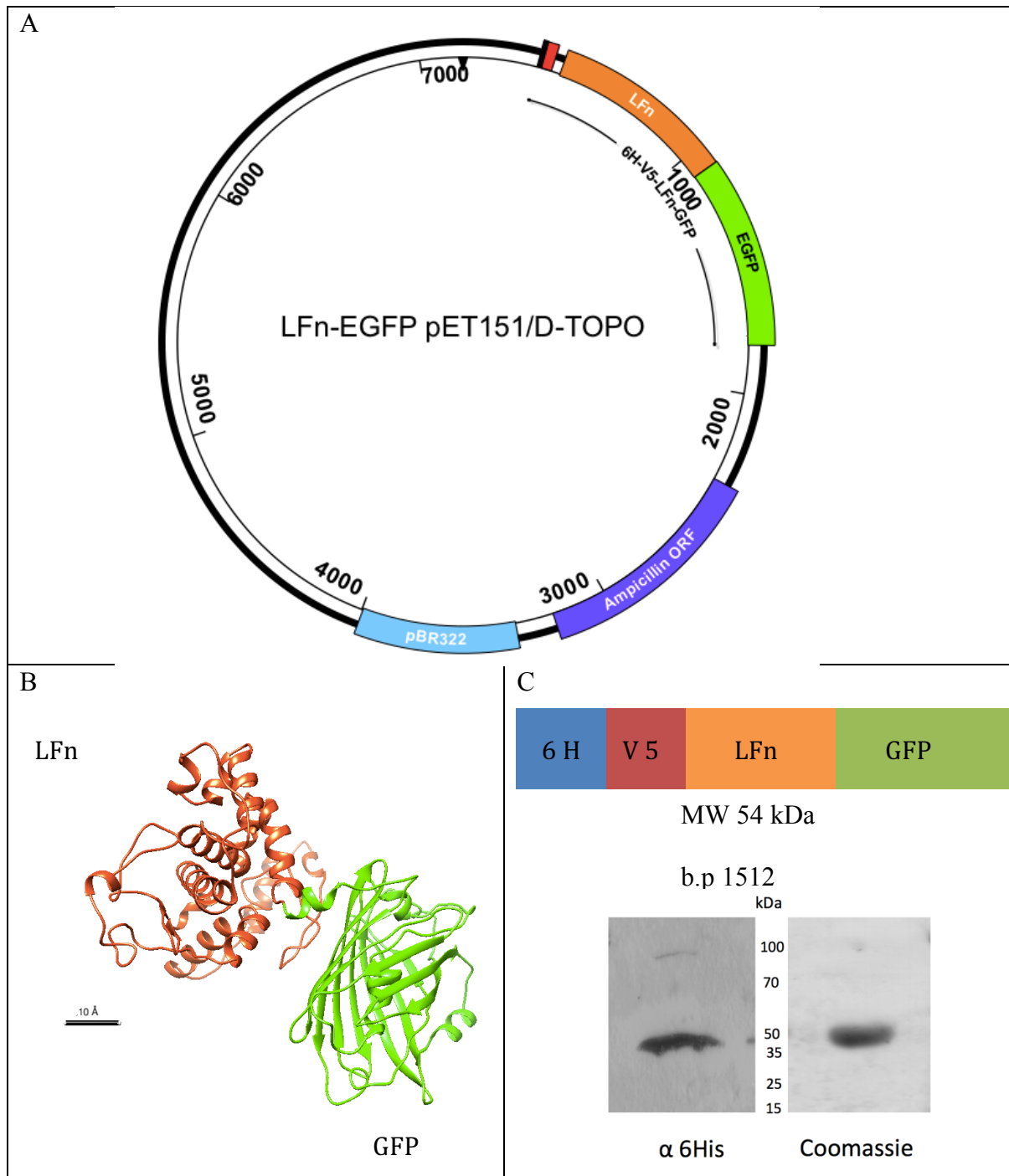


Figure 5.4111 LFn-GFP fusion construct.

In silico plasmid maps were designed (A), where ORF were analysed, primers were designed, and sequencing data was analysed (appendices 9.1). ITASSER (B) generated predicted 3D structure for LFn-GFP. Protein produced from the plasmid expression in BL21* DE3 was detected via SDS PAGE, Coomassie stain and Western blot (C) which corresponds to the predicted kDa (C), estimated from the plasmid map.

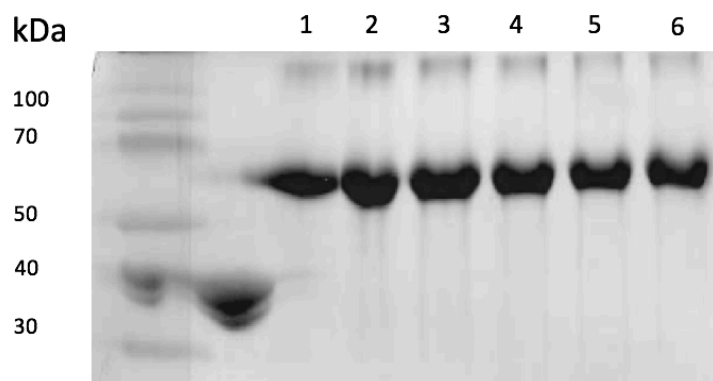


Figure 5.4112 Protein characterisation of eluted fractions from TALON[®] resin by SDS-PAGE and Coomassie staining.

Evaluation of imidazole eluted fractions LFn-GFP (fractions 1-6) following SDS-PAGE and Coomassie staining. Enriched protein fractions were pooled and evaluated for purity using SDS-PAGE and Coomassie within the limits of detection.

The *in vitro* toxicity profile of LFn-GFP was determined to control for the effects of any toxicity that might be observed experimentally. The IC₅₀ for all proteins can be found in table 5.41. The toxicities were tested in HeLa cells over a period of 24, 48 and 72 hours where, MTT readings were normalised to an untreated population of the cell type used. LFn-GFP demonstrated some toxicity having IC₅₀ of 96.2 (± 6) and 87(± 9.5) at 48 and 72 hours respectively, which was not anticipated.

This observed toxicity was at a much higher concentration, and for much longer incubation time than was required for the experiments documented herein (typically 20µg/mL for <4 hours). At 24 hours, the IC₅₀ of LFn-GFP was >500µg/mL (Figure 5.4114).

Both PA and LFn-GFP toxicity profiles were measured together, and an IC₅₀ of >200µg/mL was recorded at 24, 48 and 72 hours (Figure 5.4115). The discrepancies between these data and those describing the *in vitro* toxicity of LFn-GFP (Figure 5.4114), which found LFn-GFP to have an IC₅₀ of 96.2 (± 6) and 87(± 9.5) (at 48 and 72 hours respectively) could be due to the effects of PA, and PA translocation of LFn-GFP into the cell reducing its toxicity. This difference was found to be significantly different between LFn-GFP and PA + LFn-GFP compared at 48 hours (Figure 5.4116 A, P=<0.0001), and also at 72 hours (Figure 5.4116 B, P=<0.0001).

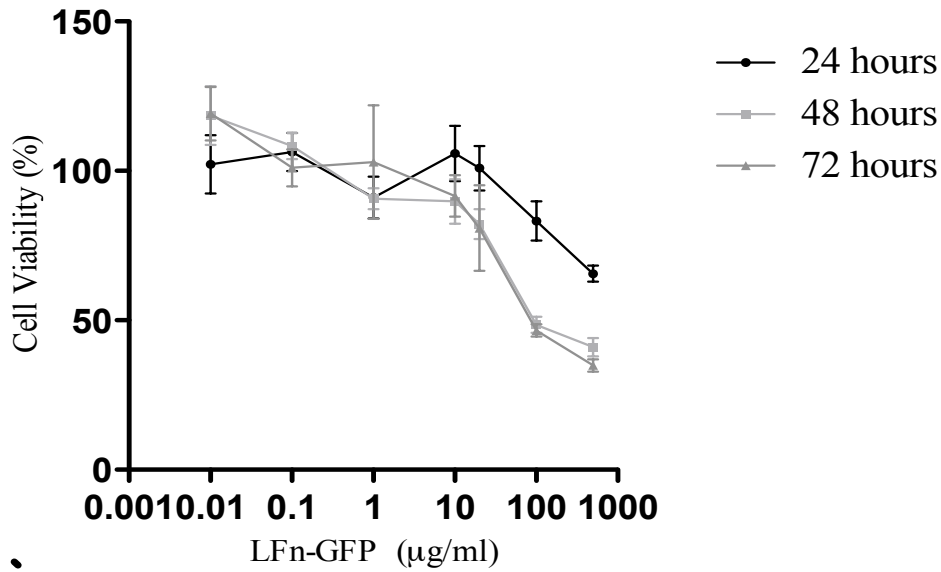


Figure 5.4114 Toxicity profile of LFn-GFP in HeLa cells at 24, 48 and 72 hours.
 Toxicity profile of LFn-GFP in HeLa cells over 24, 48 and 72 hours treated at increasing concentrations (0.1 µg/mL – 500 µg/mL), with a seeding density of 1×10^4 HeLa cells ($n=6$, \pm SEM). IC_{50} values were calculated for 24, 48 and 72 hours and was found to be >200 µg/mL, 96.2 µg/mL (\pm 6) and 87 µg/mL (\pm 9.5) respectively.

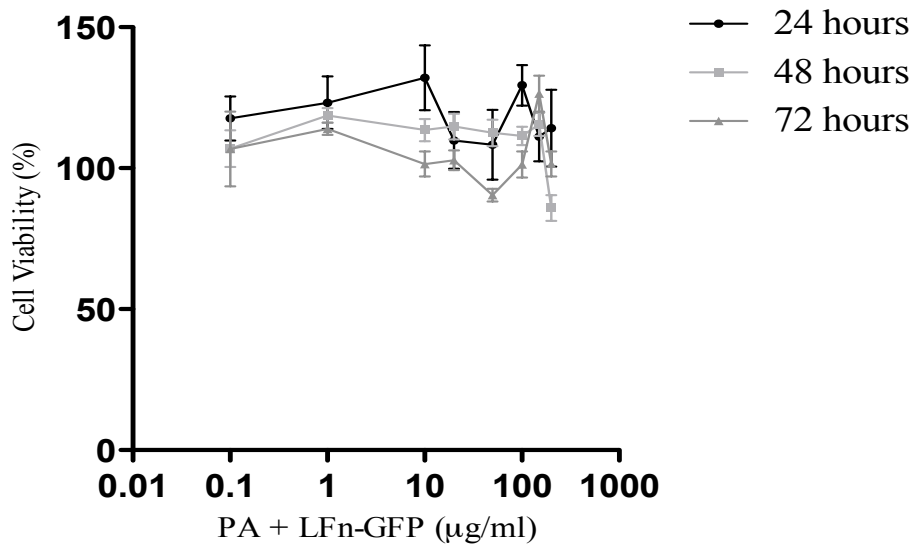


Figure 5.4115 Toxicity profile of PA + LFn-GFP in HeLa cells at 24, 48 and 72 hours.
 Toxicity profile of PA + LFn-GFP in HeLa cells over 24, 48 and 72 hours treated at increasing concentrations (0.1 µg/mL – 200 µg/mL), with a seeding density of 1×10^4 HeLa cells ($n=6$, \pm SEM). IC_{50} values were calculated for 24, 48 and 72 hours and was found to be >200 µg/mL and >200 µg/mL and >200 µg respectively.

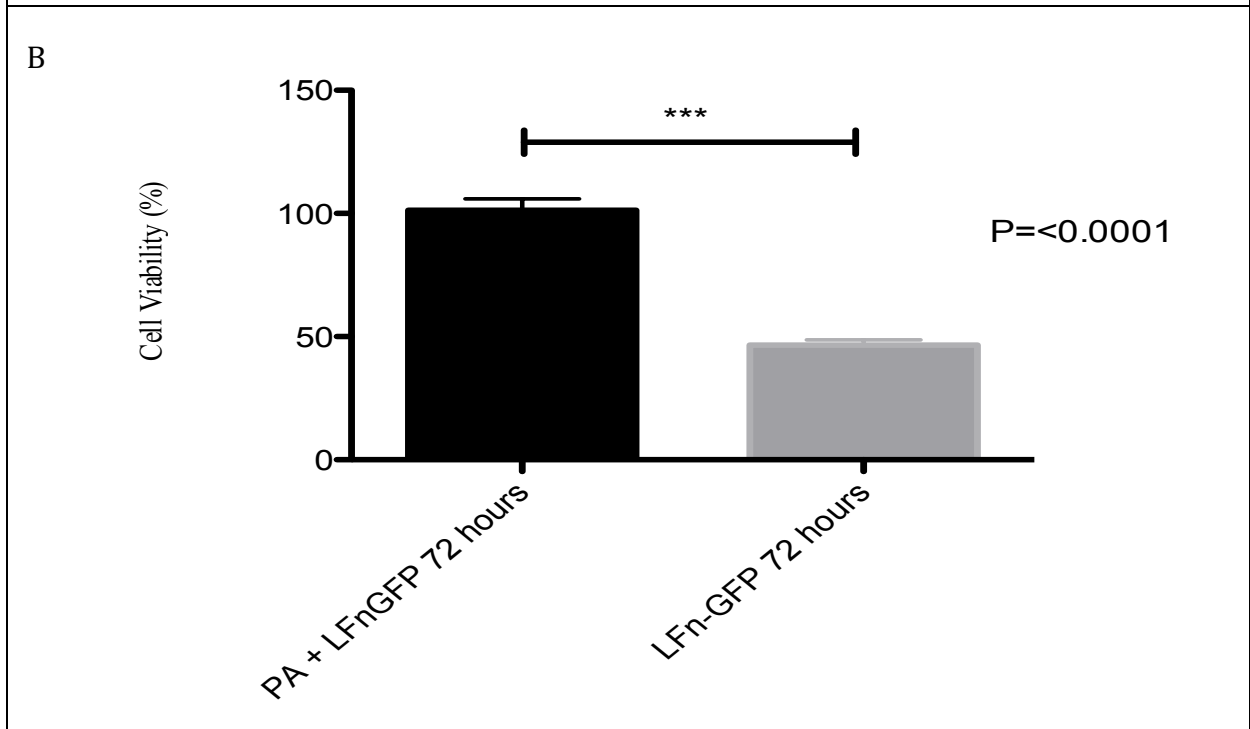
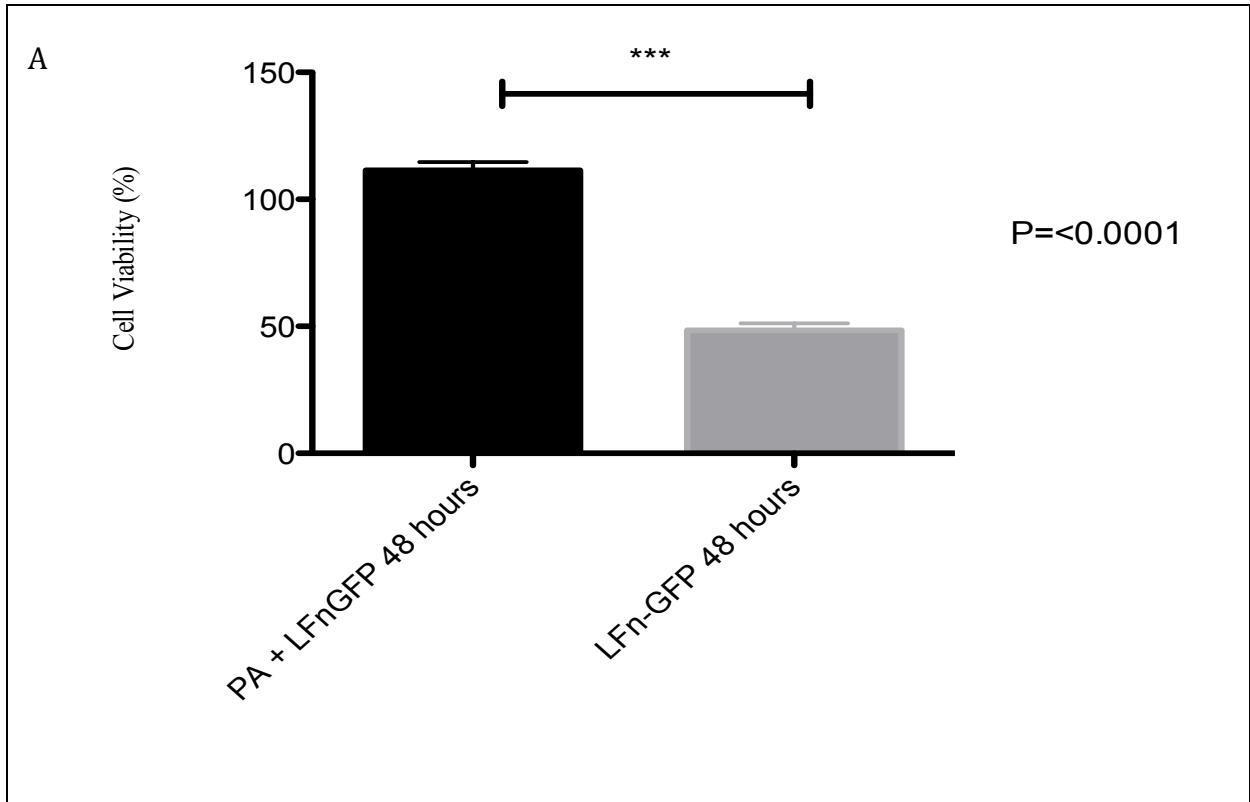


Figure 5.4116 Comparative toxicity profile of PA +LFn-GFP or LFn-GFP.
 At 48 hours (A) and at 72 hours (B) at a concentration of 100µg/mL. At 48 hours (A), there a significant reduction in IC₅₀ toxicity when LFn-GFP is in the presance of PA (P=<0.0001).

5.412 LFn-YFP protein production and characterisation

A plasmid coding for LFn-YFP was generated using recombinant PCR and the resulting PCR product sub-cloned into pET151/D TOPO. This plasmid was subsequently sequenced (see appendices 9.1). The analysis of this data showed correct alignment with the *in-silico* map (Figure 5.4121A), the ligated DNA insert being maintained within the ORF, with N-terminal 6xHis & V5 epitope tags. LFn-YFP protein produced in One Shot[®] *E.coli* BL21*DE3/plys bacteria (Invitrogen, Paisley, UK) was detectable by both Coomassie stain and immune blot using an anti-6xHis monoclonal antibody at the predicted molecular of 54 kDa (Figure 5.4121 C and D).

LFn-YFP enrichment (after affinity chromatography) was determined using SDS PAGE and staining with Coomassie G250 brilliant blue dye, and was >85% (Figure 5.4122). LFn-YFP protein yield was determined by densitometry with reference to BSA standard concentration and was calculated to be 0.8 mg/mL, yielding 3 mg/l culture. LFn-YFP *in vitro* toxicity was evaluated in the presence and absence of PA (Figures 5.4123 and 5.4124 respectively). Toxicity associated with the proteins was minimal and the IC₅₀ was found to be >200 µg/mL.

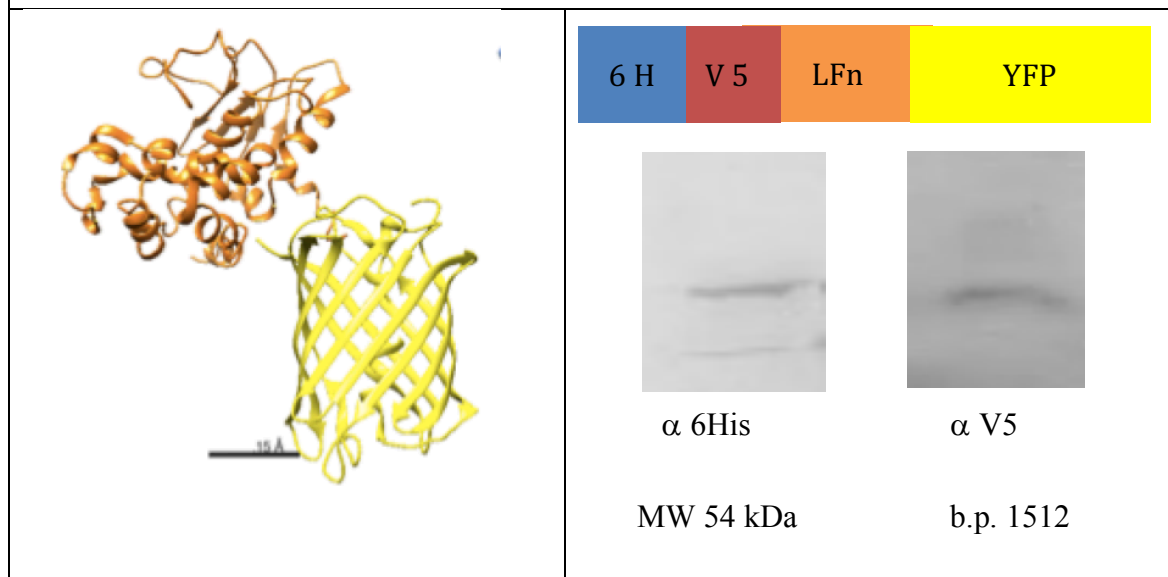
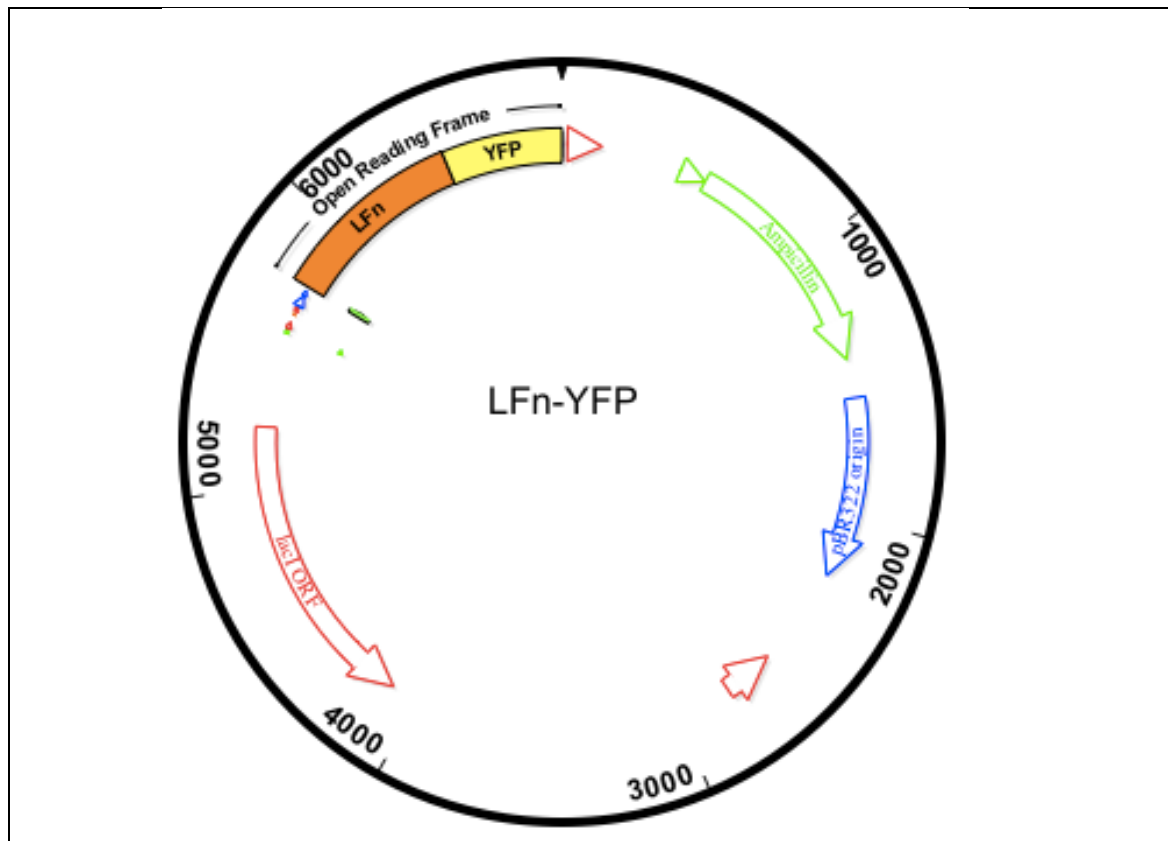


Figure 5.4121 LFn-YFP fusion construct.

In silico plasmid maps were designed (A), where ORF were analysed, primers were designed, and sequencing data was analysed (appendices 9.1). ITASSER (B) generated predicted 3D structure for LFn-GFP. Protein produced from the plasmid expression in BL21* DE3 was detected via SDS PAGE, Coomassie stain and Western blot (C) which corresponds to the predicted kDa (D), estimated from the plasmid map. A schematic depicting the ORF including epitopes, and DNA sequences (D).

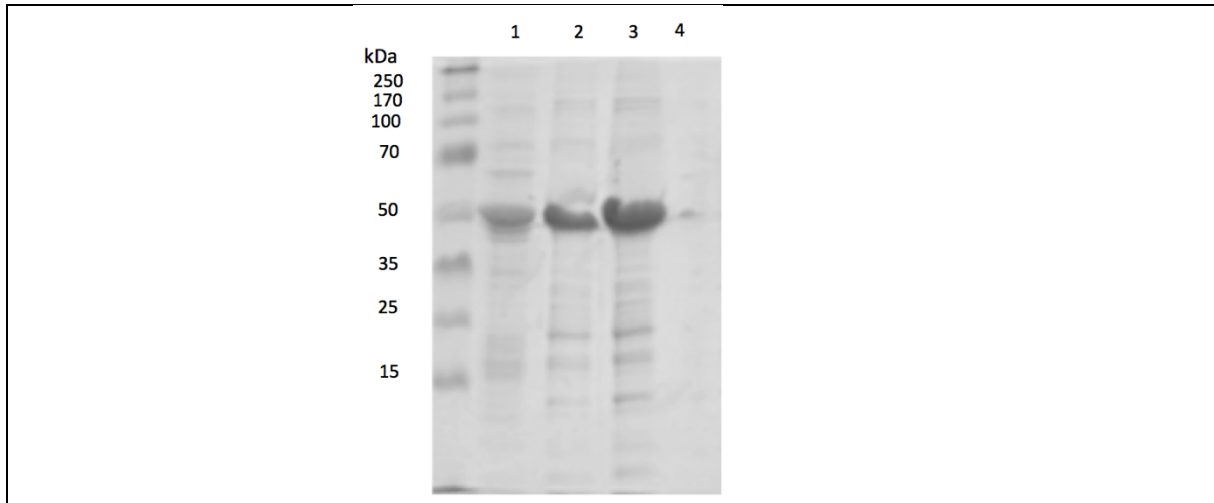


Figure 5.4122 Characterisation of protein elution from TALON® resin by SDS-PAGE and Coomassie staining.

Evaluation of imidazole eluted fractions LFn-YFP (fractions 1-4) following SDS-PAGE and Coomassie staining. Enriched fractions were pooled and evaluated for purity using SDS-PAGE and Coomassie within the limits of detection.

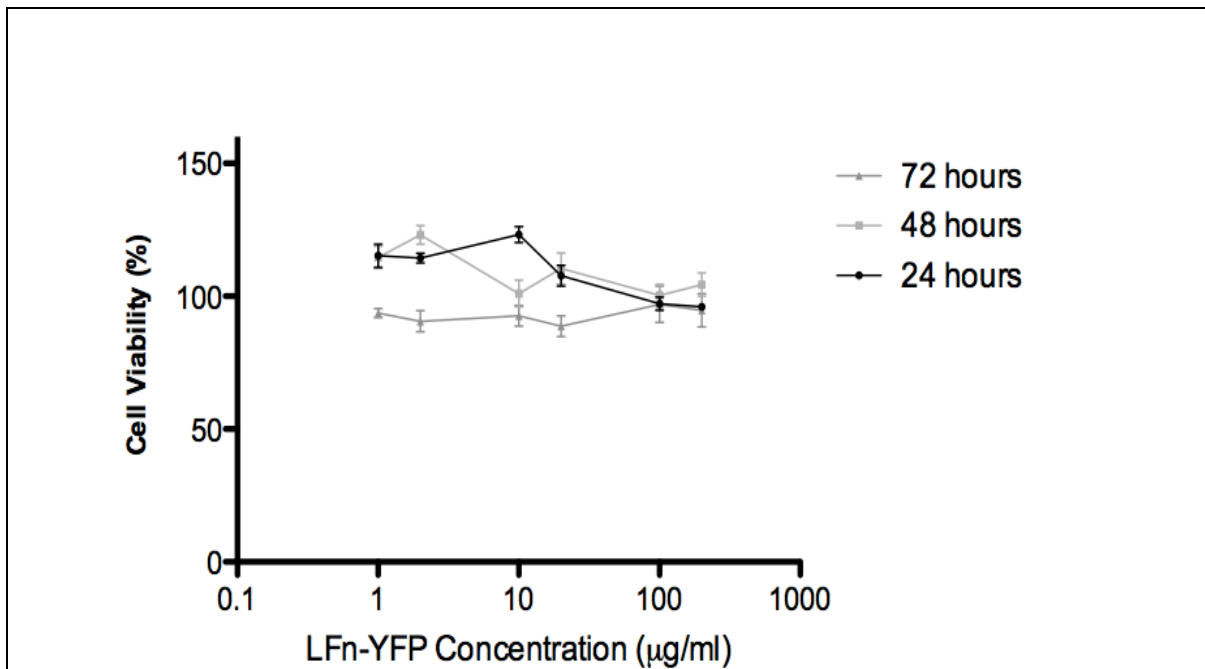


Figure 5.4123 Toxicity profile of PA + LFn-YFP in HeLa cells at 24, 48 and 72 hours.

Toxicity profile of PA + LFn-YFP in HeLa cells over 24, 48 and 72 hours treated at increasing concentrations (0.1 µg/mL – 200 µg/mL), with a seeding density of 1×10^4 HeLa cells ($n=6$, \pm SEM). IC_{50} values were calculated for 24, 48 and 72 hours and was found to be >200 µg/mL and >200 µg/mL and >200 µg respectively.

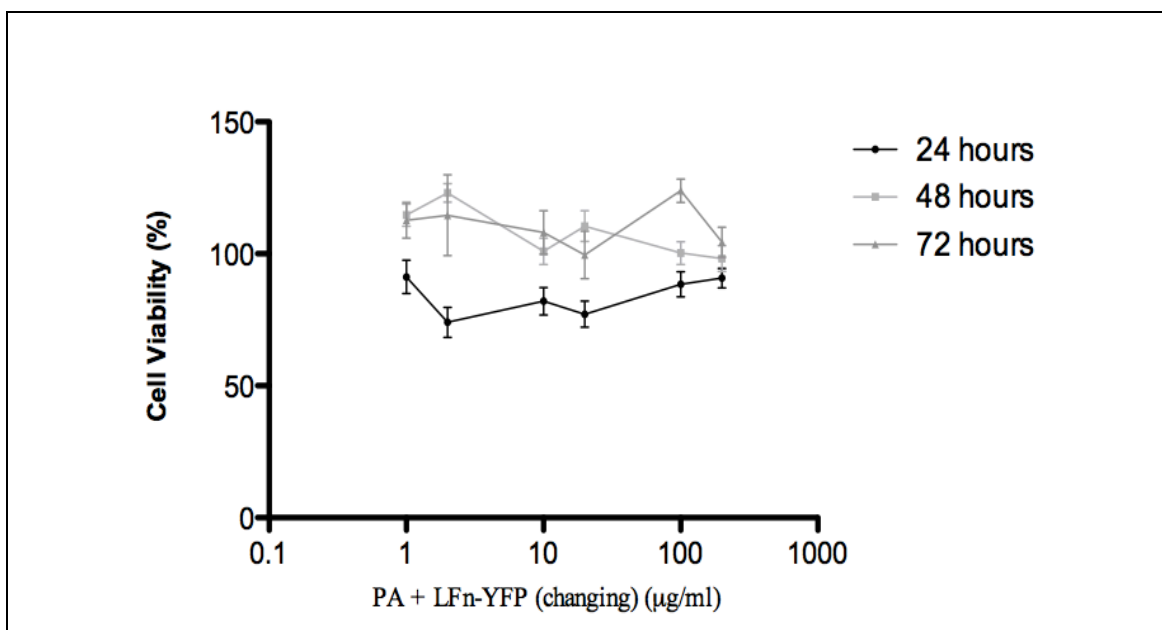
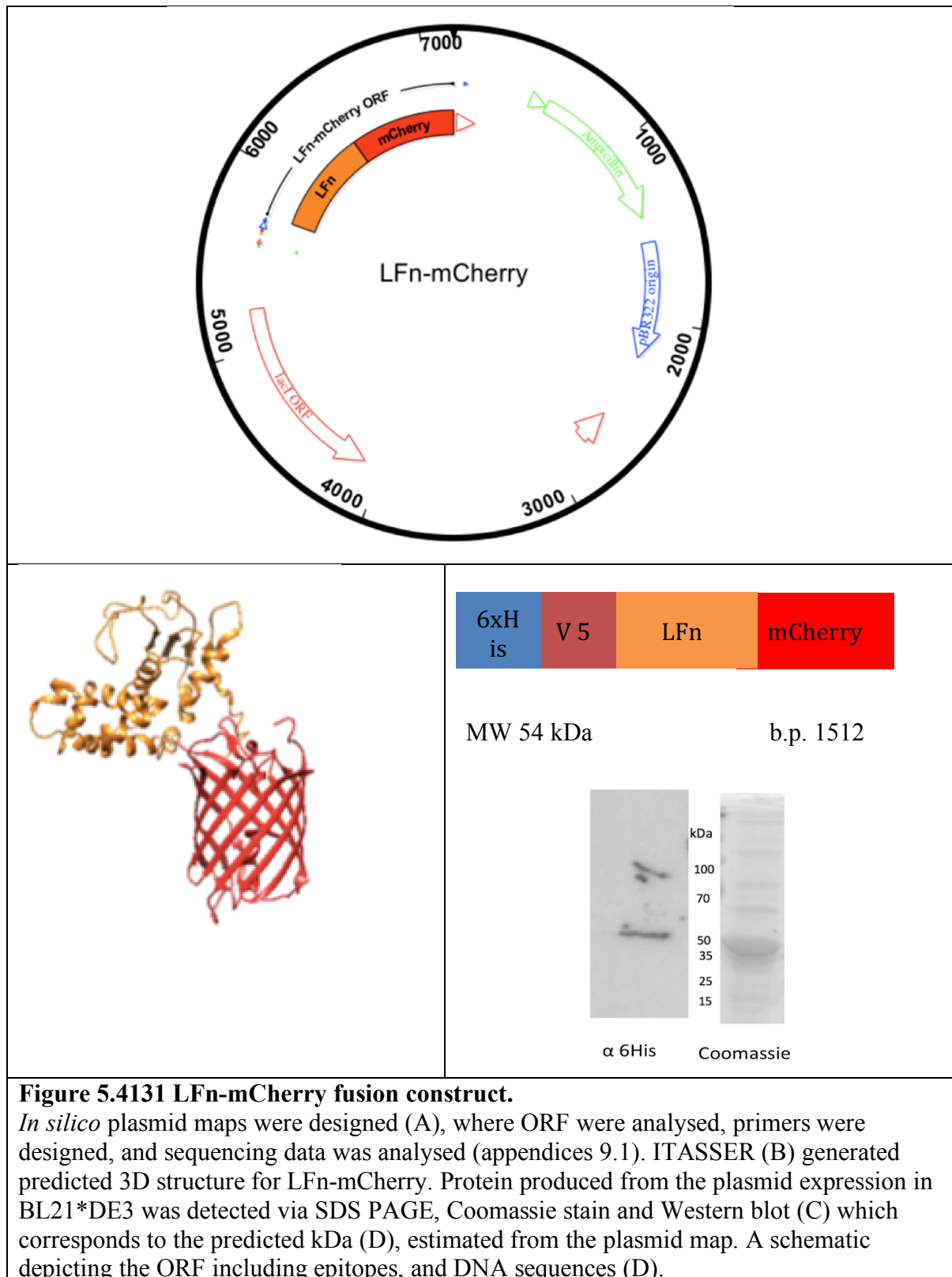


Figure 5.4124 Toxicity profile of LFn-YFP in HeLa cells at 24, 48 and 72 hours.

Toxicity profile of LFn-YFP in HeLa cells over 24, 48 and 72 hours treated at increasing concentrations (0.1 µg/mL – 200 µg/mL), with a seeding density of 1×10^4 HeLa cells (n=6, \pm SEM). IC₅₀ values were calculated for 24, 48 and 72 hours and was found to be >200 µg/mL and >200 µg/mL and >200 µg respectively.

5.413 LFn-mCherry protein production and characterisation

LFn-mCherry was synthesised by BBI in pUC19 and subsequently sub-cloned into pET151/D TOPO. This plasmid was sequenced (see appendices 9.1). The analysis of the sequence results showed correct sequence alignment relative to a prediction made *in silico* (Figure 5.4131A), the ligated DNA insert being maintained within the ORF, with N-terminal 6xHis and V5 epitope tags. LFn-mCherry protein was produced in One Shot[®] *E.coli* BL21*DE3/plys bacteria (Invitrogen, Paisley, UK) was detected by both Coomassie stain and Western blot using an anti-6xHis monoclonal antibody which decorated a protein band at the predicted molecular of 54 kDa (Figure 5.4121 C and D). Protein enrichment (after affinity chromatography) was analysed using SDS PAGE and Coomassie staining, and was calculated to be >85% (Figure 5.4132). LFn-mCherry protein yield was determined by densitometry with reference to BSA standard and was calculated to be 6mg/mL yielding 24mg/l culture.



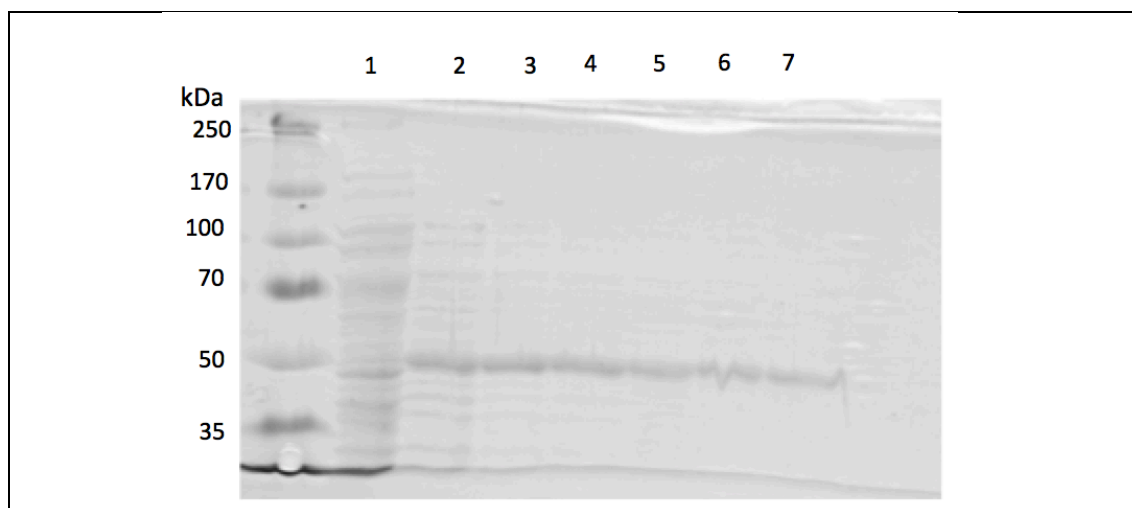


Figure 5.4132 Characterisation of protein elution from TALON® resin by SDS-PAGE and Coomassie staining.

Evaluation of imidazole eluted fractions LFn-mCherry (fractions 1-7) following SDS-PAGE and Coomassie staining. Enriched fractions were pooled and evaluated for purity using SDS-PAGE and Coomassie within the limits of detection.

Hours	24	48	72
PEI ($\mu\text{g}/\text{mL}$)	77 (± 13)	47(± 3)	52(± 2.5)
Dextran ($\mu\text{g}/\text{mL}$)	>100	>100	>100
PA ($\mu\text{g}/\text{mL}$)	>200	>200	>200
LFn-GFP ($\mu\text{g}/\text{mL}$)	>500	96.2 (± 6)	87(± 9.5)
PA+LFn-GFP ($\mu\text{g}/\text{mL}$)	>200	>200	>200
LFn-YFP ($\mu\text{g}/\text{mL}$)	>200	>200	>200
PA+LFn-YFP ($\mu\text{g}/\text{mL}$)	>200	>200	>200

Table 5.41 Summary of Protein toxicity IC₅₀

5.42 Characterisation of markers for subcellular fractionation (using Western blot) and indirect immunofluorescence microscopy

Initially the ability of a panel of antibodies to specifically recognise and detect bands of the predicted molecular weight was undertaken using whole cell lysate (of either HeLa or Vero cells) as a target.

Derlin, early endosomal antigen (EEA)1 and lactate dehydrogenase (LDH) were markers used as either controls (housekeepers) for protein expression or to identify proteins in specific subcellular fractions (Section 2.253). CMG2 and TEM8 are membrane bound receptors, which are required for PA translocation (Section 1.3 (Collier 2009)).

After PNS was prepared, the total protein concentration was assayed (Section 2.256) and 40µg of PNS was run on an SDS PAGE. This was then subjected to Western blot to ensure reliable detection of the chosen marker proteins. Vero cell (Figure 5.421, Derlin) and HeLa (Figure 5.422, Derlin) produced a protein that was decorated by the Derlin specific antibody and had an apparent molecular weight of ~25kDa. The expected MW of Derlin is 22kDa (Katiyar *et al.*, 2005). EEA1, an early endosomal marker was detected in both HeLa and Vero whole cell lysate above 100 kDa. The predicted molecular weight for EEA1 was 160 kDa (Grim *et al.*, 2011), the size discrepancy here could be attributed to post translational modification of EEA1. LDH (a cytosolic marker (Richardson *et al.*, 2010) was only detectable in Vero cell, and not in HeLa. It was detected at the predicted molecular weight of ~35 kDa (expected molecular weight of 36 kDa) (Legrand *et al.*, 1992)

TEM8 was detected in both HeLa and Vero cell whole cell lysate at ~50 kDa, which compares to the predicted molecular weight of 45kDa (Chaudhary *et al.*, 2012).

In order to determine protein location within translocation experiments, co-localisation with other endocytic structures will need to be determined via immunofluorescent microscopy.

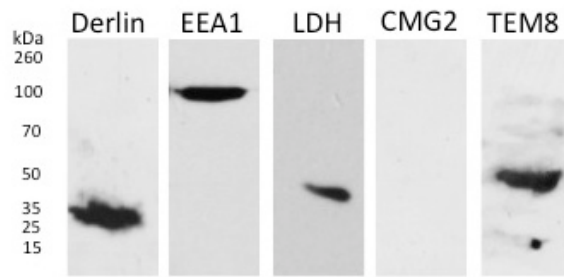


Figure 5.421 Western blot of Vero whole cell lysate for different cellular markers.

Whole cell lysate of Vero cells was evaluated via blot for cellular marker. Each lane contains 40 μ g of whole cell lysate, on an SDS PAGE gel, Western blot for either Derlin (Derlin), early endosomal marker (EEA1), lactate dehydrogenase (LDH), capillary morphogenesis gene 2 protein (CMG2), and tumour endothelial marker 8 (TEM8).

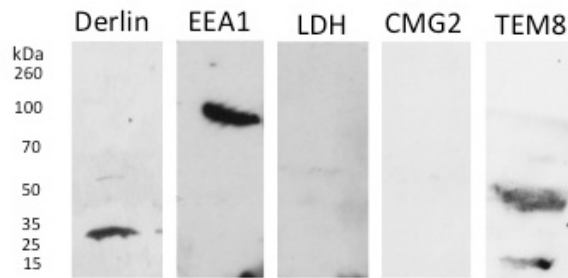


Figure 5.422 Western blot of HeLa whole cell lysate for different cellular markers.

Whole cell lysate of HeLa cells was evaluated via immune-blot for cellular marker. Each lane contains 40 μ g of whole cell lysate, on an SDS PAGE gel, blot for either Derlin (Derlin), early endosomal marker (EEA1), lactate dehydrogenase (LDH), capillary morphogenesis gene 2 protein (CMG2), and tumour endothelial marker 8 (TEM8).

To characterise these systems, detection of common cellular markers, and WGA trafficking to the LE/lysosome have been established via immune-labelling and fluorescent microscopy. Initially LAMP 1 positive structures were labelled using three different specific secondary Ab (Figure 5.423) (A) anti mouse conjugated to Texas red, (B) anti mouse conjugated to Alexa Flour-488, and anti-mouse conjugated to CY5 (C). This was to establish optimum fluorescent signal to noise ratio to use with minimal cross talk of fluorescence emission. LAMP1 positive structures were seen using all of the fluorescent probes conjugated to secondary antibodies. The CY5 –conjugated secondary antibodies (C) show notable cross talk of fluorescence emission, into both the green channel (FITC) and the red channel (TXS RED). This would make this unsuitable for further co-localisation within this study. There was minimal cross talk recorded when the anti-mouse – Alexa Fluor 488- or Texas Red-conjugated secondary antibodies were used, making either of these secondary antibodies suitable for future use within co-localisation studies. To determine the WGA-TXS RED trafficking to the LE/lysosome (4 hours post exposure) co-localisation with LAMP 1 positive structure was evaluated. This showed (Figure 5.424) WGA – TXS RED distinctive puncta. This presented co-localisation to LAMP 1 (α LAMP FITC) positive structures (MERGE). Suggesting that the location of WGA 4 hours post exposure was within late endocytic structures.

The detection of common cellular markers was also observed, Vero cells treated with WGA – TXS RED (4 hours post exposure) to identify LE/lysosome structure within the same cell population (Figure 5.425). These markers were chosen to represent early and late endocytic structures (EEA1, GM130, Transferrin receptor, WGA-TXS RED LE/lysosome structures).

This resulted in expected EEA1 distribution, seen in puncta throughout the cell; this had no co-localisation with WGA-TXS RED (A). GM130 staining (of the medial golgi) was observed around the nucleus, this demonstrated no co-localisation with WGA-TXS RED (B). Transferrin receptor (C) immuno-staining showed no co-localisation with WGA-TXS RED, and expected distributed throughout the cell.

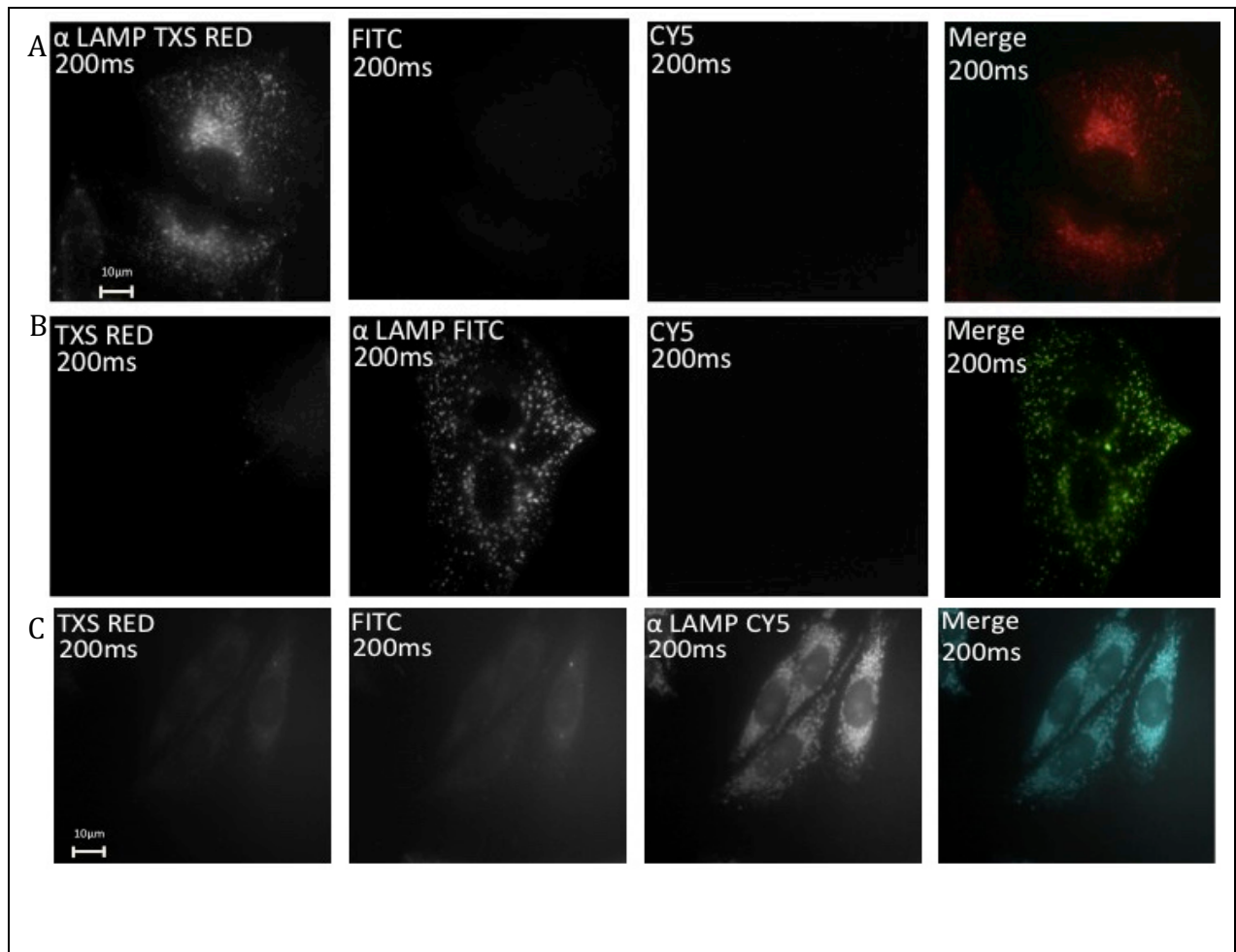


Figure 5.423 Late endosome/lysosome positive structures, labelled in Vero cells using different fluorescent probes; to measure for cross talk of fluorescence emission through of fluorescence into other channels.

Representative images of HeLa cells (seeding density 1×10^5) immuno-labelled for late endosome/lysosome structures (anti-LAMP) each row was treated with a different secondary; α -Mouse conjugated to Texas Red (A), α -Mouse conjugated to Alexa 488 (B), α -Mouse conjugated to CY5 (C).

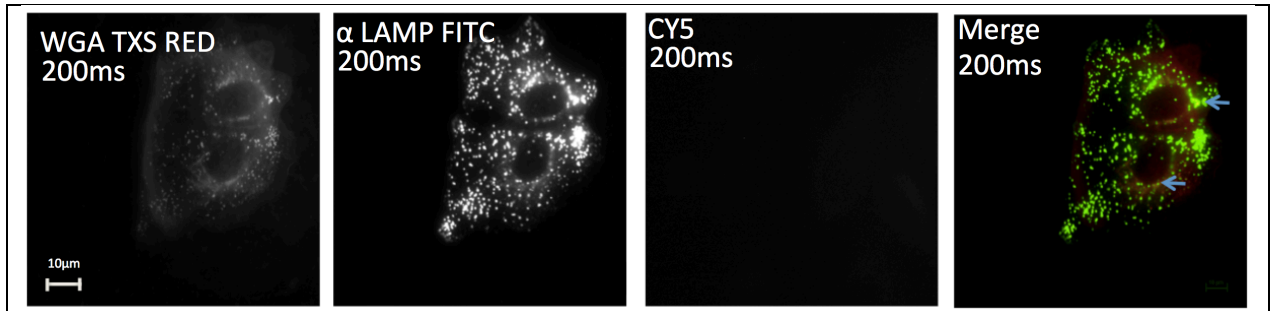


Figure 5.424 Co-localisation studies of LAMP 1 positive structure with WGA-TXS RED labelled structures, 4 hours post exposure.

Representative images of Vero cells (seeding density 1×10^5) treated with WGA-TXS RED 4 hours post exposure, and immuno-labelled with LAMP1-Alexa 488. Magnification 60x, taken at 200ms exposure.

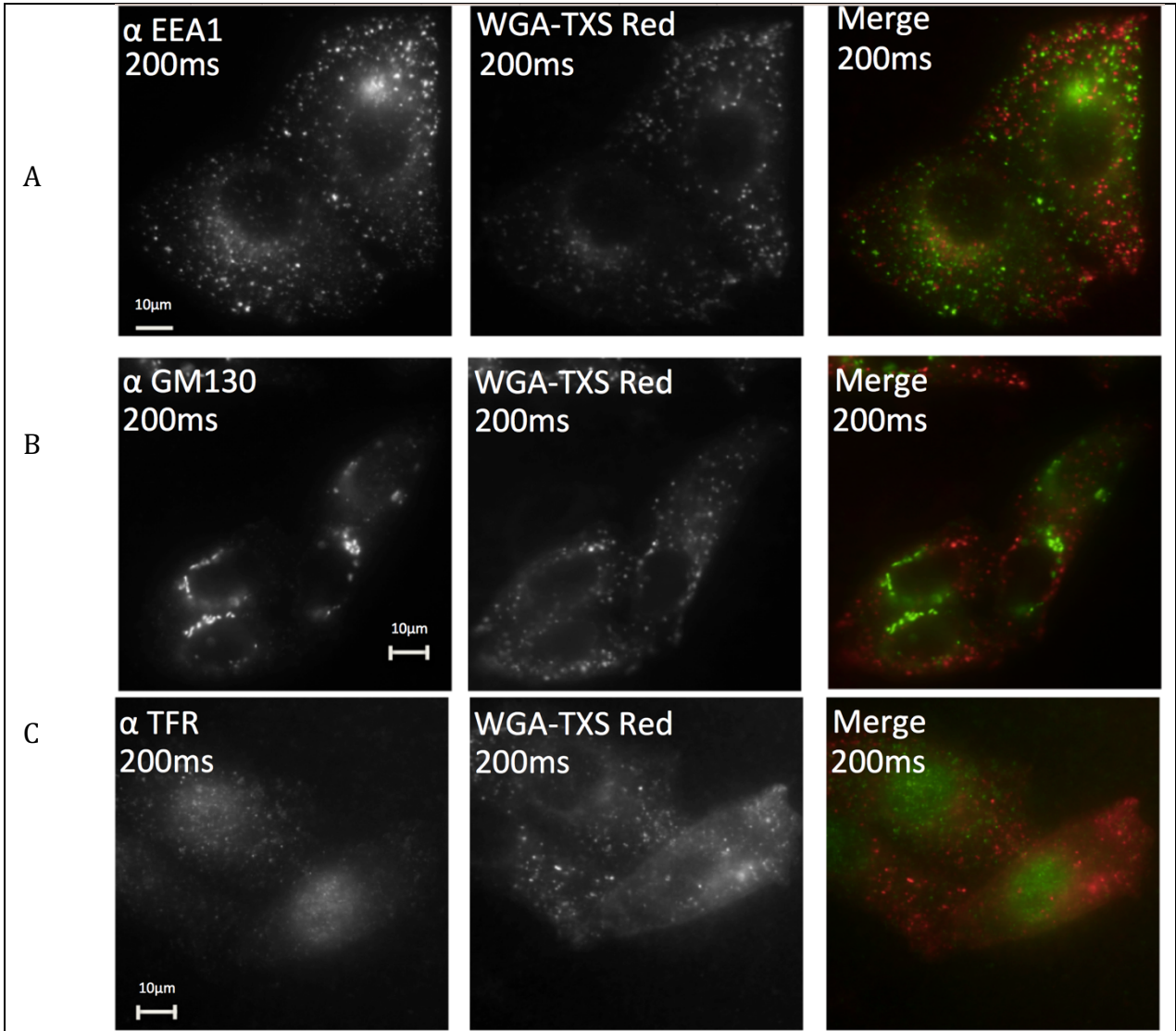


Figure 5.425 Expression of common markers in Vero cells.

Showing localisation of sub-cellular organelles with LE/ lysosomes (LE/lysosomes are labelled with WGA conjugated to Texas Red 4 hours post exposure). (A) EEA1 (early endosome) and Late endosome/Lysosome (WGA TXS RED) (B) GM130 (cis-medial Golgi) and Late endosome/Lysosome (WGA TXS RED), (C) transferrin receptor (TRF) and Late endosome/Lysosome (WGA TXS RED). Magnification 60x, taken at 200ms exposure.

5.43 Fluorescent protein cytosolic translocation in Vero cells

Determining the ability of LFn-GFP to translocate across biological membrane in the presence and absence of PA was initially tested using Vero cells, at a variety of incubation times (5, 15, 30, minutes) this was performed, in the presence and absence of PA protein, also using an EEA1 TXS RED co stain to distinguish the location of LFn-GFP from early endocytic structures to demonstrate specificity.

At a 5-minute incubation (Figure 5.431 A) in cells treated with LFn-GFP both in the presence and absence of PA, GFP is detected within the cell. There is minimal co-localisation with EEA1. These observations were also seen at 15, 30, (Figure 5.431 B and C respectively). A variety of control experiment were performed to investigate non-specific antibody labelling. Initially Vero cells were treated with no protein or LFn-GFP in the absence and presence of PA for 15 minutes, and analysed using a secondary anti-rabbit secondary conjugated to Alexa fluor 488 (the antibody previously used) only (no primary antibody was used) (Figure 5.432). This demonstrated the non-specific binding of the secondary antibody to the cells, in cells treated with no protein or primary antibody as is seen in Figure 5.431. There was detection of the antibody throughout the cell, as no primary antibody was used, this was due to non-specific binding of the antibody, causing false positives. Additionally, to this there seems to be variation in non-specific binding between cells, as determined by the presence of green fluorescence signal (Figure 5.432, GFP).

There was also some spectral bleed-through, from the A488 flour into the red fluorescent channel (Figure 5.432 untreated, Red). This data set would indicate that Vero cells are not suitable for this experiment due to the non-specific binding of the antibodies. This would also indicate that conclusions drawn about LFn-GFP translocation in the presence and absence of PA in Vero cell are actually false positives

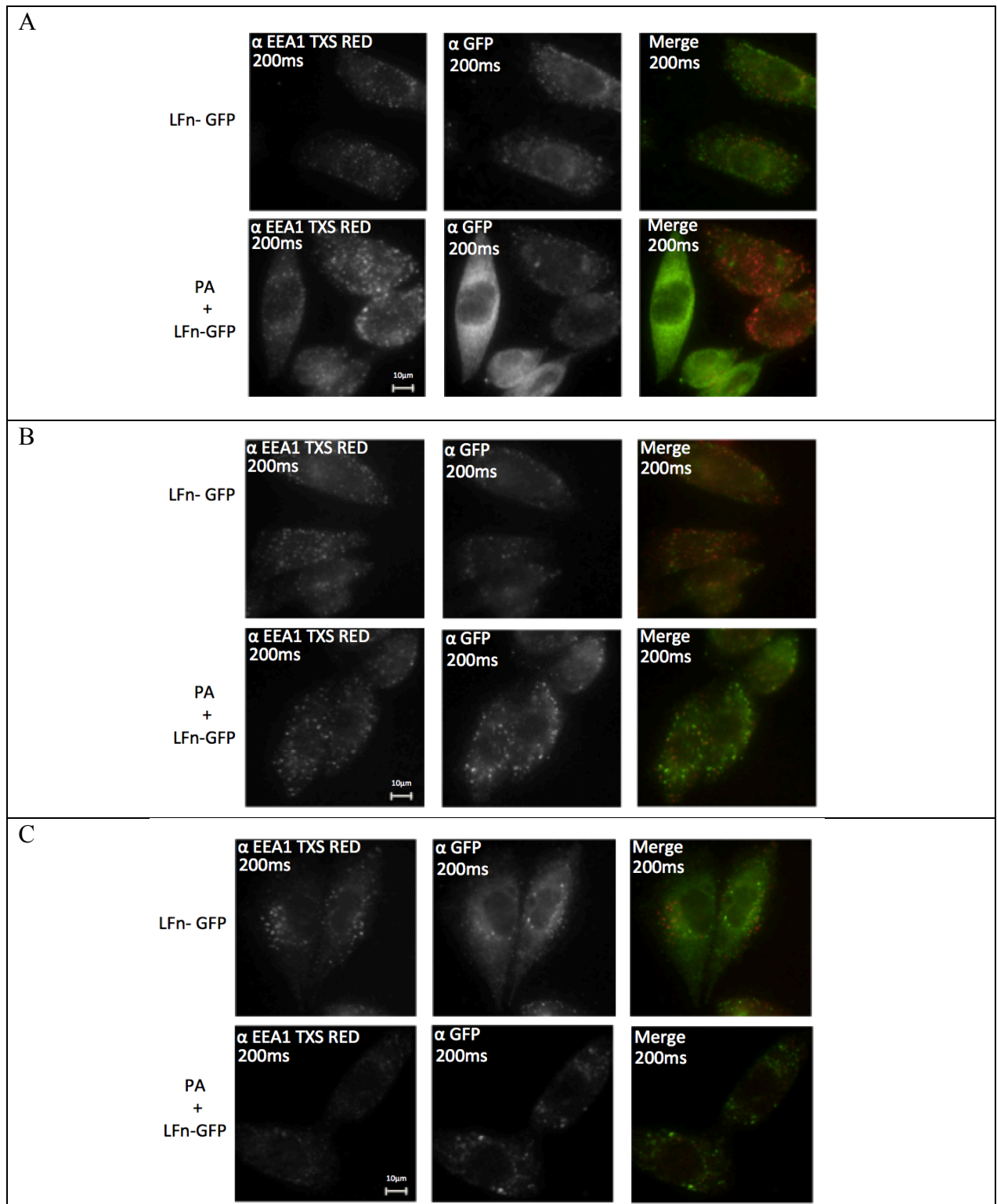


Figure 5.431 Translocation of LFn-GFP in Vero cells at 5, 15 and 30minute incubation in the presence and absence of PA.

Representative images of Vero cells (seeding density 1×10^5) treated with LFn-GFP ($20 \mu\text{g}/\text{mL}$) and PA + LFn-GFP (50 and $20 \mu\text{g}/\text{mL}$ respectively) with a 5 (A) 15 (B) and 30 (C) minute incubation time. All images were acquired at 200 ms exposure, using an anti-GFP primary antibody and anti-rabbit secondary antibody conjugated to A488 and anti-EEA1 primary antibody and secondary anti mouse conjugated to Texas Red. Magnification 60x, taken at 200ms exposure.

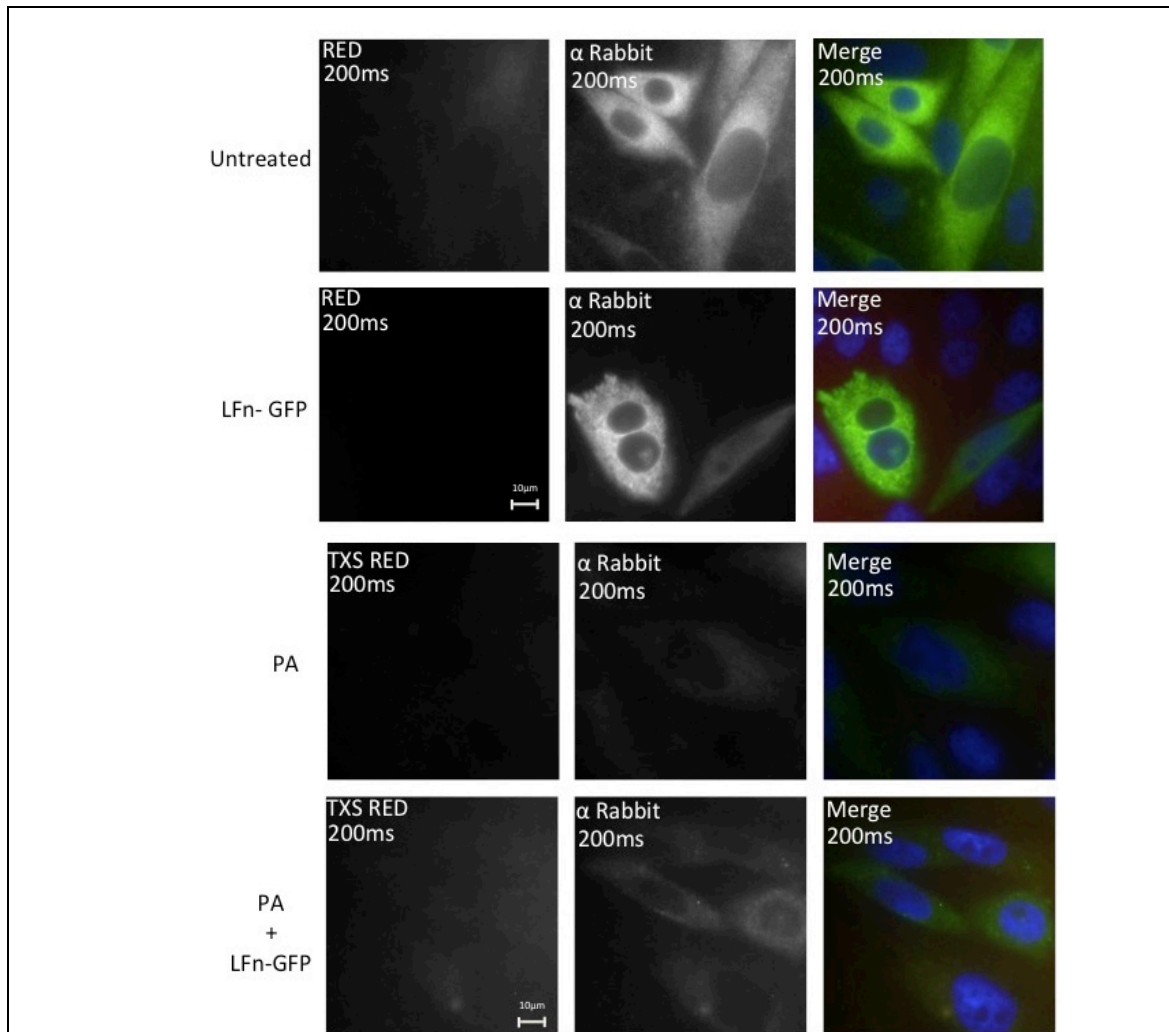


Figure 5.432 Control experiments for unspecific binding of secondary anti rabbit conjugated to A488 in Vero cells.

Representative images of Vero cells (seeding density 1×10^5) treated with no protein or LFn-GFP ($20 \mu\text{g}/\text{mL}$), with a 15-minute incubation time. All images were acquired at 200ms exposure, using an anti-rabbit secondary antibody conjugated to A488 and a DAPI nucleic acid stain. Magnification 60x, taken at 200ms exposure.

5.44 Fluorescent protein translocation using HeLa cells

An investigation was undertaken to assay the ability of LFn-GFP to translocate *in vitro* by fluorescent microscopy, where LFn-GFP translocation was evaluated in HeLa cell due to earlier findings of antibody non-specific binding in Vero cells.

At a 5 minute incubation (Figure 5.441, A) time HeLa cells treated with LFn-GFP in the absence of PA displayed minimal GFP detection. In contrast to this in the presence of PA, GFP is detectable at much higher quantities, with some cellular localisation into puncta around the membranes and within the cell. As time of cellular incubation increases, the detectable amounts of LFn-GFP in the presence of PA increased.

At 15 minutes protein incubation (Figure 5.441, B) GFP is detected within punctate localised around the cell membrane, with GFP also detectable within the cell as a green haze. In contrast at 15 minutes in the absence of PA, GFP detection is limited, although there is some green fluorescence within puncta. This is could be due to fluid phase uptake of LFn-GFP, which is minimal. However, control experiments at 4°C (Figure 5.442, A) where endocytosis should be halted, shows green fluorescence as a haze and in puncta, which would question if this really were fluid phase uptake of LFn-GFP. Additionally, GFP signal in the absence of PA may be due to auto-fluorescence from the protein. As can be seen in Figure 5.442, B, PA treated HeLa cells (in the absence of LFn-GFP) show some green signal at similar levels within puncta.

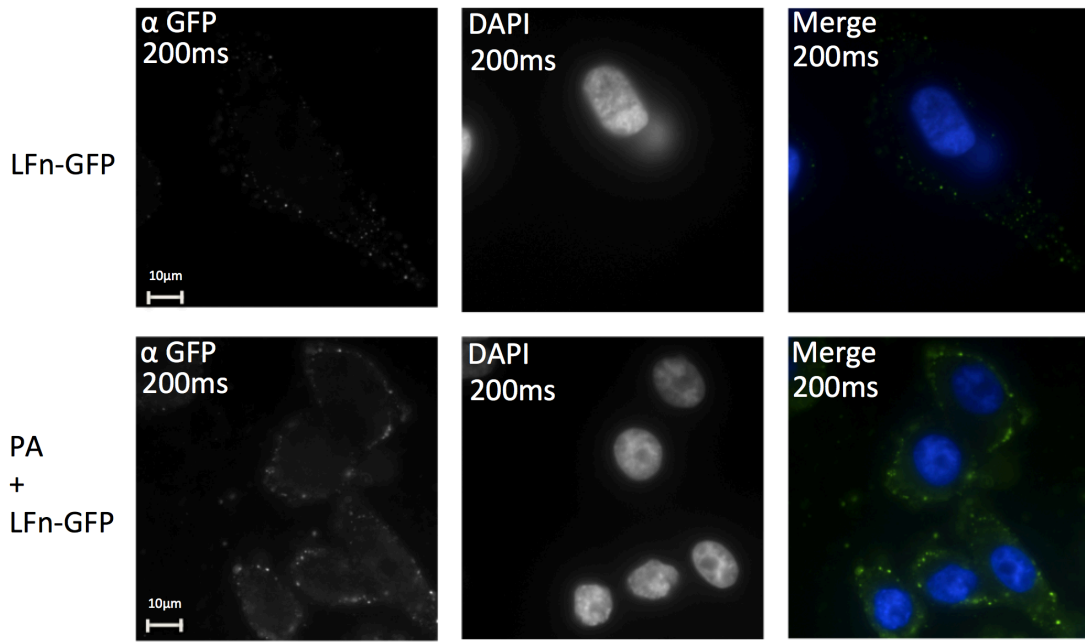
This could mean that the green signal detected is auto-fluorescence from the addition of protein. Furthermore, HeLa cells treated with no protein (Figure 5.442 B) show no green fluorescence, which would indicate that there is no non-specific binding of antibodies causing this fluorescence.

After a 30 minute incubation with LFn-GFP (Figure 5.441, C) in the presence of PA, GFP is still detectable, with punctate around the cell membrane, and is detected within the cell as both punctate and haze. In the absence of PA there is still some green signal, much lower than in the presence of PA. This could be attributed fluid phase uptake and autofluorescence.

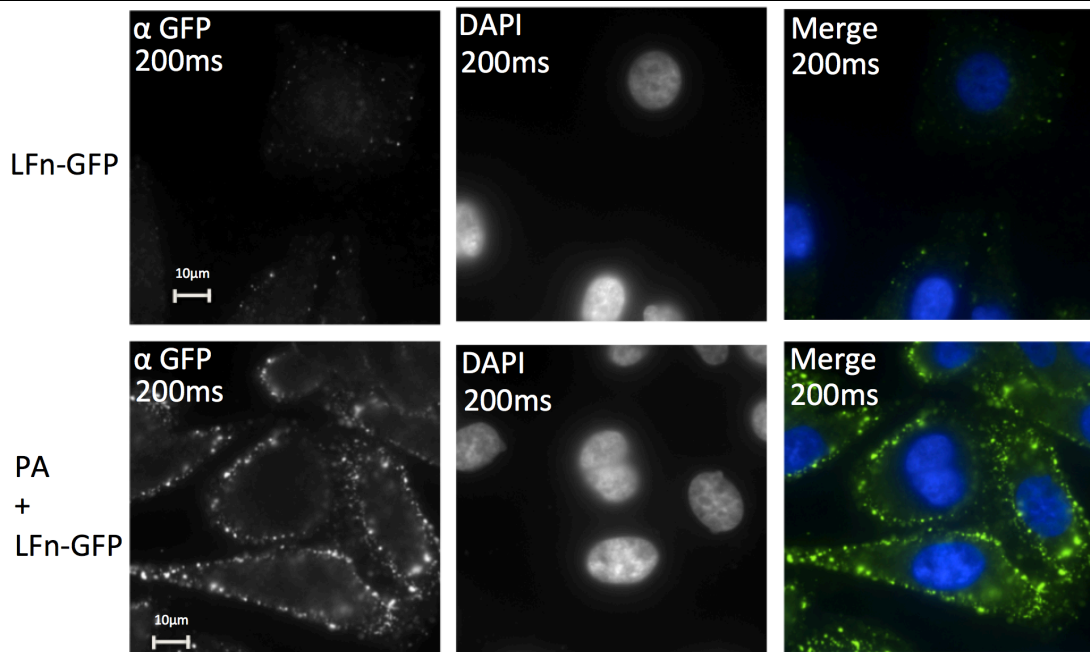
HeLa cells were incubated with LFn-GFP in the presence and absence of PA at 4°C (Figure 5.442, A), which decreases the rate of endocytosis, showed limited GFP detection in the presence and absence of PA, demonstrating the metabolic requirement for cytosolic translocation LFn-GFP.

This data set indicates that the PA pore is mediating LFn-GFP trafficking and translocation into the cell. However, to determine localisation (in the cytosol, or lysosome) as well a time course, further co-localisation studies need to be completed.

A



B



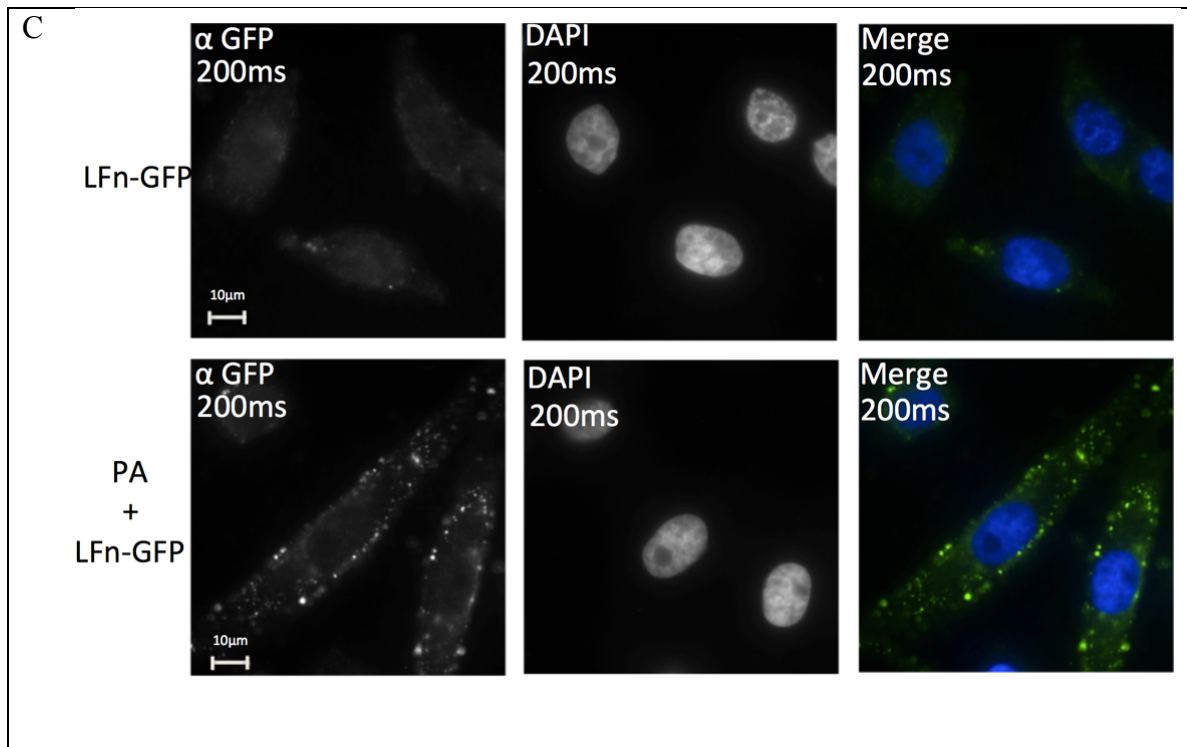


Figure 5.441 Translocation of LFn-GFP in HeLa cells at 5 minutes incubation in the presence and absence of PA.

Representative images of HeLa cells (seeding density 1×10^5) treated with LFn-GFP ($20 \mu\text{g}/\text{mL}$) and PA + LFn-GFP ($50 \mu\text{g}/\text{mL}$ and $20 \mu\text{g}/\text{mL}$ respectively) with a 5 (A) 15 (B) and 30 (C) minute incubation time. All images were acquired at 200ms exposure, using an anti-GFP primary antibody and anti-rabbit secondary antibody conjugated to Alexa 488. Magnification 60x, taken at 200ms exposure.

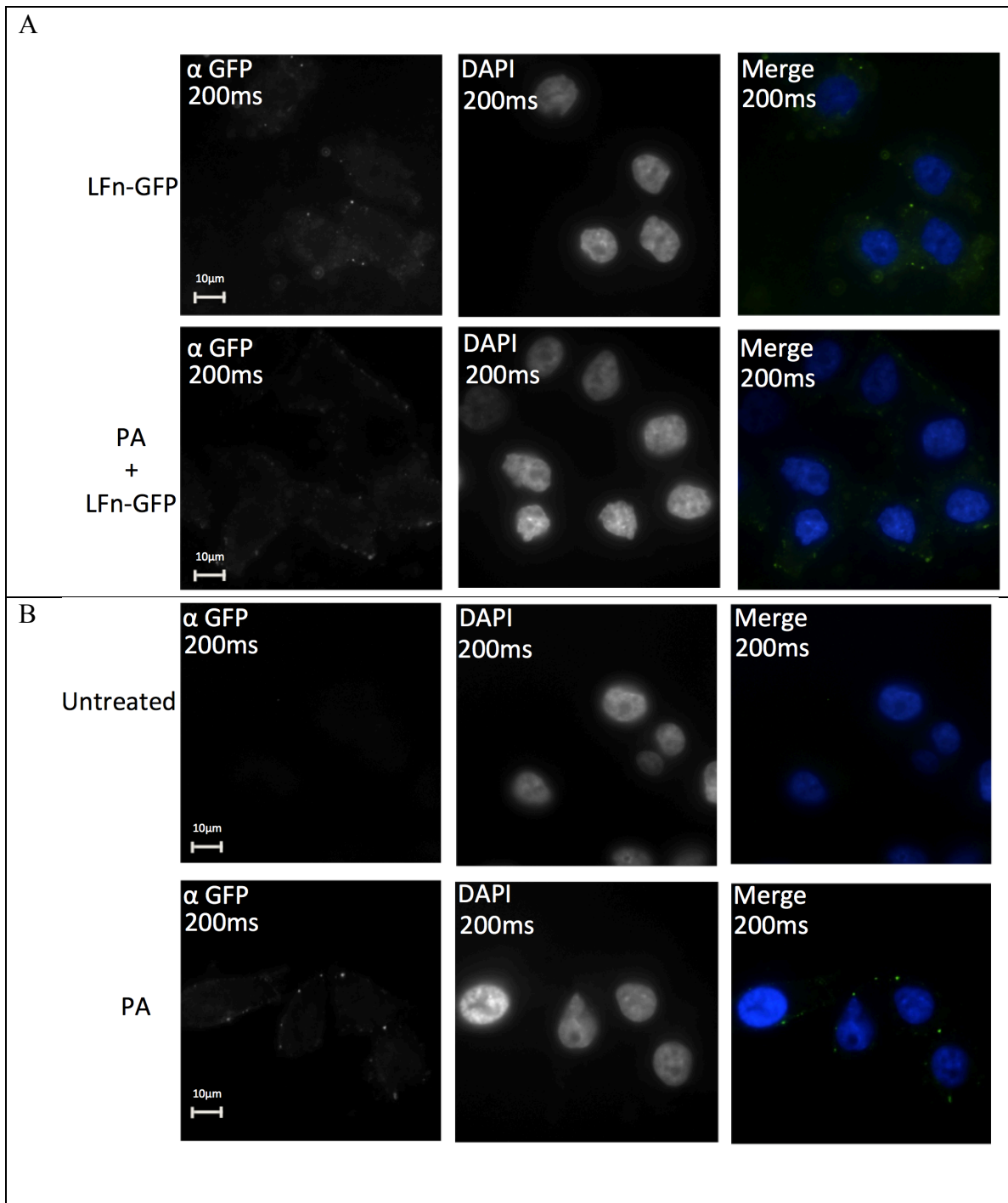


Figure 5.442 Control experiments for unspecific binding of secondary anti rabbit conjugated to A488 in HeLa cells.

Representative images of HeLa cells (seeding density 1×10^5) treated with LFn-GFP ($20 \mu\text{g}/\text{mL}$) or LFn-GFP in the presence of PA ($50 \mu\text{g}/\text{mL}$) at 4°C (A) or treated with no protein, or PA ($50 \mu\text{g}/\text{mL}$) (B) with a 15-minute incubation time. All images were acquired using an anti-rabbit secondary antibody conjugated to A488 and a DAPI nucleic acid stain. Magnification 60x, all images acquired at 200ms exposure.

5.45 Subcellular fractionation

Further to the evaluation of LFn-GFP translocation by microscopy, translocation into specific subcellular compartments was investigated. Initially translocation of LFn-GFP was investigated under three different time points 4, 6 and 16 hours in HeLa cells in the absence of PA to investigate the PA specific dependency of delivery. Membrane and cytosolic fractions were evaluated for the presence of LFn-GFP (Figure 5.451) as well as the presence of specific subcellular markers for the membrane (transferrin receptor) and the cytosol (LDH) to determine fraction purity. The cytosolic fraction was determined to be clear of any membrane contaminant (Figure 5.451, A). However, as the LDH marker failed (Figure 5.451, A), it cannot be commented on as to whether there was any cytosolic contamination in the membrane fraction. Both membrane and cytosolic fraction were evaluated for the presence of LFn-GFP using anti-V5 (an epitope at the N-terminal of the protein) specific antibody. V5 was detected in both fractions (membrane and cytosolic). Protein signal was higher within the membrane fraction, which would indicate that there was protein binding to the membrane of these cells. Given the cytosolic fraction is clear of membrane fraction contaminant, it can be assumed that the signal detected is true, which would indicate the ability of LFn-GFP to translocate in the absence of PA. With a decrease in signal over time in both fractions (Figure 5.451, B). However, HeLa cells treated with LFn-GFP at 4°C for 4 hours demonstrated limited detectable LFn-GFP on the membrane (Figure 5.451 A), and limited translocation of LFn-GFP into the cytosol.

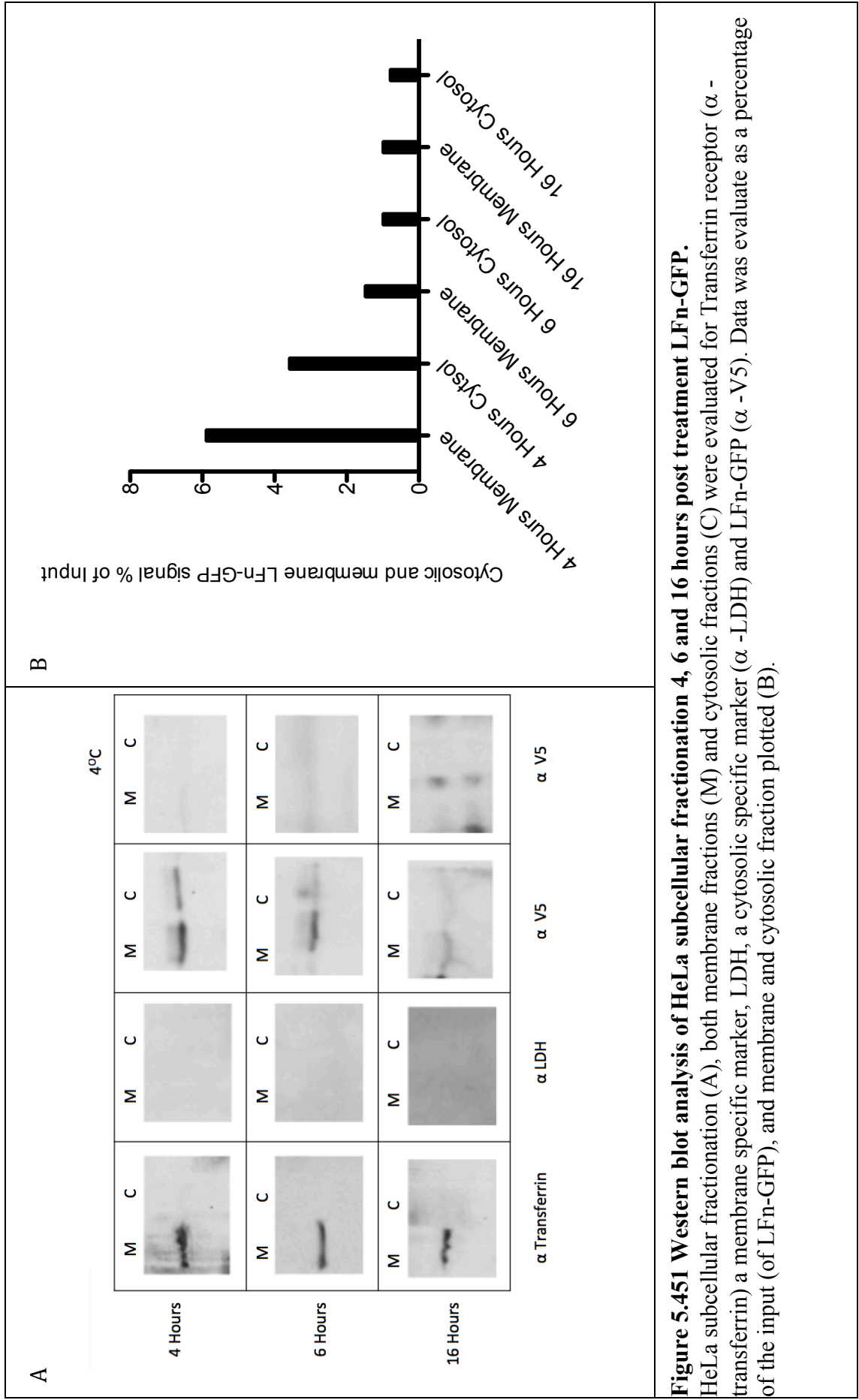


Figure 5.451 Western blot analysis of HeLa subcellular fractionation 4, 6 and 16 hours post treatment LFn-GFP.

HeLa subcellular fractionation (A), both membrane fractions (M) and cytosolic fractions (C) were evaluated for Transferrin receptor (α -transferrin) a membrane specific marker, LDH, a cytosolic specific marker (α -LDH) and LFn-GFP (α -V5). Data was evaluate as a percentage of the input (of LFn-GFP), and membrane and cytosolic fraction plotted (B).

Translocation of LFn-GFP was investigated under three different time points 4, 6 and 16 hours in HeLa cells in the presence of PA to investigate the PA specific dependency of delivery. Membrane and cytosolic fractions were evaluated for the presence of LFn-GFP (Figure 5.452) as well as the presence of specific subcellular markers for the membrane (transferrin receptor) and the cytosol (LDH) to determine fraction purity. The cytosolic fraction was determined to be clear of any membrane contaminant (Figure 5.452 A, anti-transferrin). However, as the LDH marker failed (Figure 5.452 A anti-LDH), it cannot be commented as to whether there was any cytosolic contamination in the membrane fraction. Both membrane and cytosolic fraction were evaluated for the presence of LFn-GFP. There was detection of LFn-GFP in both fractions in the presence of PA (membrane and cytosolic). Protein signal was higher in the membrane fraction than in the cytosolic fractions. Though, protein signal revealed an increased amount of proteins detected over time (Figure 5.452 B) in both fractions.

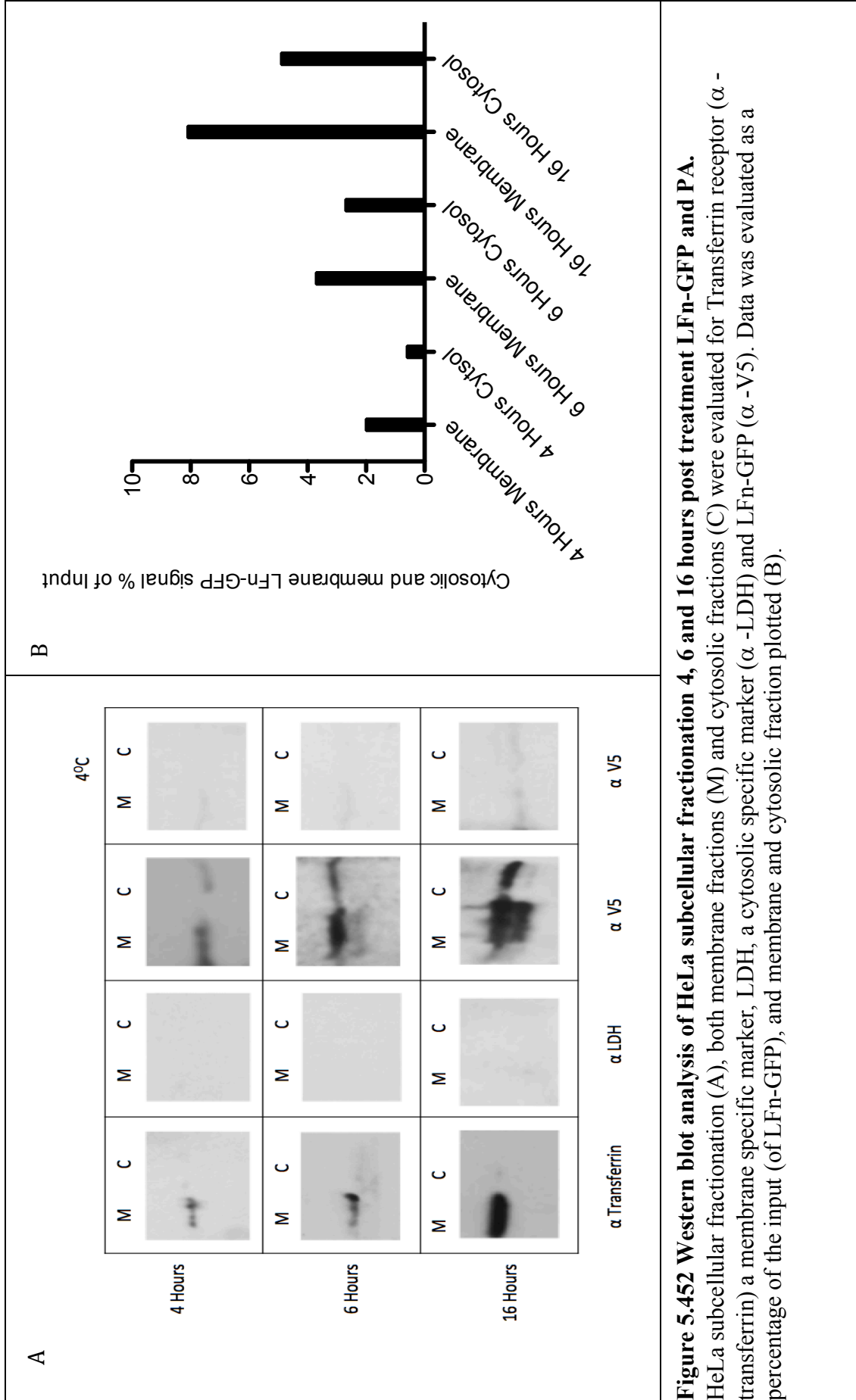


Figure 5.452 Western blot analysis of HeLa subcellular fractionation 4, 6 and 16 hours post treatment LFn-GFP and PA. HeLa subcellular fractionation (A), both membrane fractions (M) and cytosolic fractions (C) were evaluated for Transferrin receptor (α -transferrin) a membrane specific marker, LDH, a cytosolic specific marker (α -LDH) and LFn-GFP (α -V5). Data was evaluated as a percentage of the input (of LFn-GFP), and membrane and cytosolic fraction plotted (B).

In order to clarify that the membrane fraction didn't contain any of the cytosolic fractions there needs to be a positive and reliable marker for the cytosolic fraction. This has previously been LDH, however as this isn't working as a cytosolic marker, this needs to be optimised. This has importance as some of the protein (LFn-GFP) signals associated with the membrane could potentially be from cytosolic contamination, without being able to demonstrate this it cannot be determined.

To this end a variety of cytosolic targets were evaluated in HeLa whole cell lysates, to investigate if this issue could be resolved (Figure 5.453).

Four different anti-LDH antibodies were evaluated as well as an MEK, HeLa whole cell lysates samples were also evaluated for EEA1 as a control to monitor correct conditions and monitor cell concentration. This yielded one positive result where by LDH could be detected (Figure 5.453 F).

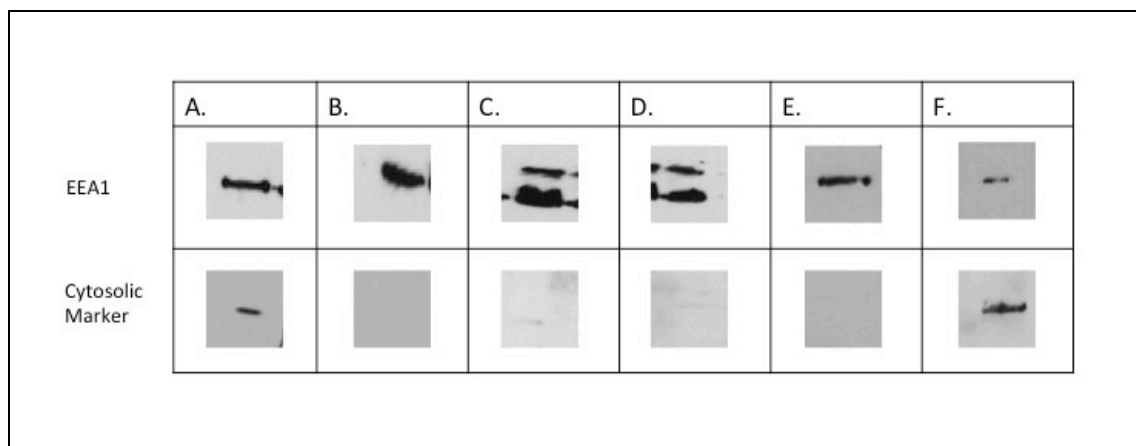


Figure 5.453 Western blot analysis of HeLa whole cell lysate.

HeLa whole cell lysate was analysed for LDH (C, D, E, F) using a variety of different antibodies, and MEK (B) and Vero whole cell lysate (A). These samples were also run against EEA1 as a control to monitor cell concentration and experimental procedures.

5.5 Discussion

Plasmids encoding LFn-GFP, LFn-YFP and LFn-mCherry were sequenced and the sequences assembled into annotated plasmid maps. The proteins produced were recognised by the appropriate antibodies (as denoted) and were detected at the predicted molecular weight (52, 54 and 54 kDa respectively).

Toxicities were measured for all proteins, and IC₅₀s were calculated where possible. LFn-GFP reached IC₅₀ after 48hours. This was unexpected for LFn-GFP as it has been documented that both entities separately are non-toxic (Pannifer *et al.*, 2001; Arora *et al.*, 1993). This could be due to the batch of production, which could possibly contain some contaminant, which may account for the toxicity. However, the same batch of protein was used for the PA + LFn-GFP toxicity study, which demonstrated no toxicity (Figure 5.4116). This also could have been due to oxidative damage to the lysosomes causing apoptosis. Conformation for this would need further study.

LFn-YFP and LFn-YFP in the presence of PA demonstrated some toxicity >200µg/mL. This gives insight into any associated cell death with addition of these proteins, and may also give rise to cell damage and related autofluorescence. Experiments where these proteins were added onto cells were performed at concentration of protein much below the IC₅₀.

In order to interpret experimental data, characterisation of the cell lines and of endocytic markers was undertaken. Western blot detection of cellular markers of HeLa and Vero PNS highlighted that most cellular markers viable. However, CMG2 wasn't detectable in either cell line (Figure 5.421). Most mammalian cell express CMG2, however in HeLa, TEM8 is predominantly expressed (Abrami *et al.*, 2010). This may account for the lack of CMG2 detection. Vero cells would presumably express CMG2 as both anthrax toxin receptors, CMG2 and TEM8, are highly expressed in kidney cells. This may suggest that there was a problem with the antibody or could have possibly been due to the concentration of CMG2

protein within the lysate as opposed to CMG2 not being expressed in either cell line (Sastalla *et al.*, 2012).

TEM8 was detectable in both HeLa and Vero cell whole cell lysate although there was second band at ~15kDa, this could possibly be due to post-translational modification of the TEM8, or a degraded form. This means that both cell lines were suitable candidates for PA translocation studies. Vero cells specifically for their use within epifluorescent microscopy due their morphology. HeLa cells are an extensively used and characterised human cell line. Epifluorescent microscopy of antibodies against specific organelle markers allowed identification of key endocytic organelles, and an evaluation of trafficking translocase cargo. These markers were chosen to represent early and late endocytic structures (early endosome, Golgi, WGA-TXS RED LE/lysosome structures). LAMP demonstrated co-localisation with WGA-TXS RED, indicating the four-hours chase time for WGA-TXS RED was sufficient to reach the lysosome. EEA1 demonstrated expected distribution, exhibiting no co-localisation with either WGA-TXS RED, GM130. Transferrin receptor immuno-staining showed no co-localisation with WGA-TXS RED and expected profile. Additionally, to this, fluors with minimal spectral bleed though were utilised (A488 or TXS-RED).

The translocation of LFn-GFP within cells was evaluated in both HeLa and Vero cells.

Despite GFP being a fluorescent protein, it wasn't detectable via epifluorescent microscopy without using an anti-GFP antibody. This could possibly have been due to the effects of pH within endosomal compartments as at pH >5 the absorbance and fluorescence of GFP are reduced (Kneen 1998). This had been attributed to the protonation of GFP.

At lower pH there are both conformational changes with GFP, which affect its absorbance and fluorescence. This may have also been due to the fact that although GFP (or portions of GFP) have translocated (given the cellular localisation) the molecule had unfolded, and re-folding was not facilitated. This conclusion, with regards to the previous findings of LFn-

RTAC cytotoxicity (Section 4.3) may indicate that although translocation is possible LFn-GFPs functionality after translocation may be an issue.

Initially there were problems with non-specific antibody binding in Vero cells. Consequently, studies with Vero cells were halted. Continuing studies with HeLa cells were used and demonstrated the same problems with GFP fluorescence. This was overcome in HeLa by using an anti-GFP antibody. HeLa displayed no issues with non-specific binding of antibodies.

These data, demonstrate that LFn-GFP was located in puncta around the cell cortex (at 5 minutes). As time, increased (15 mins) there was more GFP located in puncta around the cell cortex, and a more diffuse green haze within the cell. After a 30 min incubation with LFn-GFP green signal reduced both in punctate and as a haze within the cell which could indicate the release of LFn-GFP. It has been shown that the LFn at the final stages of translocation LFn diffuses in the cytosol (Zornetta *et al.*, 2010).

The reduction in LFn-GFP could be due to the protein diffusing into a greater cytosolic volume. Zornetta *et al.*, (2010) have demonstrated that after a 90 minutes incubation with LFn-GFP, the signal was reduced due to greater dispersion within the cytosol.

LFn-GFP has been shown to associate with EE structures after 10 minutes, however it was found that these were not positive for EEA1 or TfR, but were positive for early endosomal compartments that contain phosphatidylinositol 3-phosphate (PI3P) and Rab5, and it is thought that perhaps like other toxins (cholera toxin B chain) this early endosomal structure is distinct from the traditional EEA1- and TfR-positive endosomes but communicates with early endosomes, regulated by Rab5 (Zornetta *et al.*, 2010).

This is interesting as future co-localisation studies will require antibodies against PI3P to determine early endocytic structures as opposed to the use of EEA1. However, this set of experiments was completed in BHK (Baby Hamster Kidney) cells, and there may be

differences due to the type of cell and cellular function (Zheng *et al.*, 2014). This needs further investigation, as do the co-localisation studies to determine the endocytic trafficking and location of LFn-GFP, longer time points to determine the translocation events would also be appropriate. Zheng *et al.*, (2014) demonstrated that LFn-GFP was translocated into the cytosol after 30 minutes, with this continuing up to 120mins. They had noted however that this was much delayed compared to WT LF (which had dispersed into the cytosol after 20 min), indicating that the translocation of LF was slowed by the GFP at the C-terminal. The half-life of LF-GFP within the cytosol has been determined to be 3 hours, and so extending the experimental treatment time to this would give an overall picture of the endocytic trafficking and translocation (Zheng *et al.*, 2014). There was a decrease in GFP signal from 15 min to 30 min, which would indicate that the trafficking and translocation reached a peak at <30 min This could possibly due to cell types used and receptor expression effecting the trafficking and translocation. However, this initial work does demonstrate that LFn-GFP can translocate with the PA pore and be translocated in HeLa cells.

Subcellular fractionation demonstrated that LFn-GFP cellular uptake and cytosolic translocation wasn't dependent upon PA. a study by Khushner *et al.*, (2004) supports these finding. These studies were under taken in HeLa cells and signal was detected after an incubation period of 1hr, and was still detectable (yet a lower concentration) after 2 hours. Although the data presented here shows LFn-GFP cytosolic uptake at different time points a similar pattern is seen where by signal diminishes over time. It is interesting how LFn-GFP reaches the cytosolic compartment. Khusner *et al.*, (2003) found the LFn-GFP uptake in the absence of PA colocalised to the proteasome (hence reduced signal over time) and hypothesise that the presence of PA facilitates translocation out of the endosomal pathway which allows it to escape proteasome degradation.

However, LFn-GFP translocation in the presence of PA demonstrated a PA dependant translocation where by LFn-GFP levels increased over time in both the cytosolic and membrane fractions. This would indicate that there are more specific binding and translocation events. These PA specific translocation events occur despite the high thermostability of GFP and the literature base around this which suggests that PA cannot translocate large thermally stable proteins (Zornetta *et al.*, 2012 Verdurmen *et al.*, 2014). Excitation and emission spectra for LFn-GFP were recorded (appendices 9.3), at different temperatures. This was investigated to see what affect temperature has on the fluorescent spectra of GFP, and to infer at what temperature there was an effect on the structure of GFP and so the thermal energy required to destabilise GFP. As temperature increases the fluorescent spectra changes drastically, indicating that there is a high amount of thermal input to destabilise LFn-GFP and interrupt its fluorescence. However this work needs to be further investigated with a wider range of temperature treatment.

Previous work generated work within the lab (by Dr P. Dyer and Dr M. Pettit) has used HSDSC (Figure 5.51) to investigate the relationship of structure as a function of temperature and was found to have a T_m (thermal mid-point) 56.6°C and T_m at 84.7°C .

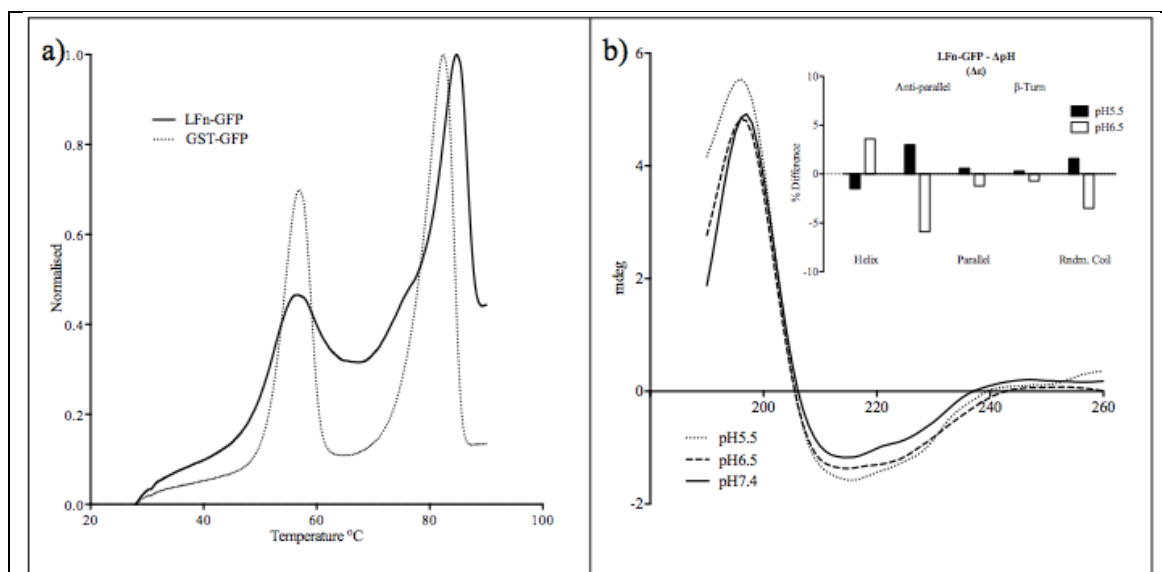


Figure 5.51 Structural analysis of LFn-GFP by HS-DSC and CD spectroscopy. HSDSC and CD plots generated by Dr.P.Dyer and Dr.M.Pettit. Normalised HS-DSC plots of LFn-GFP and GST-GFP demonstrated differential peaks associated with the unfolding kinetics. The GFP domain of LFn-GFP has a thermal midpoint of 84.7°C versus 82.4°C for the GFP domain in GST-GFP (GST-GFP data was performed by Dr M. Pettit and LFn-GFP by Dr P. Dyer). (b) CD Spectra of LFn-GFP as a function of pH (pH 5.5 - 7.4) demonstrating a degree of structural relaxation based upon molar ellipticity ($\Delta\epsilon$), generated in CDNN (Applied Photophysics, Surrey, UK) (inset).

Additionally the secondary structure of LFn-GFP was evaluated by circular dichroism. This was key to this understanding the energy required in order for GFP to transition into MG state and unfold.

The HSDSC data generated indicates that the T_m for GFP was 84.7°C (Figure 5.51 a). This was determined by comparing this HSDSC data output to that of GST-GFP where there were again two thermal midpoints. This energy input required for MG transition of the β -barrel was beyond physiological limits. Additionally, to this CD data indicated a minor state of relaxation at pH 5.5 and pH 6.5 when compared to pH 7.4 to identify if the change in pH induces MG transition in LFn-GFP as it has been shown to induce in LFn (Krantz *et al.*, 2004). The CD data suggested that the tertiary structure of GFP wasn't significantly altered at this endosomal pH where LF has been shown to undergo MG transition (Figure 5.51 b).

The fluorescence emission, HSDSC data and CD data sets suggest the energy input required for MG transition of the GFP β -barrel was beyond the physiological limits of the Brownian ratchet mechanism, and MG transition induced by endosomal pH. This could possibly suggest that MG transition and unfolding of tertiary and secondary structure of LFn-GFP are not happening. This could suggest that there are alternative mechanisms for the translocation of LFn carrying larger molecules during translocation. However, there could still be MG transition of LFn within this recombinant protein, initiating the translocation event.

A previous study showed that LFn-mCherry could not translocate (Zornetta *et al.*, 2010; Zheng *et al.*, 2014). This was suggested to be due to LFn-mCherry being more resistant to unfolding.

However, LFn-YFP has been shown to initiate translocation, but the YFP Section of the recombinant protein couldn't translocate through the pore and blocked the pore (Basilio *et al.*, 2011). This would suggest that the MG transition and initiation of translocation of LFn, isn't a large enough force to drive translocation of mCherry and YFP. This would indicate other factors are involved given that the 9 point mutation between EGFP and YFP are involved with accelerating the oxidation step in chromophore formation, and to remove proton and chloride sensitivity (Rekas *et al.*, 2002), as opposed to increasing protein stability.

Interestingly GFP, YFP and mCherry have similar structures (Figure 5.52 A, and B), and so the assumption that mCherry and YFP are more resistant to unfolding may not represent the entire story, also this the EGFP and mCherry display different surface charge (Figure 5.52 C) and this could have an impact upon translocation, although yet is untested. Possibly mCherry could become immobilised in the negatively charged PA pore due to electrostatic interactions being stronger than with GFP as opposed to the ability of the protein to unfold (Krantz *et al.*, 2008).

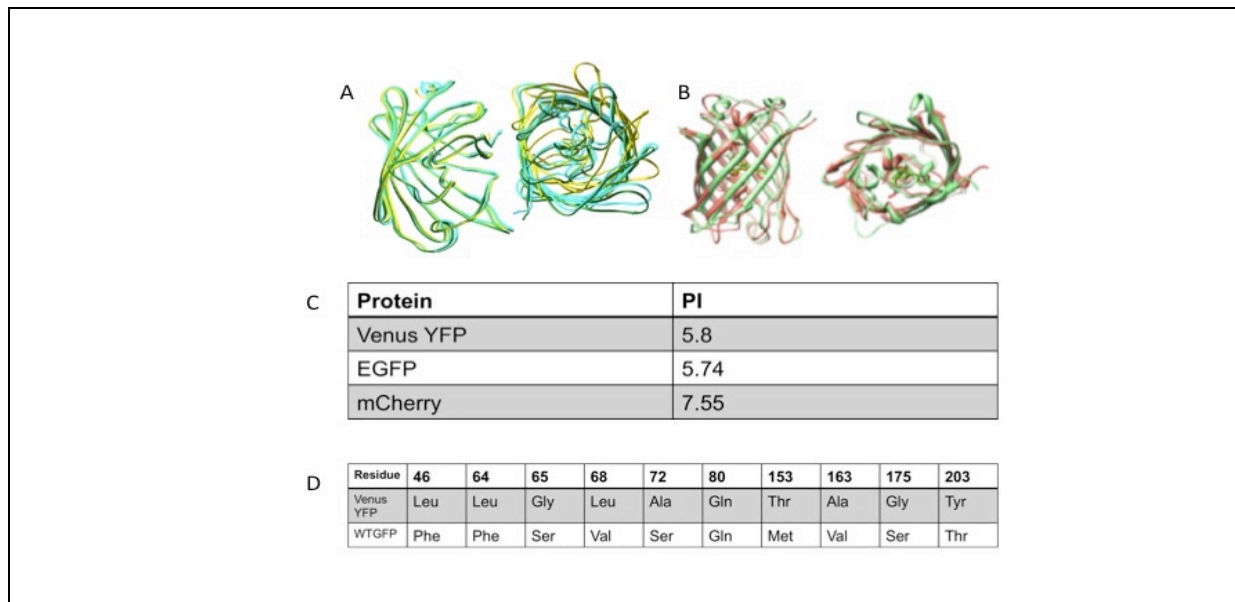


Figure 5.52 Comparison of fluorescent probe structure.

Showing (A) the crystal structure of Venus YFP (yellow), and GFP (Green) superimposed (Adapted from Rekas *et al.*, 2002). B shows the crystal structure of GFP (Green) and mCherry (Red) superimposed. The comparison of isoelectric points of Venus YFP, EGFP, and mCherry (C) the point mutations between Venus YFP and WTGFP (D).

YFP has a similar surface charge to GFP, so there is a question, what stops the translocation of this protein, as opposed to EGFP which can translocate especially as YFP demonstrated a variance of only 9 different residues (Rekas *et al.*, 2002). LFn-YFP has previously been tested in a cell free system using lipid bilayers, with the PA pore inserted into them, and translocation driven through increased voltage. This system has been demonstrated to translocate LFn (Zhang *et al.*, 2004; Krantz *et al.*, 2006).

There could be an answer in experimental design (non-cell system), and the translocation of LFn-YFP *in vitro* may yield some answers as the suitability of non-cell systems to investigate translocation of protein through the anthrax pore.

The PA pore is cation selective, this has been demonstrated by N-terminal fusions of polycationic stretches (Lys, Arg, His) which have been sufficient to facilitate translocation (Zhang *et al.*, 2004).

This could indicate that pI and pKa could also play a large factor in the translocation of these fluorescent molecules.

With regard to the published data describing the translocation of different types of cargo which seem to have varying success in delivery, it's important to consider that the experimental models change, the concentration of PA and LF fusion protein used changed, amount of material delivered into the cytosol varies based on the cell type (*i.e.* number of anthrax receptors expressed), and variation in incubation times (rate of endocytosis). This is particularly evident when looking to the translocation of LFn-GFP by Kushner *et al.*, 2003 who determined that this could translocate without needing PA. Where as Zornetta *et al.*, 2010 demonstrated a PA dependence. These conclusions although within the context of their experiments, are conflicting, and so these factors are important to consider. Western blot analysis and microscopy are also semi-quantative methods of analysis. The delivery of fluorescent proteins requires further investigation with respect to the cargo protein's melting temperature and the fate of the chromophore during translocation as well the translocation of these protein across different model systems.

5.6 Conclusions

Here it was demonstrated that LFn-GFP could undergo cellular uptake and be delivered into the cytosol in a PA dependent and independent manner (in HeLa cells). With differences in cytosolic and membrane amounts of these proteins in both pathways (PA dependent and independent).

Given the requirement (during epifluorescent microscopy) for indirect imaging (with the use of primary and secondary antibodies) this may indicate there is an issue with LFn-GFP translocation; it could potentially be that although translocated, LFn-GFP may not be re-folded correctly, or there is a cellular breakdown of GFP once translocated

This could also however be due to pH within these endocytic compartments reducing the GFP fluorescence (Campbell and Choy 2001).

If it were due to the translocation process this gives us insights into the PA translocase, which may unfold GFP, but lacks the ability of facilitate re-folding. However, these proteins require further investigation with respect to the cargo protein's melting temperature and structure, to determine if the forces generated by this translocase are sufficient to facilitate unfolding of these stable constructs.

Chapter 6 – Investigating the structural dynamics associated with cargo binding and translocation in real time.

6.1 Novelty Statement

Here we have demonstrated: 1) an ability to make and characterise lipid nanodiscs, 2) an ability to insert recombinant PA63 into these nanodiscs, 3) an ability to demonstrate an interaction between PA63 inserted into lipid nanodiscs and LFn-GFP and 4) an ability to follow structural changes in PA and LFn-GFP induced by a decrease in pH using neutron reflectometry.

This study has shown, for the first time, the use of PA inserted into a lipid nanodiscs to model cargo binding (LFn-GFP) and translocation as a function of pH.

Significance: A mechanistic understanding of both PA and its cargo during translocation is critical to our understanding of ATx biology, that may lead to the development of more effective treatments for *B. anthracis* exotoxins.

6.2 - Introduction

As previously discussed, antibiotic therapy has not been 100% effective against people exposed to *B. anthracis*, due in part to the secretion of an exotoxin (see Section 1.1).

Consequently, to generate more effective therapies, a means to inhibit the action of the toxin would be of great value (Nestorovich and Bezrukov 2014).

Understanding the molecular dynamics that drives toxin activity (specifically the action of the PA translocase) will enable the development of new therapeutic targets that prevent the associated immune modulation of anthrax intoxication (Section 1.3).

Many native proteins function within complex dynamic environments (Seddon 2004, Cross *et al.*, 2010). Many biophysical techniques (*e.g.*, NMR, X-ray crystallography, circular dichroism) employed to investigate protein structure and function are only amenable to

simple environments restricting their application and their associated analytical inferences. The development of ‘native’ like membranes, mimicking the properties of biological membranes allows for their investigation in a detergent free, but stabilised environment *in vitro* (Carpenter *et al.*, 2008).

In order to gain insight into this translocation process, it has been necessary to investigate the molecular structure of the PA pore, and bound cargo, during these translocation events. A major challenge to the investigation of membrane spanning pores and protein complexes has been the isolation of functionally active, water soluble, monodispersed forms, allowing for the mechanistic studies to progress in biologically relevant environments (Seddon *et al.*, 2004). The investigation of protein complexes has been typically hindered by two main issues; the isolation of functional proteins within their native environment and their poor solubility. Indeed, some membrane proteins cannot be readily obtained from their native environments (due to low concentrations on cellular surfaces), so high yields of functional and stable proteins are hard to obtain (Drew *et al.*, 2005). PA specifically is rapidly insoluble under acidic conditions and forms amorphous aggregates (Katayama *et al.*, 2008, Vernier *et al.*, 2009).

The majority of previous investigations into PA pore translocation have utilised electrophysiological techniques and planar bilayer systems (Table 5.1). Whilst planar bilayer systems have been shown to be valuable in investigating PA pore translocation (Basilio *et al.*, 2010), these systems do not fully replicate the native environment, where these membranes lack the PA receptor and any other functionally relevant proteins (Kintzer *et al.*, 2015). In an attempt to address this problem liposomal preparations have been used to characterise membrane proteins, however liposomes are large, unstable and difficult to prepare with precisely controlled size, and stoichiometry. Liposomes containing the PA pore in the

membrane have previously been documented (Sun *et al.*, 2008). However, there were issues with concentration of membrane inserted PA pores and the relative instability of liposomal preparations (Katayama *et al.*, 2009).

Finally, often membrane integrating proteins exhibit poor solubility in aqueous solutions, requiring stabilisation with hydrophobic materials, *i.e.*, phospholipids or detergents. The use of detergents to stabilise proteins of this nature has been shown to cause structural alterations affecting the downstream functionality (Ren *et al.*, 2004). To this end, a strategy for PA pore insertion into lipid nanodisc was developed in an attempt to model cargo binding (LFn-GFP) and translocation as a function of pH.

6.21 Nanodisc Technology

Despite problems associated with membrane protein isolation, they remain an important area of study due to their fundamental role in biochemical processes and their importance as pharmaceutical targets. Model membrane systems are essential to understanding protein complexes in intricate biological membranes.

A key development in this area has been the use of self-assembled lipid-nanodiscs incorporating integral membrane proteins for structural investigations. These are phospholipid bilayers, stabilised in solution by an encircling amphipathic helical protein belt, termed a membrane scaffold protein (MSP) (Sligar 2016). Several membrane proteins have been isolated and investigated using the nanodisc platform (Table 6.23).

This technology appears to be an appealing model system for the solubilisation, isolation and biophysical studies of membrane proteins. They form as highly stable, soluble membrane mimetics, whereby lipid composition can be controlled, and enriched using affinity tags (*e.g.*, 6xHis) to the nanodiscs (Bayburt and Sligar 2010). This system offers advantages over other

methods (liposomes, or detergent micelles) in terms of size and stability (Borch and Hammann 2009). The membrane composition can be chosen with different mixtures of phospholipids and cholesterol.

In this system, the membrane protein target is transiently solubilised with a detergent, in the presence of phospholipids and MSP. Removal of the detergent results in the spontaneous assembly of the lipid-nanodisc containing the integral membrane protein (Chuler *et al.*, 2013).

Protein of interest	Reference
G-protein coupled receptors	Leitz <i>et al.</i> , 2006, Whorton <i>et al.</i> , 2008
Sec translocon	Alami <i>et al</i> 2007, Taufik <i>et al</i> 2007
TAR receptor	Boldog <i>et al.</i> , 2008
Cytochrome P450	Denisov <i>et al</i> 2006, Luthra <i>et al.</i> , 2013
Cholera toxin	Tark <i>et al.</i> , 2010
Protective antigen	Katayama <i>et al</i> 2010, Akkledevi <i>et al.</i> ,2013
Table 6.21 - Examples of integral membrane protein successfully self-assembled into nanodiscs (SEC – bacterial secretory protein, TAR – Aspartate Receptor).	

6.22 Protective Antigen characterisation

The PA pre-pore structure has been resolved using X-ray crystallographic techniques to a resolution of 2.1Å (Petosa *et al.*, 1997). Information relating to the structure of the PA pore is still being resolved, (Jiang *et al.*, 2015). However, mapping the beta-barrel of the PA pore has been dependent upon using low resolution single particle reconstruction electron microscopy (EM) techniques (Jiang *et al.*, 2015) and of membrane inserted forms of PA in lipid nanodiscs (Katayama *et al.*, 2010, Akkledevi *et al.*, 2013).

Typically, PA has had problems with aggregation causing inherent difficulties in crystallising a functional pore. This has hindered investigation of its structure in a near native dynamic setting; looking at changes of the PA translocon, and the translocating cargo during this

process (Gogol *et al.*, 2013, Katayama *et al.*, 2010).

It was demonstrated by Katayama *et al.*, 2008 that PA could be inserted into nanodiscs overcoming aggregation issues by using a molecular scaffold; the chaperonin GroEL. This showed that the PA pore formed stable complexes with GroEL and resolved the structure of a functional PA pore at ~23–25 Å resolution by using negative-stain EM. In addition to this the predominant 1 : 1 stoichiometry (1PA pore:1 nanodisc) simplified their reconstruction and analysis of the pore, allowing for visualisation of structural diversity, with particular attention to the internal lumen of the PA pore (Katayama *et al.*, 2010). However, there was a significant proportion of both the GroEL bound and free PA pores, that formed distorted structures of the PA pore when bound to GroEL. Moreover, Akkledevi *et al.*, (2013) devised a method for self-assembly of nanodiscs, around a PA pore with relatively high yield. Where a single cys on the LFn was transiently linked to an agarose surface via a disulfide bridge. Allowing the PA pre-pore to bind to the immobilised LFn. A lipid nanodisc was allowed to form following exposure of the hydrophobic barrel of the PA pore. This procedure of PA pore insertion into nanodiscs was optimised yielding an insertion rate of ~43% (Akkladevi *et al.*, 2013).

6.23 Neutrons to investigate functional proteins

To look at these biological interactions neutron reflectometry has provided information on assembly, surface association and material penetration (Table 6.241). Allowing the study of complex biological samples in an aqueous environment, detailing structural changes of membranes and proteins at the Angstrom scale (Krueger *et al.*, 2001). The intensity of this beam is affected by the thickness, scattering length density and interface roughness of the sample layers.

Neutron methodologies can achieve high resolution in complex systems allowing detailed structure to be resolved, which are unapproachable by other techniques due to the complexity

of the biological systems (Lakey 2009). The differential sensitivity of neutrons with the use of hydrogen (H) and its isotope deuterium (D), can be exploited for isotopic contrast within biological systems (Clifton *et al.*, 2013). It is important to note that the stability and functional dynamics of proteins within a D₂O solvent can change from its native condition regardless of the good signal-to-background ratio (Tehei *et al.*, 2001).

The limitations associated with this method, include the requirement for large quantities of proteins, which are often hydrophobic and the expense associated with the deuteration of proteins and lipids (Gabel *et al.*, 2002). Studies of membrane proteins isolated into nanodiscs have previously been studied using small angle neutron reflectometry and small angle neutron scattering (Kynde *et al.*, 2014) (Table 6.241).

The combination of these two methodologies could be a powerful tool in the characterisation and analysis of the PA pore, and cargo translocation events.

Where neutron contrast variation allows for the specific identification of proteins or lipid matrices, which can be discriminated from host substrates, and the pore isolation into nanodisc allows for PA pore enrichment, and stabilisation (Katayama *et al.*, 2010). This can help enlighten the structure and function involved in the isolated active biological agent. Allowing the study of the translocation mechanism, and any changes that are occurring during this time to the PA pore, and to the cargo. In order to understand the translocation process of PA, and its bound cargo proteins, being able to differentiate each part of this complex system are essential.

Membrane Protein	Method of study	Reference
Monomeric bacteriorhodopsin	SANS	Kynde <i>et al.</i> , 2014
Cytochrome P450 oxidoreductase	NR	Bertram <i>et al.</i> 2015
Colicin-receptor complex	SANS, NR	Clifton <i>et al.</i> , 2012
Translocation and assembly module (TAM)	NR	Shen <i>et al.</i> , 2014
Melittin	NR	Kruger <i>et al.</i> , 2001
Prion protein	NR	Le Brun <i>et al.</i> , 2014
Secretory component	SANS	Bonner <i>et al.</i> , 2007
Neurologin	SANS	Comoletti <i>et al.</i> , 2007
Table 6.241 Examples of membrane proteins studies using neutrons.		

The overarching aim of this chapter was to to investigate the binding and translocation of cargo as a function of pH through the PA pore, stabilised in lipid-nanodiscs.

- 1) To develop and characterise recombinant LFn-Cys, MSP1D1, and the deuterated production of PA, LFn-GFP, LFn-Cys and MSP1D1.
- 2) To develop and characterise the complex of PA pore containing lipid-nanodiscs.
- 3) The use neutron reflectometry to investigate protein translocation through the PA pore.

6.3 Chapter Specific Methods

6.31 Materials

MSP1D1(M6574-5MG) was purchased from Sigma-Aldrich (Dorset UK). The bacterial expression plasmid pMSP1D1 was a gift from Stephen Sligar (Addgene plasmid # 20061) DMPC (860345C) was purchased from Avanti Lipids (Suffolk,UK). Cell Mask (C10046) was purchased from Thermo Fisher Scientific (Paisley, UK).

6.32 Methods

6.321 Preparation of Nanodisc (no protein inserted)

The preparation of nanodiscs as adapted from the previously published protocol (Akkledevi *et al.*, 2013). Sepcifically, hydrogenated POPC (hPOPC) or DMPC (hDMPC) was made to a final concentration of 162 μ M. The chloroform was evaporated for 1 hour and the resultant precipitate suspended in a 2.5 mL of 25 mM sodium cholate. 2.5 μ M of the His-tagged MSP1D1 was added to the mixture (final volume 4mL). Following incubation at room temperature for one hour, Sodium cholate was removed by dialysis, at a ratio of 1:1000 PBS for 2 hours at 4°C and repeated a further three times. The dialysed sample was stored at -20°C until required.

6.322 Preparation of Nanocomplex (containing PA and LFn-Cys).

6.3221 LFn-Cys on beads

Activated Thiol–Sepharose[®] 4B (Sigma-aldrich) beads (2.5g) was re-suspended in deionised water and washed in 20 mL of water. To this 10mL of 40 μ M LFn-Cys was added. The resultant suspension was incubated for 2 hours at 4°C and the supernatant collected for analysis. Sedimented beads (coated with LFn-Cys), were suspended in 3mL of 20 mM Tris-HCl buffer (pH 7.4) and stored 4°C until the pre-pore had been prepared.

6.3222 Preparation of Nanodisc mixture

POPC or DMPC either hydrogenated or deuterated was prepared as previously described in Section 6.321 without dialysis.

6.3223 Preparation of the pre-pore

Purified PA (83KDa) protein was treated with a final concentration of 500ng/mL of trypsin (50ug/mL) for 20mins, the reaction was stopped with protease inhibitor (1μL). To this 1mL of 2M urea was added to 1mL of bead slurry (previously made in Section 6.3221) and combined with the pre-pore preparation. This mixture was then incubated at 37°C for 5 minutes.

6.3224 Nanocomplex formation

LFn-Cys bound PA-pore slurry was combined with the initial MSP1D1, POPC, and sodium cholate mixture (see chapter 6.3222) and dialysed in 3L of 50 mM NaCl, 50 mM Tris-HCl, pH 7.5, for 3 hours, and repeated for a further three times. Collected beads were sedimented by centrifugal force, the supernatant collected for analysis. Sedimented beads were washed 25 times in 50 mM NaCl, 50mM Tris-HCl, pH 7.5 buffer to remove any empty self-assembled nanodiscs. The nanocomplex (containing LFn-PA-Nanodisc) was uncoupled from the bead matrix by adding DTT to a final concentration of 100mM. This mixture was incubated at room temperature on an orbital shaker for 30 min. The bead slurry was subjected to sedimentation by centrifugation separating the beads from the nanocomplex. The resultant supernatant was collected and stored at -20°C for analysis.

6.33 Transmission electron microscopy

To carbon-coated Cu 300 mesh grids 50ul of either the ND or NC (Section 6.3224) was applied and stained with 1% (W/V) methylamine tungstate and images captured at 60,000x magnification using the JEOL 1200EXII TEM.

6.34 Analysis of nanodiscs and nanocomplexes by Flow Cytometry

ND and NC were prepared as previously described (Section 6.3222 and 6.3224 respectively) and a PBS control. To these preparations 10 μ L of CellMask[®], 1 μ L of anti-PA antibodies was added and incubated for 30 mins. Subsequently, 1 μ L of anti-rabbit secondary antibody conjugated to Alexa Fluor-488 was added and incubated for a further 30mins. Buffer controls were set up to assess for non-specific interaction of cell mask, primary (anti-PA) and secondary antibodies (Alexa Fluor 488). Samples were analysed using a Accuri C6 sampler, and data was assembled on FlowJo (an analysis platform for single-cell flow and mass cytometry analysis).

6.35 Determination of translocation events using Neutron Reflectometry

Neutron reflectometry was undertaken at the Insitute Laue Langevin (ILL, Grenoble), on the Fluid Interfaces Grazing Angles Reflectometer (FIGARO).

This is a time of flight reflectometer and is used for studies at liquid and solid / liquid interfaces in soft matter and biology. Hydrogenated nanodiscs and nanocomplexes were prepared according to the stated protocol (chapter 6.3222 and 6.3224). NC and ND made from 1,2-dimyristoyl-*sn*-glycero-3-phosphocholine (DMPC) and MSP1D1 was dialysed in the presence of a reducing agent, in TrisHCl, 50mM β -mercaptoethanol (BME).

Neutrons of wavelengths ranging between 2 Å and 30 Å and at two incident angles, namely 0.8° and 3.2°, were used giving a Q-range from $\sim 0.002 \text{ \AA}^{-1}$ to $\sim 0.32 \text{ \AA}^{-1}$. Prior to ND adsorption, baseline measurements were performed in PBS dissolved in D₂O, H₂O, and for silica matched water (SiMW, a mixture of 38% v/v D₂O and 62% H₂O). Characterisation of the ND and NC adsorption at the solid-liquid interface was performed at pH 7.4. Binding and interaction of deuterated LFn-GFP with the both ND and NC were followed in real time at pH 7.4 and 37°C mimicking physiological conditions and at pH 5.5 mimicking the acidity of late endosomes. Measurements were performed in a variety of solvents, namely PBS in

H₂O, D₂O, SiMW and buffer matched for an SLD of 4.0 MW (a mixture of 64% D₂O and 36% H₂O). Data was reduced, reflectivity calculations partitioning the interfaces based on Scattering Length Density, thickness, roughness and hydration was fitted using RasCal 2014b (A. V. Hughes, ISIS, Rutherford Appleton Laboratory) exported and plotted in Prism 6.0 (GraphPad, US).

6.3 Results

6.31 Developing and characterising protein constructs

The generation of self-assembled PA lipid-nanodiscs was accomplished by immobilising LFn-Cys to thiol sepharose beads, a PA pore was formed around LFn-Cys, and lipid-nanodisc self-assembled around this complex. The enrichment occurs due to the PA pore bound to the thiol beads. In order to accomplish this several proteins were produced; PA, LFn-Cys, MSP1D1 and LFn-GFP. Both hydrogenated (see chapter 3.2) and deuterated forms of the proteins were made and characterised.

Protective antigen and LFn-GFP have been previously characterised in chapters 3 (Section 3.3) and Chapter 4 (Section 4.3) respectively. The culture and production in H₂O 2xYT was characterised and protein yield and purity analysed.

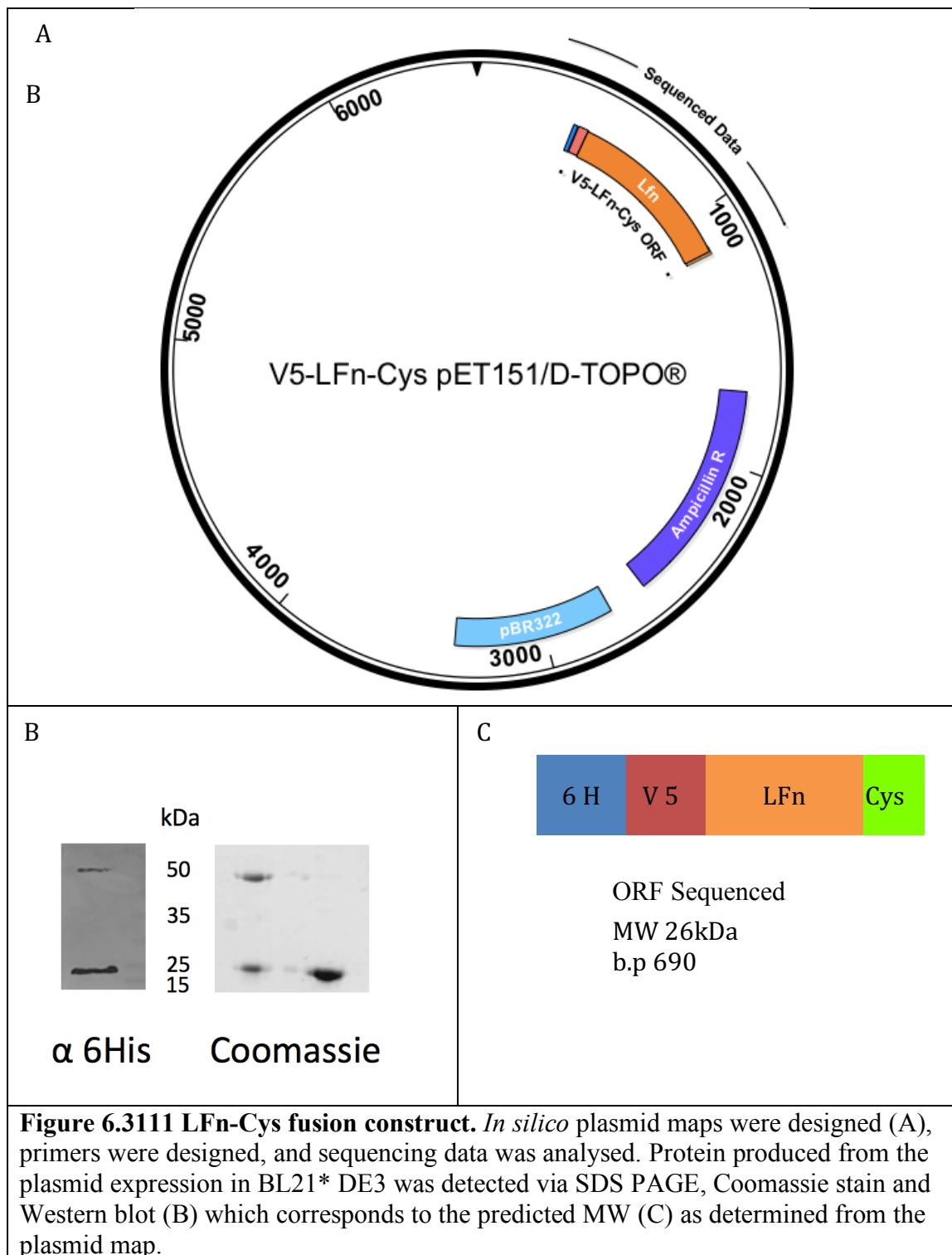
6.311 Production and characterisation of LFn-Cys protein

LFn with a C terminal cysteine (reactive thiol group) was sub-cloned into a pET151 D/TOPO vector. Oligonucleotides were designed to add a cysteine to the C-terminus of the LFn DNA sequence. This was amplified by PCR from the vector containing the LFn sequence.

Subsequent cloning of this into pET151/D-TOPO vector resulted in several positive clones, as determined by PCR (Figure 6.3112 A). Two clones were then further analysed based on positive Western blot (Figure 6.3112 B) using a “mini-induction” protocol described in (Section 2.231) and sequenced. The analysis of the sequence data showed correct sequence alignment to the design. The LFn-Cys DNA sequence was within the correct ORF with an N-terminal 6xHis and V5 epitope tag. Clone 1 was selected for continued use, protein production and characterisation.

LFn-Cys produced in One Shot[®] *E.coli* BL21*DE3 bacteria (Invitrogen, Paisley, UK) was detectable by both Coomassie stain and Western blot using an anti-6xHis monoclonal antibody at the predicted molecular weight of 26kDa (Figure 6.3111 C), as expected from the design (Figure 6.3111 D) and as previously detected by the mini-induction (Figure 6.3111 B).

LFn-Cys protein was run on an SDS PAGE, and subjected to Coomassie stain in both the presence (reduced state) and absence (non-reduced state) of BME (2-mercaptoethanol, a reducing agent) in the Laemmli sample buffer, to observe the effects that the thiol group (within the cysteine) has on the dimerisation of the protein. This showed 48% of LFn-Cys with an apparent molecular weight of ~50kDa and the remaining 52% at the predicted molecular weight of 26kDa, indicating dimerization of the protein driven by disulphide bonds between two reactive cysteine groups. The purity of LFn-Cys was >95%, as determined by densitometry after Coomassie stain (Figure 6.3113), yielding approximately 5 mg/L of bacterial culture.



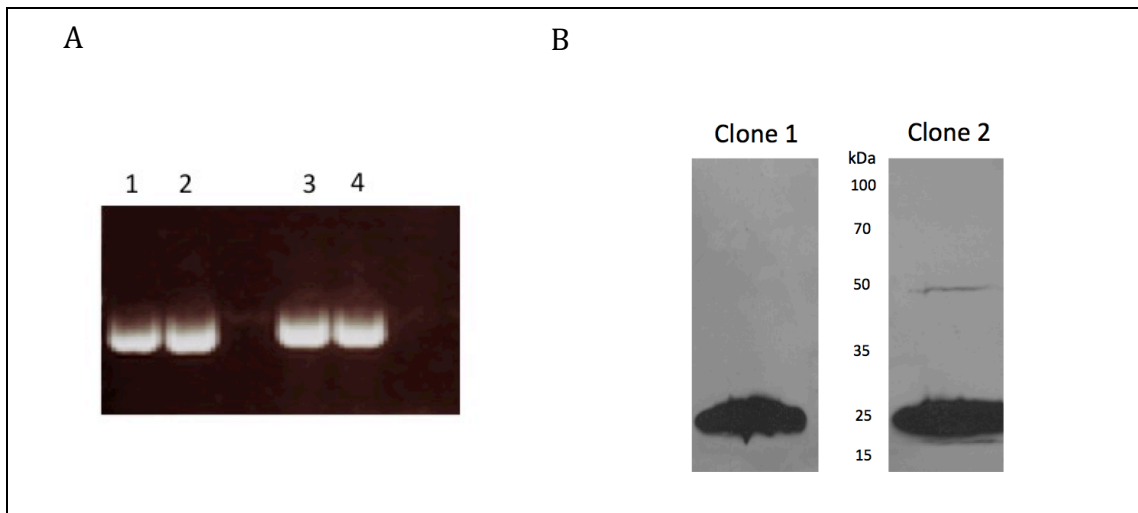


Figure 6.3112 Characterisation of LFn-Cys. Showing (A) Gel electrophoresis of clones analysed by PCR for LFn-Cys. (B) Western blot detection of clones 1 and 2, post “mini-induction” for LFn-Cys using an anti 6xHis antibody.

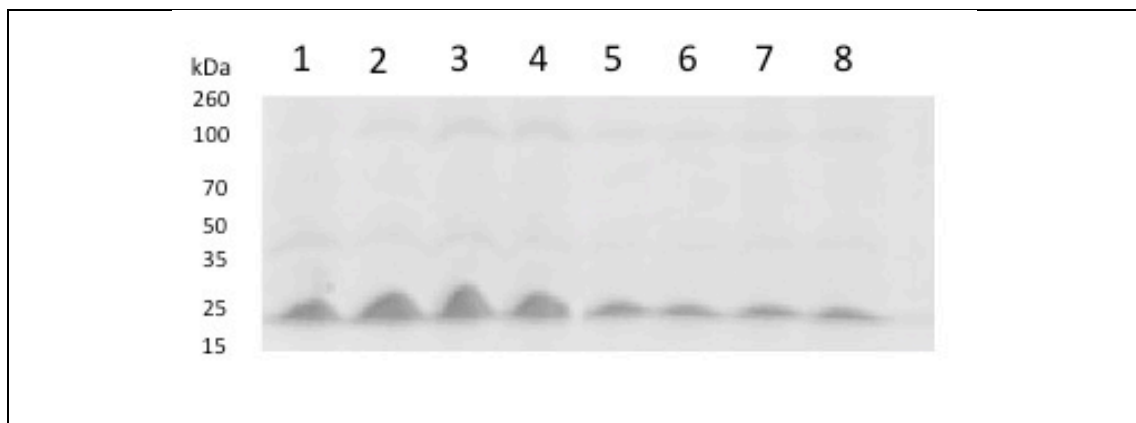
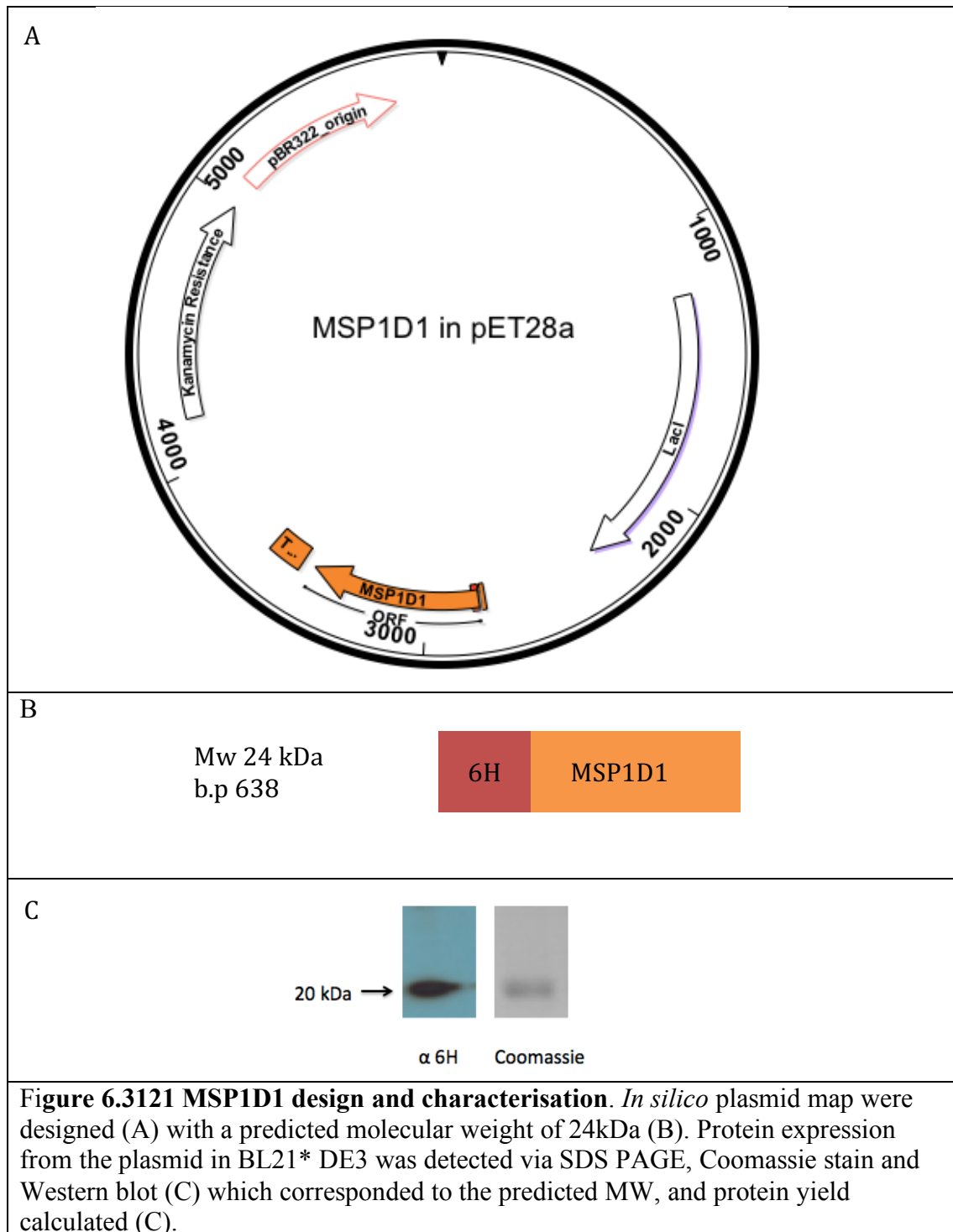
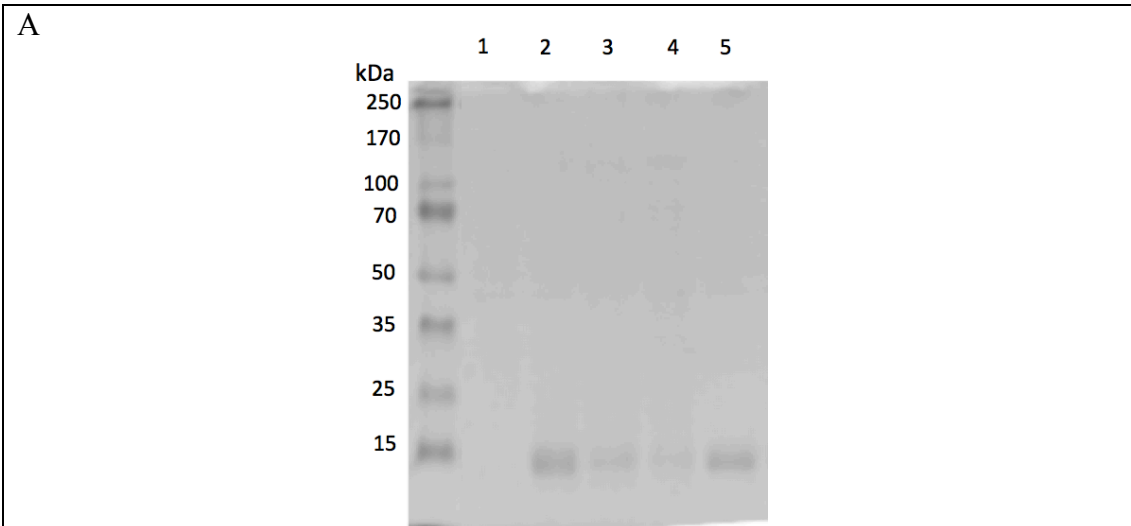


Figure 6.3113 Protein elution from TALON[®] resin and determination of concentration and purity of pooled fractions by SDS-PAGE and Coomassie staining. LFn-Cys protein yield and purity were determined via SDS PAGE, and Coomassie stain. Showing fractions 1-8 (1mL eluted fractions) for LFn-Cys.

6.312 Membrane scaffold protein production and characterisation

A bacterial expression plasmid encoding for the protein MSP1D1 was purchased from Addgene (Plasmid Number 20061), the plasmid map was generated to identify the ORF (Figure 6.3121 A) for MSP1D1 with an N-terminal 6xhis epitope tag (Figure 6.3121 B) (Denisov *et al.*, 2004). The predicted molecular weight of this protein was calculated *in silico* to be 24kDa. Protein yield and purity was determined (Figure 6.3121C and Figure 6.3122) after expression in One Shot ® *E.coli* BL21*DE3 bacteria (Invitrogen, Paisley, UK). This was detectable by both Coomassie stain and Western blot using an anti-6xHis monoclonal antibody at the predicted molecular weight of ~24 kDa (6.3121 A).





B

Plasmid	Construct	Yield	Purity
MSP1D1	6H MSP1D1	5-6mg/l	>85%

Figure 6.3122 Protein elution from TALON[®] resin by SDS-PAGE and Coomassie staining. MSP1D1 protein yield and purity were determined via SDS PAGE, and Coomassie stain. Showing pooled fractions 1-5 (1mL eluted fractions) for MSP1D1.

6.32 Development and characterisation of PA inserted into lipid nanodisc

PA inserted into self-assembled lipid-nanodiscs (termed nanocomplex within this study (NC)) and 'empty' lipid-nanodiscs which contain no protein (ND) were made and evaluated initially for the presence of 6xHis and PA (Figure 6.321 A and B respectively). These lipid-nanodiscs were made with MSP1D1 purchased from Sigma-Aldrich. Signal for 6xHis was not detected for self-assembled empty NDs (Figure 6.321 A-1), it however was detected for nanocomplex preparations in the bead slurry (A-2) after dialysis and sedimentation (A-3), following the wash step (A-4) and elution from the bead (A-5). Two molecular weights were detected (Figure 6.321 A) at an apparent molecular weight of ~60 kDa and ~240 kDa for samples A-2, A-3 and A-4. This indicated the presence of a high molecular weight complex, with the 6xHis affinity tag (~240 kDa). In A-3 the high molecular weight complex self-assembled nanodiscs, which have formed after dialysis, have not bound LFn-Cys-PA pore. In A-4, first wash step, similarly a high molecular weight would be suggestive of self-assembled ND. It is unlikely that high MW signal was due to PA, as during the trypsinisation process the 20kDa fraction of PA (which contains the 6xHis epitope tag) was cleaved and removed from the system. Also, to this (Figure 6.321 B) there was no detectable PA signal in all preparations, using a polyclonal antibody directed against both subunits of PA (Chapter 3, Section 3.3, Figure 3.311 C).

In sample A-5, eluted NC, there was no detectable signal for both 6xHis and PA. This would indicate that there were no NC formed, no NC were eluted, or the concentration of the protein was too low to be detected and this sample would need to be further concentrated. Given that there was no detectable PA in any samples this may have been a cause for concern. However, row 6, shows some detectable signal for 6xHis at ~60kDa, this sample was 10 μ L of the bead slurry after elution (50mM DTT) treatment of the beads indicating incomplete de-coupling of

the complex from the beads. Though there was no signal for the higher MW product seen previously.

One point of concern was the lack of any signal for the ND and the NC samples for both 6xHis and PA. To this end, the experiment was repeated, and the volume of eluted ND and NC was increased from 10 μ L to 20 μ L and the detection of the V5 epitope was evaluated for LFn-Cys signal still coupled to the beads post elution in 50mM DTT (Figure 6.322). Four samples were run on an SDS PAGE, transferred onto a nitrocellulose membrane and analysed for the presence of PA, V5 and 6H. The four samples were the last wash (1), beads after elution (2), eluted NC (3) and ND (4). In sample 1 (the last wash of the beads) there was no detectable signal in any of the samples. This would suggest that the wash steps are sufficient. Sample 2 (beads after elution), demonstrated detection in all three antibodies; there was detectable signal of PA at ~60kDa.

There was also signal of the V5 epitope tag, which was only present on the LFn-Cys. This would suggest that the de-coupling of the LFn-Cys from the beads was insufficient, and at least some of the complex was still attached to the bead matrix. Detection of 6xHis was observed, but given the previous result of V5 detection this isn't surprising, and supports the notion that there were still NCs bound to the bead matrix, which contain PA. Unfortunately, there was no PA, or V5 signal for the NC, there was however signal for 6xHis indicating eluted NC at sufficient concentrations for MSP1D1 to be detected. This was unlikely to be contamination of free ND (without PA-LFn-Cys) due to the lack of signal of the last wash samples, which presumably would have also contained free ND. Additionally, 6xHis signal was detected for the ND sample. This can only confirm the presence of MSP1D1 however in a detectable concentration, and not ND formation.

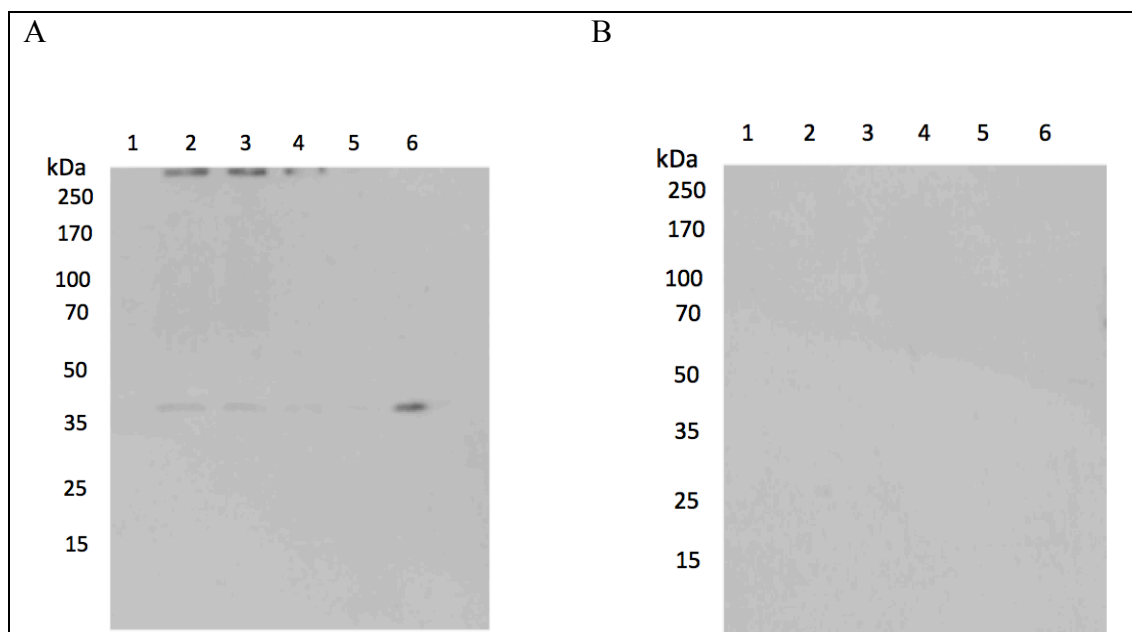


Figure 6.321 Initial characterisation of ND and NC self assembly. This was characterized by SDS PAGE and western blot against 6xHis (A) and PA (B). with 6 different sample, ND (1) Bead slurry after dialysis and centrifugation containing NC (2), Supernatant of centrifuged bead slurry (3), Wash step (4), elution of NC (50mM DTT) (5) and beads after elution (6).

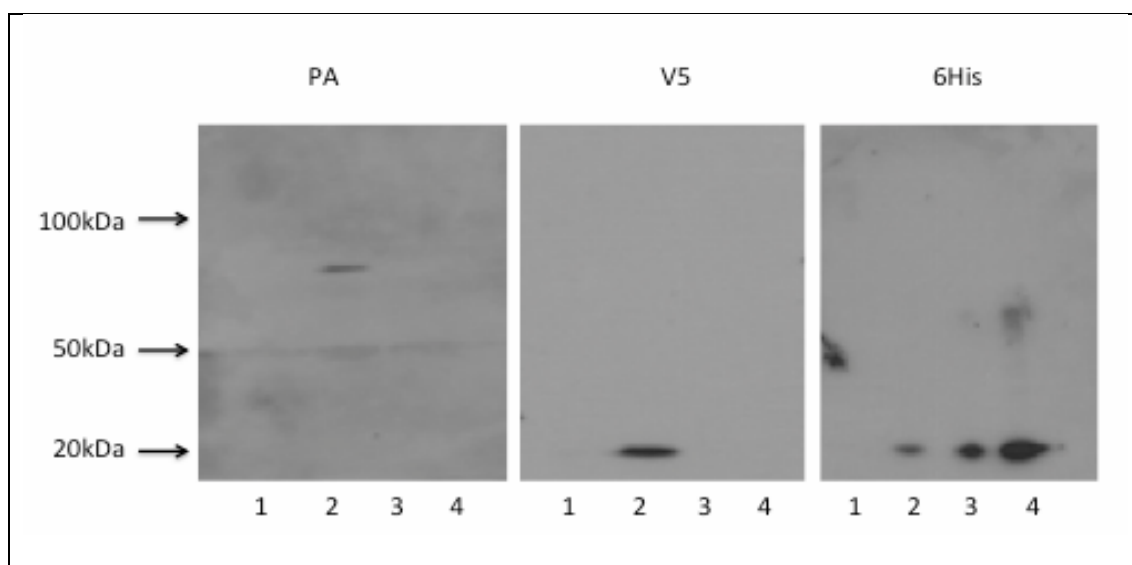
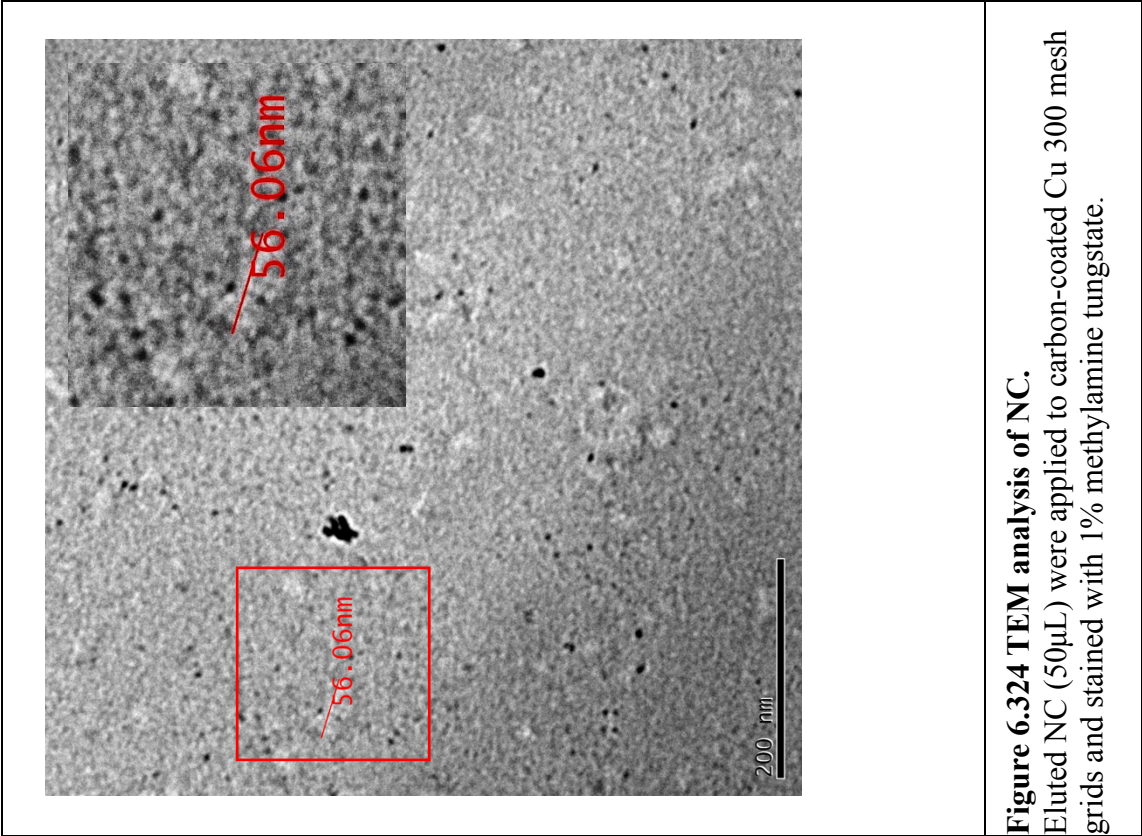
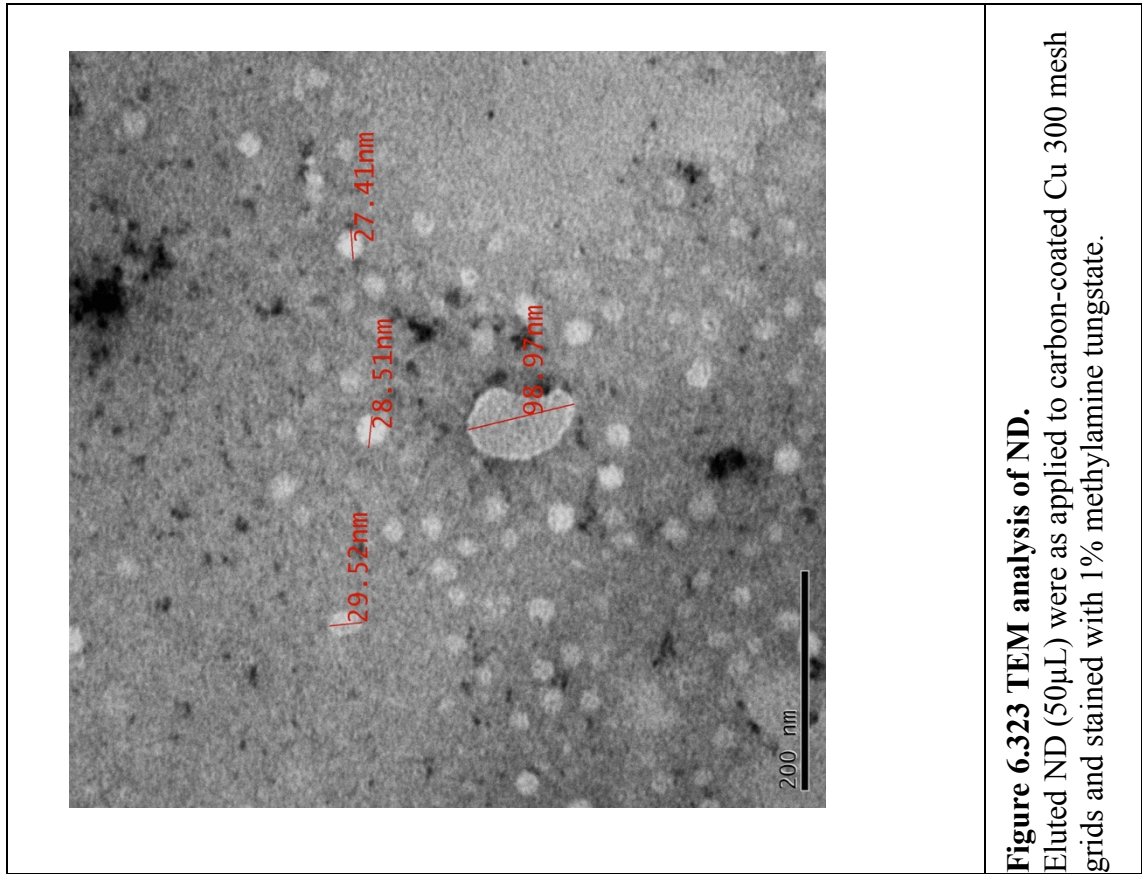


Figure 6.322 Characterisation of ND and NC self assembly. This was characterised by SDS PAGE and western blot against PA, V5 and 6xHis. With 4 different samples, the last wash of the beads (1) beads after elution (2), elution of NC (50mM DTT) (3) and ND (4).

6.321 Characterisation of lipid-nanodiscs and nanocomplexes by TEM

To confirm the self-assembly of both ND, and NC TEM analysis was performed, by negative staining with methylamine tungstate (Chapter 6.326). Figure 6.323 shows lighter grey circular structures, ranging in diameter; 99% between 20-30nm, and 1% ranging from 95-100nm (n=200). There was a high density of these structures, similar to previously published images of similar nanodisc preparations (v.m Hernández-Rocamora *et al.*, 2012). Thus confirming the generation, with corresponding western blot data, the self-assembly of NDs. The evaluation of the NC under the same conditions (Figure 6.324), demonstrated reduced concentration of NC compared to NDs with the presence of amorphous structures in the preparation. In addition, the analysis was performed at the limits of resolution of the available TEM. However, some structures (measured in red) were identified to have similar morphological characteristics to previously published cryo-EM data of PA in nanodisc (Katayama *et al.*, 2010, Akkledevi *et al.*, 2013). This combined with the previous data set would suggest that NC concentration was an issue, but there were NC structures present. As such an alternative method of analysis was explored.



6.322 ND characterisation by Flow Cytometry

To investigate this further, flow cytometry was used to evaluate the presence of the PA in the NC population by fluorescence looking at side scatter (SS). Although both forward scatter (FS) and side scatter (SS) can be measured, one of the issues associated with the measurement of nanoparticles is their relative size, ND/NC being too small to differentiate between NC and ND. For these experiments, the presence of fluorescence using a lipid marker CellMask® (FL3, red channel) and anti-PA primary and anti-rabbit A-488 (FL1, green) would indicate the presence of lipid nanodisc and PA respectively. Several samples were analysed which composed of primarily either buffer, ND or NC in presence of CellMask®, primary antibody (anti-PA) and secondary antibody (anti-rabbit A488) or as individually stained preparations. Figure 6.325 A and B shows buffer samples analysed for both forward scatter and side scatter, as well as fluorescence. Figure 6.325 B shows the forward and side scatter for buffers with various treatments of antibody and cell mask. This data showed fluorescent particulates in the buffer preparations. This was suggestive of aggregates of antibodies or fluorescent dye particulates. The relative low count rate of this particulates was of particular interest when compared to the particulate count of the nanoparticles. Figure 6.325 A shows the green fluorescence (FL1-A) and red fluorescence (FL3-A) for buffer samples (PBS) with a combination of primary antibody, secondary antibody and cell mask. There was a notable shift in population signal between buffer with primary antibody and buffer with primary and secondary antibodies. Although the buffer with secondary antibody had a low count rate, when also in the presence of primary antibody there was an increased count rate and a shift toward the right, indicating there was green fluorescence. This was most probably due to aggregates of primary and secondary antibodies as indicated by the increase in particle count and the presence of green fluorescence.

As fluorescent populations within these buffers (when an antibody was present) were detected, it was critical to evaluate these controls when looking at NC and ND when labelled with antibodies. Figure 6.329 shows ND and NC samples under FS and SS where the populations have been selected. It can be seen here that there seems to be greater diversity populations in terms of size (FS) and fluorescence (SS). One of the issues here could be associated with preparation of the samples, whilst NC are bound to beads, washed several times, and then eluted, ND undergo far less sample 'clean up' and population selection. These gated samples were then compared for FS and SS (Figure 6.326 A and B), which overlapped consistently (Figure 6.327 B), demonstrating that there are no discernable size difference within the detection limits of the flow cytometer ($>800\text{nm}$) between ND and NC, and populations selected were indistinct within the limits of detection. These populations were then compared for fluorescence (Figure 6.327 A). Although there was some sample cross over (where red overlays blue), a shift of the NC sample (blue) towards the right was observed when compared to the ND sample (red). Thus, indicating that there was a population within the gated group with more significant signal in the FL1 (green) channel, indicative of the presence of PA associated with the NC, than there was within the ND population.

Next the samples were assessed to see how cell mask was affecting these results. The data was compiled (Figure 6.327) to look at ND and NC in the presence and absence of cell mask. As this may stain all lipid content, this may affect the diverse populations (specifically within the ND population) accounting for why there was a less visible differentiation between the two groups. Figure 6.327 A shows ND, NC and buffer samples all treated with primary antibody, secondary antibody and cell mask. As can be seen there was small shift in population to the right for the NC samples (red) and a shift to the left of the ND sample

(blue). However much of the sample was still consistently overlaying, not surprising as both samples contained lipid. When the same data was analysed without the cell mask (Figure 6.327 B), this shift in population can be more evidently seen. There was a shift in the population where by the NC (red) was more towards the right meaning there was most likely PA within this sample. There was also a far higher count rate of samples within a much more well-defined area, meaning that the NC are far less diverse in size and complexity than the ND. Again, this was most likely due to the preparation of the sample, where in the NC any free proteins and lipid are removed prior to sample elution, whereas for ND these steps have not been undertaken. These results demonstrated that there was a population of PA within the NC. However, the limits of detection of the flow cytometer ($>800\text{nm}$) limited any information in changes in size and homogeneity (as the NC are too small to be detected by the forward scatter, and only fluorescence was detected in the side scatter channel).

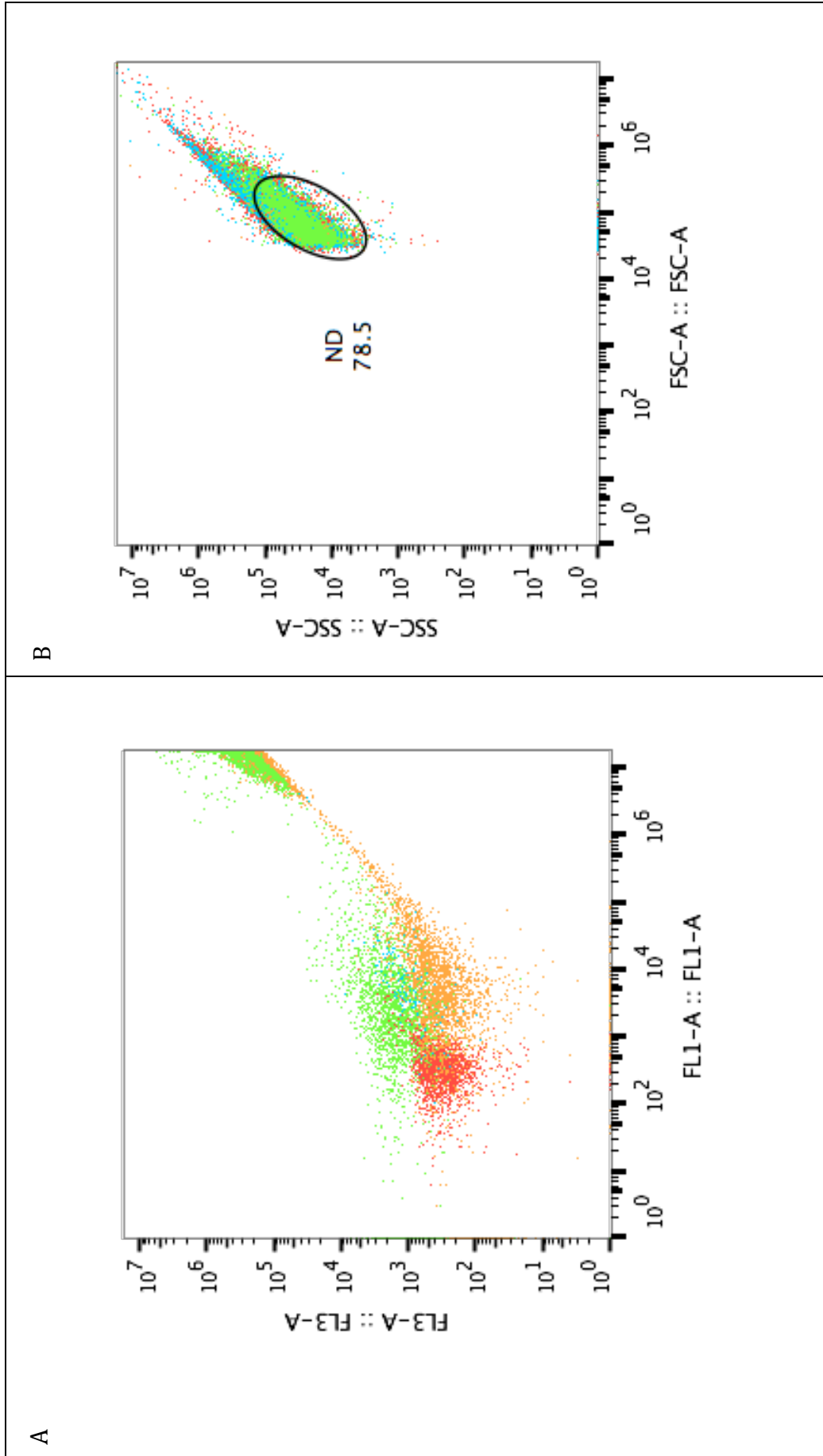


Figure 6.325 Flow cytometry analysis of Buffer solutions.

Flow cytometry analysis of buffer samples (PBS) with a combination of antibodies and lipid stain showing red fluorescent signal (FL3-A) and green fluorescent signal (FL1-A)(A). For both NC and ND. Green is buffer + primary(P) and secondary(S) Ab, and cell mask(CM), orange is buffer + P and S, blue is buffer + S, and red is buffer + P. Forward scatter (FSC-A) and side scatter (SSC-A) (B) is also shown. Green is buffer + P Ab, orange is buffer + S Ab, blue is buffer + P,S CM and red is buffer + P and S Ab.

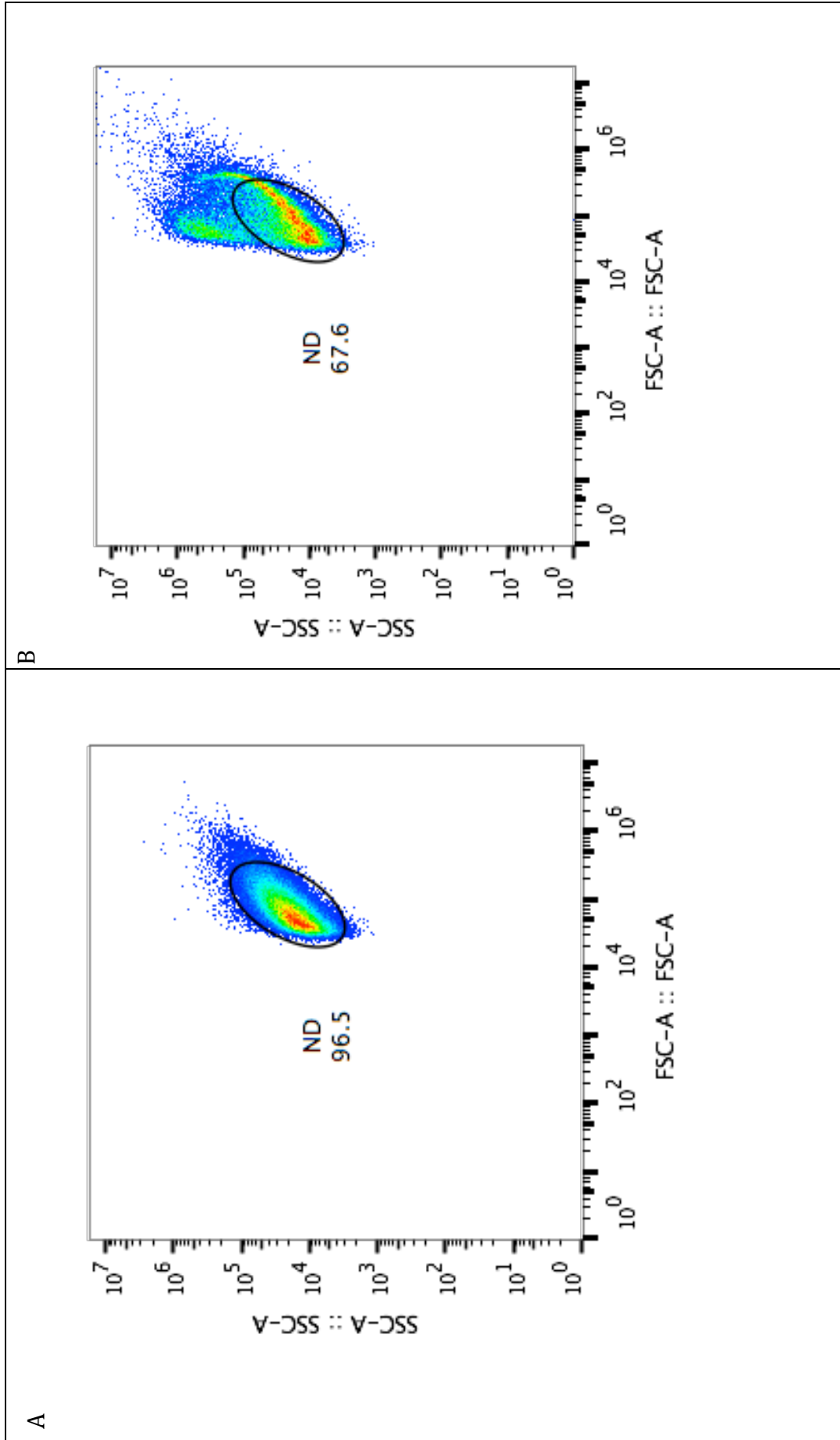


Figure 6.326 Flow cytometry analysis of ND and NC. Flow cytometry analysis of NC (A) and ND (B) in buffer (PBS), stained with cell mask and a primary antibody to PA and a secondary antibody conjugated to A488. This shows forward scatter (FSC-A) and side scatter (SSC-A). Demonstrating the whole population within the samples, which have been gated for a sub-population.

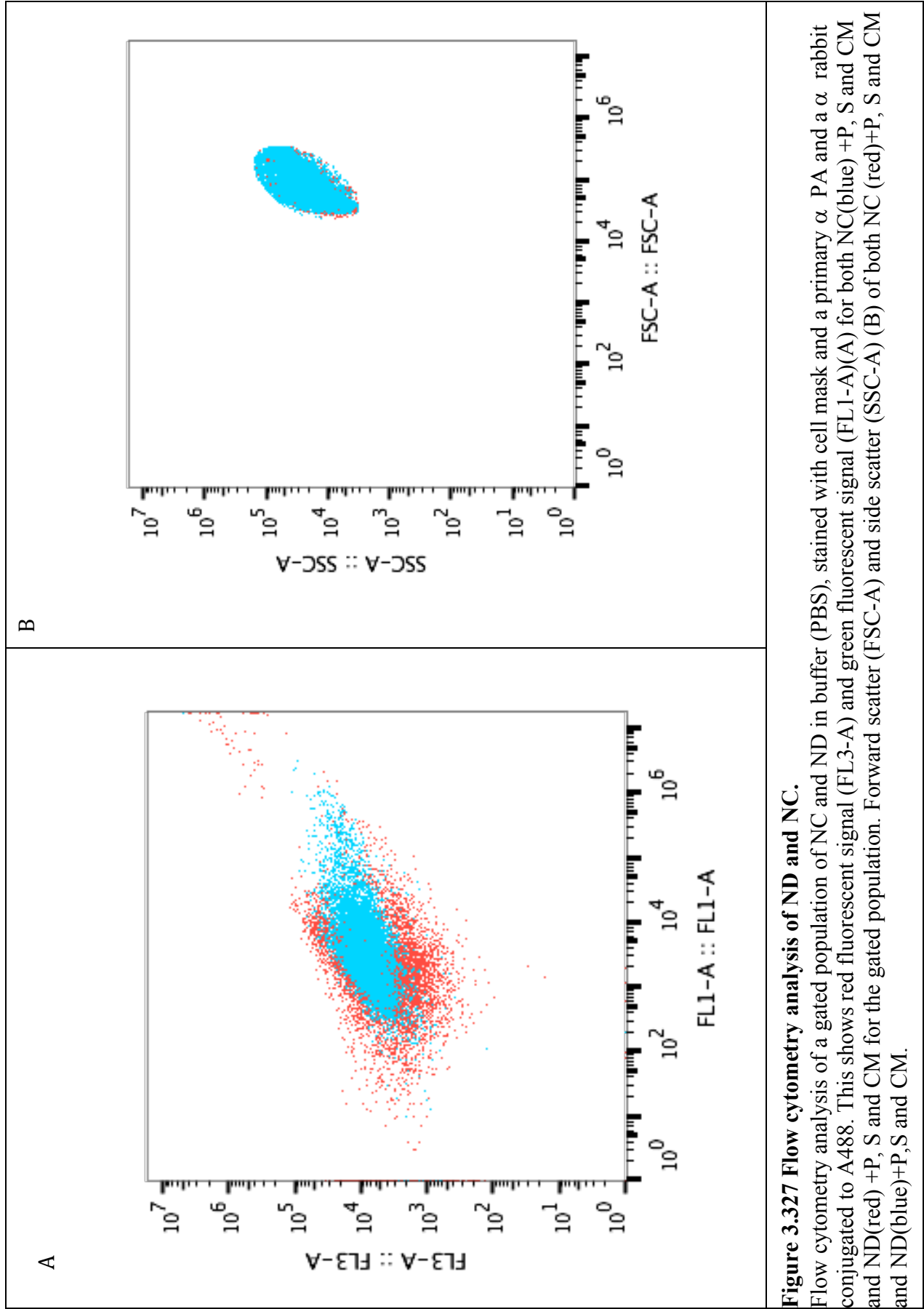
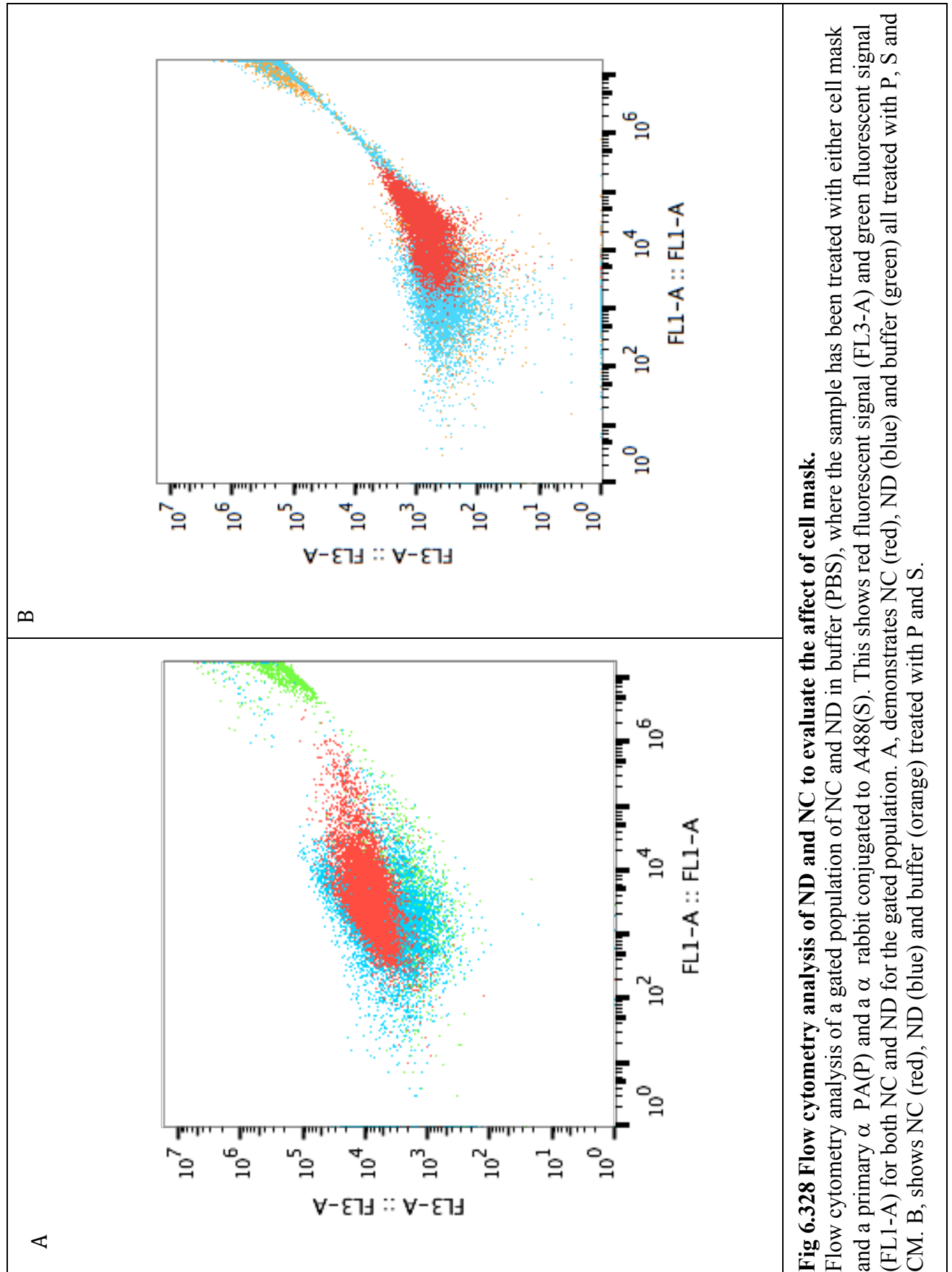


Figure 3.327 Flow cytometry analysis of ND and NC.

Flow cytometry analysis of a gated population of NC and ND in buffer (PBS), stained with cell mask and a primary α PA and a α rabbit conjugated to A488. This shows red fluorescent signal (FL3-A) and green fluorescent signal (FL1-A)(A) for both NC(blue) +P, S and CM and ND(red) +P, S and CM for the gated population. Forward scatter (FSC-A) and side scatter (SSC-A) (B) of both NC (red)+P, S and CM and ND(blue)+P, S and CM.



6.33 Production of deuterated proteins and NC formation using deuterated proteins

Due to unforeseen problems with the commercial availability of deuterated POPC (dPOPC) an alternative fully deuterated lipid, DMPC, was sourced for neutron reflectometry experiments. Additionally, MSP1D1 was recombinantly produced in deuterated culture media.

Thus far analysis of both ND and NC had seemed promising, however due to these changes and possible issues with concentration, both ND and NC were further characterised to determine if using the new MSP1D1, recombinantly expressed in *E.coli*, could still facilitate the self-assembly of ND and NC, as well as investigating if the concentration of NC could be increased by TCA precipitation and re-suspension in a more suitable volume (see method 2.253)

It was essential to characterise protein production in D₂O as bacterial growth in these conditions could be affected and lead to a significant reduction in protein yield (Sivashanmugam *et al.*, 2009). To this end MSP1D1, PA LFn-cys and LFn-GFP were cultured in D₂O. MSP1D1 was produced in One Shot[®] *E.coli* BL21*DE3 bacteria (Invitrogen, Paisley, UK) and cultured in D₂O 2XYT. This was purified and the resultant protein was evaluated for protein yield and purity. The yield from this culture was 4mg/L, and no significant difference in protein yield was observed in the two culture conditions, hydrogenated or deuterated media (Figure 6.3131).

Protective antigen was produced in One Shot[®] *E.coli* BL21*DE3 bacteria (Invitrogen, Paisley), UK and cultured in D₂O 2XYT. The purified protein was evaluated for protein yield, and purity. The yield was determined to be 1.5 mg/l. This produced a reduced yield when compared to PA production in H₂O (Section 3.2). Additionally, there appeared to be a reduced purity of the PA83 unit as determined by apparent molecular weight.

LFn-GFP produced in One Shot[®] *E.coli* BL21*DE3 bacteria (Invitrogen, Paisley, UK and cultured in D₂O 2xYT. This produced a similar yield to hydrogenated LFn-GFP of 8mg/L, with a high purity as determined by densitometry after Coomassie staining. There was however another band detected at an apparent MWt of 70kDa, which was also observed with hydrogenated LFn-GFP production.

The purity of LFn-Cys was >95%, as determined by densitometry after Coomassie stain (Figure 3.123). The LFn-Cys protein yielded 5 mg/L. Deuterated LFn-Cys produced in One Shot[®] *E.coli* BL21*DE3 bacteria (Invitrogen, Paisley, UK and cultured in D₂O 2XYT (see method) expressed well, yielding 5mg/L, similar to the production of hydrogenated LFn-Cys. The purity of this was very high (>95%). Although the production of deuterated PA ideally would need to be optimised, the expense of deuterium oxide was prohibitive and the amounts of PA produced was sufficient for continuing experiments.

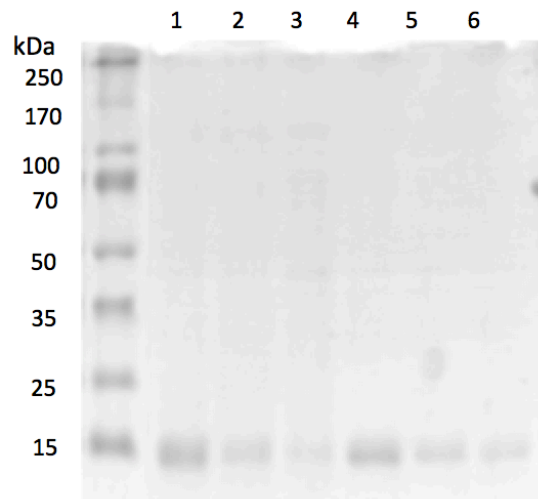


Figure 6.3131 Deuterated MSP1D1 Protein elution from TALON[®] resin and determination of concentration and purity of pooled fractions by SDS-PAGE and Coomassie staining.

Deuterated MSP1D1 protein yield and purity were determined via SDS PAGE, and Coomassie stain. Showing fractions 1-6 (1mL eluted fractions) for MSP1D1.

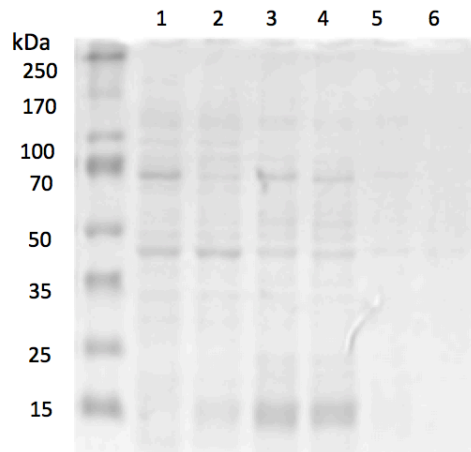


Figure 6.3132 Deuterated PA Protein elution from TALON[®] resin and determination of concentration and purity of pooled fractions by SDS-PAGE and Coomassie staining.

Deuterated PA protein yield and purity were determined via SDS PAGE, and Coomassie stain. Showing fractions 1-6 (1mL eluted fractions) for PA.

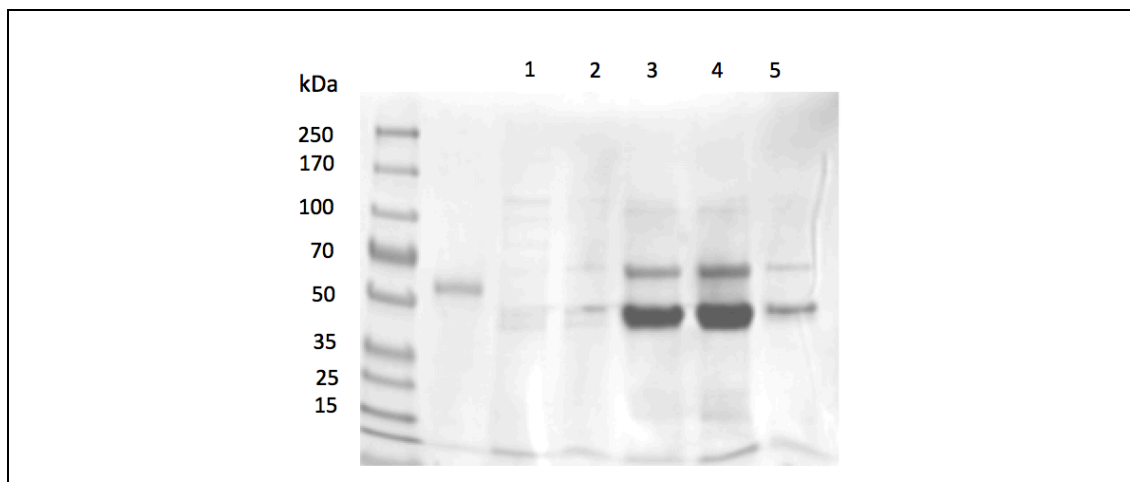


Figure 6.3133 Deuterated LFn-GFP Protein elution from TALON[®] resin of pooled fractions by SDS-PAGE and Coomassie staining.
Deuterated LFn-GFP protein showing fractions 1-5 (1mL eluted fractions) for LFn-GFP.

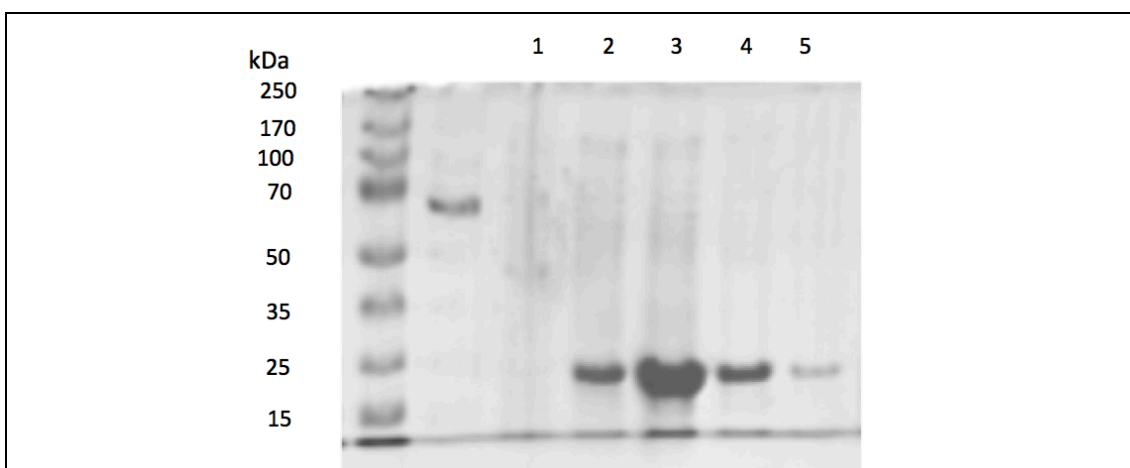


Figure 6.3134 Deuterated LFn-Cys Protein elution from TALON[®] resin of pooled fractions by SDS-PAGE and Coomassie staining.
LFn-Cys protein showing fractions 1-5 (1mL eluted fractions) for LFn-Cys.

Protein	Yield	Purity
PA	1.5mg/L	>85%
LFn-Cys	5mg/L	>85%
MSP1D1	4mg/L	>85%
LFn-GFP	8mg/L	>85%

Table 6.31 Summary of protein yields when cultured in D₂O.

The new MSP1D1 and DMPC were used to make ND and NC, these samples were subjected to TCA precipitation (Section 2.253) and analysed by SDS PAGE and Western Blot analysis (Figure 6.3135). Four samples were analysed, ND (1), NC made with purchased MSP1D1 (2), ND (3) and NC (4) made with MSP1D1 recombinantly expressed under hydrogenated media conditions. This protein enrichment step was proven to be successful, as defined by the positive detection of anti-6xHis, anti-PA and anti-V5 in the nanocomplexes and anti-6xHis in the ND. Additionally, the analysis for the NC with the recombinantly produced protein belt (4) was shown to exhibit a similar MW when compared to NC assembled with purchased belt protein (2). Thus, indicating comparative functional activity of recombinant MSP1D1 with commercially available preparations. Furthermore, the deuteration of protein/lipids did not influence the self-assembly of the NC (Figure 6.3136) as defined by detectable levels of PA and 6xHis.

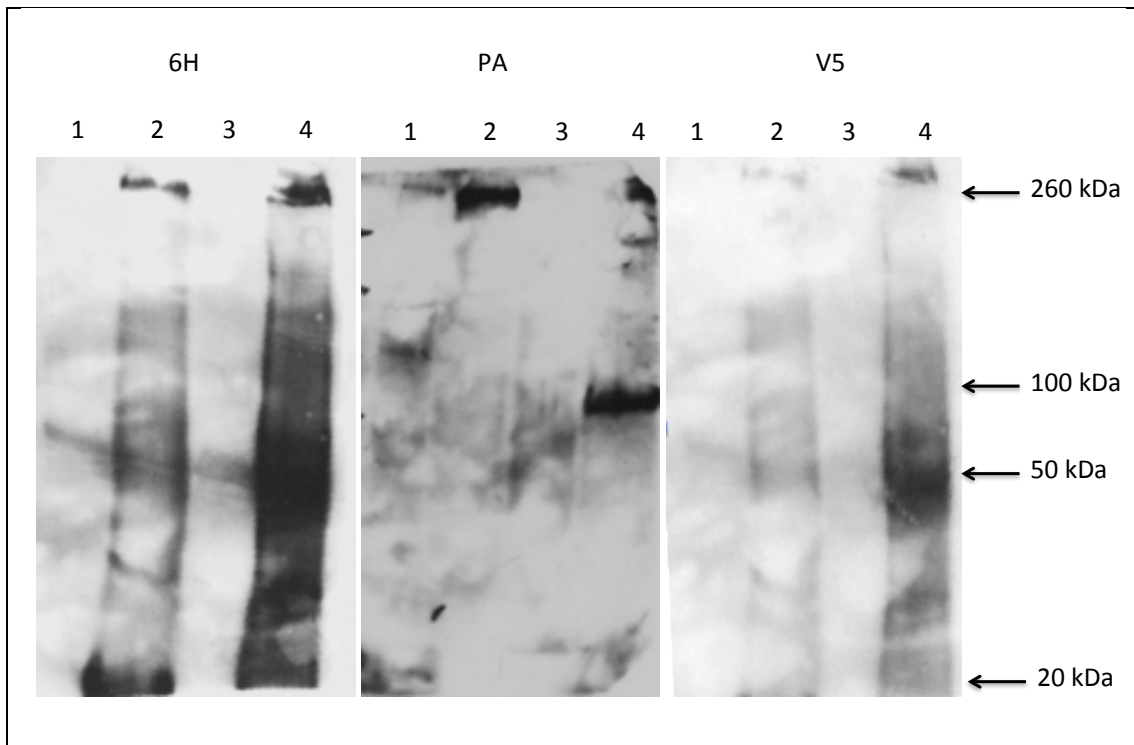


Figure 6.3135 Western blot analysis of NC and ND.

Four samples were analysed, ND(1), NC made with purchased MSP1D1 (2) ND (3) made with MSP1D1 expressed within the lab and NC (4) made with MSP1D1 expressed within the lab.

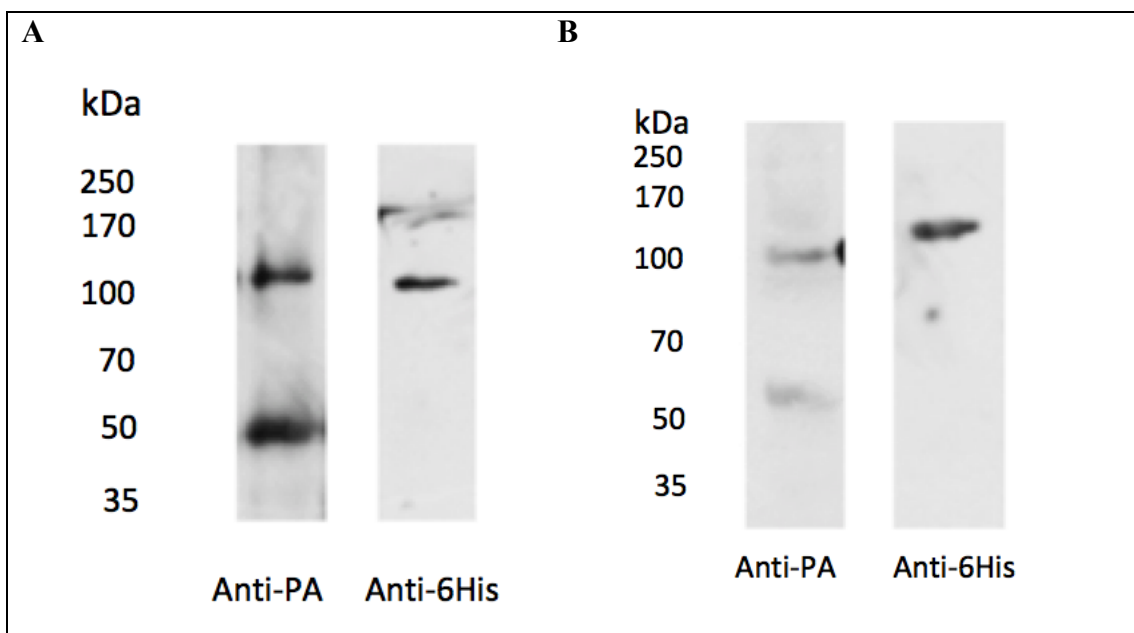


Figure 6.3136 showing Western blot results for NC formation.

Showing H-ND and D-PA (A) and D-ND and H-PA (B) to evaluate the presence of PA in the ND.

6.34 Determination of LFn-GFP translocation using Neutron Reflectometry

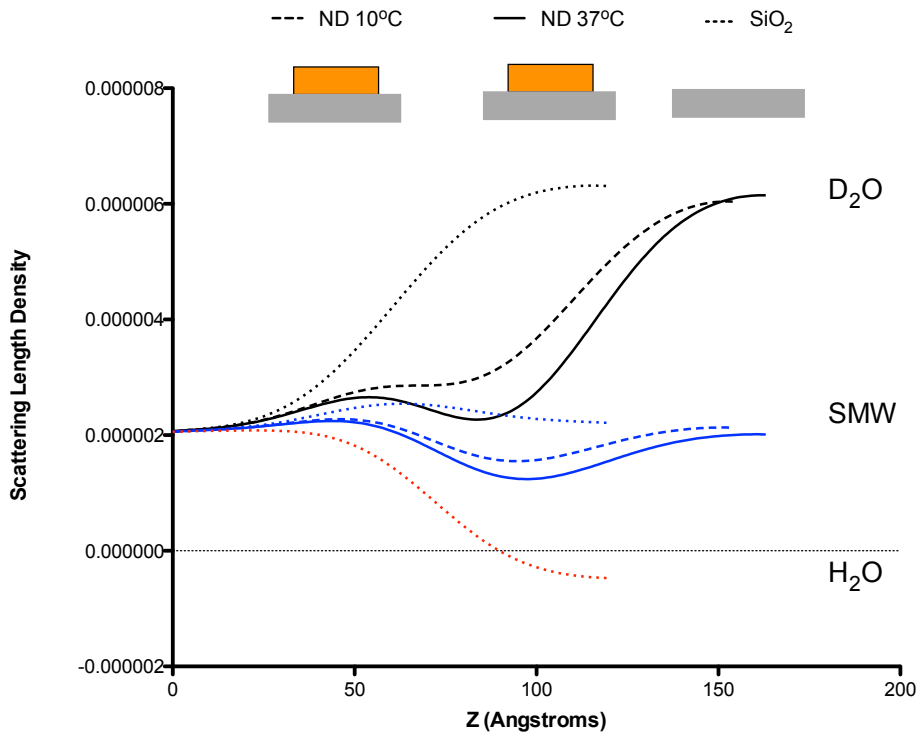
Neutron reflectometry (NR) is a powerful tool for the investigation of complex biological systems. Due to the potential for contrast matching, it has been possible to look at the biophysics of specific parts of these biological systems. To this end, the previously characterised ND and NC consisting of hDMPC, hMSP1D1 and dPA were characterised by NR, where dLFn-GFP was flushed into the system, to determine the initial binding and any structural changes that occurred. The pH of this system was changed to pH 5.5 (similar to that of endosome, which was thought to be an important in MG transitions that initiate translocation) and the interface characteristics of this system were investigated. SLD's for proteins were predicted from Biomolecular Scattering Length Density Calculator (<https://www.ncnr.nist.gov/resources/sldcalc.html>) (Appendices 9.6).

Initially the SiO₂ layer, and the adsorption of ND to the silica surface were evaluated, at 10°C and at 37°C. This demonstrated an 82% coverage as determined by the hydration of the ND layer (~18% hydration) and a layer thickness of 44Å, similar to previously published data (Bertram *et al.*, 2015). A small reduction in layer thickness 44Å to 43.9 Å was observed with an increase in temperature from 10°C to 37°C attributed to the temperature being above the T_m for DMPC (24°C). The hydration of the layer had changed from 18% to 10% (from 10°C to 37°C respectively). The roughness of this layer, reduced from 24Å to 22.2Å (from 10°C to 37°C respectively), indicating a reduction in the thickness of the layer and increase in coverage and a more defined ND-buffer interface.

Following the addition of LFn-GFP two models were generated to explore whether the LFn-GFP was interacting with the silica surface or the nanodisc layer (Figure 6.342). For NR fit where LFn-GFP was modeled as a layer on top of the ND, the hydration for this layer was 90% indicating a diffuse layer on top of the ND of LFn-GFP. The roughness increased to

28.6Å, and the LFn-GFP layer was 15Å. The fit for samples within the ND layer demonstrated a roughness of 23.5Å and a hydration of 10%. The best fit of the two, were where LFn-GFP was sitting within the ND layer, indicating that LFn-GFP is interacting with the silica layer.

A



B

Project Name : hNDs_10C_37C.mat

Type : Standard Layers Geometry : Solid / Liquid

Parameters: Layers Experimental Params Contrast 1 Contrast 2 Contrast 3 Contrast 4 Contrast 5 Contrast 6 Contrast 7 Contrast 8 Contrast 9 Contrast 10

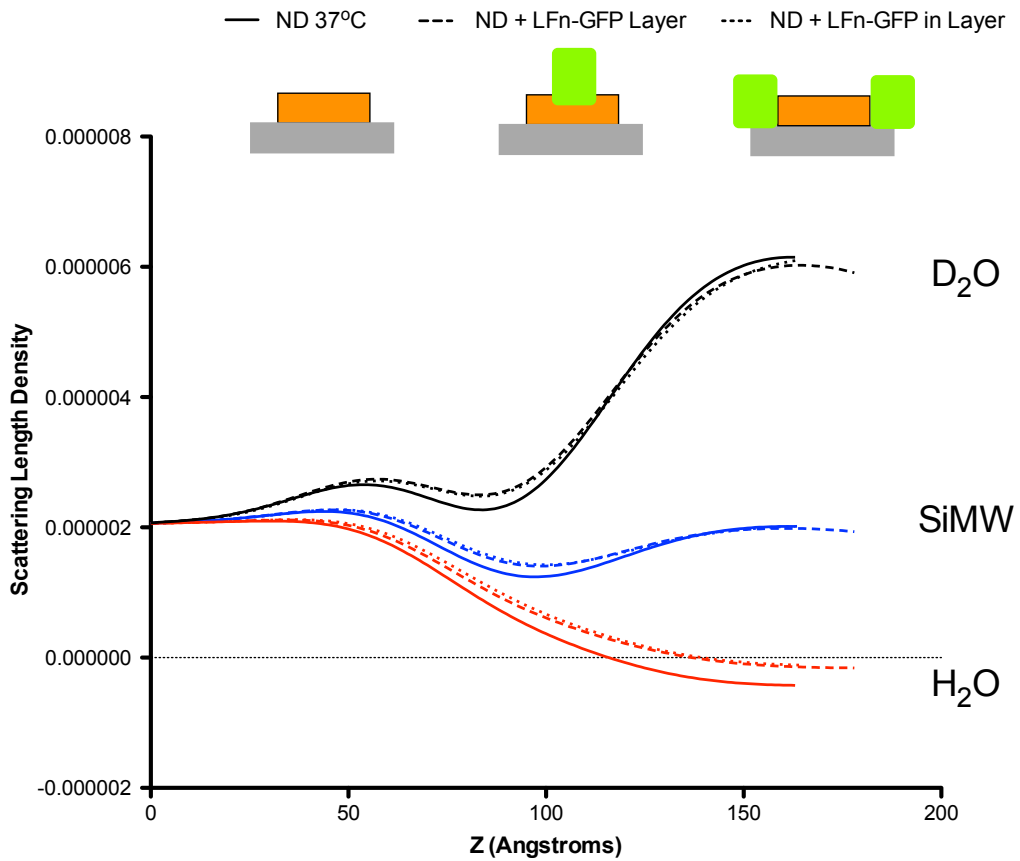
(un)ch...

Fit?	Parameter Name	Lower Bound	Value	Upper Bound
<input checked="" type="checkbox"/>	Substrate Roughness	2	20.3054	25
<input checked="" type="checkbox"/>	SiO2 SLD	0.000E0	3.470E-6	1
<input checked="" type="checkbox"/>	SiO2 Thickness	2	20.3501	40
<input checked="" type="checkbox"/>	SiO2 Hydration	0.000E0	23.72	50
<input checked="" type="checkbox"/>	CW Thick	0.000E0	0.000E0	20
<input checked="" type="checkbox"/>	CW Rough	3	17.4896	20
<input checked="" type="checkbox"/>	CW Hydration	0.000E0	0.000E0	100
<input checked="" type="checkbox"/>	ND 10C Thick	30	34.3941	45
<input checked="" type="checkbox"/>	ND SLD	0.000E0	5.685E-7	2.000E-6
<input checked="" type="checkbox"/>	ND 10C Rough	3	24.9169	25
<input checked="" type="checkbox"/>	ND 10C Hydr	10	14.7283	50
<input checked="" type="checkbox"/>	ND 37C Thick	30	43.2954	45
<input checked="" type="checkbox"/>	ND 37C Rough	3	22.2374	25
<input checked="" type="checkbox"/>	ND 37C Hydr	10	10.0722	50

6.341 Neutron Reflectometry Fit for hND at 10°C and 37°C.

ND adhered to silica surface and NR data fitted in RasCal. This shows the NR profile and the fit for ND 10°C and 37°C (A). The fit and SLD data were exported and plotted in prism. Cartoons depicting the layers and the corresponding dataset were imposed onto the SLD plot graph. The RasCal fit outputs for ND layer at 10°C and 37°C (B).

A



B

Project Name : hNDs_10C_37C_LFnGFPLayer+ND.mat

Type : Standard Layers Geometry : Solid / Liquid

Parameters: Layers Experimental Params Contrast 1 Contrast 2 Contrast 3 Contrast 4 Contrast 5 Contrast 6 Contrast 7 Contrast 8 Contrast 9 Contrast 10 Contrast 11 Contrast 12 Contrast 13

(un)ch...

Fit?	Parameter Name	Lower Bound	Value	Upper Bound
	Substrate Roughness	2	20.3054	25
	SiO ₂ SLD	0.000E0	3.270E-6	1
	SiO ₂ Thickness	0.000E0	20.350E-6	40
	SiO ₂ Hydration	0.000E0	0.000E0	50
	CW Thick	0.000E0	0.000E0	50
	CW Rough	0.000E0	17.288E-6	50
	CW Hydration	0.000E0	0.000E0	100
	ND 10C Thick	0.000E0	34.384E-6	45
	ND 10C SLD	0.000E0	5.683E-7	2.000E-6
	ND 10C Rough	0.000E0	24.918E-6	50
	ND 37C Hydr	0.000E0	18.285E-6	50
	ND 37C Thick	0.000E0	43.285E-6	45
	ND 37C Rough	0.000E0	7.237E-6	50
	ND 37C Hydr	0.000E0	10.072E-6	50
	Ln-GFP Thick	2.000E-6	2.000E-6	5.000E-6
	Ln-GFP RLD	0.000E0	28.625E-6	50
	Ln-GFP Rough	0.000E0	8.170E-7	3.000E-6
	Ln-GFP Hydr	0.000E0	24.810E-6	50
	ND GFP SLD	0.000E0	13.813E-6	50
	ND GFP Rough	0.000E0	13.813E-6	50
	ND GFP Hydr	0.000E0	13.813E-6	50

C

Project Name : hNDs_10C_37C_LFN-GFPinND.mat
 Type : Standard Layers Geometry : Solid / Liquid

Contrast 4	Contrast 5	Contrast 6	Contrast 7	Contrast 8	Contrast 9	Contrast 10	Contrast 11	Contrast 12	Contrast 13
Parameters	Layers	Experimental Params	Contrast 1	Contrast 2	Contrast 3				
(un)ch...									
Fit?	Parameter Name	Lower Bound	Value	Upper Bound					
	Substrate Roughness	?	20.2054	25					
	SiO2 SLD	0.000E0	3.470E-6	1					
	SiO2 Thickness	0.000E0	25.74	40					
	SiO2 Hydration	0.000E0	20.3591	30					
	CW Thick	0.000E0	1.7889	20					
	CW Rough	0.000E0	0.000E0	100					
	CW Hydration	0.000E0	0.000E0	20					
	ND 10C Thick	0.000E0	5.683E-7	2.000E-6					
	ND 10C SLD	0.000E0	5.683E-7	2.000E-6					
	ND 10C Rough	0.000E0	7.7288	25					
	ND 10C Hydr	10	43.2882	50					
	ND 37C Thick	0.000E0	3.02374	45					
	ND 37C Rough	0.000E0	10.0722	50					
	LFn-GFP Thick	0.000E0	2.000E-6	100					
	LFn-GFP SLD	2.000E-6	2.000E-6	5.000E-6					
	LFn-GFP Rough	0.000E0	0.000E0	30					
	LFn-GFP Hydr	5.300E-7	100	30					
	ND GFP SLD	0.000E0	8.67E-7	3.000E-6					
	ND GFP Rough	0.000E0	353.007	25					
	ND GFP Hydr	0.000E0	10.08	50					

6.342 Neutron Reflectometry Fits for ND + LFN-GFP.

ND + LFN-GFP adhered to silica surface and NR data fitted in RasCal. Showing the NR profile and the fit for ND + LFN-GFP as a layer on top of the ND and inserted within the ND layer (A). The fit and SLD data were exported and plotted in prism. Cartoons depicting the layers and the corresponding dataset were imposed onto the SLD fit graph. The RasCal fit outputs for LFN-GFP as a layer on top of ND layer (B) and the output for LFN-GFP in the ND layer (C).

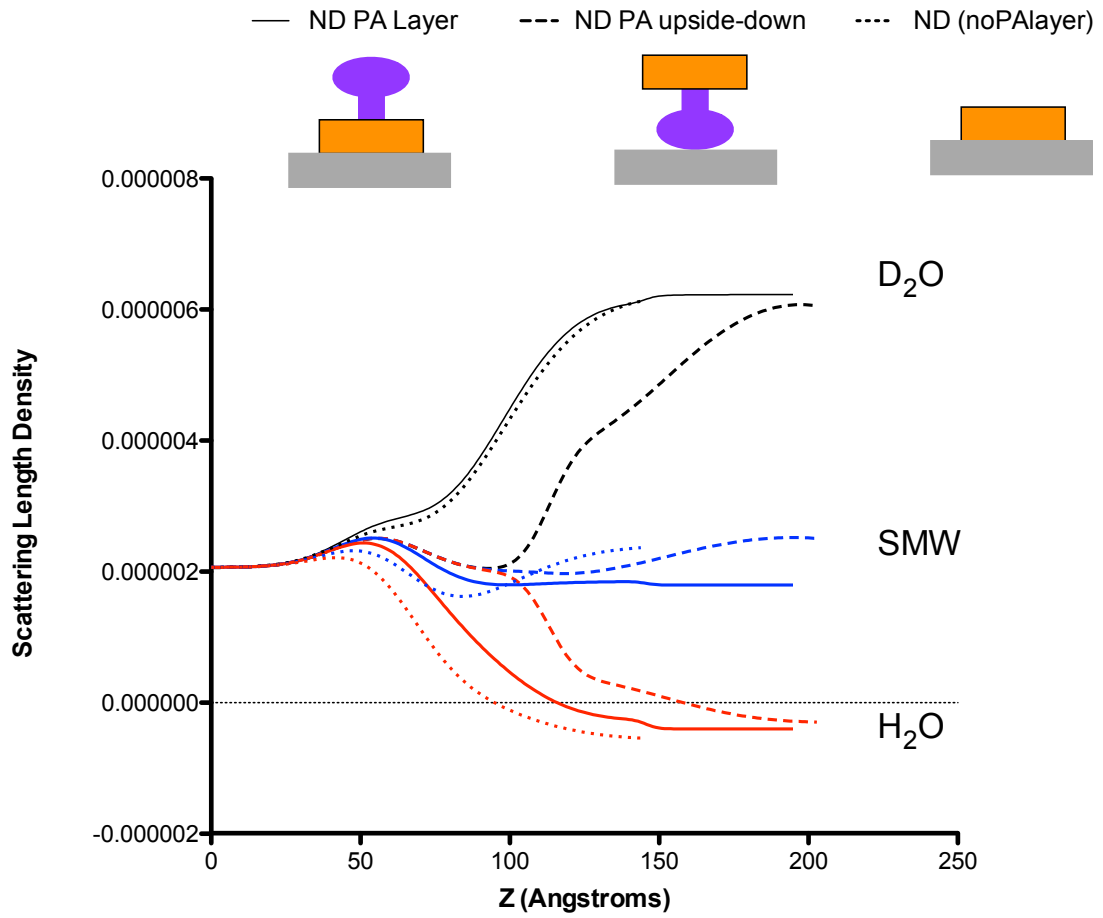
NC was then investigated, this was initially adhered to the silica surface. Several models were assessed to account for disparity of sample orientation. This data was assessed to account for the PA pore to be upside-down, no PA layer and the PA in the predicted orientation (Figure 6.343). The modeling demonstrated that the PA pore in an upside-down orientation and no PA layer could be discounted, suggesting that the orientation is of the ND on the silica surface with the mushroom cap above. This was demonstrated to be the best fit model (Figure 6.343) for the NC sample.

There was significantly lower coverage of the NC (hydration 69%) as compared to the ND sample (hydration 10%) associated with the lower concentration of NC due to the required selection and enrichment of the PA containing NC samples. These samples demonstrated a disc on the surface with a diffuse layer away from the surface. The layer above the ND (PA pore), was very diffuse (a hydration of 96.7), which would suggest that there was either very low coverage of NC to the silica, or that there was perhaps some NC adsorbed which didn't contain PA. For this fit (with PA in the correct orientation) The NC had a ND thickness of 32.6 Å and a hydration of 69% with a PA thickness of 87Å and a hydration of 99.9%.

For NC the fits for the PA pore in the correct orientation were assessed as a function of temperature. As the temperature was changed from 10°C to 37°C there was a small change in the thickness of these samples from 38Å to 32Å, which can be attributed to the temperature being above the T_m for DMPC (24°C) resulting in a reduction in the thickness of the nanodisc. Following the addition of LFn-GFP (Figure 6.345), the hydration distribution altered from 69% to 57% for the NC layer and went from 99.9% to 85% for the PA layer, suggesting interaction of LFn-GFP with both layers. To this end, when the pH of the sample was changed to pH5.5 there is a change in distribution of the ND layer and of the PA layer where there was a further reduction in hydration to 38% (from 57%) and an increase in the

hydration of the layer to 90.8 (from 85%) in the PA layer. This would indicate a redistribution of LFn-GFP, from the PA pore into the ND layer.

A



B

Project Name : hNDDPA_10C_UpSideDownPALayer.mat
 Type : Standard Layers Geometry : Solid / Liquid

Parameters Layers Experimental Params Contrast 1 Contrast 2 Contrast 3 Contrast 4 Contrast 5 Contrast 6

(un)ch...

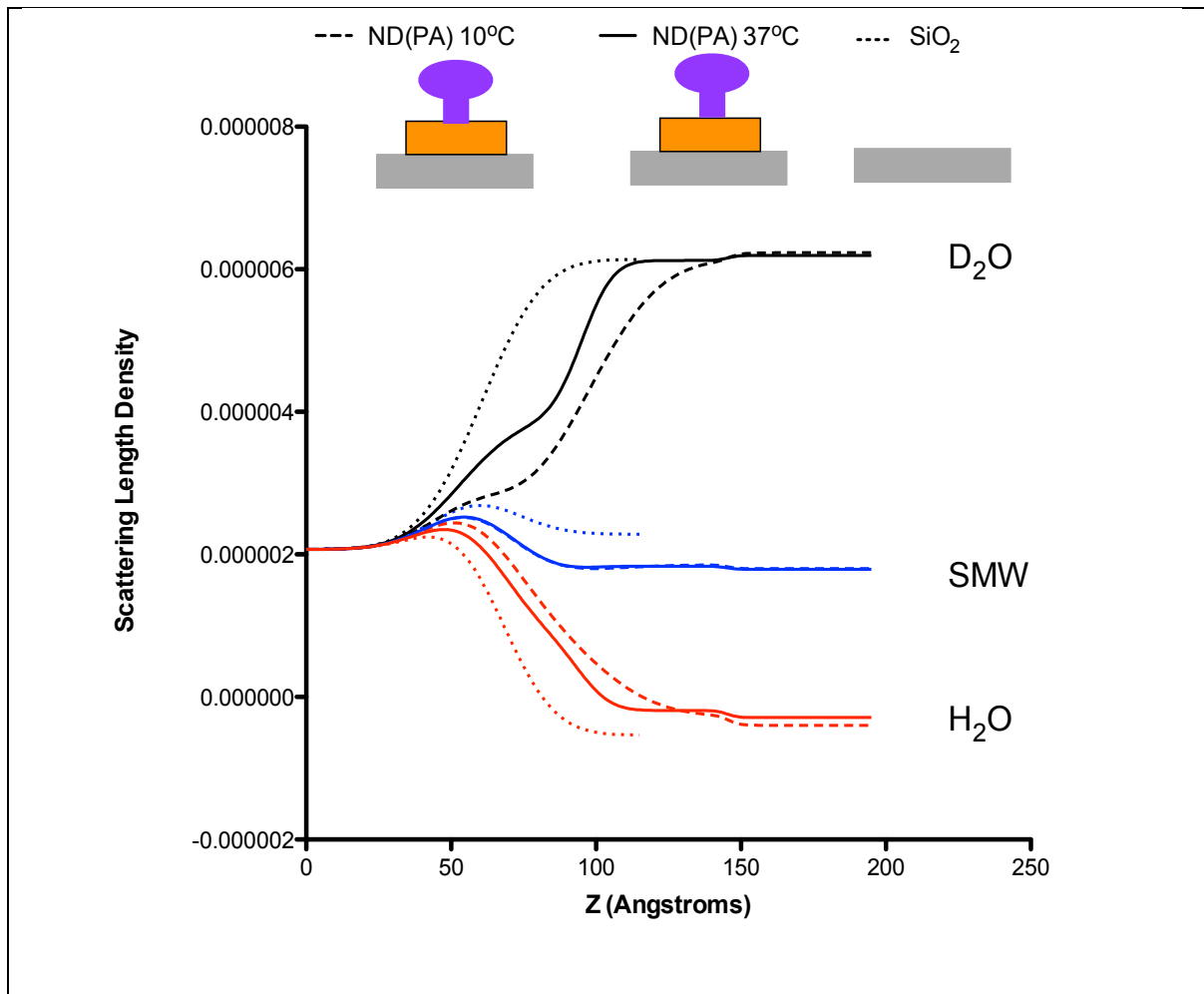
Fit?	Parameter Name	Lower Bound	Value	Upper Bound
	Substrate Roughness	2	15.1282	25
	SiO ₂ SLD	0.000E0	3.470E-6	2
	SiO ₂ Thickness	0.000E0	13.0283	40
	SiO ₂ Hydration	0.000E0	1.205E-8	50
	CW Thick	0.000E0	0.8297	20
	CW Rough	0.000E0	1	100
	CW Hydration	0.000E0	39.8336	65
	ND SLD	5.680E-7	1.270E-6	2.000E-6
	ND 10C Thick	10	74.284	50
	ND 10C Rough	10	50	200
	PA inner 10C Thick	2.000E-6	2.000E-6	3.500E-6
	PA inner 10C SLD	0.000E0	4.25E-7	50
	PA inner 10C Rough	0.000E0	6.790E-8	100
	PA inner 10C Hydr			

C

Project Name : hNDDPA_10C_37C_NoPALayer.mat				
Type : Standard Layers		Geometry : Solid / Liquid		
Parameters Layers Experimental Params Contrast 1 Contrast 2 Contrast 3 Contrast 4 Contrast 5 Contrast 6 Contrast 7 Contrast 8 Contrast 9 Contrast 10				
(un)ch...				
Fit?	Parameter Name	Lower Bound	Value	Upper Bound
<input checked="" type="checkbox"/>	Substrate Roughness	2	15.1691	25
<input checked="" type="checkbox"/>	SiO ₂ SLD	0.000E0	3.470E-5	1
<input checked="" type="checkbox"/>	SiO ₂ Thickness	0.000E0	1.273E-5	40
<input checked="" type="checkbox"/>	SiO ₂ Hydration	0.000E0	1.089E-5	50
<input checked="" type="checkbox"/>	CW Thick	0.000E0	0.8797	30
<input checked="" type="checkbox"/>	CW Rough	0.000E0	3	20
<input checked="" type="checkbox"/>	CW Hydratop	0.000E0	100	100
<input checked="" type="checkbox"/>	ND 10C Thick	5.680E-7	6.307E-7	2.000E-6
<input checked="" type="checkbox"/>	ND 10C Rough	10	72.763	50
<input checked="" type="checkbox"/>	ND 10C Hydr	30	17.0078	100
<input checked="" type="checkbox"/>	PA inner 10C Thick	50	0.000E0	200
<input checked="" type="checkbox"/>	PA inner 10C SLD	2.000E-6	3.500E-6	3.500E-6
<input checked="" type="checkbox"/>	PA inner 10C Rough	0.000E0	0.000E0	100
<input checked="" type="checkbox"/>	PA inner 10C Hydr	0.000E0	100	100
<input checked="" type="checkbox"/>	ND 37C Thick	30	3	25
<input checked="" type="checkbox"/>	ND 37C Rough	0.000E0	15.6559	25
<input checked="" type="checkbox"/>	ND 37C Hydr	30	43.8377	25
<input checked="" type="checkbox"/>	PA inner 37C Thick	50	0.000E0	200
<input checked="" type="checkbox"/>	PA inner 37C Rough	3	0.000E0	20
<input checked="" type="checkbox"/>	PA inner 37C Hydr	0.000E0	100	100

6.343 Neutron Reflectometry Fits for NC with PA in different orientations.

NC (which contain PA) adhered to silica surface and NR data fitted in RasCal. This shows the NR profile and the fit for NC as a layer with PA in two different orientations or none (A). The fit and SLD data were exported and plotted in prism. Cartoons depicting the layers and the corresponding dataset were imposed onto the SLD fit graph. The RasCal fit output for PA as a layer with the cap of the mushroom at the ND, upside down PA (B) and the output for no PA in the ND (C).



Project Name : hNDdPA_10C_37C.mat

Type : Standard Layers Geometry : Solid / Liquid

Parameters Layers Experimental Params Contrast 1 Contrast 2 Contrast 3 Contrast 4 Contrast 5 Contrast 6 Contrast 7 Contrast 8 Contrast 9 Contrast 10

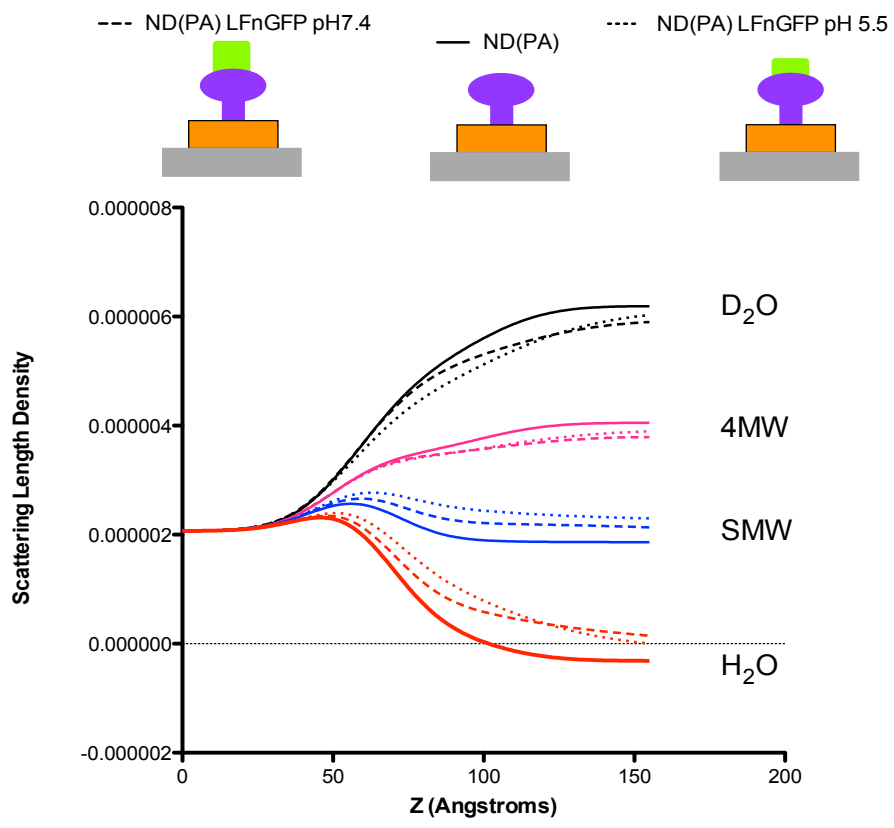
(un)ch...

Fit?	Parameter Name	Lower Bound	Value	Upper Bound
<input checked="" type="checkbox"/>	Substrate Roughness	2	14.9916	25
<input checked="" type="checkbox"/>	SiO ₂ Thickness	0.000E0	3.420E-6	40
<input checked="" type="checkbox"/>	SiO ₂ Hydration	0.000E0	1.628E-6	20
<input checked="" type="checkbox"/>	CW Thick	0.000E0	4.767E-6	20
<input checked="" type="checkbox"/>	CW Rough	3	0.8767	20
<input checked="" type="checkbox"/>	CW Hydration	0.000E0	100	100
<input checked="" type="checkbox"/>	ND 10C Thick	5.680E-7	30.2935	2.000E-6
<input checked="" type="checkbox"/>	ND 10C Rough	10	1.625E-6	50
<input checked="" type="checkbox"/>	ND 10C Hydr	10.000E6	10.000E6	50
<input checked="" type="checkbox"/>	PA inner 10C Thick	2.000E-6	3.500E-6	3.500E-6
<input checked="" type="checkbox"/>	PA inner 10C Rough	0.000E0	96.8321	100
<input checked="" type="checkbox"/>	PA inner 10C Hydr	0.000E0	8.3957	50
<input checked="" type="checkbox"/>	ND 37C Thick	5.680E-7	30.2935	2.000E-6
<input checked="" type="checkbox"/>	ND 37C Rough	10	1.625E-6	50
<input checked="" type="checkbox"/>	ND 37C Hydr	10.000E6	10.000E6	50
<input checked="" type="checkbox"/>	PA inner 37C Thick	2.000E-6	3.500E-6	3.500E-6
<input checked="" type="checkbox"/>	PA inner 37C Rough	0.000E0	97.2322	100
<input checked="" type="checkbox"/>	PA inner 37C Hydr	0.000E0	8.3957	50

6.344 Neutron Reflectometry Fit for NC with PA in the correct orientation at 10°C and 37°C.

ND adhered to silica surface and NR data fitted in RasCal. This shows the NR profile and the fit for NC 10°C and 37°C (A). The fit and SLD data were exported and plotted in prism. Cartoons depicting the layers and the corresponding dataset were imposed onto the SLD plot graph. The RasCal fit output for PA as a layer in the correct orientation at 10°C and at 37°C (B).

A



B

Project Name : hNDdPA_10C_37C_LFnGFP.mat

Type : Standard Layers Geometry : Solid / Liquid

Contrast 5	Contrast 6	Contrast 7	Contrast 8	Contrast 9	Contrast 10	Contrast 11	Contrast 12	Contrast 13	Contrast 14
Parameters	Layers	Experimental Params			Contrast 1	Contrast 2	Contrast 3	Contrast 4	
(un)ch...									
Fit?	Parameter Name	Lower Bound		Value				Upper Bound	
	Substrate Roughness	2		14.9931				25	
	SiO ₂ STD	0.000E0		3.470E-6				4	
	SiO ₂ Thickness	0.000E0		15.2509				40	
	SiO ₂ Hydration	0.000E0		8.562E-8				20	
	CW Thick	0.000E0		0.8797				20	
	CW Rough	0.000E0		2				100	
	CW Hydration	0.000E0		38.5684				55	
	ND 10C Thick	5.680E-7		2.000E-6				2.000E-6	
	ND 10C Rough	10		60.9908				20	
	PA inner 10C Thick	10		4.435E-6				20	
	PA inner 10C Rough	2.000E-6		4.435E-6				4.500E-6	
	PA inner 10C Hydr	0.000E0		4.435E-6				80	
	ND 37C Thick	30		16.8548				100	
	ND 37C Rough	0.000E0		68.8526				30	
	PA inner 37C Thick	80		87.0311				20	
	PA inner 37C Rough	0.000E0		68.8895				90	
	PA inner 37C Hydr	0.000E0		2.6899E-6				30	
	ND En-GFP STD	2.000E-6		2.6899E-6				4.500E-6	
	ND En-GFP Rough	0.000E0		17.4381				30	
	PA En-GFP STD	2.000E-6		17.4381				4.500E-6	
	PA En-GFP Rough	0.000E0		32.5432				30	
	PA En-GFP Hydr	0.000E0		85.7132				100	

C

Project Name : hNDdPA_10C_37C_LFnGFP_pH5.mat

Type : Standard Layers Geometry : Solid / Liquid

Contrast 8	Contrast 9	Contrast 10	Contrast 11	Contrast 12	Contrast 13	Contrast 14	Contrast 15	Contrast 16	Contrast 17	Contrast 18
Parameters	Layers	Experimental Params	Contrast 1	Contrast 2	Contrast 3	Contrast 4	Contrast 4	Contrast 5	Contrast 6	Contrast 7
(un)ch...										
Fit?	Parameter Name	Lower Bound	Value	Upper Bound						
	Substrate Roughness	2	14.9931	25						
	SiO2 ID	0.000E0	3.470E-6	40						
	SiO2 Thickness	2	15.7683	50						
	SiO2 Hydration	0.000E0	8.592E-8	50						
	CW Thick	0.000E0	0.8237	20						
	CW Rough	0.000E0	100	100						
	NW Hydration	0.000E0	38.3684	2.000E-6						
	NW ID	5.680E-7	2.000E-6	2.000E-6						
	NW 10C Thick	2	21.1893	25						
	NW 10C Hydr	10	69.9309	20						
	PA inner 10C Thick	2.000E-6	4.467E-6	4.500E-6						
	PA inner 10C Rough	0.000E0	48.7638	100						
	PA upper 10C Hydr	30	3.8458	55						
	NW 37C Thick	0.000E0	16.8371	30						
	NW 37C Rough	0.000E0	68.8326	20						
	PA inner 37C Thick	80	87.0317	200						
	PA inner 37C Rough	0.000E0	29.8895	100						
	PA inner 37C Hydr	2.000E-6	2.8939E-6	4.500E-6						
	ND En-GFP SLD	0.000E0	17.1391	30						
	ND En-GFP Rough	0.000E0	28.9398	30						
	PA En-GFP SLD	2.000E-6	3.243E-6	4.500E-6						
	PA En-GFP Rough	0.000E0	35.7432	100						
	ND pH5 SLD	2.000E-6	2.776E-6	4.500E-6						
	ND pH5 Rough	0.000E0	38.0497	30						
	ND pH5 Hydr	0.000E0	3.277E-6	4.500E-6						
	PA pH5 Rough	0.000E0	90.8871	100						

6.345 Neutron Reflectometry Fits for NC + LFn-GFP.

NC + LFn-GFP adhered to silica surface and NR data fitted in RasCal. This shows the NR profile and the fit for NC + LFn-GFP as a layer on top of the NC, and a change in distribution as the pH is adjusted (A). The fit and SLD data were exported and plotted in prism. Cartoons depicting the layers and the corresponding dataset were imposed onto the SLD fit graph. The RasCal fit outputs for NC + LFn-GFP (B) and a change in distribution as the pH is adjusted (C).

6.4 Discussion

The biophysical investigation of the PA pore has mostly been the formation of ion permeable active PA pores, with some efforts into the imaging of the PA pore inserted into lipid nanodiscs using cryo-EM (Akkledevi *et al.*, 2013, Katayama *et al.*, 2010). However, investigation in real time, observing changes that occur to the proteins during the translocation process have yet to be investigated and combining the ND technology, with the investigative power of neutrons will lead to a better understanding of membrane pore dynamics. This chapter has made advancements towards this goal, by developing and characterising ND and NC and undertaking initial investigations using specular neutron reflectometry.

The development of the LFn-Cys construct was successfully cloned into a pET151 D-TOPO cassette. This protein produced was purified (>95% Purity) although there seemed to be a duplex present, as predicted due to the propensity for cysteine residues to form disulphide bridges in non-reducing environments. This issue was resolved by the addition of TCEP to LFn-Cys.

The plasmid for MSP1D1 was purified and transformed into BL21*pLYS. The was produced at yields that were usable for future experiments. PA and LFn-GFP have been previously produced and described in previously chapters.

In order to determine if nanodisc self-assembly occurred around the PA pore, and to undertake initial characterisation, NCs were constructed using previously published methodology (Akkledevi *et al.*, 2013). The characterisation data (Figure 6.321) would suggest that there were issues with the uncoupling of the NC from the bead slurry, or there was an insufficient concentration of the eluted fractions, where by the sample was too dilute and so the epitopes could not be detected within the limits of detection by Western blot

analysis. This required further investigation and so another batch of NC and ND was produced, where three epitopes were evaluated (Figure 6.322) PA to detect for the presence of PA in the sample, V5 which would have detected the presence of LFn-Cys, and 6xHis for the detection of LFn-Cys and MSP1D1 (26 kDa and 24 kDa respectively). This data supported the notion that there were issues with the uncoupling of the construct from the thiol beads, however it was shown that both ND and NC were detectable by Western blot, however problems still remained for detection of PA. Following this, the samples were then characterised by TEM, after a methylamine tungstate stain. TEM analysis of ND yielded positive results where round structures could be seen, ranging between 20-30 nm in diameter. This, taken with the previous western blot analysis confirmed the presence of formed NDs. TEM analysis of NC confirmed issues with lower concentration and density of the NC, compounded by the limits of resolution of the equipment used. Structures similar to previously published PA nanocomplexes were noted albeit at significantly lower concentrations (Akkledevi *et al.*, 2013), however the resolution was not sufficient to enable full analysis. Nevertheless, TEM analysis did yield results that ND were being formed and the western blot data, was representative of ND and not just free protein.

The production of deuterated proteins was generally successful, there were a few issues with bacterial growth, however this didn't seem to hamper the production of the protein. This meant that the development of a deuterated ND and deuterated NC (where by the lipid and MSP1D1 were deuterated and the protein was hydrogenated, and where the lipid and MSP1D1 were hydrogenated and the protein was deuterated) could be produced and characterised. The proteins; dMDP1D1, dPA, dLFn-GFP and dLFn-Cys all produced well, with high purity and a high enough concentration for use (Figures 6.3131, 6.3132, 6.3133, 6.3134 respectively). In consideration of the associated problems, of low concentration and the associated limits of detection, with the characterisation of the ND

and NC TCA precipitation was used and shown to be effective in enriching the signal to detectable levels. These data yielded positive results with PA, 6xHis and V5 being detected at distinct bands at above 260kDa for the NC samples, and 6xHis signal for the ND samples. This work requires further optimisation due to high background signal on the western blot. It is possible that there are smaller bands on the 6xHis blot for the NC that could indicate a sub-population of ND within the NC sample. As the aim of this was to look at deuterated forms of the NC, two different deuterated forms were made dNC (dlipid, dMSP1D1 hPA) and hNC (hlipid, hMSP1D1, dPA). These were also subject to TCA precipitation and run on and SDS PAGE gel and subjected to Western blot analysis for PA and 6xHis. These both demonstrated detectable signal, with a much-improved signal to noise ratio. These again would demonstrate the successful formation of the NC, and demonstrated that deuteration had no effect on the self-assembly of this system.

To investigate the successful isolation of PA into nanodiscs flow cytometry was used (Figure 6.325). These data again supported that there was a population of NC containing PA, indicating that the NC (containing the PA pore) had been successfully made. Although due to the size of the PA pore and this NC structure, analysing these constructs proved difficult due to contaminants and the limits of detection of the equipment.

ND and NC (hDMPC:dPA) analysis by neutron reflectometry has demonstrated that ND and NC can be detected. However due to the synthesis of the NC, the surface coverage was far lower than with ND and the layer of PA was found to be even more diffuse. This is however an advantage as sample purity may be increased and improve enrichment of PA positive ND, although sample concentration would ideally be further increased.

Once LFn-GFP was flushed into the system, there was a small change in the thickness of the ND layer, where the best fit suggested the LFn-GFP was interacting with the silica surface, and adhering in between the ND layer. There was a more substantial change in the LFn-GFP

layer, in the presence PA, which indicated a layer on top of the PA layer. When the pH was reduced (to pH5.5) a change in distribution was observed indicating that LFn-GFP had moved from the PA pore into the PA and ND layer. This has demonstrated that the initiation and translocation of these events can be studied and changes in the thickness of layer can be determined, attributed with key events in the translocation process. This seems to correspond with the literature, where a change in MG transition (due to endosomal pH change) can initiate translocation (Chapter 1.5).

6.5 Conclusion

The data presented herein demonstrated the successful assembly of PA into nanodiscs, with neutron reflectometry a successful tool in the analysis of these complexes. We have demonstrated that PA inserted into NC can be detected and when LFn-GFP was added to these complexes binding takes place. When the pH of the chamber was lowered to mimic endosomal pH (pH5.5) there was a reduction in LFn-GFP protein layer. This would indicate that the protein was inserting into the PA pore. These data sets demonstrate that key steps in the translocation process can be evaluated, to give a real-time map of key translocation events, and associated changes to the proteins as these events occur. It also provides opportunities to explore these events under different conditions.

Chapter 7 General Discussion and Future works

7.1 General Discussion

The aim of this work was to investigate the translocation of material through the PA pore.

Given the impact of *B.anthraxis*, as a naturally occurring disease and as a potential bioterrorist threat (Chapter 1) understanding the mechanisms and limitations of exotoxin translocation is vital, in developing therapeutics to block translocation events.

Despite the trafficking pathway of ATx being well defined (chapter 1.4) there, are a few guidelines for the successful design of a viable translocase substrate (Chapter 1.5). However, proteins need to have a mixture of cationic and anionic residues, so that protonation during the translocation process can occur and facilitate passage through the cationic PA translocase potentially via Brownian ratchet mechanism, driven by pH. The data presented here works towards understanding these mechanisms, by means of evaluating the ability of structures to translocate that have inherently different properties.

The literature has demonstrated that proteins of a much larger (e.g GFP 5nm) size than the internal lumen of the PA pore (1.5nm) can translocate (Zornetta *et al.*, 2010; Zheng *et al.*, 2014). The energetics associated with complete unfolding of such stable proteins would require a large amount of energy, of which a Brownian ratchet mechanism may not be able to generate (Feld, *et al.*, 2012; Nablo *et al.*, 2013), as well as refolding once translocated which would question the requirement for molten globular transition.

Chapter 3 demonstrated the ability of the PA translocase to facilitate the delivery of a supramolecular structure, consisting of an ASO bound to LFn-GAL4 structure by sequence specificity.

This was a noteworthy find, as this would suggest that unfolding of the LFn-GAL4 is unlikely, as this complex would have lost its therapeutic payload during translocation had it in fact unfolded. Given the limiting internal diameter of the PA pore ($\sim 1.5\text{nm}$) (Kintzer *et al.*, 2010) this raises questions as to the requirements for MG transition. Perhaps there is a more dynamic system of translocation as opposed to a rigid pore (Dyer *et al.*, 2015). Further to this Chapter 4 demonstrated the ability of LFn-RTAC to translocate in the presence of PA, however compared to the toxicity of commercially available RTAC it was demonstrated to be far less toxic. Suggesting that perhaps there was less translocation (despite dose being far higher than required of commercial RTAC, and LFn-RTAC), or that the protein may not have been functional despite being translocated, (due to problems re-folding once through the PA pore). This could potentially explain the inability of LFn-RTAC to translocate, where by the charge of the molecule could potentially be driving strong adherence forces within the translocase channel, and the lack of lysine residues on the structure of RTAC (Deeks *et al.*, 2003). Lysine residues have been reported to facilitate the translocation of DTA across the PA pore (with multiple lysine residues either at the C-terminal or the N-terminal (Sharma and Collier 2014)). This may suggest a mechanism in which the side chain chemistries affect the possible translocation.

Given that it has been demonstrated that 6xHis has been sufficient to initiate translocation through the PA pore, and that this LFn-RTAC contains an N-terminal 6xHis, similarly this also contains LFn which has been demonstrated to initiate translocation) it would be determined that it doesn't seem that the α -clamp is a rate limiting step within the context of these studies. It could be that perhaps ϕ - clamp is the rate limiting step within this study where by the LFn-RTAC is docking within the α -clamp, and upon translocation, is unable to pass due to the ϕ - clamp due to the charge of LFn-RTAC.

This study also demonstrated that LFn-GFP can translocate in the presence and absence of PA in HeLa cells. However, the pattern of translocation in the presence and absence of PA differ (Chapter 5).

With regard to these published data on different types of cargo which seem to have varying success in delivery, it's important to consider that the experimental models change, the concentration of PA and LF fusion protein dosed changes, amount of material delivered into the cytosol varies based on the cell type (*i.e.* number of anthrax receptors expressed), and varieties in incubation times (rate of endocytosis). This was particularly evident when looking to the translocation of LFn-GFP by Kushner *et al.*, 2003, who determined that this could translocate without needing PA, suggesting that PA may target LF to the endosomal pathway and allow it to enter the cytosol; Whereas Zornetta *et al.*, 2010 demonstrated a PA dependence.

These conclusions although correct in line with the data presented, are conflicting, and so these factors are important to consider. However, with the ambiguity of materials that can translocate; *e.g.* fluorescent probes (GFP is a stable fluorescent protein) is yet more complicated, when other groups (Verdurmen *et al.*, 2014) have demonstrated PA can only translocate proteins with a low thermostability. There are several questions that remain unanswered regarding the PA/LFn delivery platform.

This has demonstrated an array of proteins that can translocate in a PA specific manner.

Despite not being native to PA, demonstrating an array of side chain chemistries, complexities and stability. Given the varied parameters and results within this study and in the literature, it maybe that the model of translocation may be more dynamic in nature.

Whereby the PA pore is not rigid, and translocation (thought driven by pH in a Brownian ratchet mechanism, and docking sites within the PA pore) of the protein may allow for unfolded substrates to translocate by protein compression and PA pore dilating. There could

also be other mechanisms (Figure 7.12) at play such as PA causing membrane disruption and facilitating the release of translocating material. This however is less likely given the data generated demonstrating (Chapter 3, Figure 3.359) punctuated BSA-Txs red co-localising with PA, and limited cytosolic BSA-Txs red.

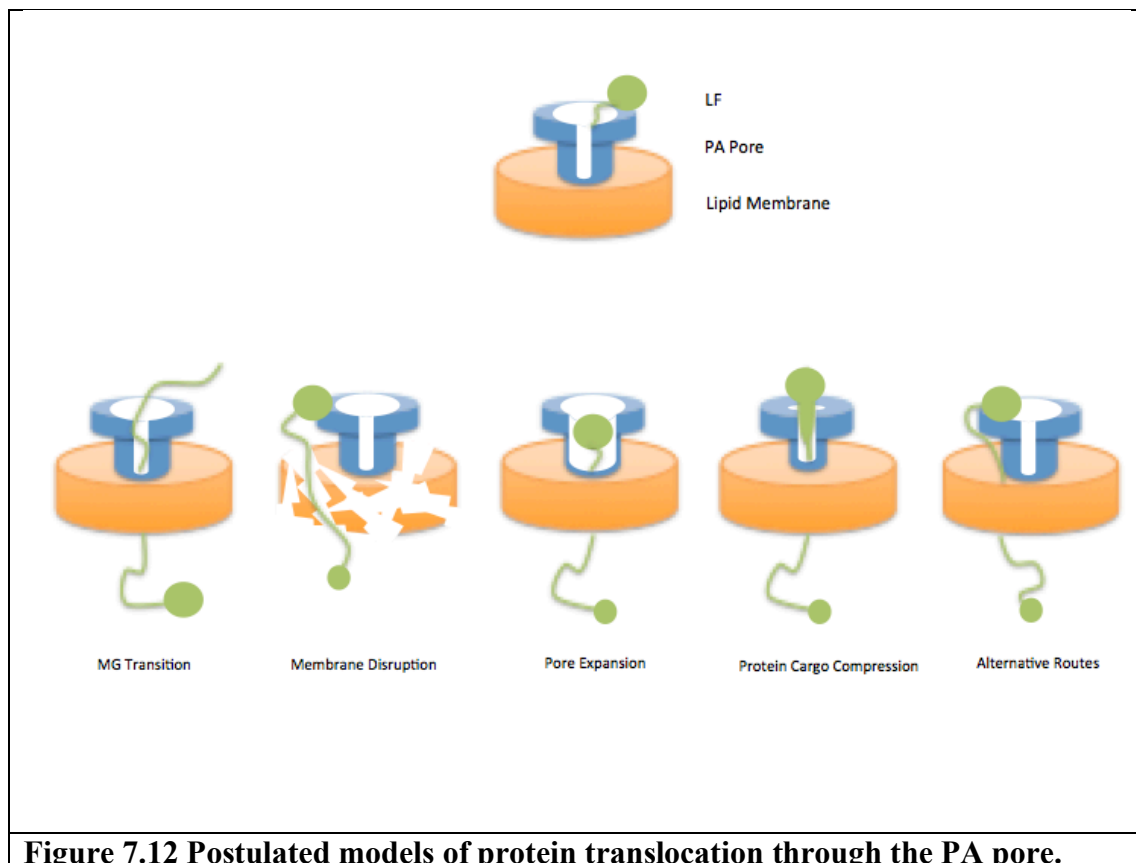


Figure 7.12 Postulated models of protein translocation through the PA pore.

Initial investigations into mapping protein translocation in real time, evaluating structural changes which occur in both the PA translocase and the translocating material have been investigated within this study. The development of PA inserted into nanodiscs were characterised, the binding of LFn-GFP to the pore and changes induced by pH were studied using neutron reflectometry.

This study demonstrated that NC could be adhered to the silica, and that PA could be detected within these NC. The binding of LFn-GFP to PA could also be detected, and there was a structural change in the layer size when the pH was reduced from pH 7.4 to pH 5.5.

This change was associated with LFn-GFP being inserted further into the PA pore. Although these are initial studies it demonstrates the ability of this methodology to monitor binding and translocation of material.

In conclusion, this thesis has demonstrated a variety of material to translocate through the PA, indicating potential utility in delivering macromolecular therapeutics (Chapter 3), which have long been hindered by the need to reach cytosolic compartments (Munsell *et al.*, 2017). It was demonstrated that although LFn-RTAC is a cationic substrate, the ability of this to be translocated is limited as demonstrated by cellular toxicity (Chapter 4). The structural stability of GFP and size of the protein has not inhibited the ability of it to translocate into the cytosol. Additionally, the ability of LFn-GFP to translocate in the absence of PA has also been documented (Chapter 5).

The binding interactions of LFn-GFP to PA, and the changes to translocating material at pH 5.5 have been documented and have been investigated using neutron reflectometry. These works have demonstrated novel findings about the PA pore, and the cargo that can translocate.

7.2 Future Works

Future investigation is focused into the translocation of a variety of material through the PA pore in order to investigate the requirement for MG transition as an essential part of substrate translocation through the PA pore. Had time permitted to continue this work, the following would have been investigated:

7.21 Can the PA pore deliver a supramolecular assembly to the cytosol (Chapter 3)?

Further work into this chapter involves the optimisation of radiolabelling ASO, which was started (Appendices 9.4). Had time permitted this would have been further optimised and this used for accurately quantifying the amount of ASO in subcellular compartments, to evaluate the efficiency of this system in delivery.

Long term work for the development of this delivery platform into mainstream clinical use would be investigated, considering target disease, tissue specificity and cellular uptake.

7.22 Can a thermodynamically plastic cationic substrate (LFn-RTAC) translocate through the PA pore (Chapter 4)?

In order to determine if the loss of observed activity was due to the inability to translocate or due to LFn-RTAC not being active once translocated (due to mis-folding) future investigations would have involved further study into the delivery of LFn-RTAC to cytosolic compartments by subcellular fractionation to determine location. Evaluation of LFn-RTAC by HSDSC and CD of the protein under different pHs would demonstrate it's ability for MG transition.

7.23 Can structurally stable fluorescent molecules translocate through the PA pore (Chapter 5)?

Future work within this chapter requires the investigation of translocation and cellular localisation of LFn-YFP and LFn-mCherry. This will highlight differences in the endocytic trafficking and translocation of these recombinant proteins by subcellular fractionation and microscopy, on a variety of cell lines to determine what difference this has on translocation. Once the ability of these proteins to translocate had been evaluated the structural stability of these constructs would further be investigated.

Investigating the structural characteristics of LFn recombinant proteins at a variety of pHs which represent different endocytic compartments, may aid in the analysis structural variation encountered by the protein during endocytic trafficking and translocation.

Furthermore, evaluating the unfolding and refolding energetics of these protein by HSDSC will be an important investigation of protein linearisation under physiological conditions within the cell, which may add additional explanations for differences in translocation properties.

Part of this would also be to the characterisation of receptor expression, and may give insight into the ability of cells to translocate LFn recombinant proteins to the cytosol. This will primarily involve the characterisation of Vero and HeLa for TEM8 and CMG2. This will be accomplished by detecting receptor levels by flow cytometry, Western blot and epifluorescent microscopy

7.24 Can the structural dynamics associated with cargo binding and translocation be evaluated by neutron reflectometry in real time (Chapter 6)?

Had time permitted, further studies would have involved the investigation of the material during translocation in real time assessing changes, which occur to these proteins and to study to what extent there are changes within the PA pore. Which would give insights into

the molecular dynamics of the PA pore and of the material during translocation. Additionally, to this, determine the true SLD of the protein components within this system would further support the fit data.

7.25 What is the effect of Octomerisation on Protein Translocation?

Mutant forms of PA, which force PA⁸ to form have been demonstrated within the literature (Phillipes *et al.*, 2013). Studying the translocation capabilities of these constructs may be able to infer if this has an effect on the size of translocating material.

7.26 Is the PA pore a dynamic system?

To investigate the PA pore as a dynamic system as opposed to a being static (as currently suggested within the literature base) LFn-Cys would be conjugated to 5nm, 10nm and 20nm colloidal gold. The pre-pore X-ray structure has an average diameter of ~3.5nm and narrows to 1.5 nm in some regions (Petosa *et al.*, 1997). The colloidal gold being bigger than the internal diameters within the PA pore, and not having the capacity to linearise, would demonstrate if the pore could function as a dynamic system. Additionally, to this, the increasing size of the colloidal gold nanoparticle will provide an indication into the extent of the size that can translocate. LFn-gold particle translocation will be evaluated by atomic force microscopy, and western blot for detection of the streptavidin-colloidal gold.

Chapter 8 References

- Aartsma-Rus, A., & Krieg, A. M. (2017). FDA Approves Eteplirsen for Duchenne Muscular Dystrophy: The Next Chapter in the Eteplirsen Saga. *Nucleic Acid Therapeutics*, 27(1), 1–3. <http://doi.org/10.1089/nat.2016.0657>
- Abrami, L., Bischofberger, M., Kunz, B., Groux, R., & van der Goot, F.G., 2010. Endocytosis of the Anthrax Toxin Is Mediated by Clathrin, Actin and Unconventional adaptors, *PLoS Pathogens*, 6(3), p.e1000792.
- Abrami, L., Brandis, L., Moayeri, M., Brown, M.J., Krantz, B.A., Leppla, S.H., Van der Goot, F.G., 2013. Hijacking Multivesicular Bodies Enables Long-Term and Exosome-Mediated Long-Distance Action of Anthrax, *Cell Reports*, 5(4), pp986-996
- Abrami, L., Lindsay, M., Parton, R.G., Leppla, S.H., Goot, F.G.V., 2004. Membrane insertion of anthrax protective antigen and cytoplasmic delivery of lethal factor occur at different stages of the endocytic pathway, *The journal of cell biology*, 166(5), pp.645-651.
- Abrami, L., Liu, S., Cosson, P., Leppla, S.H., van der Goot, F.G., 2003. Anthrax toxin triggers endocytosis of its receptor via a lipid raft-mediated clathrin-dependent process *The Journal Of Cell Biology*, 160(3), pp.321–328.
- Abrami, L., Reig, N., Van Der Goot, F.G., 2005. Anthrax toxin: the long and winding road that leads to the kill, *Trends in Microbiology*, 13(2), pp.72-78
- Akkaladevi, N., Hinton-Chollet, L., Katayama, H., Mitchell, J., Szerszen, L., Mukherjee, S., Gogol, E.P., Pentelute, B.L., Collier, R.J., Fisher, M.T., 2013. Assembly of anthrax toxin pore: Lethal-factor complexes into lipid nanodiscs, *Protein Science*, 22(4), pp.492-501
- Albrecht, M.T., Li, H., Williamson, D., LeButt, C.S., Flick-Smith, H.C., Quinn, C.P., Westra, H., Galloway, D., Mateczun, A., Goldman, S., Groen, H., Baillie, L.W.J., 2007. Human Monoclonal Antibodies against Anthrax Lethal Factor and Protective Antigen Act Independently To Protect against *Bacillus anthracis* Infection and Enhance Endogenous Immunity to Anthrax, *Infection and Immunity*, 75(11), pp.5425–5433
- Anaraki, S., Addiman, S., Nixon, G., Krahe, D., Gosh, R., Brooks, T., Lloyd, G., Spencer, R., Walsh, A., McCloskey, B., Lightfoot, N., 2008. Investigations and control measures following a case of inhalation anthrax in East London in a drum maker and drummer, *Euro-surveillance*, 18(13), pp.19076.
- Andrew W. Artenstein, Steven M. Opal; Novel Approaches to the Treatment of Systemic Anthrax. *Clin Infect Dis* 2012; 54 (8): 1148-1161. doi: 10.1093/cid/cis017
- Arora, N. & Leppla, S. H., 1993. Residues 1–254 of anthrax toxin lethal factor are sufficient to cause cellular uptake of fused polypeptides. *Journal of Biological Chemistry*, 268, 3334-3341.
- Arora, N. & Leppla, S.H., 1994. Fusions of anthrax toxin lethal factor with shiga toxin and diphtheria toxin enzymatic domains are toxic to mammalian cells. *Infection and*

Immunity, 62(11), pp.4955–4961.

Arora, N., Klimpel, K.R., Singh, Y. and Leppla, S.H., 1992. Fusions of anthrax toxin lethal factor to the ADP-ribosylation domain of *Pseudomonas* exotoxin A are potent cytotoxins which are translocated to the cytosol of mammalian cells. *Journal of Biological Chemistry*, 267(22), pp.15542-15548.

Artenstein, A.W., Opal, S.M., 2012. Novel Approaches to the treatment of systemic Anthrax, *Clin Infect Dis*, 54(8), pp.1148-1161.

Atlas, R. M., 2002. Bioterrorism: From Threat to Reality. *Annual Review Of Microbiology*, 56(1), pp.167.

Bachran, C., Morley, T., Abdelazim, S., Fattah, R.J., Liu, S. and Leppla, S.H., 2013. Anthrax toxin-mediated delivery of the *Pseudomonas* exotoxin A enzymatic domain to the cytosol of tumor cells via cleavable ubiquitin fusions. *MBio*, 4(3), pp.e00201-13

Backer, M.V., Patel, V., Jehning, B.T., Claffey, K.P., Karginov, V.A. and Backer, J.M., 2007. Inhibition of anthrax protective antigen outside and inside the cell. *Antimicrobial agents and chemotherapy*, 51(1), pp.245-251.

Baillie, L., Townend, T., Walker, N., Eriksson, U., Williamson, D., 2004. Characterization of the human immune response to the UK anthrax vaccine, *FEMS Immunology and Medical Microbiology*, 42(2), pp. 267-270.

Bann, J. G., 2012. Anthrax toxin protective antigen—Insights into molecular switching from prepore to pore. *Protein Science: A Publication of the Protein Society*, 21(1), pp.1–12.

Bartlett, J.G., Inglesby, T.V., Borio, J., 2002. Management of Anthrax, *Confronting Biological Weapons* 35(2), pp.851-855.

Basilio, D., Jennings-Antipov, L.D., Jakes, K.S., Finkelstein, A., 2011. Trapping a translocating protein within the anthrax toxin channel: implications for the secondary structure of permeating proteins. *Journal of General Physiology*, 137(4), 343-356.

Basilio, D., Juris, S.J, Colleir, R.J., Finkelstein, A., 2009. Evidence for a Proton–Protein Symport Mechanism in the Anthrax Toxin Channel, *Journal of General Physiology*, 133(3), pp.307-314

Bayburt, T.H. and Sligar, S.G., 2010. Membrane protein assembly into Nanodiscs. *FEBS letters*, 584(9), pp.1721-1727.

Bertram, N., Laursen, T., Barker, R., Bavishi, K., Møller, B.L. and Cárdenas, M., 2015. Nanodisc films for membrane protein studies by neutron reflection: Effect of the protein scaffold choice. *Langmuir*, 31(30), pp.8386-8391.

Bhatnagar, R., Batra, S., 2001. Anthrax Toxin, *Critical Review Microbiology*, 27(3), pp.167-200

Blanke, S., Milne, J.C., Benson, E., Collier, R.J., 1996. Fused polycationic peptide mediates delivery of diphtheria toxin A chain to the cytosol in the presence of anthrax protective antigen, *Proceedings of the National Academy of Sciences of the United States of America*, 93(16): 8437–8442.

Blaustein RO. The anthrax toxin channel: a barrel of LFs. *The Journal of General Physiology*. 2011;137(4):337-341. doi:10.1085/jgp.201110622.

Boll, W., Ehrlich, M., Collier, R.J. and Kirchhausen, T., 2004. Effects of dynamin inactivation on pathways of anthrax toxin uptake. *European journal of cell biology*, 83(6), pp.281-288.

Bonner, A., Almogren, A., Furtado, P.B., Kerr, M.A. and Perkins, S.J., 2009. Location of secretory component on the Fc edge of dimeric IgA1 reveals insight into the role of secretory IgA1 in mucosal immunity. *Mucosal immunology*, 2(1), pp.74-84.

Borch, J. and Hamann, T., 2009. The nanodisc: a novel tool for membrane protein studies. *Biological chemistry*, 390(8), pp.805-814.

Bossi, P., Tegnell, A., Baka, A., van Loock, F., Hendriks, J., Werner, A., Maidhof, H., Gouvras, G., 2004. Bichat guidelines for the clinical management of anthrax and bioterrorism-related anthrax. *Euro Surveillance*, 9(12), 500.

Bradley, K.A., Mogridge, J., Mourez, M., Collier, R.J., Young, J.A.T., 2001. Identification of the cellular receptor for anthrax toxin. *Nature*, 414, 225-229.

Bravata DM, Holty JC, Wang E, Lewis R, Wise PH, McDonald KM, Owens DK. Inhalational, Gastrointestinal, and Cutaneous Anthrax in Children A Systematic Review of Cases: 1900 to 2005. *Arch Pediatr Adolesc Med*. 2007;161(9):896-905. doi:10.1001/archpedi.161.9.896

Brookmeyer, R., Johnson, E., Barry, S., 2005. Modelling the incubation period of anthrax, *Statistics in medicine*, 24(4), pp.531-542.

Cardarelli, F., Digiaco, L., Marchini, C., Amici, A., Salomone, F., Fiume, G., Rossetta, A., Gratton, E., Pozzi, D., Caracciolo, G. 2016. The intracellular trafficking mechanism of Lipofectamine-based transfection reagents and its implication for gene delivery, *Scientific Reports* 25879(6).

Carey, M., Kakidani, H., Leatherwood, J., Mostashari, F., Ptashne, M., An amino-terminal fragment of GAL4 binds DNA as a dimer, *Journal of Molecular Biology*, 209(3), pp.423-432.

Carpenter, E.P., Beis, K., Cameron, A.D. and Iwata, S., 2008. Overcoming the challenges of membrane protein crystallography. *Current opinion in structural biology*, 18(5), pp.581-586.

- Chaudhary, A. and St. Croix, B., 2012. Selective blockade of tumor angiogenesis. *Cell Cycle*, 11(12), pp.2253-2259.
- Chavarría-Smith J, Vance RE., 2013. Direct Proteolytic Cleavage of NLRP1B Is Necessary and Sufficient for Inflammasome Activation by Anthrax Lethal Factor. *PLoS Pathog* 9(6): e1003452
- Chen, Z., Moayeri, M., & Purcell, R. (2011). Monoclonal Antibody Therapies against Anthrax. *Toxins*, 3(8), 1004–1019. doi:10.3390/toxins3081004
- Cherubin P, Garcia MC, Curtis D, et al. Inhibition of Cholera Toxin and Other AB Toxins by Polyphenolic Compounds. Mantis NJ, ed. *PLoS ONE*. 2016;11(11):e0166477. doi:10.1371/journal.pone.0166477.
- Chitlaru, T., Altboum, Z., Reuveny, S., Shafferman, A., 2011. Progress and novel strategies in vaccine development and treatment of anthrax, *Immunology Reviews*, 239(1), pp.221–236
- Clifton, L.A., Neylon, C. and Lakey, J.H., 2013. Examining protein–lipid complexes using neutron scattering. *Lipid-Protein Interactions: Methods and Protocols*, pp.119-150.
- Collier, R. J., 2009. Membrane translocation by anthrax toxin. *Molecular Aspects of Medicine*, 30(6), 413–422.
- Collier, R. J., Young, J. A. T., 2003. ANTHRAX TOXIN, *Annual Review of Cell and Developmental Biology*, 19(1), pp. 45-70.
- Comoletti, D., Grishaev, A., Whitten, A.E., Tsigelny, I., Taylor, P. and Trehwella, J., 2007. Synaptic arrangement of the neuroligin/ β -neurexin complex revealed by X-ray and neutron scattering. *Structure*, 15(6), pp.693-705.
- Cryan, L. M., & Rogers, M. S., 2011. Targeting the anthrax receptors, TEM-8 and CMG-2, for anti-angiogenic therapy. *Frontiers in Bioscience : a Journal and Virtual Library*, 16, pp.1574–1588.
- Cybulski, R.J., Sanz, P., O'Brien, A.D., 2009. Anthrax vaccination strategies, *Mol Aspects Med*, 30(6), pp. 490-502.
- de Smet, M. D., Meenken, C., & van den Horn, G. J. (1999). Fomivirsen – a phosphorothioate oligonucleotide for the treatment of CMV retinitis. *Ocular Immunology & Inflammation*, 7(3/4), 189-198.
- Dias, N. and Stein, C.A., 2002. Antisense oligonucleotides: basic concepts and mechanisms. *Molecular cancer therapeutics*, 1(5), pp.347-355.
- Dixon. T.C., Meselson, M., Guillemin, J., Hanna, P.C., 1999. Anthrax, *The New England Journal of Medicine*, 341(11), pp. 815-826.
- Doganay, L., Welsby, P.D., 2006. Anthrax:a disease in waiting? *Postgrad Med J*, 82(973), pp. 754–756.

Dowling, O., Difeo, A., Ramirez, M.C., Tukel, T., Narla, G., Bonafe, L., Kayserili, H., Yuksel-Apak, M., Paller, A.S., Norton, K., Teebi, A.S., Grum-Tokars, V., Martin, G.S., Davis, G.E., Glucksman, M.J., Martignetti, J.A., 2003. Mutations in Capillary Morphogenesis Gene-2 Result in the Allelic Disorders Juvenile Hyaline Fibromatosis and Infantile Systemic Hyalinosis. *American Journal of Human Genetics*, 73(4), pp. 957-966.

Dübel, S and Janice M. Reichert⁴ Sally D. Bolmer¹ and Thi-Sau Migone (2014). *Raxibacumab, Human Monoclonal Antibody against Anthrax Toxin*. -: Wiley. pp.1899-1908.

Duric, P., Cosic, G., Rajcevic, S., Petrovic, V., Tomkovic, M., Subic, Z., Dimitric, M., 2012. Three probable cases of cutaneous anthrax in autonomous province of Vojvodina, Serbia, *Eurosurveillance*, 5(17), pp.1-3.

Durrheim, D. N., Freeman, P., Roth, I., & Hornitzky, M. (2009). Epidemiologic Questions from Anthrax Outbreak, Hunter Valley, Australia. *Emerging Infectious Diseases*, 15(5), pp. 840–842.

Dyer, P.D., Kotha, A.K., Gollings, A.S., Shorter, S.A., Shepherd, T.R., Pettit, M.W., Alexander, B.D., Getti, G.T., El-Daher, S., Baillie, L. and Richardson, S.C., 2016. An in vitro evaluation of epigallocatechin gallate (eGCG) as a biocompatible inhibitor of ricin toxin. *Biochimica et Biophysica Acta (BBA)-General Subjects*, 1860(7), pp.1541-1550.

Feld, G. K., Brown, M. J., & Krantz, B. A., 2012. Ratcheting up protein translocation with anthrax toxin. *Protein Science : A Publication of the Protein Society*, 21(5), pp.606–624.

Feld, G. K., Thoren, K. L., Kintzer, A. F., Sterling, H. J., Tang, I. I., Greenberg, S. G., Krantz, B. A., 2010. Structural basis for the unfolding of anthrax lethal factor by protective antigen oligomers. *Nature Structural & Molecular Biology*, 17(11), pp.1383–1390.

Feld, G.K., Kintzer, A.F., Tang, I.I., Thoren, K.L., Krantz, B.A, 2012. Domain flexibility modulates the heterogeneous assembly mechanism of anthrax toxin protective antigen, *J Mol Biol.*, 415(1), pp.159-174.

Fiset, P.O. and Gounni, A.S., 2001. Antisense oligonucleotides: problems with use and solutions. *Rev Biol Biotech*, 1(2), p.27.

Frankel, A.E., Burbage, C., Fu, T., Tagge, E., Chandler, J. and Willingham, M.C., 1996. Ricin toxin contains at least three galactose-binding sites located in B chain subdomains 1 α , 1 β , and 2 γ . *Biochemistry*, 35(47), pp.14749-14756.

Froude, J.W., Thullier, P., Pelat, T., 2011. Antibodies Against Anthrax: Mechanism of Action and Clinical Application, *Toxins*, 3(11), pp.1433-1452.

Gao-Sheridan, S., Zhang, S., Collier, R.J., 2003. Exchange characteristics of calcium ions bound to anthrax protective antigen. *Biochemical and Biophysical Research Communications*, 300(1), pp.61-64.

Gardner, K.H., Pan, T., Narula, S., Rivera, E., Coleman, J.E., 1991. Structure of the binuclear metal-binding site in the GAL4 transcription factor, *Biochemistry*, 30(47), pp.11292-11302.

Gaur, R., Gupta, P.K., Goyal, A., Wels, W., & Singh, Y., 2002. Delivery of nucleic acid into mammalian cells by anthrax toxin. *Biochemical and Biophysical Research Communications*, 297(5), pp.1121–1127.

Geary, R.S., Baker, B.F. and Crooke, S.T., 2015. Clinical and preclinical pharmacokinetics and pharmacodynamics of mipomersen (Kynamro®): a second-generation antisense oligonucleotide inhibitor of apolipoprotein B. *Clinical pharmacokinetics*, 54(2), pp.133-146.

Goel, KA. 2015. Anthrax: A disease of biowarfare and public health importance, world Journal of Clinical Cases, 3(1):20-33.

Gogol, E.P., Akkaladevi, N., Szerszen, L., Mukherjee, S., Chollet-Hinton, L., Katayama, H., Pentelute, B.L., Collier, R.J. and Fisher, M.T., 2013. Three dimensional structure of the anthrax toxin translocon–lethal factor complex by cryo-electron microscopy. *Protein Science*, 22(5), pp.586-594.

Grimm, M. O. W., Kuchenbecker, J., Grösgen, S., Burg, V. K., Hundsdörfer, B., Rothhaar, T. L., Hartmann, T. (2011). Docosahexaenoic Acid Reduces Amyloid β Production via Multiple Pleiotropic Mechanisms. *The Journal of Biological Chemistry*, 286(16), 14028–14039.

Gruenberg, J. 2001. The endocytic pathway: a mosaic of domains. *Nature Reviews Molecular Cell Biology*, 2, 721-730 | doi:10.1038/35096054

Grunow, R., Verbeek, L., Jacob, D., Holzmann, T., Birkenfeld, G., Wiens, D., Reischl, U. (2012). Injection Anthrax—a New Outbreak in Heroin Users. *Deutsches Ärzteblatt International*, 109(49), pp.843–848.

Gupta, P.K., Moayeri, M., Crown, D., Fattah, R.J., Leppla, S.H., & Antopolsky, M., 2008. Role of N-Terminal Amino Acids in the Potency of Anthrax Lethal

Hansen, J. and Bross, P., 2010. A cellular viability assay to monitor drug toxicity. *Protein Misfolding and Cellular Stress in Disease and Aging: Concepts and Protocols*, pp.303-311. Factor. *PLoS ONE*, 3(9), pp.3130.

Hanks, S., Adams, S., Douglas, J., Arbour, L., Atherton, D.J., Balci, S., Bode, H., Campbell, M.E., Feingold, M., Keser, G., Kleijer, W., Mancini, G., McGrath, J.A., Muntoni, F., Nanda, A., Teare, M.D., Warman, M., Pope, M., Superti-Furga, A., Futreal, A., Rahman, N., 2003. Mutations in the Gene Encoding Capillary Morphogenesis Protein 2 Cause Juvenile Hyaline Fibromatosis and Infantile Systemic Hyalinosis. *American Journal of Human Genetics*, 73(4), pp.791–800.

Henderson, D.H., 1999. The looming of Threat of Bioterrorism, *Science*. 283(5406), pp.1279-1282.

Hendricks, K. A., Wright, M. E., Shadomy, S. V., Bradley, J. S., Morrow, M. G., Pavia, A. T., the Workgroup on Anthrax Clinical Guidelines. (2014). Centers for Disease Control and Prevention Expert Panel Meetings on Prevention and Treatment of Anthrax in Adults. *Emerging Infectious Diseases*, 20(2), e130687.

Holty, J.C., 2006. Systematic Review: A Century of Inhalational Anthrax Cases from 1900 to 2005. *Ann Intern Med*, 144(4), pp.144:270-280.

Hosten, T. A., Zhao, K., Han, H. Q., Liu, G., & He, X. H. (2014). Alicaforsen: An Emerging Therapeutic Agent for Ulcerative Colitis and Refractory Pouchitis. *Gastroenterology Research*, 7(2), 51–55. <http://doi.org/10.14740/gr599w>

Huotari, J., & Helenius, A. (2011). Endosome maturation. *The EMBO Journal*, 30(17), 3481–3500. <http://doi.org/10.1038/emboj.2011.286>

Inglesby, T. V., 1999. Anthrax: a possible case history, *emerging infectious diseases*, *Emerging Infectious Disease*, 5(4), pp.556-560

Inglesby, T.V, O'Toole, T., Henderson, D.A., Bartlett, J.G., Ascher, M.S., Eitzen, E., Friedlander, A.M., Gerberding, J., Haur, J., Huges, J., McDade, J., Osterholm, M.T., Parker, G., Perl, G., Russell, P.K., Tonat, K., 2002. Anthrax as a Biological Weapon, 2002 Updated Recommendations for Management, *The Journal of the American Medical Association*, 287(17), pp. 2236- 2252.

Janowiak, B.E., Fischer, A., Collier, R.J., 2010. Effects of introducing a single charged residue into the phenylalanine clamp of multimeric anthrax protective antigen. *Journal of Biological Chemistry*, 285(11), pp.8130-8137.

Jernigan, D. B., Raghunathan, P. L., Bell, B. P., Brechner, R., Bresnitz, E. A., Butler, J. C., The National Anthrax Epidemiologic Investigation Team. (2002). Investigation of Bioterrorism-Related Anthrax, United States, 2001: Epidemiologic Findings. *Emerging Infectious Diseases*, 8(10), 1019–1028.

Jernigan, J.A., Stephens, D.S., Ashfor, D.A., Omenaca, C., Topiel, M.S., Galraith, M., Tapper, M., Fisk., T.L., Zaki, S., Popovic, T., Meyer, R.F., Quinn, C.P., Harper, S.A., Fridkin, S.K., Sejvar, J.J., Shepard, C.W., McConnell, M., Guarner, J., Shieh, W.J., Malecki, J.M., Gerberding, J.J., Hughes, J.M., Perkins, B.A., 2001. Bioterrorism-Related Inhalational Anthrax: The First 10 Cases Reported in the United States, *Emerg Infect Dis*, 7(6), pp.933-44.

Jiang, J., Pentelute, B. L., Collier, R. J., & Zhou, Z. H. (2015). Atomic structure of anthrax PA pore elucidates toxin translocation. *Nature*, 521(7553), 545–549. <http://doi.org/10.1038/nature14247>

Jones, M.E., Vos, V., 2002. Anthrax and Wildlife, *Rev. sci. tech. Off. int. Epiz*, 21(2), pp.359-383.

Juliano, R.L., 2016. The delivery of therapeutic oligonucleotides. *Nucleic acids research*,

p.236.

Katayama, H., Janowiak, B. E., Brzozowski, M., Juryck, J., Falke, S., Gogol, E. P., Fisher, M. T. (2008). GroEL as a molecular scaffold for structural analysis of the anthrax toxin pore. *Nature Structural & Molecular Biology*, 15(7), pp.754–760.

Katayama, H., Wang, J., Tamac, F., Cholleta, L., Gogold, E.P., Collier, R.J., Fishera, M.T., 2010. Three-dimensional structure of the anthrax toxin pore inserted into lipid nanodiscs and lipid vesicles, *Proceedings of the National Academy of Sciences*, 107(8), pp.3453–3457

Katiyar, S., Joshi, S., & Lennarz, W. J. (2005). The Retrotranslocation Protein Derlin-1 Binds Peptide:N-Glycanase to the Endoplasmic Reticulum. *Molecular Biology of the Cell*, 16(10), 4584–4594. <http://doi.org/10.1091/mbc.E05-04-0345>

Keim, P., Smith, K. L., Keys, C., Takahashi, H., Kurata, T., & Kaufmann, A. (2001). Molecular Investigation of the Aum Shinrikyo Anthrax Release in Kameido, Japan. *Journal of Clinical Microbiology*, 39(12), pp.4566–4567.

Kintzer, A. F., Thoren, K. L., Sterling, H. J., Dong, K. C., Feld, G. K., Tang, I. I., Krantz, B. A. (2009). The Protective Antigen Component of Anthrax Toxin Forms Functional Octameric Complexes. *Journal of Molecular Biology*, 392(3), pp.614–629.

Kintzer, A.F., Sterling, H.J., Tang, I.I., Abdul-Gader, A., Miles, A.J., Wallace, B.A., Williams, E.R., & Krantz, B.A., 2010b. Role of the Protective Antigen Octamer in the Molecular Mechanism of Anthrax Lethal Toxin Stabilization in Plasma. *Journal of Molecular Biology*, 399(5), pp.741–758.

Kintzer, A.F., Sterling, H.J., Tang, I.I., Abdul-Gader, A., Miles, A.J., Wallace, B.A., Williams, E.R., Krantz, B.A., 2010a. Anthrax toxin receptor drives protective antigen oligomerization and stabilizes the heptameric and octameric oligomer by a similar mechanism. *PLoS ONE*, 5(11), pp.13888.

Kintzer, A.F., Tang, I.I., Schawel, A.K., Brown, M.J., Krantz, B.A., 2012. Anthrax toxin protective antigen integrates poly- γ -D-glutamate and pH signals to sense the optimal environment for channel formation. *Proc Natl Acad Sci U S A*, 109(45), pp.18378-18383.

Klimpel, K.R., Molloy, S.S., Thomas, G., Leppla, S.H., 1992. Anthrax toxin protective antigen is activated by a cell surface protease with the sequence specificity and catalytic properties of furin. *Proceedings of the National Academy of Sciences*, 89(21), pp.10277-10281.

Kneen, M., Farinas, J., Li, Y., Verkman, A.S., 1988. Green fluorescent protein as a noninvasive intracellular pH indicator. *Biophys J*, 74(3), pp.1591-9.

Kole, R., Krainer, A.R. and Altman, S., 2012. RNA therapeutics: beyond RNA interference and antisense oligonucleotides. *Nature reviews Drug discovery*, 11(2), pp.125-140.

Krantz, B. A., Melnyk, R. A., Zhang, S., Juris, S. J., Lacy, D. B., Wu, Z., Collier, R. J.

(2005). A Phenylalanine Clamp Catalyzes Protein Translocation Through the Anthrax Toxin Pore. *Science (New York, N.Y.)*, 309(5735), 777–781.
<http://doi.org/10.1126/science.1113380>

Krantz, B.A., Finkelstein, A., Collier, R.J., 2006. Protein translocation through the anthrax toxin transmembrane pore is driven by a proton gradient. *Journal of Molecular Biology*, 355(5), pp.968-979.

Krantz, B.A., Trivedi, A.D., Cunningham, K., Christensen, K.A., & Collier, R.J., 2004. Acid-induced unfolding of the amino-terminal domains of the lethal and edema factors of anthrax toxin. *Journal of molecular biology*, 344(3), pp.739–756.

Krueger, S., Meuse, C.W., Majkrzak, C.F., Dura, J.A., Berk, N.F., Tarek, M. and Plant, A.L., 2001. Investigation of hybrid bilayer membranes with neutron reflectometry: probing the interactions of melittin. *Langmuir*, 17(2), pp.511-521.

Kummerfeldt, C. E. (2014). Raxibacumab: potential role in the treatment of inhalational anthrax. *Infection and Drug Resistance*, 7, 101–109.

Kushner, N., Zhang, D., Touzjian, N., Essex, M., Lieberman, J. and Lu, Y., 2003. A fragment of anthrax lethal factor delivers proteins to the cytosol without requiring protective antigen. *Proceedings of the National Academy of Sciences*, 100(11), pp.6652–6657.

Kushner, N., Zhang, D., Touzjian, N., Essex, M., Lieberman, J., & Lu, Y., 2003. A fragment of anthrax lethal factor delivers proteins to the cytosol without requiring protective antigen. *Proceedings of the National Academy of Sciences*, 100(11), pp.6652–6657.

Kutrowska, B. W., Narczyk, M., Buszko, A., Bzowska, A., & Clark, P. L. (2007). Folding and unfolding of a non-fluorescent mutant of green fluorescent protein. *Journal of Physics. Condensed Matter: An Institute of Physics Journal*, (28), 285223. Advance online publication. <http://doi.org/10.1088/0953-8984/19/28/285223>

Kynde, S.A., Skar-Gislinge, N., Pedersen, M.C., Midtgaard, S.R., Simonsen, J.B., Schweins, R., Mortensen, K. and Arleth, L., 2014. Small-angle scattering gives direct structural information about a membrane protein inside a lipid environment. *Acta Crystallographica Section D: Biological Crystallography*, 70(2), pp.371-383.

Lacy, B.D., Mourez, M., Fouassire, A., Collier, J.R., 2002., Mapping the Anthrax Protective Antigen Binding Site on the Lethal and Edema Factors. *The Journal Of Biological Chemistry*, 277(4), pp. 3006–3010.

Lacy, D.B., Collier, R. J., 2002. Structure and function of anthrax toxin, *Curr Top Microbiol Immunol*. 271(3), pp.61-85.

Lacy, D.B., Wigelsworth, D.J., Melnyk, R.A., Harrison, S.C., & Collier, R.J., 2004. Structure of heptameric protective antigen bound to an anthrax toxin receptor: a role for receptor in pH-dependent pore formation. *Proceedings of the National Academy of Sciences*, 101(36), pp.13147–13151.

Le Brun, A.P., Haigh, C.L., Drew, S.C., James, M., Boland, M.P. and Collins, S.J., 2014. Neutron reflectometry studies define prion protein N-terminal peptide membrane binding. *Biophysical journal*, 107(10), pp.2313-2324.

Lee, Yan, et al. "A protein nanocarrier from charge-conversion polymer in response to endosomal pH." *Journal of the American Chemical Society* 129.17 (2007): 5362-5363.

Leppla, S. H. (1982). Anthrax toxin edema factor: a bacterial adenylate cyclase that increases cyclic AMP concentrations of eukaryotic cells. *Proceedings of the National Academy of Sciences of the United States of America*, 79(10), pp. 3162–3166.

Leuber M, Kronhardt A, Tonello F, Dal Molin F, Benz R (2008) Binding of N-terminal fragments of anthrax edema factor (EF(N)) and lethal factor (LF(N)) to the protective antigen pore. *Biochim Biophys Acta* 1778: 1436–1443.M.

Levin, D.B., de Amorim, G.V., 2003. Potential for Aerosol Dissemination of Biological Weapons: Lessons from Biological Control of Insects, *Biosecur Bioterror* 1(1), pp.1-3.

Liao, X., Rabideau, A.E. and Pentelute, B.L., 2014. Delivery of antibody mimics into mammalian cells via anthrax toxin protective antigen. *Chembiochem*, 15(16), pp.2458-2466.

Liu, H., Bergman, N. H., Thomason, B., Shallom, S., Hazen, A., Crossno, J., ... Hanna, P. C. (2004). Formation and Composition of the *Bacillus anthracis* Endospore . *Journal of Bacteriology*, 186(1), 164–178. <http://doi.org/10.1128/JB.186.1.164-178.2004>

Liu, S., Crown, D., Miller-Randolph, S., Moayeri, M., Wang, H., Hu, H., Morley, T., & Leppla, S.H., 2009. Capillary morphogenesis protein-2 is the major receptor mediating lethality of anthrax toxin in vivo. *Proceedings of the National Academy of Sciences*, 106(30), pp.12424–12429.

Liu, S., Moayeri, M., & Leppla, S. H. (2014). Anthrax lethal and edema toxins in anthrax pathogenesis. *Trends in Microbiology*, 22(6), 317–325. <http://doi.org/10.1016/j.tim.2014.02.012>

Liu, S., Zhang, Y., Hoover, B., & Leppla, S. H. (2013). The Receptors that Mediate the Direct Lethality of Anthrax Toxin . *Toxins*, 5(1), pp. 1–8.

Liu, S., Zhang, Y., Moayeri, M., Liu, J., Crown, D., Fattah, R., ... Leppla, S. H. (2013). Key tissue targets responsible for anthrax toxin-induced-lethality. *Nature*, 501(7465), 63–68. <http://doi.org/10.1038/nature12510>

Lundin, K.E., Gissberg, O. and Smith, C.E., 2015. Oligonucleotide therapies: the past and the present. *Human gene therapy*, 26(8), pp.475-485.

Mamedov, T., Chichester, J. A., Jones, R. M., Ghosh, A., Coffin, M. V., Herschbach, K., Yusibov, V. (2016). Production of Functionally Active and Immunogenic Non-Glycosylated Protective Antigen from *Bacillus anthracis* in *Nicotiana benthamiana* by Co-Expression with Peptide-N-Glycosidase F (PNGase F) of *Flavobacterium meningosepticum*. *PLoS ONE*, 11(4), e0153956.

<http://doi.org/10.1371/journal.pone.0153956>

Martchenko, M., Jeong, S.-Y., & Cohen S.N., 2010. Heterodimeric integrin complexes containing $\beta 1$ -integrin promote internalisation and lethality of anthrax toxin. *Proceeding of the National Academy of Science*, 107(35), pp.15583-15588.

Maynard, J.A., Maassen, C.B., Leppla, S.H., Brasky, K., Patterso, J.L., Iverson, B.L., Georgiou, G., 2002. Protection against anthrax toxin by recombinant antibody fragments correlates with antigen affinity, *Nature Biotechnology*, 20(6), pp.597-601.

Mehra, V., Khanna, H., Chandra, R. and Singh, Y., 2001. Anthrax-toxin-mediated delivery of a 19 kDa antigen of *Mycobacterium tuberculosis* into the cytosol of mammalian cells. *Biotechnology and applied biochemistry*, 33(2), pp.71-74.

Miller, C.J., Elliot, J.L., Collier, R.J., 1999. Anthrax protective antigen: prepore-to-pore conversion. *Biochemistry*, 38(32), pp. 10432-10441.

Milne, J.C., Blanket, S.R., Hanna, P.C. and Collier, R.J., 1995. Protective antigen-binding domain of anthrax lethal factor mediates translocation of a heterologous protein fused to its amino-or carboxy-terminus. *Molecular microbiology*, 15(4), pp.661-666.

Moayeri, M., Leppla, S.H., 2004. The roles of anthrax in pathogenesis, *Current Opinion in Microbiology*, 7(1), pp.19-24

Moayeri, M., Wiggins, J.F., Leppla, S.H., 2007. Anthrax Protective Antigen Cleavage and Clearance from the Blood of Mice and Rats. *Infection and Immunity*, 75(11), pp.5175-5184.

Mogridge, J., Cunningham, K., Lacey, D.B., Mourez, M., Collier, R.J., 2002. The lethal and edema factors of anthrax toxin bind only to oligomeric forms of the protective antigen, *Proceedings of the National Academy of Sciences*, 99(10), pp.7045-7048.

Mogridge, J., Mourez, M., Collier, R.J., 2001. Involvement of Domain 3 in Oligomerization by the Protective Antigen Moiety of Anthrax Toxin. *Journal of Bacteriology*, 183(6), pp.2111-2116.

Mohammed, A.F., Abdul-Wahid, A., Huang, E.H.B., Bolewska-Pedyczak, E., Cydzik, M., Broad, A.E. and Gariépy, J., 2012. The *Pseudomonas aeruginosa* exotoxin A translocation domain facilitates the routing of CPP-protein cargos to the cytosol of eukaryotic cells. *Journal of Controlled Release*, 164(1), pp.58-64.

Molin, F.D., Tonello, F., Ladant, D., Zornetta, I., Zamparo, I., Benedetto, G.D., Zaccolo, M., Montecucco, C., 2006. Cell entry and cAMP imaging of anthrax edema toxin, *EMBO*, 25(22), pp.5405-5413

Munsell, E., L Ross, N. and O Sullivan, M., 2016. Journey to the center of the cell: Current nanocarrier design strategies targeting biopharmaceuticals to the cytoplasm and nucleus. *Current pharmaceutical design*, 22(9), pp.1227-1244.

Nablo, B.J., Panchal, R.G., Bavari, S., Nguyen, T.L., Guissio, R., Ribot, Wil., Friedlander, A., Chabot, D., Reiner, J.E., Robertson, J.W.F., Balijepalli, A., Halverson,

K.M., Kasianowicz, J.J., 2013. Anthrax toxin-induced rupture of artificial lipid bilayer membranes, *THE JOURNAL OF CHEMICAL PHYSICS*, 139(6), pp.065101

Neumeyer, T., Tonello, F., Molin, F.D, Schiffler, B., Benz, R., 2006. Anthrax Edema Factor, Voltage-dependent Binding to the Protective Antigen Ion Channel and Comparison to LF Binding: *The Journal of Biological Chemistry*, 281(43), pp.32335–32343.

Nestorovich, E.M. and Bezrukov, S.M., 2014. Designing inhibitors of anthrax toxin. *Expert opinion on drug discovery*, 9(3), pp.299-318.

Nguyen, T., Nancy, C., 2010. Public Health and Environmental Response to the First Case of Naturally Acquired Inhalational Anthrax in the United States in 30 Years: Infection of a New York City Resident Who Worked With Dried Animal Hides, *Journal of Public Health Management & Practice* 16(3):189-200. doi: 10.1097/PHH.0b013e3181ca64f2

Nguyen, T.L. 2004. Three-dimensional Model of the Pore Form of Anthrax Protective Antigen. Structure and Biological Implications, *Journal of Biomolecular Structure and Dynamics*, 22(3), pp. 253-265

Pannifer, A.D., Wong, T.Y., Schwarzenbacher, R., Renatus, M., Petrosa, C., Bienkowska, J., Lacy, D.B., Collier, R.J., Park, S., Leppla, S.H., Hanna, P., Liddington, R.C., 2001. Crystal structure of the anthrax lethal factor. *Nature*, 414, pp. 229-233.

Paul D.R. Dyer, Thomas R. Shepherd, Alexander S. Gollings, Susan A. Shorter, Monique A.M. Gorrington-Patrick, Chun-Kit Tang, Beatrice N. Cattoz, Les Baillie, Peter C. Griffiths, Simon C.W. Richardson, 2015. Disarmed anthrax toxin delivers antisense oligonucleotides and siRNA with high efficiency and low toxicity, *Journal of Controlled Release*, 220(A):316-328.

Pentelute, B. L., Barker, A. P., Janowiak, B. E., Kent, S. B. H., & Collier, R. J., 2010. A semisynthesis platform for investigating structure-function relationships in the N-terminal domain of the anthrax lethal factor. *ACS Chemical Biology*, 5(4), pp.359–364.

Petosa, C., Collier, J.R., Klimpel, K.R., Leppla, S.H., Liddington, R.C., 1997. Crystal Structure of the Anthrax toxin Protective Antigen, *Nature*, 385(3) pp.833-838.

Puhar, A., Montecucco, C., 2007. Where and how do anthrax toxins exit endosomes to intoxicate host cells. *Trends in Microbiology*, 15(11), pp. 477-482.

Rainey, G.J.A., Wigelsworth, D.J., Ryan, P., Scobie, H.M., Collier, R.J., & Young, J.A.T., 2005. Receptor-specific requirements for anthrax toxin delivery into cells. *Proceeding of the National Academy of Science*, 102,(37), pp.13278-13283.

Qa'dan, M., Christensen, K.A., Zhang, L., Roberts, T.M. and Collier, R.J., 2005. Membrane insertion by anthrax protective antigen in cultured cells. *Molecular and cellular biology*, 25(13), pp.5492-5498.

Ren, G., Quispe, J., Leppla, S.H. and Mitra, A.K., 2004. Large-scale structural changes accompany binding of lethal factor to anthrax protective antigen: a cryo-electron

microscopic study. *Structure*, 12(11), pp.2059-2066.

Schiffmiller, A. and Finkelstein, A., 2015. Ion conductance of the stem of the anthrax toxin channel during lethal factor translocation. *Journal of Molecular Biology*, 427(6), pp.1211-1223.

Schuler, M.A., Denisov, I.G. and Sligar, S.G., 2013. Nanodiscs as a new tool to examine lipid–protein interactions. *Lipid-Protein Interactions: Methods and Protocols*, pp.415-433.

Seddon, A.M., Curnow, P. and Booth, P.J., 2004. Membrane proteins, lipids and detergents: not just a soap opera. *Biochimica et Biophysica Acta (BBA)-Biomembranes*, 1666(1), pp.105-117.

Sellman, B.R., Nassi, S. & Collier, R.J., 2001. Point mutations in anthrax protective antigen that block translocation. *The Journal of Biological Chemistry*, 276(11), pp.8371–8376.

Sharma, V.K, Sharma R.K, Singh S.K, 2014. Antisense oligonucleotides: modifications and clinical trials, *Medicinal Chemical Communications*. 5, 1454-1471.

Shen, H.H., Leyton, D.L., Shiota, T., Belousoff, M.J., Noinaj, N., Lu, J., Holt, S.A., Tan, K., Selkrig, J., Webb, C.T. and Buchanan, S.K., 2014. Reconstitution of a nanomachine driving the assembly of proteins into bacterial outer membranes. *Nature communications*, 5, p.5078.

Shen, Y., Zhukovskaya, N. L., Zimmer, M. I., Soelaiman, S., Bergson, P., Wang, C.-R., Tang, W.-J. (2004). Selective inhibition of anthrax edema factor by adefovir, a drug for chronic hepatitis B virus infection. *Proceedings of the National Academy of Sciences of the United States of America*, 101(9), 3242–3247.
<http://doi.org/10.1073/pnas.0306552101>.

Singh, B., Prasad, S. 2008. Modelling of Economic Losses due to Some Important Diseases in Goats in India . *Agricultural Economics Research Review* , 21, 297-302.

Sirisanthana, T., Brown, A.E., 2002. Anthrax of the Gastrointestinal Tract, *Emerging Infectious Diseases*, 8(7), pp.649-651.

Slater, L. H., Hett, E. C., Clatworthy, A. E., Mark, K. G., & Hung, D. T., 2013. CCT chaperonin complex is required for efficient delivery of anthrax toxin into the cytosol of host cells. *Proceedings of the National Academy of Sciences of the United States of America*, 110(24), pp.9932–9937.

Spencer, R. C. (2003). *Bacillus anthracis*. *Journal of Clinical Pathology*, 56(3), pp. 182–187.

St.Croix, B., Rago, C., Velculescu, V., Traverso, G., Romans. K.E., Montgomery, E., Lal, A., Riggins, G.J., Lengaur, C., Vogelstein, B., Kinzler, K.W., 2000. Genes expressed in human tumor endothelium, *Science*, 289(5482), pp.1197-1202.

Sun, J., Lang, A.E., Aktories, K., Collier, R.J., 2008. Phenylalanine-427 of anthrax protective antigen functions in both pore formation and protein. *Proceedings of the National Academy of Sciences*, 105(11), pp. 4346-4351.

Takahashi, H., Keim, P., Kaufmann, A. F., Keys, C., Smith, K. L., Taniguchi, K....Kurata, T. (2004). Bacillus anthracis Bioterrorism Incident, Kameido, Tokyo, 1993. *Emerging Infectious Diseases*, 10(1), 117-120.

Tang, W.J., & Guo, Q., 2009. The Adenylyl Cyclase Activity of Anthrax Edema Factor. *Molecular Aspects of Medicine*, 30(6), pp.423–430.

Thoren, K. L., & Krantz, B. A., 2011. The unfolding story of anthrax toxin translocation. *Molecular Microbiology*, 80(3), pp.588–595.

Thoren, K. L., Worden, E. J., Yassif, J. M., & Krantz, B. A., 2009. Lethal factor unfolding is the most force-dependent step of anthrax toxin translocation. *Proceedings of the National Academy of Sciences of the United States of America*, 106(51), pp.21555–21560.

Verdurmen, W.P., Luginbühl, M., Honegger, A. and Plückthun, A., 2015. Efficient cell-specific uptake of binding proteins into the cytoplasm through engineered modular transport systems. *Journal of Controlled Release*, 200, pp.13-22.

Wheelis, M., Casagrande, R., Madden, L.V., 2002. Biological Attack on Agriculture: Low-Tech, High-Impact Bioterrorism, *BioScience* , 52(7), pp.569-576.

Williams, A.S., Lovell, S., Anbanandam, A., El-Chami, R., Bann, J.G., 2009. Domain 4 of the anthrax protective antigen maintains structure and binding to the host receptor CMG2 at low pH. *Protein Science*, 18(11), pp. 2277-2286.

Wong, E., & Goldberg, T. (2014). Mipomersen (Kynamro): A Novel Antisense Oligonucleotide Inhibitor for the Management of Homozygous Familial Hypercholesterolemia. *Pharmacy and Therapeutics*, 39(2), 119–122.

Wood, S.L., Brewer, F., Ellison, R., Biggio, J.R. and Edwards, R.K., 2016. Prenatal carrier screening for spinal muscular atrophy. *American Journal of Perinatology*, 33(12), pp.1211-1217.

Wynia-Smith, S.L., Brown, M.J., Chirichella, G., Kemalyan, G., Krantz, B.A. 2012. Electrostatic Ratchet in the Protective Antigen Channel Promotes , *The Journal of Biological chemistry*, 287, pp. 43753-43764.

Young, J.A.T., Collier, R.J., 2007. Anthrax Toxin: Receptor Binding, Internalization and Translocation. *Annual Review of Biochemistry*, 76, pp.243-265.

Zhang, S., Finkelstein, A., Collier, R.J., 2004 A. Evidence that translocation of anthrax toxin's lethal factor is initiated by entry of its N terminus into the protective antigen channel. *Proceedings of the National Academy of Sciences*, 101(48), 1232-1241.

Zhang, S., Udho, E., Wu, Z., Collier, R. J., & Finkelstein, A., 2004. Protein Translocation through Anthrax Toxin Channels Formed in Planar Lipid Bilayers. *Biophysical Journal*, 87(6), 3842–3849.

Zornetta, I., Brandi, L., Janowiak, B., Molin, F.D., Tonello, F., Collier J.R., Montecucco C. 2010. Imaging the cell entry of the anthrax oedema and lethal toxins with fluorescent protein chimeras, *Cellular microbiology*, 12(10), 1435–1445.

Chapter 9 Appendices

9.1 Plasmid sequencing

Plasmid sequences were evaluated using mega-align. For each sequence, the data was analysed for an area encoding the ORF and the plasmid sequence to determine correct orientation, and the correct sequence of the insert. The sequences below are the ORF for the gene, which was sequenced and assembled.

LFn-GAL4

```
ATGGGTAAACCGATTCCGAACCCGCTGCTGGGCCTGGACTCTACTATGGAACGCAACAAAAC
TCAGGAGGAACACCTGAAAGAGATCATGAAACACATTGTTAAAATCGAGGTGAAAGGCGAAG
AAGCGTTAAAAAGGAGGCTGCCGAAAAGCTGCTGGAGAAGGTACCGTCTGATGTGCTGGAA
ATGTATAAAGCGATTGGTGGCAAAATCTACATCGTGGATGGTGATATTACCAAACACATCTC
CCTGGAAGCACTGAGCGAAGACAAGAAGAAGATCAAAGATATCTACGGCAAGGACGCGCTGC
TGCACGAGCATTACGTTTACGCAAAAAGAAGTTACGAACCGGTGCTGGTTATCCAGTCCAGC
GAGGATTACGTCGAAAATACGGAAAAAGCTCTGAACGTATATTACGAAATTGGTAAAATCCT
GTCTCGTGACATTCTGAGCAAAATTAACCAACCTTATCAGAAGTTCCTGGACGTTCTGAACA
CCATCAAAAACGCTTCTGACTCCGACGGCCAGGACCTGCTGTTCACTAATCAGCTGAAAGAAC
ATCCGACCGATTTCTCTGTAGAATTCCTGGAACAGAACTCTAACGAGGTCCAAGAAGTTTTT
GCCAAAGCATTTCGCGTACTACATCGAGCCGACGATCGCGACGTGCTGCAGCTGTACGCTCCA
GAAGCCTTCAACTATATGGACAAATCAATGAACAAGAAATCAACCTGTCTATGAAACTGCT
GTCCTCCATCGAACAGGCTTGCATATCTGTGCTGTAAGAACTGAAATGCTCTAAAGAAA
AACCGAAATGCGCGAAATGCCTGAAAAACAACCTGGGAATGTCGCTATTCCCCTAAAACCAA
CGTTCTCCACTGACCCGTGCGCACCTGACCGAAGTAGAATCCCGTCTGGAACGTCTGGAGCAG
CTGTTTCTGCTGATTTTCCCGCGTGAAGACCTGGACATGATCCTGAAAATGGATAGCCTGCA
GGATATCAAAGCACTGCTGACCGGTCTGTTTGTGCAGGACAACGTCAACAAAGACGCTGTTA
CTGATCGCCTGGCGAGCGTTGAAACTGATATGCCGCTGACCTGCGTCAGCACCGTATCTCCG
CAACGAGCTCCAGCGAAGAATCTAGCAACAAAGGTCAGCGCCAGCTGACCGTTAGCCACCACC
ATCACCACCACTAA
```

LFn-RTAC

```
GAAGGAGATATACATATGCATCATCACCATCACCATGGTAAGCCTATCCCTAACCTCTCCTC
GGTCTCGATTCTACGAAAACCTGTATTTTCAGGGAATTGATCCCTTcaccATGGAACGTAAC
AAGACGCAGGAAGAGCACCTGAAGGAGATCATGAAGCACATCGTCAAATCGAGGTCAAAGG
TGAGGAGGCTGTCAAGAAAGAGGCTGCTGAGAACTGCTGGAGAAAGTCCCGAGCGATGTGC
TGGAGATGTACAAAGCAATCGGCGGTAAAATCTATATCGTGGACGGCGACATCACGAAACAC
ATCAGCCTGGAGGCACTGTCTGAAGACAAAAAGAAAATCAAAGACATCTATGGTAAAGACGC
CCTGCTGCACGAGCACTACGTGTACGAAAAGAAGGTTACGAACCGGTGCTGGTAATCCAGT
CCTCCGAAGACTACGTGGAAAACACCGAAAAAGCCCTGAACGTGTAACGAAATCGGTAAA
ATCCTGAGCCGTGACATCCTGAGCAAAATCAACCAGCCATACCAGAAATTCCTGGACGTGCTG
AACACGATCAAAAACGCCAGCGACAGCGACGGCCAGGACCTGCTGTTACCAACCAGCTGAA
AGAACACCCAACCGACTTCAGCGTGGAAATTCCTGGAACAGAACTCCAACGAAGTTCAGGAAG
TTTTCGCCAAAGCTTTCGCCTACTACATCGAACCTCAGCACCGCGACGTTCTGCAACTGTACG
CACCAGAAGCATTCAACTACATGGATAAGTTCAACGAACAGGAAATCAACCTGAGCATGATC
TTCCCGAAACAGTACCCGATCATCAACTTACCAGCTGCCGGTGAACCGTTCAGTCTACACC
AACTTCATCCGTGCAGTTCGCGGTGCTCTGACCACTGGTGCAGATGTTTCGTCATGATATCCCG
```

GTACTGCCGAATCGTGTAGGTCTGCCGATTAATCAACGTTTCATCCTGGTAGAACTGAGCAA
CCACGCAGAACTGTCCGTTACCCTGGCTCTGGATGTTACTAACGCTTACGTTGTAGGTTACCG
TGCTGGTAACTCCGCTTATTTCTTCCATCCGGATAACCAGGAAGATGCGGAAGCTATCACTCA
TCTGTTACCGATGTTCCAGAACCGCTATACCTTTGCGTTTGGCGGCAACTATGATCGCCTGGA
ACAGCTGGCTGGTAACCTGCGTGAACATCGAACTGGGTAACGGCCCGCTGGAAGAAGCTA
TTTCTGCGCTGTATTACTACTCCACCGGCGCACTCAACTGCCGACTCTGGCGCGTTCTTTCA
TTATTTGTATCCAAATGATTTCCGAAGCGGCGCGTTTTCAGTATATTGAAGGCGAAATGCGC
ACCCGTATTTCGCTATAACCGCCGTTCCGCGCCGGATCCGTCTGTAATTACTCTGGAAAATTCT
TGGGGCCGCTGTCTACCGCGATTCAAGAATCTAATCAGGGCGCGTTTGGCTCTCCGATTAG
CTGCAGCGTCGTAATGGCTCCAAATTTCTGTTTATGATGTTTCTATTCTGATTCCGATTATT
GCGCTGATGGTTTATCGCTGCGCGCCGCTCCTTCTTCTCAGTTTTAA

LFn-YFP

GAAGGAGATATACATATGCATCATCACCATCACCATGGTAAGCCTATCCCTAACCTCTCCTC
GGTCTCGATTCTACGGAAAACCTGTATTTTCAGGGAATTGATCCCTTcaccATGGAACGCAAC
AAAACCTCAGGAGGAACACCTGAAAGAGATCATGAAACACATTGTTAAAATCGAGGTGAAAG
GCGAAGAAGCGGTTAAAAGGAGGCTGCCGAAAAGCTGCTGGAGAAGGTACCGTCTGATGTG
CTGGAAATGTATAAAGCGATTGGTGGCAAATCTACATCGTGGATGGTGATATTACCAAACA
CATCTCCCTGGAAGCACTGAGCGAAGACAAGAAGAAGATCAAAGATATCTACGGCAAGGACG
CGCTGCTGCACGAGCATTACGTTTACGCAAAGAAGGTTACGAACCGGTGCTGGTTATCCAG
TCCAGCGAGGATTACGTCGAAAATACGGAAAAGCTCTGAACGTATATTACGAAATTGGTAA
AATCCTGTCTCGTGACATTCTGAGCAAAATTAACCAACCTTATCAGAAGTTCCTGGACGTTT
TGAACACCATCAAAAACGCTTCTGACTCCGACGGCCAGGACCTGCTGTTCACTAATCAGCTGA
AGAACATCCGACCGATTTCTCTGTAGAATTCCTGGAACAGAACTCTAACGAGGTCCAAGAA
GTTTTTGCCAAAGCATTTCGCGTACTACATCGAGCCGAGCATCGCGACGTGCTGCAGCTGTAC
GCTCCAGAAGCCTTCAACTATATGGACAAATTCAATGAACAAGAAATCAACCTGTCTGTGAG
CAAGGGCGAGGAGCTGTTACCCGGGGTGGTGGCCATCCTGGTCCGAGCTGGACGGCGACGTAA
ACGGCCACAAGTTCAGCGTGTCCGGCGAGGGCGAGGGCGATGCCACCTACGGCAAGCTGACCC
TGAAGTTCATCTGCACCACCGGCAAGCTGCCCGTGCCCTGGCCCACCCTCGTGACCACCTTCG
GCTACGGCCTGAAGTGCTTCGCCCCTACCCCGACCACATGAAGCAGCAGCACTTCTTCAAGT
CCGCCATGCCCCAAGGCTACGTCCAGGAGCGCACCATCTTCTTCAAGGACGACGGCAACTACA
AGACCCGCGCCGAGGTGAAGTTCGAGGGCGACACCCTGGTGAACCGCATCGAGCTGAAGGGC
ATCGACTTCAAGGAGGACGGCAACATCCTGGGGCACAAGCTGGAGTACAACACTACAACAGCCA
CAACGTCTATATCATGGCCGACAAGCAGAAGAACGGCATCAAGGTGAACTTCAAGATCCGCC
ACAACATCGAGGACGGCAGCGTGCAGCTCGCCGACCACTACCAGCAGAACCCCCATCGGGC
ACGGCCCCGTGCTGCTGCCGACAACCACTACCTGAGCTACCAGTCCAAGCTGAGCAAAGACC
CCAACGAGAAGCGCGATCACATGGTCCTGCTGGAGTTCGTGACCGCCGCGGGATCACTCAG
GCATGGACGAGCTGTACAAG

LFn-mCherry

GAAGGAGATATACATATGCATCATCACCATCACCATGGTAAGCCTATCCCTAACCTCTCCTC
GGTCTCGATTCTACGGAAAACCTGTATTTTCAGGGAATTGATCCCTTcaccATGGAGCGTAAC
AAGACGCAAGAGGAACACCTGAAGGAAATCATGAAGCACATCGTCAAATCGAGGTCAAAGG
TGAGGAGGCAGTTAAGAAAGAGGCAGCAGAGAAACTGCTGGAGAAAGTGCCATCTGACGTTT
TGAAATGTACAAAGCGATCGGTGGTAAAATCTACATCGTCCGACGGTGACATCACGAAACAC
ATCAGCCTGGAGGCACTGTCTGAAGATAAAAAGAAAATCAAGGACATCTACGGTAAAGACCG
GCTGCTGCACGAGCACTACGTGTACGAAAAGAGGGTTACGAACCTGTGCTGGTAATCCAAT
CTTCTGAAGACTACGTGGAAAACACGGAAAAGCTCTGAACGTCTACTACGAAATCGGCAAA
ATCCTGTCCCGGACATCCTGTCTAAAATCAACCAGCCATACCAGAAATTCCTGGACGTGCTG

AACACCATTAAGAACGCTAGCGACAGCGACGGTCAAGATCTGCTGTTCACTAACCAACTGAA
AGAACACCCTACTGACTTCAGCGTGGAATTCCTGGAACAGAACTCTAACGAAGTGCAGGAAG
TGTTTCGAAAAGCGTTTCGCTTACTACATTGAACCACAGCACCGTGACGTTCTGCAGCTGTATG
CTCCGGAAGCTTCAATTACATGGACAAGTTCAACGAACAGGAAATTAACCTGAGCATGGTA
TCCAAAGGCGAAGAAGACAACATGGCCATTATCAAAGAGTTCATGCGCTTCAAAGTACACAT
GGAAGGCTCCGTTAACGGTCACGAATTCGAAATTGAGGGCGAAGGCGAAGGCCGTCCGTACG
AAGGTACTCAGACTGCTAAACTGAAAGTTACCAAAGGCGGTCCGCTGCCGTTTGCTGGGAT
ATTCTGTCTCCGCAGTTTATGTATGGTTCTAAAGCGTATGTTAAACATCCGGCCGATATTCCG
GACTATCTGAAACTGTCCTTTCCGGAAGGTTTCAAATGGGAACGCGTTATGAACTTTGAAGA
CGGCGGTGTTGTTACCGTTACCCAGGATTCTTCCCTGCAGGATGGTGAATTCATCTACAAAGT
TAAACTGCGTGGCACCAACTTTCCGAGCGATGGTCCGGTTATGCAGAAGAAAACCTATGGGTT
GGGAAGCGAGCTCCGAACGTATGTATCCGGAAGATGGTGCCTGAAAGGTGAAATCAAACAG
CGTCTGAAACTGAAAGATGGCGGCCATTATGATGCGGAAGTAAAAACCACCTACAAAGCGAA
GAAACCGGTACAGCTGCCGGGCGGTATAATGTAAACATCAAACCTGGATATTACCTCCATA
ATGAAGATTATACCATTTGTTGAACAGTATGAACGTGCCGAAGGCCCGCCATTCCACCG

LFn-GFP

GAAGGAGATATACATATGCATCATCACCATCACCATGGTAAGCCTATCCCTAACCTCTCCTC
GGTCTCGATTCTACGGAACCTGTATTTTCAGGGAATTGATCCCTTACCATGGAACGCAA
CAAACCTCAGGAGGAACACCTGAAAGAGATCATGAAACACATTGTTAAAATCGAGGTGAAAG
GCGAAGAAGCGGTTAAAAAGGAGGCTGCCGAAAAGCTGCTGGAGAAGGTACCGTCTGATGTG
CTGGAAATGTATAAAGCGATTGGTGGCAAATCTACATCGTGGATGGTGTATATTACCAAACA
CATCTCCCTGGAAGCACTGAGCGAAGACAAGAAGAAGATCAAAGATATCTACGGCAAGGACG
CGCTGCTGCACGAGCATTACGTTTACGCAAAAAGAAGGTTACGAACCGGTGCTGGTTATCCAG
TCCAGCGAGGATTACGTCGAAAATACGGA AAAAGCTCTGAACGTATATTACGAAATTGGTAA
AATCCTGTCTCGTGACATTCTGAGCAAAATTAACCAACCTTATCAGAAGTTCCTGGACGTTT
TGAACACCATCAAAAACGCTTCTGACTCCGACGGCCAGGACCTGCTGTTCACTAATCAGCTGA
AGAACATCCGACCGATTTCTCTGTAGAATTCCTGGAACAGAACTCTAACGAGGTCCAAGAA
GTTTTTGCCAAAGCATTTCGCTACTACATCGAGCCGACGATCGCGACGTGCTGCAGCTGTAC
GCTCCAGAAGCCTTCAACTATATGGACAAATTCATGAACAAGAAATCAACCTGTCTATGGC
CAGCAAAGGAGAAGAACTTTTCACTGGAGTTGTCCCAATTCTTGTGAATTAGATGGTGTATG
TTAATGGGCACAAATTTTCTGTCAAGTGGAGAGGGTGAAGGTGATGCAACATACGGAAAACCT
ACCCTTAAATTTATTTGCACTACTGGAAAACCTACCTGTTCCATGGCCAACTTGTCACTACT
CTCTCTTATGGTGTTCATGCTTTTCCCGTTATCCGGATCATATGAAACGGCATGACTTTTTTC
AAGAGTGCATGCCGAAGGTTATGTACAGGAACGCACTATATCTTTCAAaGATGACGGGAAC
TACAAGACGCGTGCTGAAGTCAAGTTTGAaGGtGaTACCCTtGTaATCGTATCGAGTTAA

LFn-Cys

GAAGGAGATATACATATGCATCATCACCATCACCATGGTAAGCCTATCCCTAACCTCTCCTC
GGTCTCGATTCTACGGAACCTGTATTTTCAGGGAATTGATCCCTTACCATGGAACGCAA
CAAACCTCAGGAGGAACACCTGAAAGAGATCATGAAACACATTGTTAAAATCGAGGTGAAAG
GCGAAGAAGCGGTTAAAAAGGAGGCTGCCGAAAAGCTGCTGGAGAAGGTACCGTCTGATGTG
CTGGAAATGTATAAAGCGATTGGTGGCAAATCTACATCGTGGATGGTGTATATTACCAAACA
CATCTCCCTGGAAGCACTGAGCGAAGACAAGAAGAAGATCAAAGATATCTACGGCAAGGACG
CGCTGCTGCACGAGCATTACGTTTACG
CAAAAGAAGGTTACGAACCGGTGCTGGTTATCCAGTCCAGCGAGGATTACGTGCAAAAATACG
GAAAAGCTCTGAACGTATATTACGAAATTGGTAAAATCCTGTCTCGTGACATTCTGAGCAA

AATTAACCAACCTTATCAGAAGTTCCTGGACGTTCTGAACACCATCAAAAACGCTTCTGACTC
CGACGGCCAGGACCTGCTGTTCACTAATCAGCTGAAAGAACATCCGACCGATTTCTCTGTAGA
ATTCCTGGAACAGAACTCTAACGAGGTCCAAGAAGTTTTTGCCAAAGCATTCGCGTACTACA
TCGAGCCGCAGCATCGCGACGTGCTGCAGCTGTACGCTCCAGAAGCCTTCAACTATATGGACA
AATTCAATGAACAAGAAATCAACCTGTCTAGATGCGCATAA

9.2 PropKa Output

SUMMARY OF THIS PREDICTION		SUMMARY OF THIS PREDICTION	
RESIDUE	pKa	RESIDUE	pKa
ASP 37 A	3.39	TYR 115 A	10.24
ASP 75 A	3.99	TYR 123 A	19.03
ASP 96 A	3.74	TYR 152 A	10.25
ASP 100 A	3.10	TYR 153 A	10.42
ASP 110 A	2.79	TYR 154 A	10.70
ASP 124 A	3.77	TYR 183 A	11.31
ASP 201 A	2.62	TYR 194 A	9.98
ASP 244 A	2.96	TYR 243 A	9.82
GLU 41 A	4.62	TYR 257 A	10.44
GLU 61 A	4.89	LYS 239 A	10.25
GLU 67 A	4.60	ARG 26 A	12.31
GLU 99 A	4.33	ARG 29 A	11.71
GLU 102 A	3.60	ARG 31 A	12.27
GLU 127 A	4.64	ARG 39 A	13.53
GLU 135 A	4.31	ARG 48 A	12.95
GLU 138 A	4.57	ARG 56 A	14.19
GLU 145 A	3.55	ARG 85 A	12.69
GLU 146 A	4.37	ARG 114 A	11.43
GLU 177 A	5.20	ARG 125 A	12.21
GLU 185 A	5.02	ARG 134 A	14.40
GLU 187 A	5.74	ARG 166 A	11.94
GLU 208 A	8.22	ARG 180 A	12.65
GLU 220 A	4.58	ARG 189 A	12.13
C- 263 A	3.36	ARG 191 A	11.86
HIS 40 A	6.06	ARG 193 A	12.46
HIS 65 A	6.60	ARG 196 A	12.31
HIS 94 A	6.24	ARG 197 A	13.17
HIS 106 A	6.59	ARG 213 A	12.15
CYS 171 A	12.14	ARG 234 A	12.72
CYS 259 A	9.60	ARG 235 A	13.62
TYR 6 A	11.30	ARG 258 A	11.87
TYR 21 A	14.09	N+	6 A
TYR 80 A	13.40		7.59
TYR 84 A	14.35		8.00
TYR 91 A	11.22		10.00

Protein charge of folded and unfolded state as a function of pH

pH	unfolded	folded
0.00	27.00	26.99
1.00	26.98	26.92
2.00	26.77	26.29
3.00	25.06	23.02
4.00	17.62	16.19
5.00	6.97	8.53
6.00	2.54	3.68
7.00	-0.11	0.66
8.00	-1.70	-1.06
9.00	-4.21	-2.52
10.00	-11.11	-5.90
11.00	-18.11	-11.98
12.00	-23.87	-20.40
13.00	-34.94	-29.49
14.00	-39.35	-35.19

The pI is 7.33 (folded) and 6.95 (unfolded)

Figure 9.21 PropKa output for LFn-RTAC.

9.3 Thermostability of LFn-GFP

LFn-GFP was analysed after being heat treated, at a variety of temperatures (70°C, 80°C, 85°C, 90°C), by fluorescent spectroscopy to give insights into the stability of the protein. Initially the excitation spectra had been taken for each LFn-GFP treated at a different temperature (Figure 9.31). The excitation maxima peak was taken at 468nm for all LFn-GFP samples and plotted, showing identical excitation spectra's. This was then used during measuring the emission spectra, as the excitation wavelength. Emission spectra were then measured. The emission spectra were plotted of each temperature, along with the emission spectra of LFn-GFP treated at 4°C (the optimal storage condition for proteins to limit degradation).

LFn-GFP treated under normal conditions (4°C) has two emission peaks 497 and 547 (Figure 9.31). LFn-GFP treated at increasing temperatures showed a considerable change in the protein fluorescent emission spectra. At 70°C there are two peaks at emission maxima's 500nm and 525nm (Figure 9.32). At 80°C there are two emission maxima's; 502nm 518nm (Figure 9.32). LFn-GFP treated at 85°C has a single emission maxima peak at 510nm (Figure 9.33) and at 90°C there is no peak (Figure 9.24). This has shown a distinctive difference in the emission spectra of LFn-GFP, treated at different temperatures, as compared to LFn-GFP that has been maintained at 4°C. This could indicate that the fluorophore has been irreversibly changed/destroyed as the temperature increases.

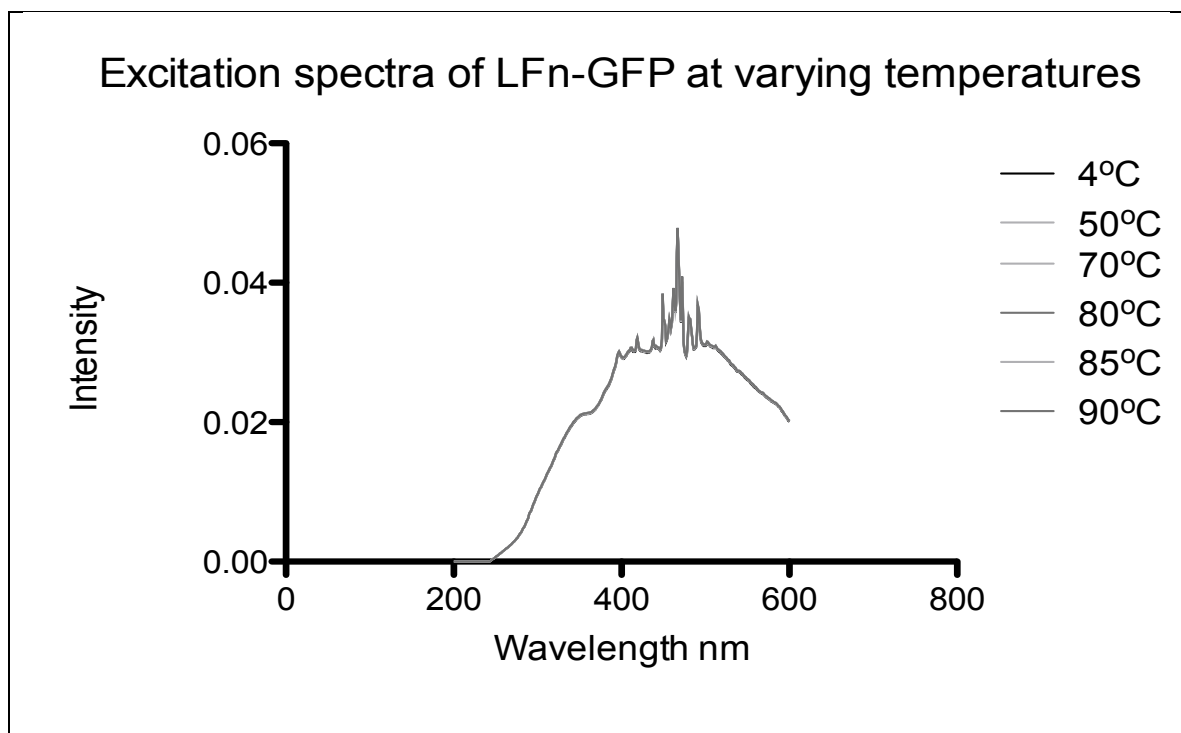


Figure 9.31 Excitation spectra of LFn-GFP.

Showing the excitation spectra of LFn-GFP, treated under normal conditions (4°C) and at increasing temperatures.

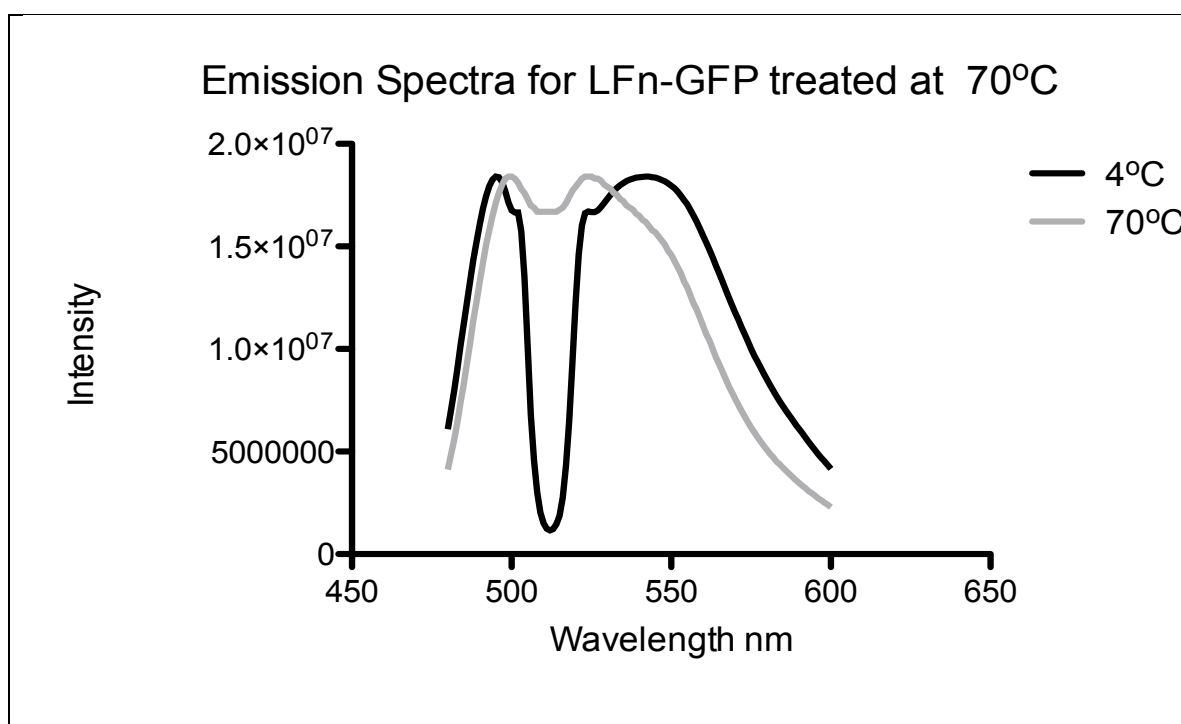


Figure 9.32 Emission spectra of LFn-GFP treated at 70°C.

Showing the emission spectra of LFn-GFP, treated under normal conditions (4°C) and heated treated at 70°C. Emission of LFn-GFP treated at 70°C is altered showing two emission maxima's, without a reduction in intensity in between, as is seen in LFn-GFP treated at 4°C, indicating there is some change of fluorophore structure.

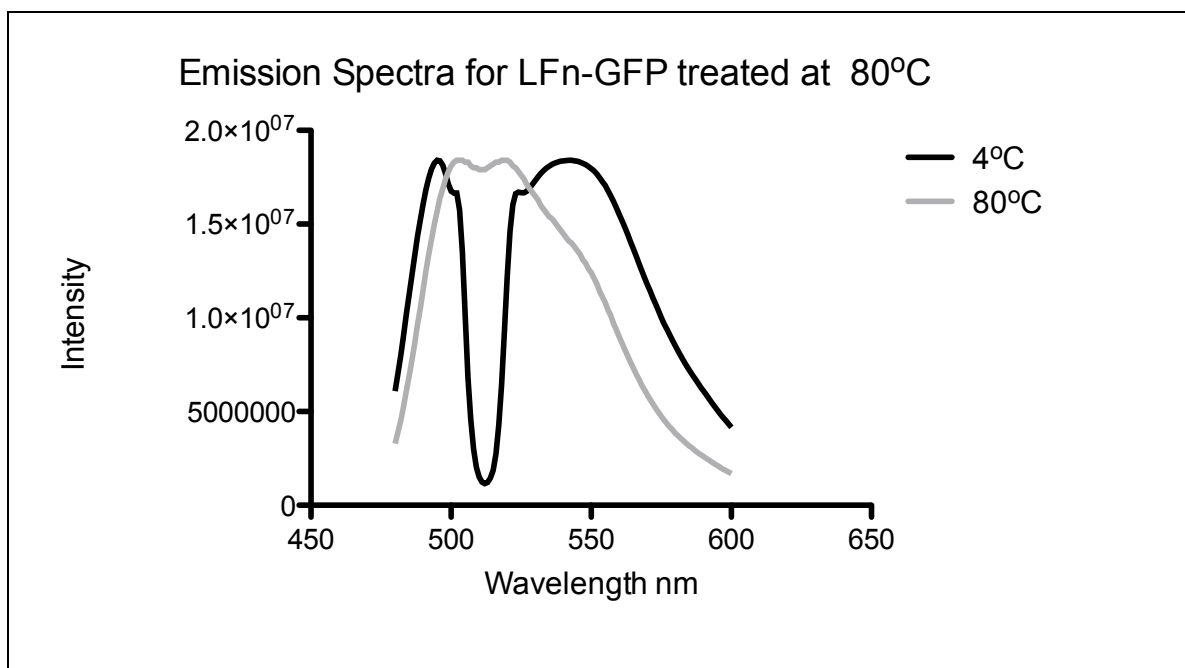


Figure 9.32 Emission spectra of LFn-GFP treated at 80°C. Showing the emission spectra of LFn-GFP, treated under normal conditions (4°C) and heated treated at 80°C. Emission of LFn-GFP treated at 80°C is altered showing two emission maxima's, with-out a reduction in intensity in between as is seen in LFn-GFP treated at 4°C, indicating there is some change of fluorophore structure.

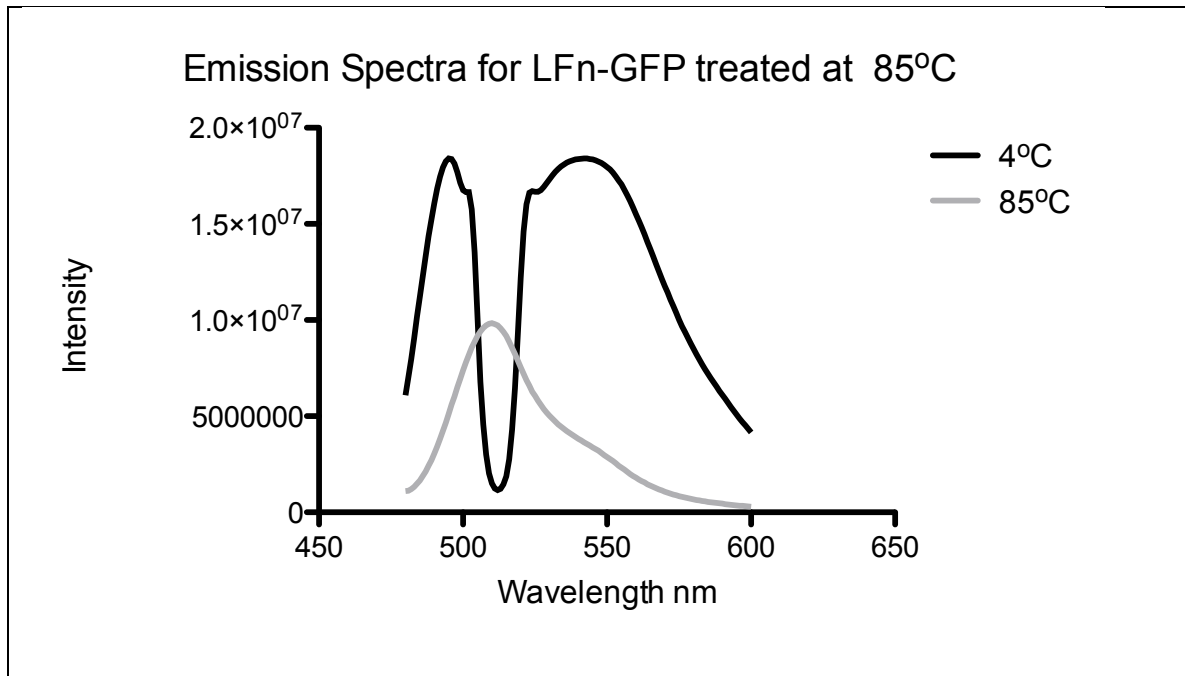


Figure 9.33 Emission spectra of LFn-GFP treated at 85°C. Showing the emission spectra of LFn-GFP, treated under normal conditions (4°C) and heated treated at 85°C. Emission of LFn-GFP treated at 85°C is show only a single emission maxima, indicating there is some loss of fluorophore structure.

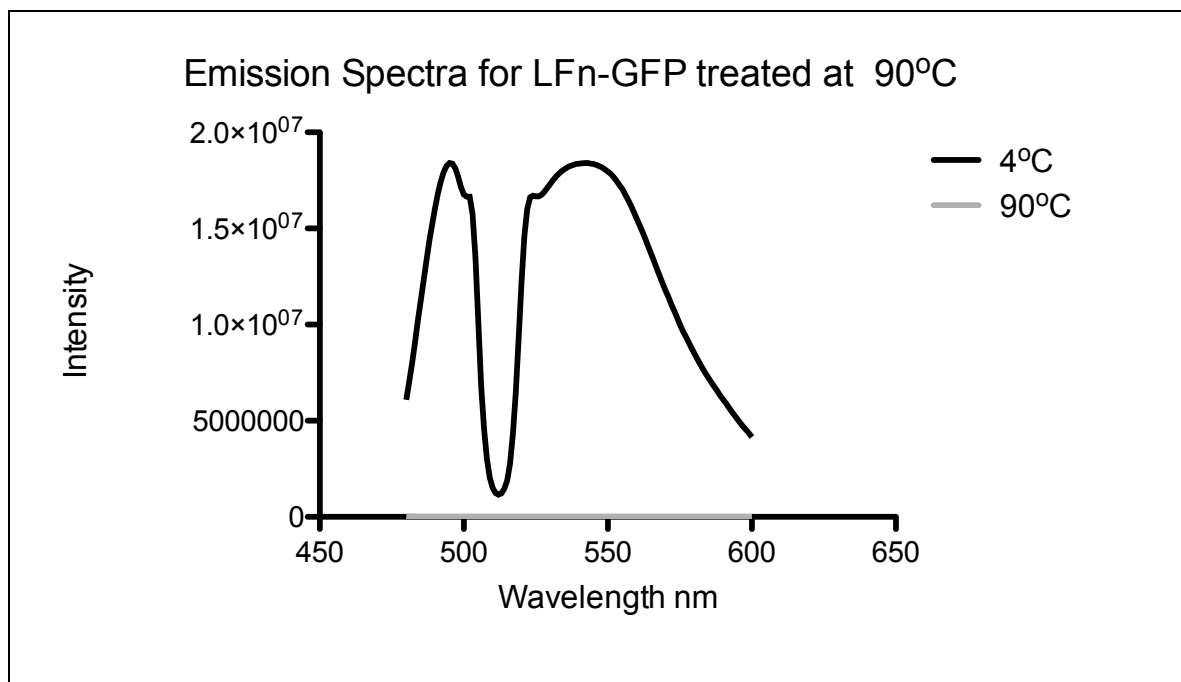


Figure 9.34 Emission spectra of LFn-GFP treated at 90°C.

Showing the emission spectra of LFn-GFP, treated under normal conditions (4°C) and heated treated at 90°C. There is no emission of LFn-GFP treated at 90°C, indicating there is total loss of fluorophore structure.

9.4 Radiolabelling of Oligonucleotides

To determine if these oligonucleotides can be radiolabelled, they were subjected to polynucleotide kinase 5' end labeling. Four different concentration of labelled oligonucleotide were run on a native page gel (Figure 3.332 B), and exposed to an X-ray film for two weeks (this was an optimised time line and the earliest possible detection of exposure time).

Although the experimental procedure of radio-labelling oligonucleotides will need further investigation to make the efficiency of incorporation, and purification of labelled oligonucleotide higher, this was successful. Further to this, analysis of the incorporation could be further improved by the use of a solid-state scintillation counter. This could have been a useful tool for future experiments to look at the quantitation of oligonucleotide translocated, and the protein knockdown that is associated with a quantified amount of ASO delivered to the cytosol.

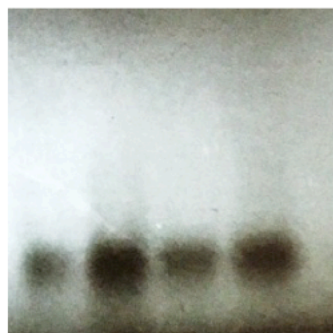
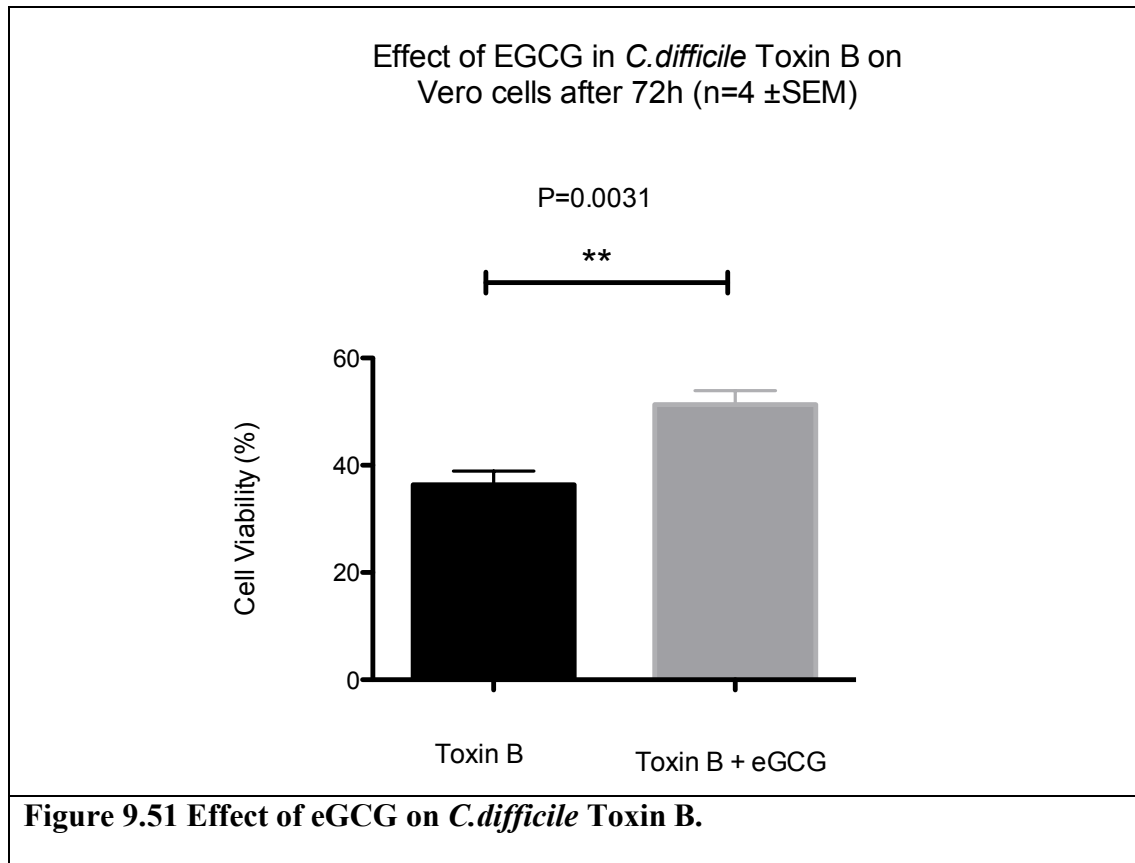


Figure 9.41 Characterisation of ASO.

ASO were labelled with phosphorus-32, and their detection measured by film radiographs.

9.5 Effects of EGCG on the A-B toxin *C.difficile*

Vero cells were treated with *C.difficile* protein toxin B. This demonstrated a significantly reduction of toxicity, when in the presence of eGCG ($p=0.0031$). Indicating that eGCG inhibits protein binding and cytotoxicity.



9.6 Scattering Length Density Calculator Outputs

Biomolecular Scattering Length Density Calculator

Table 1. The Total number of residues, Chemical composition, Molecular weight in kilodaltons, scattering length, scattering length density (ρ), molecular volume and number of exchangeable hydrogens for the inputed protein given it's sequence, % deuteration, % D₂O concentration and % exchange.

The sequence submitted was called "LFn-GFP"

The sequence submitted was

```
"MHHHHHHGKPIP NPLLGLDSTENLYFQGIDPFTMERNKTQEEHLKEIMKHIVKIEVK
GEEAVKKEAAEKLLEKVPDVL
MYKAIGGKIYIVDGDITKHISLEALSEDKKKIKDIYGKDALLHEHYVYAKEGYEPL
VIQSSEDYVENTEKALNVYYEIG
KILSRDILSKINQPYQKFLDVLNTIKNASDSDGQDLLFTNQLKEHPTDFSVEFLEQNSN
EVQEVFAKAFAYYIEPQHRDV
LQLYAPEAFNYMDKFNEQEINLSMASHGEELFTGVVPILVELDGDVNGHKFSVSGEG
EGDATYGKLTLLKFICTTGKLPVP
WPTLVTTFSYGVQCFSRYPDHMKRHDFFKSAMPEGYVQERTISFKDDGNYKTRAEV
KFEGDTLVNRIELKGIDFKEDGNI
LGHKLEYNYNSHNVIYITADKQKNGIKANFKIRHNIEDGVSQVLADHYQQNTPIGDGPV
LLPDNHYLSTQSALS KDPNEKRD HMLLEFVTAAGITHGMDELYKS."
```

The percentage of D₂O in the solution is "100"

The percentage of deuteration is "0"

The percentage of exchange is "90"

The concentration of the biomolecule in mg/ml is "0"

Total number of residues is 503.

Chemical composition C2580 N 673 O 755 S 12 H 3853.5 P 0

The molecular weight of the biomolecule is 58.381 kDa

The Scattering length is 2134.21 x10⁻¹²Å

The scattering length density (ρ_s) of the molecule is 3.041 x10⁻³Å⁻³

The scattering length density (ρ) of the solvent is $6.376 \times 10^6 \text{ \AA}^{-3}$

The molecular volume is 70174.3 \AA^3

The number of exchangeable hydrogens at pH 7.0 is 858.5

The density of the biomolecule is 1.38 g/ml

The estimate of intensity at zero angle $I(0)$ of the biomolecule is 0 cm^3

Figure 1. The scattering length density (ρ) of the inputed protein (it's sequence, % deuteration and % exchange) as a function of increasing D₂O concentration (from 0 to 100% in 5% intervals).

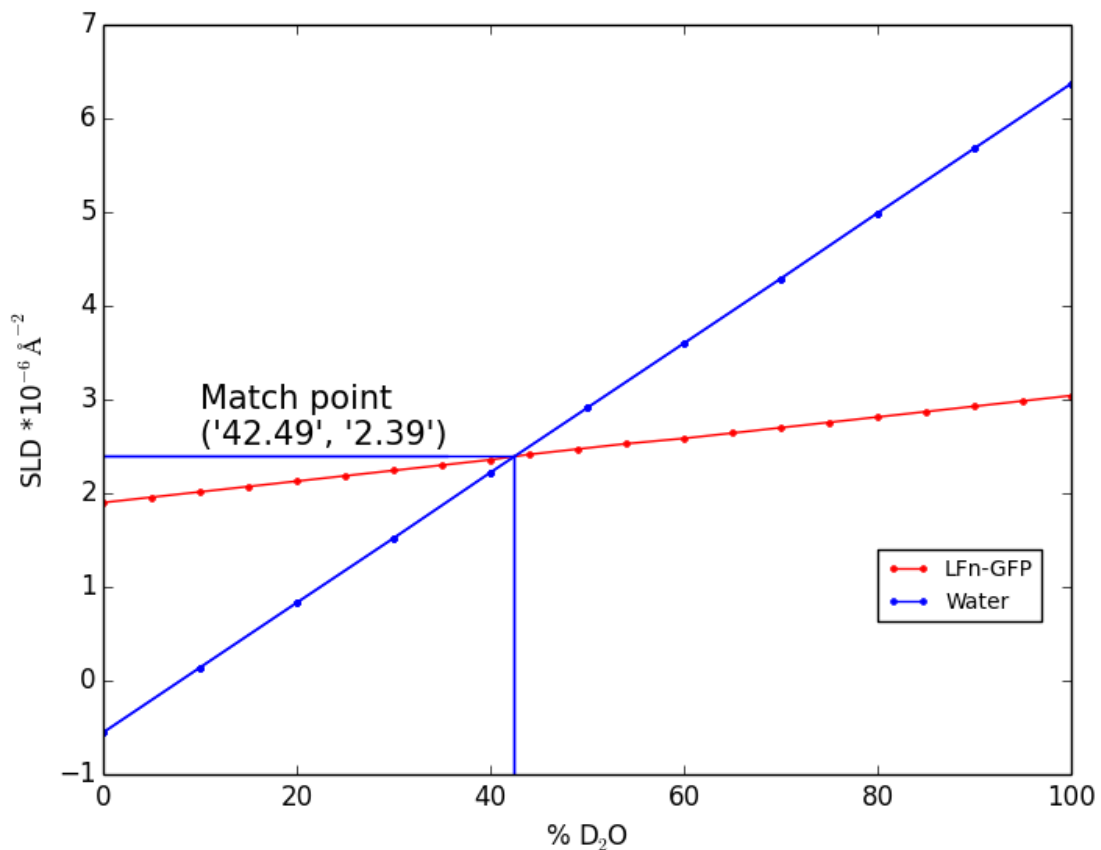
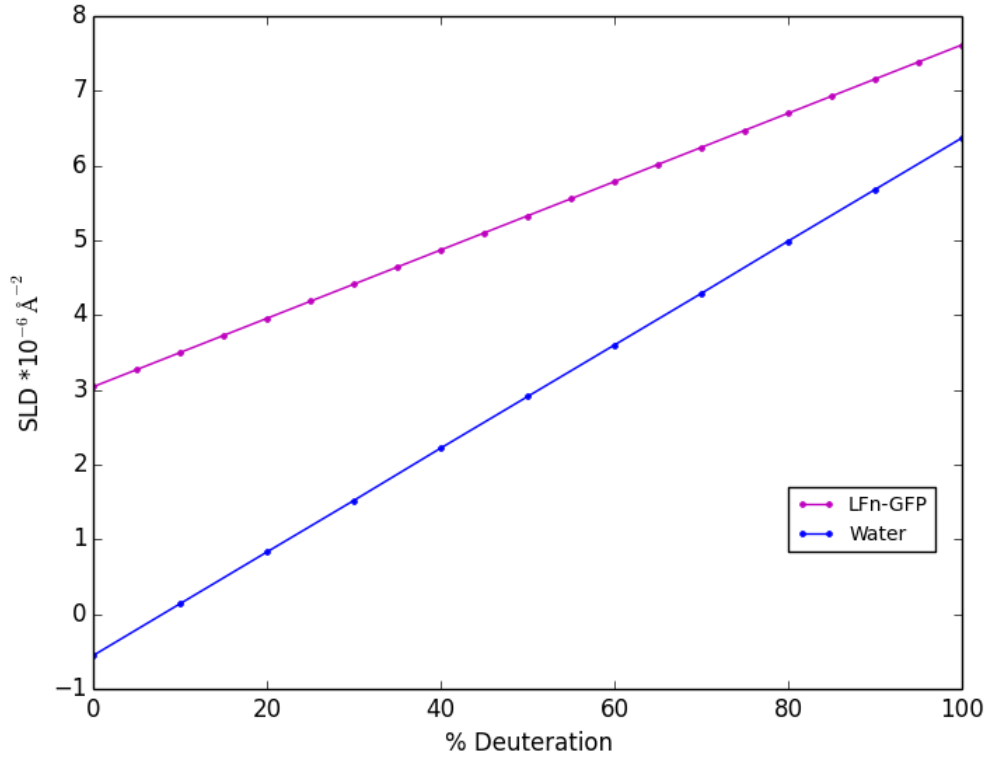


Figure 2. The scattering length density (ρ) of the inputed protein (it's sequence, % D₂O and % exchange) as a function of increasing percentage deuteration (from 0 to 100% in 5% intervals).

intervals).

There is no match point for your system



Biomolecular Scattering Length Density Calculator

Table 1. The Total number of residues, Chemical composition, Molecular weight in kilodaltons, scattering length, scattering length density (ρ), molecular volume and number of exchangeable hydrogens for the inputed protein given it's sequence, % deuteration, % D₂O concentration and % exchange.

The sequence submitted was called "Protective Antigen"

The sequence submitted was

"STSAGPTVPDRDNDGIPDSLEVEGYTVDVKNKRTFLSPWISNIHEKKGLTKYKSSPE
KWSTASDPYSDFEKVTGRIDKNV
SPEARHPLVAAAYPIVHVDMENILSKNEDQSTQNTDSQTRTISKNTSTSRHTHTSEVHG
NAEVHASFFDIGGSVSAGFSNS
NSSTVAIDHSLSLAGERTWAETMGLNTADTARLNANIRYVNTGTAPIYNVLPPTSLV
LGKNQTLATIKAKENQLSQILAP
NNYYPSKNLAPIALNAQDDFSSTPITMNYNQFLELEKTKQLRLDTDQVYGNIAATYNF
ENGRVRVDTGSNWSEVLPQIQET
TARIIFNGKDLNLVERRIA AVNPSDPLETTKPDMTLKEALKIAFGFNPNLQYQGGK
DITEFDNFDDQQTSQNIKNQLA
ELNATNIYTVLDKIKLNAKMNILIRDKRFHYDRNNAVGADES VVKEAHREVINSSTE
GLLNIDKDIRKILSGYIVEIE
DTEGLKEVINDRYDMLNISSLRQDGKTFIDFKKYNDKLPLYISNPNYKVVVYAVTKE
NTIINPSENGDTSTNGIKKILIF SKKGYEIG."

The percentage of D₂O in the solution is "100"

The percentage of deuteration is "0"

The percentage of exchange is "90"

The concentration of the biomolecule in mg/ml is "0"

Total number of residues is 568.

Chemical composition C2792 N 771 O 875 S 6 H 4338.5 P 0

The molecular weight of the biomolecule is 64.758 kDa

The Scattering length is $2438.75 \times 10^{-4} \text{Å}$

The scattering length density (ρ_m) of the molecule is $3.167 \times 10^{-4} \text{Å}^{-3}$

The scattering length density (ρ_s) of the solvent is $6.376 \times 10^{-4} \text{Å}^{-3}$

The molecular volume is 77005.9 Å³

The number of exchangeable hydrogens at pH 7.0 is 1051.5

The density of the biomolecule is 1.4 g/ml

The estimate of intensity at zero angle I(0) of the biomolecule is 0 cm³

Figure 1. The scattering length density (ρ) of the inputed protein (it's sequence, % deuteration and % exchange) as a function of increasing D₂O concentration (from 0 to 100% in 5% intervals).

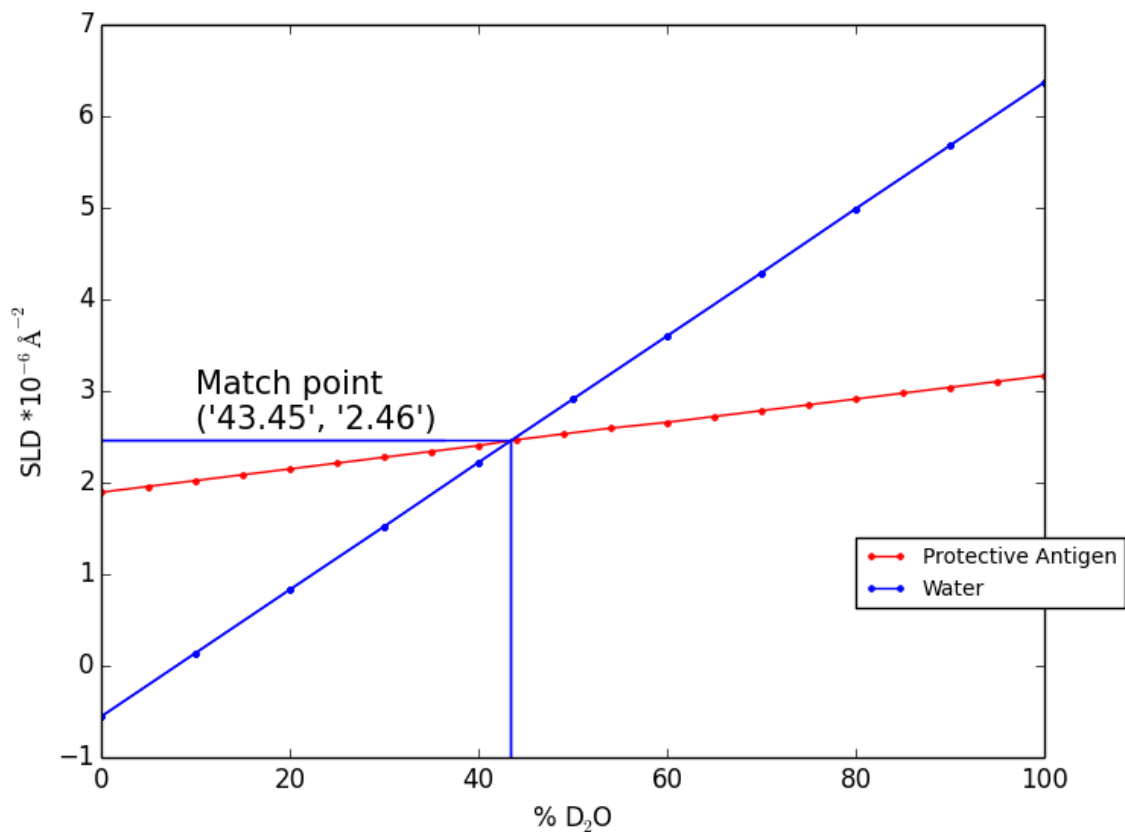


Figure 2. The scattering length density (ρ) of the inputed protein (it's sequence, % D₂O and % exchange) as a function of increasing percentage deuteration (from 0 to 100% in 5% intervals).

There is no match point for your system

